DISSERTATION

AEROSOL RETRIEVAL OVER LAND USING BACKGROUND COMPOSITES OF GEOSTATIONARY SATELLITE DATA

Submitted by

Kenneth R. Knapp

Department of Atmospheric Science

In partial fulfillment of the requirements

for the Degree of Doctor of Philosophy

Colorado State University

Fort Collins, Colorado

Spring 2000

UMI Number: 9981347

Bell & Howell Information and Learning Company
300 North Zeeb Road
P.O. Box 1346
Ann Arbor, MI 48106-1346

COLORADO STATE UNIVERSITY

February 8, 1999

WE HEREBY RECOMMEND THAT THE DISSERTATION PREPARED UNDER OUR SUPERVISION BY KENNETH R. KNAPP ENTITLED AEROSOL RETRIEVAL OVER LAND USING BACKGROUND COMPOSITES OF GEOSTATIONARY SATELLITE DATA BE ACCEPTED AS FULFILLING IN PART REQUIREMENTS FOR THE DEGREE OF DOCTOR OF PHILOSOPHY

Committee on Graduate Work

Adviser

Department Head

ABSTRACT OF DISSERTATION

AEROSOL RETRIEVAL OVER LAND USING BACKGROUND COMPOSITES OF GEOSTATIONARY SATELLITE DATA

Over the past decade, aerosol research has seen substantial growth in knowledge and remote sensing capabilities. Aerosols – especially those influenced anthropogenically – are now seen as a significant source of uncertainty in the global radiative balance. Also, aerosol remote sensing will soon be able to monitor aerosols more accurately with the launch of the Terra satellite and its suite of instruments, i.e. the Moderate Resolution Imaging Spectrometer (MODIS). While this and other satellites will provide measurements of aerosol properties over data-sparse regions, the diurnal characteristics will remain unknown because the instruments are limited to once-per-day observations from polar-orbiting satellites. However, observations from the Eighth Geostationary Operational Environmental Satellite (GOES-8) visible channel allow measurement of the aerosol diurnal cycle.

Herein, a method is developed which uses GOES-8 to retrieve aerosol optical depth (AOD). A background composite is compiled for each satellite observation time from imagery during the course of a month and is then corrected for atmospheric extinction to obtain a surface reflectance. Optical depths are then retrieved using a radiative transfer model.

However, satellite remote sensing requires accurate radiance measurements, so the GOES-8 visible sensor was calibrated from August 1995 through 1999. Results suggest a 5.6% annual degradation in sensor response. These results were used to retrieve AOD over South America in 1995 and 1998. The biomass burning regions provide an area with strong aerosol signal and the recent Smoke, Clouds and Radiation-Brazil (SCAR-B) field experiment provided a relatively well-described biomass burning aerosol.

The GOES AOD retrieval was highly correlated with ground truth sites in South America. An increase in the GOES imagery availability in 1998 provided a comparison of daily average values, which resulted in correlation coefficients of 0.91 and 0.97. Retrievals from 1995 also compared well with retrievals from aircraft imagery. Ten retrievals were collocated with AOD estimates from the MODIS airborne simulator, of which, eight were highly correlated. The 1998 retrievals were also compared to satellite radiative flux estimates. In general, correlation was high when the number of comparison points were high. Finally, methods for estimating aerosol mass emission rates from biomass burning are discussed and compared.

Kenneth R. Knapp

Department of Atmospheric Science

Colorado State University

Fort Collins, Colorado 80523

Spring 2000

ACKNOWLEDGMENTS

- Many thanks to my advisor, Dr. Thomas Vonder Haar who has supported my research on aerosols for five and a half years.

- Thanks also to my dissertation committee: Drs. Mahmood Azimi-Sadjadi, Yoram Kaufman, Sonia Kreidenweis and Graeme Stephens for their support.

- Insightful discussions with Andy Jones, Yoram Kaufman, Tom Greenwald, Sundar Christopher, and Steve Miller have also been very helpful.

- Thanks also to the TVH students of past and present who are too numerous to list.

- Thanks also to those who provided data for this research:
  - CIRA – GOES imagery
  - Brent Holben – AERONET data
  - Dennis Chesters – GOES calibration and spectral information
  - www.ssmi.com – for the SSM/I wind data
  - Rong-Rong Li – for the MAS aerosol optical depth retrievals
  - NASA Langley DAAC – CERES data
  - Frank Evans – Mie scattering code
  - Sonia Kreidenweis and NASA/GSFC Code 916– for ECMWF reanalysis wind data
  - Si-Chee Tsay – CAR data

- This research has been supported by Department of Defense Center for Geosciences/Atmospheric Research Agreement # DAAL01-98-2-0078 and the Center for Earth Atmosphere Studies (CEAS under NASA Contract #NCC5-288).

And special thanks to my wife, Carrie, who has patiently shared her new husband with this dissertation.

Table of Contents

1. Introduction

1.1 Purpose

Aerosols – microscopic particles suspended in the atmosphere – have a lifetime of days to weeks in the atmosphere, yet can affect our lives in many ways. To the common man, these particulates are called haze or smog and often are the blame for poor visibility on "hazy, hot and humid" summer days. They are the source of spectacular sunsets, especially after large volcanic eruptions. Aerosols can also hinder military and civilian aircraft operations alike. One won't soon forget the news of John F. Kennedy Jr.'s plane crashing near Martha's Vineyard, which was likely caused by poor visibility in heavy haze (Prospero et al., 1999). To the Department of Defense, aerosols can also decrease the performance of optically-guided weaponry.

In atmospheric science, aerosols can affect weather and climate in many ways. Aerosols scatter shortwave radiation, effectively increasing the regional albedo. This albedo increase has a cooling effect on the climate and is termed the direct effect, because aerosols directly interact with radiation. The indirect effect is where aerosols act as cloud condensation nuclei. A significant change in their atmospheric abundance can affect the distribution and possibly the amount of liquid cloud water in a cloud; this, in turn, can affect the cloud albedo and lifetime. To the atmospheric chemist, an aerosol provides a surface for heterogeneous reactions in the atmosphere. To the oceanographer, they represent noise in satellite remote sensing of ocean color and sea surface temperature. Ocean color measurements can provide information on chlorophyll concentrations. To those interested in surface vegetation, aerosols represent a significant noise that must be corrected. This dissertation will help the understanding of aerosols over land.

For these reasons, it is important to understand where and when aerosols form and how they are transported. Networks have been developed and used to determine the aerosol optical properties around the U.S. and the world. For example, the interagency monitoring of protected visual environments (IMPROVE) network measures chemical and optical properties of aerosols at national parks around the U.S. Also, the aerosol robotic network (AERONET) measures aerosol optical properties around the globe. Conversely, smaller intensive field campaigns have helped to understand aerosol sources, transports and optical properties for specific aerosol types. Examples include TARFOX (Tropospheric Aerosol Radiative Forcing Observational Experiment - Russell et al., 1999) where aerosols transported off the Eastern Coast of the U.S. were studied and SCAR-B (Smoke, Clouds and Radiation – Brazil, Kaufman et al., 1998) which investigated the biomass burning aerosol. These networks and field campaigns only measure aerosols over a finite area. Satellites can provide near-global coverage of the Earth with time scales on the order of days or less and thus can be used to fill in the gaps between these in situ datasets. These satellite observations can also provide information in data sparse areas. The Geostationary Operational Environmental Satellite (GOES) has a temporal coverage which will enable a better understanding of the aerosol temporally and spatially.

The primary tradeoff between geostationary and polar-orbiting satellites is between temporal and spatial coverage. Polar-orbiting satellites can view the entire

Earth during a 12 hour period. However, the temporal resolution is 12 hours, often measuring one daylight and one night condition for each location. This limits the study of atmosphere to features with no diurnal cycle, or where that cycle is known. Currently, the aerosol diurnal cycle is not well-understood. As will be shown here, one can exist at different locations such that observations from a polar orbiting instrument will miss a significant portion of the cycle. Thus, geostationary observations of the aerosol diurnal cycle are needed to supplement the global aerosol analysis from polar-orbiting sensors.

Also, satellite aerosol remote sensing studies have primarily been limited to ocean regions. Aerosols are more easily detected over water than land for two reasons. First, the ocean provides a dark background over which aerosols generally increase the reflectance. Second, the background is consistent; it varies little with time or space and thus can be characterized quite accurately. Conversely the land surface is brighter, so satellites are less sensitive to aerosols. Also, land surface reflectance can vary temporally and spatially, which can increase uncertainty in aerosol remote sensing over land.

The GOES aerosol optical depth (GOES-AOD) retrieval algorithm takes advantage of a calibrated sensor on the new GOES-series of satellites. Prior to GOES-8, the GOES series was uncalibrated and had a low signal-to-noise (S/N) ratio. The new generation of GOES (beginning with GOES-8) has a higher S/N ratio and 10-bit quantization. Yet the instrument still has a broad spectral response (0.52-0.72μm) and no onboard calibration. This study will investigate the ability of the GOES satellite to remotely sense aerosol optical depth over land.

The GOES-AOD algorithm can sense aerosols over land at high temporal and spatial scales with an uncertainty of ±33% in AOD, calculated from an uncertainty study. This algorithm is validated against ground-truth measurements of biomass burning aerosols, showing an uncertainty near ±20-30%. The algorithm is also compared to aircraft retrievals of aerosol optical depth and results are generally within ±0.2. These retrievals are compared to satellite estimates of shortwave and longwave radiation fluxes. Correlations are found for shortwave fluxes, while longwave fluxes are generally uncorrelated with retrieved aerosol optical depth. The GOES-AOD algorithm is also used to estimate aerosol mass emission rates of these biomass burning areas.

The goal of this dissertation is to demonstrate the viability of using both geostationary and polar orbiting satellites for climatological studies of the earth. While the instruments launched on the Earth Observation System (EOS) platforms have specific channels to derive aerosol optical properties, they lack the diurnal observations to fully quantify the aerosol effects. Conversely, the GOES instruments have only one channel specifically sensitive to aerosols, yet can observe the diurnal changes in aerosol properties. By combining the observations of the systems, the advantages of both systems can be utilized.

The next chapter describes aerosols, followed by the past and current aerosol remote sensing research. The radiative transfer model used to retrieve aerosol optical depth from GOES-8 is then described, followed by a description of the instruments used herein. The visible sensor in the GOES-8 Imager has a degrading throughput, thus the instrument is calibrated in chapter 7 The GOES aerosol optical depth retrieval algorithm is then described, along with a sensitivity study. The algorithm is validated in chapter 9 followed by application of the retrieval results to the aerosol direct effect and estimations of aerosol mass emission rates of biomass burning. Conclusions are then made and directed toward future work.

2. Aerosols

2.1 Physical Properties

The term aerosol encompasses any particle (except cloud droplets) suspended in the atmosphere, but usually with a radius between 0.005 μm to 10 μm (Wallace and Hobbs, 1977; Houghton, 1985, AT621 Class Notes). Particles smaller than 0.005μm generally have a very short lifetime in the atmosphere as they are strongly affected by Brownian diffusion and grow by coagulation with other particulates. Particles larger than 10μm have a large terminal velocity (~1 cm s^{-1} or more) and settle out of the atmosphere within hours of insertion. Aerosols are generally described by their size distribution, chemical composition and shape.

The size distribution describes the frequency distribution of particle number per radius. The size distribution can be measured by such instruments as optical particle counters, stage impactors or differential mobility analyzers. An example of an aerosol size distribution is given in figure 2.1 which was measured during the Southern Hemisphere Marine Aerosol Characterization Experiment (ACE-1) off the southern coast of Australia. Aerosol distributions can be described by mathematical models, which will be discussed further in the next section. The size distribution is used in remote sensing to determine the scattering characteristics of the aerosols.

In remote sensing applications aerosols are generally characterized as being dominated by one of the following constituents: sulfates (and other industrial compounds), sea salt, black carbon, and mineral dust (e.g., Hess et al., 1998). These categories are also described by Lenoble and Brogniez (1984) as water soluble (i.e., sulfate), dust-like, soot and oceanic (i.e., sea salt). A description of each type follows. Other aerosol types, which are present in the atmosphere in smaller quantities, include organics, nitrate, or stratospheric aerosols. Also, other aerosol classifications exist such as the categories measured by the IMPROVE network: sulfate, nitrate, organic carbon, light absorbing carbon, soil, non-soil, salt, coarse mass, and reconstructed fine mass.

Sulfates have two primary gas-phase sources: phytoplankton production of dimethylsulfide (DMS) in the oceans and anthropogenic production of SO_2. Both compounds oxidize in the atmosphere to produce sulfate (AT621 notes). Therefore, sulfate aerosols are found in abundance over the deep ocean and downwind of large industrial regions (e.g., the eastern U.S. and eastern Asia). Also, because sulfates are generally formed through chemical reactions in the atmosphere, they tend to be small. However, sulfates are also hygroscopic, so they readily absorb water. Sulfates are generally spherical and scatter visible radiation.

Sea salt (as the name suggests) is produced from the evaporation of ocean spray over the ocean, so it has no significant anthropogenic source. Because it often forms from the evaporation of small droplets, sea salt can be quite large; a characteristic radius is 0.13μm. Sea salt and sulfate (derived from DMS) make up a large portion of the aerosols over the deep oceans.

Mineral dust comes from the winds picking up dust and lofting them high into the atmosphere (from tens of meters to kilometers). The major sources of these are the desert regions of the world. So strong is this source that Saharan dust palls were among the first aerosols to be observed from meteorological satellites (Carlson and Prospero, 1972). Mineral dust is also present most anywhere the wind blows. Anthropogenic influences have recently been studied as a significant influence on climate (Haywood et al., 1999). Mineral dusts are generally larger aerosols, yet can have a long lifetime when lofted kilometers into the atmosphere by dust storms. For example, Saharan dust is often detectable over southern Florida having been transported thousands of kilometers.

Black carbon in the atmosphere is generally due to combustion. Significant sources include biomass burning areas in Central and South America as well as Africa. Black carbon is the primary atmospheric aerosol which absorbs visible radiation.

2.2 Size Distributions

The frequency of aerosol size as a function of aerosol radii – the size distribution – is primarily affected by formation type and water vapor uptake. Three regimes categorize the aerosol size: the fine particle, accumulation and large modes. Particles that make up the fine particle mode generally have a radius less than 0.1μm and are formed through gas-to-particle conversion or condensation on smaller particles. The accumulation mode is generally the radius range from 0.1 to 1 μm. Large mode ($r > 2\mu$m) aerosols are usually formed by the wind (such as sea spray or dust) and have shorter lifetimes. Large mode aerosols are also referred to as coarse mode.

Aerosol particles can significantly be affected by the water vapor content of the air. Most aerosol particles have some amount of liquid water on them. Aerosols which are hygroscopic will have more water on them and their size will be largely dependent on the atmospheric relative humidity. Thus simple changes in the relative humidity can significantly change the aerosol size distribution.

Aerosols are described by an aerosol size distribution, n(r). This is the number of aerosol particles per radius size. A number of different size distribution models have been used in recent years to simulate the aerosol optical effects. Lenoble and Brogniez (1984) provide an in-depth comparison of these different aerosol models.

Early remote sensing applications used Junge size distributions which can be described by:

$$n(r) = \begin{matrix} Cr^{-(v+1)} & r_1 < r < r_2 \\ 0 & r < r_1, r > r_2 \end{matrix}$$

where C is a constant (related to the amount of aerosol present), r_1 and r_2 are the radius limits of the distribution and v is used to fit the measured size distributions. Slight modifications of the Junge size distribution, such as the Power law, are also prominent in the literature. This size distribution lends itself to aerosol remote sensing because the v parameter is related to the spectral optical extinction. The Junge model has one variable parameter, v.

The log-normal distribution is also a widely-used size distribution, described by:

$$n(r) = \frac{C}{r \ln \sigma} \exp\left[-\frac{\ln^2 r / r_m}{2 \ln^2 \sigma} \right],$$

where the distribution is described by two variables: the geometric mean radius (r_m, sometimes called the mode radius or mean radius) and σ is the standard deviation of the distribution. Multi-modal log-normal distributions are used frequently, where each mode represents a different aerosol type. This is simply:

$$n(r) = \sum_{i=1}^{N} f_i \frac{C}{r \ln \sigma_i} \exp\left[-\frac{\ln^2 r / r_{m,i}}{2 \ln^2 \sigma_i} \right],$$

where f_i is the fraction of each aerosol type being model for N aerosol types. This method is used herein to model the aerosol optical effects, following the multi-modal aerosol distributions of Kaufman et al. (1997). In general, the modeled modes describe modes observed in the atmosphere. These modes define the four aerosol types used in the MODIS over-land aerosol retrieval algorithm, defined by Kaufman et al. (1997). The definitions of the four aerosol types are given in Table 2.1.

The refractive index and aerosol shape are primarily determined by the aerosol formation process. The refractive index – generally a function of chemical composition – describes how well the aerosol particulate scatters and absorbs radiation and is discussed next.

2.3 Aerosol Optical Properties and Mie Scattering

The following description of Mie theory and resulting information about atmospheric aerosol effects on radiation was presented in the AT772 class. The primary problem that Mie theory attempts to solve is:

What happens when an electric field interacts with an atmospheric particle?

This is of primary importance when studying the radiative effects of aerosol and trying to "count" the aerosol through "optical" means (optically meaning the use of an electric field that is within the visible range in the electromagnetic spectrum). Many scientists near the turn of the century focused their work on this problem. The ensemble of their collective work is summarized by the Mie theory of scattering and absorption, although many are attributed to its coincident discovery (Bohren and Huffman, 1983). The reader is referred to Bohren and Huffman (1983) for a more thorough treatment of this problem. What is described below is a summary of their detailed derivation. Note: Bohren and Huffman (1983) refer to particle radius as a, yet in this dissertation r is used to denote radius. The variable a is used in this chapter only, to maintain continuity between this summary and the original work.

Even Bohren and Huffman (1983) themselves admit that this derivation can be tedious and mathematically arduous, for example they note:

> "The mathematics, divorced from physical phenomena, can be somewhat boring. For this reason, a few illustrative examples are sprinkled throughout the chapter." (Bohren and Huffman, 1983, pg. 82)

And also, that:

> "Whereas the mathematics of Mie theory is straightforward, if somewhat cumbersome, the physics of the interaction of an electromagnetic wave with a sphere is extremely complicated." (Bohren and Huffman, 1983, pg. 82)

Again, those who have a better understanding of spherical harmonics and electromagnetic theory should feel welcome to follow along with Bohren and Huffman (1983) Chapter 4 [hereafter BH83 and references will be made to the equation numbers in BH83 when applicable]. The rest can follow this simple description of the theory described in 5 general steps.

The first step is the general solution of Maxwell's equations. This solution is in terms of the vector functions **M** and **N** which can be described by vector spherical harmonics. The solution is such that any electromagnetic field must satisfy these equations.

The second step is the description of an electromagnetic plane wave. This wave is considered as traveling along some arbitrary direction, such as along the x-axis, and is thus described by (BH83 Eq. 4.21) :

$$E_i = E_0 e^{ikx\cos\theta} \hat{e}_x \tag{2.1}$$

where the subscript i represents the incident plane wave E_i, k is the wavenumber ($k=2\pi/\lambda$, where λ is the wavelength) and x is some distance along $\hat{e}_x$ (the unit vector along the x-direction) and E_0 is the initial magnitude of the wave. This wave can also be described in terms of spherical harmonics by (BH83 Eq. 4.37):

$$E_i = E_o \sum_{n=1}^{\infty} i^n \frac{2n+1}{n(n+1)} \left(\mathbf{M}_{o1n}^{(1)} - i\mathbf{N}_{e1n}^{(1)} \right) \tag{2.2}$$

where now the terms $\mathbf{M}_{o1n}^{(1)}$ and $\mathbf{N}_{e1n}^{(1)}$ represent spherical harmonics, where **M** is an odd function and **N** is an even function (subscripts o and e, respectively) from step one. The summation along m is limited to m=1 because of orthogonality of the functions. Also, **M** and **N** are derived in terms of their components which include, among other things, functions of Legendre polynomials. BH83 interestingly note at this point that the transform was mathematically difficult and that:

> "This is undoubtedly the result of the unwillingness of a plane wave to wear the guise in which it feels uncomfortable; expanding a plane wave in spherical wave functions is somewhat like trying to force a square peg into a round hole. However, the reader who has painstakingly followed the derivation of [equation 2.2], and thereby acquired virtue through suffering, may derive some comfort from the knowledge that it is relatively clear sailing from here on." (BH83, pg. 92-93)

The third step is the calculation of the interaction of the plane wave with a dielectric sphere. Supposing the plane wave is incident upon a "homogeneous, isotropic, sphere of radius a" (BH83, pg. 93), the corresponding electric and magnetic fields can be derived. The scattered electric (E_s) and magnetic (H_s) fields are then (BH83 Eq. 4.45):

$$E_s = \sum_{n=1}^{\infty} E_n \left(ia_n \mathbf{N}_{e1n}^{(3)} - b_n \mathbf{M}_{o1n}^{(3)} \right) \tag{2.3}$$

$$H_s = \frac{k}{\omega\mu} \sum_{n=1}^{\infty} E_n \left(ib_n \mathbf{N}_{o1n}^{(3)} - a_n \mathbf{M}_{e1n}^{(3)} \right) \tag{2.4}$$

now the superscript (3) denotes the spherical harmonic terms are radial-dependent (that is, dependent upon the scattering angle) Hankel functions.

The fourth step is linking the above noted solutions to more physical quantities such as scattering angle, size of the sphere, and the refractive index of the sphere and surrounding media. Note the introduction of the spherical harmonic coefficients a_n and b_n in equation 2.3. These terms are Ricatti-Bessel functions that describe the scattering as a function of the refractive index of the sphere (m) and the size parameter (χ = ka=$2\pi a/\lambda$ where the refractive index, m, of the medium is 1). It is noted that these functions tend toward unity as m approaches one, such that the scattering field disappears as the particle becomes less discernible (BH83).

The Legendre polynomials found in the solution of **M** and **N** are combined with angle-dependent terms to form (BH83 Eq. 4.46):

$$\pi_n = \frac{P_n^1}{\sin\theta}, \quad \tau_n = \frac{dP_n^1}{d\theta} \tag{2.5}$$

which are functions calculated through upward recurrence, given $\pi_0 = 0$, $\pi_1 = 1$, (BH83 Eq. 4.47)

$$\pi_n = \frac{2n-1}{n-1}\mu\pi_{n-1} - \frac{n}{n-1}\pi_{n-2} \text{ and } \tau_n = n\mu\pi_n - (n+1)\pi_{n-1} \tag{2.6}$$

where now $\mu=\cos\theta$, θ is the angle between a non-scattered incident wave and the scattered wave and P_n^1 is a Legendre polynomial. These functions are plotted for n=1 through 5 in figure 2.2. The functions π_n and τ_n allow the description of the angular aspects of the scattered field using the solutions of **M** and **N** from step one. The scattered field will be, in part, a summation of the fields shown in figure 2.2 as well as modes for n > 5. It is important to note that the forward mode (near θ = 0°) is always positive, with the width of the mode decreasing as n increases (because as n increases, so do the number of lobes in τ_n and π_n). The corresponding mode at θ = 180° exists for every other value of n. Also, as n increases the forward mode becomes larger. Thus as n (which corresponds to the size of the sphere) increases, so does intensity of the forward scattering mode of the calculated phase function.

The fifth step is the combining of these steps to find a final solution of the scattered electric field. Equations 2.3 and 2.4 now allow the scattered components of the electric field to be written as:

$$E_{s\theta} \sim E_o \frac{e^{ikx}}{-ikx} \cos\phi \sum_n \frac{2n+1}{n(n+1)} \left(a_n \tau_n + b_n \pi_n\right) \tag{2.7}$$

$$E_{s\phi} \sim -E_o \frac{e^{ikx}}{-ikx} \sin\phi \sum_n \frac{2n+1}{n(n+1)} \left(a_n \pi_n + b_n \tau_n\right) \tag{2.8}$$

or more commonly:

$$E_{s\theta} \sim E_o \frac{e^{ikx}}{-ikx} \cos\phi S_2 \text{ and } E_{s\phi} \sim -E_o \frac{e^{ikx}}{-ikx} \sin\phi S_1 \tag{2.9}$$

where (BH83 Eq. 4.74):

$$S_1 = \sum_n \frac{2n+1}{n(n+1)} \left(a_n \pi_n + b_n \tau_n\right) \text{ and } S_2 = \sum_n \frac{2n+1}{n(n+1)} \left(a_n \tau_n + b_n \pi_n\right) \tag{2.10}$$

The scattered intensity of initially unpolarized light is thus:

$$I_s = S_{11} I_i \tag{2.11}$$

Where (BH83 Eq. 4.77):

$$S_{11} = \tfrac{1}{2}(|S_2|^2 + |S_1|^2) \tag{2.12}$$

S_{11} is better known as the phase function of a particle, $P(\theta,m,\chi)$. It describes the intensity of light at some scattered angle (θ) from the incident direction. Thus the Mie solution derives the scattering parameters in terms of the size of the sphere, refractive index of the sphere and medium, and the wavelength of radiation.

2.3.1 Scattering Efficiency

BH83 derive the scattering and extinction cross sections (C_{sca} and C_{ext}, respectively) as:

$$C_{sca} = \frac{2\pi}{k^2} \sum_n (2n+1)\left(|a_n|^2 + |b_n|^2\right) \tag{2.13}$$

$$C_{ext} = \frac{2\pi}{k^2} \sum_n (2n+1) \mathrm{Re}\{a_n + b_n\} \tag{2.14}$$

where the value is the area of radiation affected (absorbed or scattered) by the sphere. C_{sca} and C_{ext} are the cross-sectional area of the incident radiation that is scattered or extincted by the sphere. This value is generally normalized by the physical cross section of the sphere, which defines the extinction (scattering) efficiency, Q_{ext} (Q_{sca}):

$$Q_{ext,sca} = \frac{C_{ext,sca}}{\pi a^2} \tag{2.15}$$

Q_{ext} values are shown in figure 2.3 for three values of m. In general, Q_{ext} remains near zero until a certain size parameter is reached, where the efficiency significantly increases. A maximum efficiency is quickly attained, then the efficiency decreases and then asymptotes to a value of two. The portion of the efficiency curve to the left of the maximum efficiency is known as the reddening area. In this portion, the extinction efficiency increases with increasing size parameter, thus it is inversely proportional to wavelength. Thus red light is transmitted more effectively than the blue light, which provides the world with red sunsets.

The damped oscillations asymptote to a value of two, regardless of m as χ goes to infinity. This is described as the extinction paradox: that no matter the refractive index, if the particle is significantly larger than the wavelength of radiation then the extinction of that particle is twice its cross sectional area. This is because extinction is not only the radiation directly removed from the incident wave by reflection or scattering, but also that which the particle refracts. Thus, a particle refracts as much light as is incident upon its cross sectional area when χ is sufficiently large. It is interesting to note that this paradox is independent of refractive index, except that as m decreases it takes larger particles before the oscillation is significantly damped. It will also be shown that the extinction paradox also exists regardless of absorption.

The refractive index is the ratio of the speed of light in the particle to that in a vacuum. Thus, as the refractive index increases to large values, smaller particles can affect the radiation more. This is seen in Figure 2.3 that the size parameter of maximum Q_{ext} decreases with increasing m. For instance, when $\lambda = 0.55$ μm, the maximum Q_{ext} at m = 1.33 is about an 0.52μm radius particles, however the radius of such a particle increases to 5.2μm for m = 1.03. So, a particle with a small refractive index needs to be larger before it significantly affects the radiation.

Absorption is incorporated in Mie calculations by increasing the imaginary portion of the refractive index. Absorption is calculated from Mie code results as the difference between the extinction and scattering efficiencies. An example of Q_{ext} for an absorbing particle is shown in Figure 2.4, with related Q_{sca} and absorption efficiency (Q_{abs}). Features like the reddening area and the extinction paradox remain prevalent when absorption is included. The Q_{sca} parameter represents the oscillating portion of Q_{ext}, while Q_{abs} does not oscillate. Q_{abs} does show an increase of absorption with m near the reddening area, and reaches a maximum in absorption near the maximum Q_{ext}. The amount of absorption in figure 2.4 is somewhat large compared to general atmospheric aerosols. Figure 2.5 shows the Q_{ext} as the absorption increases. For small imaginary values, the absorption (and the affect on the Q_{ext} spectrum) is small. However, for significant absorptive materials, Q_{ext} takes on a shape more similar to Q_{abs} in figure 2.4 because the Q_{sca} is very small

Q_{ext} is a microphysical quantity that needs to be modified before use in the radiative transfer equations. This is the difference between microphysical optical properties (e.g. Q_{ext} for each particle) and bulk optical properties (e.g. extinction of an aerosol size distribution). The extinction coefficient ($b_{ext,\lambda}$) at some wavelength, λ, is related to Q_{ext} by:

$$b_{ext,\lambda} = \int_0^\infty n(r)\pi r^2 Q_{ext,\lambda}\,dr \qquad (2.16)$$

where n(r) is the aerosol size distribution and r is the radius of the particle. This equation demonstrates how an aerosol size distribution affects the bulk radiative properties. $b_{ext,\lambda}$ was calculated for various wavelengths from the sample ACE-1 size distribution (figure 2.1) and is plotted in Figure 2.6, note the similarities to previous plots of Q_{ext}. The scattering decreases with wavelength for wavelengths longward of 0.1μm, thus transmitted light would appear red (again, the reddening region). Also, scattering becomes negligible for $\lambda > 3\mu$m.

The aerosol optical depth, τ, is then the vertical integral of b_{ext}:

$$\tau_\lambda = \int_0^\infty b_{ext,\lambda}\,dz$$

τ is related to the transmittance, T, of radiation through an atmosphere along the zenith angle μ via Beer's law:

$$T = \exp(-\tau/\mu)$$

Thus as τ increases, the transmission of solar radiation through the atmosphere decreases.

The Mie solution for scattering is convenient for spheres with a radius near the magnitude of the wavelength of radiation. This is because the convergence of equation 2.10 is dependent on the size parameter; convergence occurs more quickly for smaller particles. It becomes quite time consuming to perform Mie calculations for $\chi > 1000$. Therefore, it is more convenient to use geometric optics to calculate scattering properties of particles much larger than the wavelength of radiation. Also for very small particles, it is more efficient to use the approximation that the particles scatter as a Rayleigh scatterer – which has a simpler solution for scattering.

The amount of scattering is dependent also on the number of scatterers. Q_{ext} for atmospheric molecuies is very small at solar radiation wavelengths, however it has a significant number of scatterers. Figure 2.7 shows the Rayleigh, Mie and geometric optics regimes of scattering solution for various sizes of atmospheric particles and various wavelengths (after Kidder and Vonder Haar, 1995; Wallace and Hobbs, 1977). In general, aerosols have a significant impact at solar wavelengths, where χ ~ 1-20. Aerosols can also scatter and absorb terrestrial radiation, but only if the number of coarse mode aerosols is very large.

2.3.2 The Phase Function, P(θ)

The phase function is the angular distribution of radiation scattered by an atmospheric aerosol. As described above, phase function is defined by equation 2.12 for Mie scattering. An example of a phase function calculated by the FORTRAN Mie code provided by BH83 (bhmie.f) is given in figure 2.8 for a monodisperse size distribution (or for one particle) of χ = 100, 10, 1, and 0.1. These phase functions have been normalized (as is generally done) by:

$$1=\frac{1}{4\pi}\int P(\theta,m,\chi)d\Omega=\frac{1}{4\pi}\int_0^{2\pi}\int_0^{\pi}P(\theta,m,\chi)\sin\theta d\theta d\phi=\frac{1}{2}\int_0^{\pi}P(\theta,m,\chi)\sin\theta d\theta \quad (2.17)$$

As can be seen in figure 2.8, the forward scattering peak significantly increases with χ. Also notable is that with the larger χ values are the ripples caused by the numerous modes of the τ_n and π_n functions in equations 2.7 and 2.8. However, atmospheric aerosols are generally not monodisperse, but polydisperse, sometimes modeled by log-normal, gamma or power-law distributions. Phase functions of actual (or modeled) size distributions are calculated from the phase function of each particle size, weighted by the number distribution of each particle size, in a similar manner to b_{ext} (Eq. 2.16):

$$P(\theta)=\frac{1}{C_{sca}}\int_0^\infty n(r)P(\theta,m,\chi)dr \qquad (2.18)$$

Figure 2.9 shows the calculation of the phase function for the example ACE-1 size distribution (Figure 2.1, assuming m = 1.33 + 0.0i). The gray lines represent the Mie phase function for each radius bin in the example size distribution. The heavy black line is the average of the phase functions weighted by n(r).

2.3.3 Nonsphericity

The above calculations all have a common assumption: scattering particles are completely spherical. This section will show some comparisons of $P(\theta)$ and C_{ext} for spherical vs. non-spherical particles. While Mie theory holds only for spherical particles, it provides an excellent "first-order" approximation toward the understanding of the full non-spherical scattering:

> "On the one hand, there are those who scoff at the use of the Mie theory to describe any properties of nonspherical particles, the type of particles that are likely to inhabit planetary atmospheres and the interstellar medium; on the other hand, there are those who unquestioningly use Mie theory for any and every aspect of light interaction with such particles. Neither attitude is enlightened. The Mie theory, limited though as it may be, does provide a first-order description of optical effects in non-spherical particles, and it correctly describes many small-particle effects that are not intuitively obvious." (BH83, pg. 83)

The following calculations for nonspherical particles are performed with T-matrix code developed by Mike Mishchenko (Mishchenko et al., 1995). Calculations are made for particles with m = 1.33 + 0.0i at λ = 0.55 μm.

The intuitive change of spherical versus non-spherical particles is that the scattering phase function will change. The term a/b defines the sphericity of the nonspherical particles where a/b represents the ratio of the lengths of the axes of an ellipse. An oblate spheroid is a solid created by rotating an ellipse about its minor axis (something akin to the classical flying saucer). Conversely, the prolate spheroid is a solid rotated about its major axis (something akin to a kernel of rice). For these calculations, a/b is the ratio of the axis of rotation to the other axis. Thus when a/b = 1 a sphere is defined. Figures 2.10 and 2.11 show phase functions for different monodisperse particle shapes. In figure 2.10, particles become more like oblate spheroids as a/b increases greater than 1. In figure 2.11, particles become more like prolate spheroids as a/b decreases less than 1. The primary change from spherical to nonspherical in both figures is that particles become more forward scattering: the forward scattering mode ($\theta < 20°$) increases and the backward scattering mode ($\theta > 150°$) significantly decreases. An interesting and important change is also in the extinction cross sections (Figure 2.12). C_{ext} is at a maximum for spherical particles, and monotonically decreases as the particles become less spherical.

The calculations for a polydisperse aerosol distribution are shown for a log-normal distribution ($r_g = 0.5$, $\sigma = 2.$). Again for oblate (Figure 2.13) and prolate (Figure 2.14) spheroids, nonspherical particles have less scattering in the backward direction. The change seems a bit less when a polydisperse distribution of particles is considered. Again, the C_{ext} decreases as the particle becomes less spherical (Figure 2.15). Relatively, the change in C_{ext} is about the same for mono- or polydisperse particles. For a/b = 1.5 (a mildly nonspherical particle), the decrease from that of a spherical particle is C_{ext} is 2.3% and 1.4% for monodisperse and polydisperse distributions, respectively.

Table 2.1 – MODIS-Land aerosol definitions from Kaufman et al. (1997). f_i has been normalized such that $\Sigma f_i = 1$. (The single scatter albedo is held constant for each mode of a distribution to fix the single scatter albedo to a certain value).

Aerosol	Mode	r_m (μm)	σ	f_i	ω_o
Continental	Water Soluble	0.005	2.97	0.35	0.96
	Dust-like	0.500	2.97	8×10^{-7}	0.96
	Soot	0.0118	2.00	0.65	0.96
Biomass burning	Accumulation	0.0448	1.82	0.999909	0.90
	Coarse	0.982	3.52	0.000091	0.90
Urban	Accumulation 1	0.036	1.82	0.895	0.96
	Accumulation 2	0.114	1.57	0.105	0.96
	Salt	0.990	1.35	2×10^{-4}	0.96
	Coarse	0.670	2.56	3×10^{-7}	0.96
Dust	Mode 1	0.001	2.12	0.987	0.92
	Mode 2	0.0218	3.19	0.013	0.92
	Mode 3	6.24	1.89	2×10^{-6}	0.92

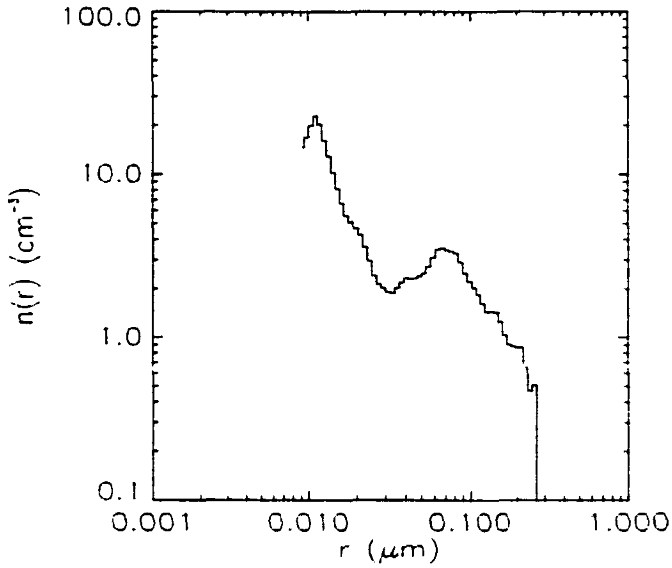

Figure 2.1 – Aerosol size distribution measurement from the ACE1 field experiment (S. Kreidenweis, personal communication, 1999).

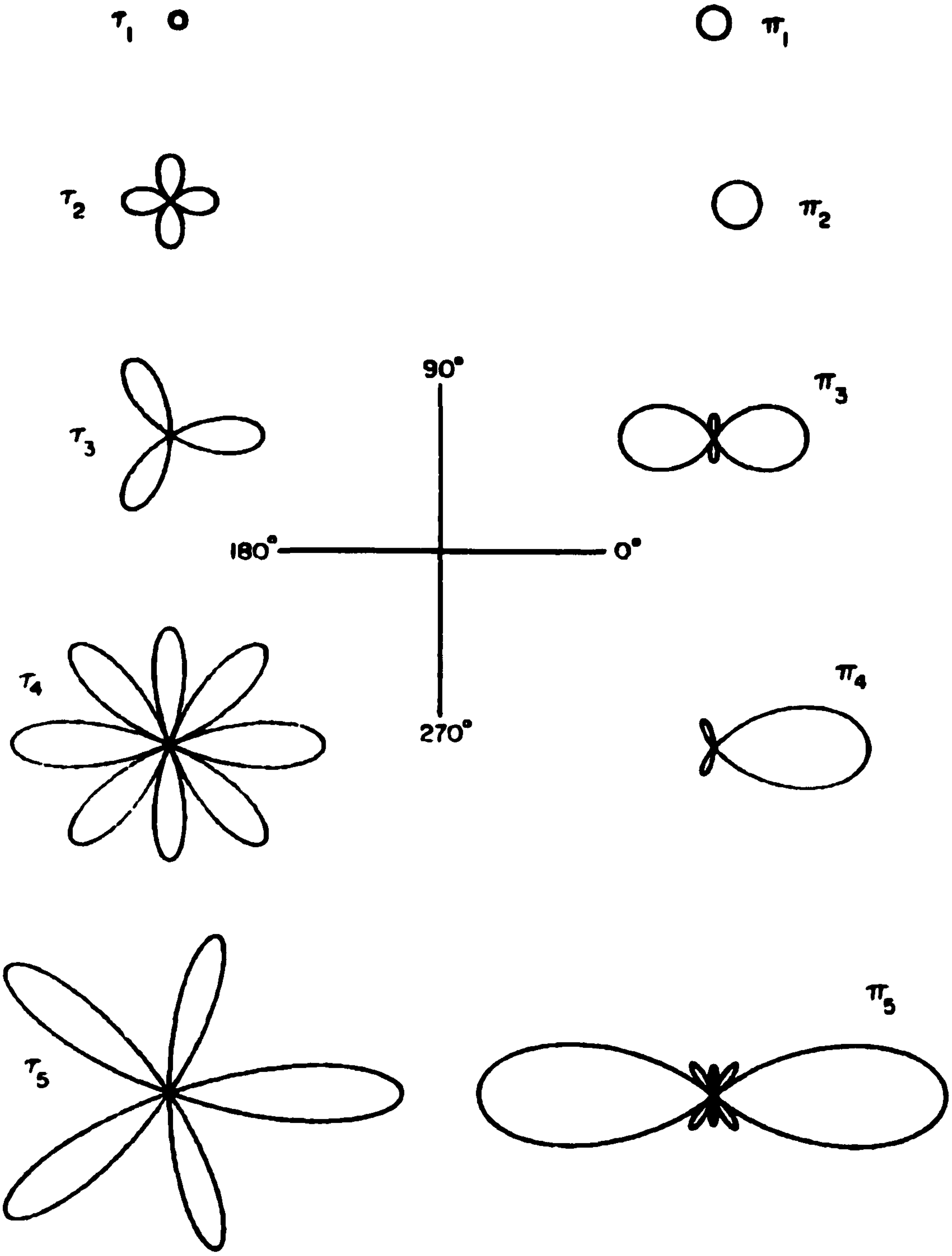

Figure 2.2 – The angle-dependent functions π_n and τ_n for n = 1-5. (from BH83, figure 4.3)

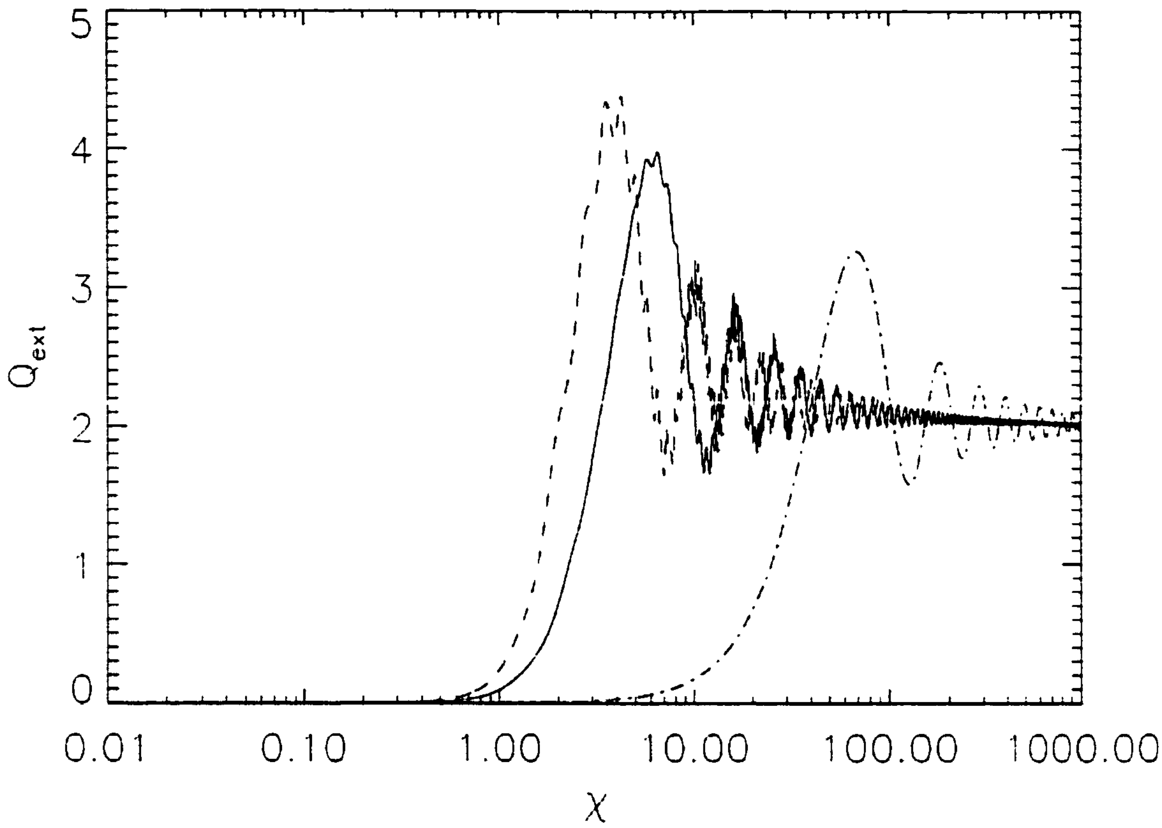

Figure 2.3 – Extinction coefficient as a function of size parameter for the following refractive indices: 1.33 (solid), 1.53 (dashed), and 1.03 (dash-dot)

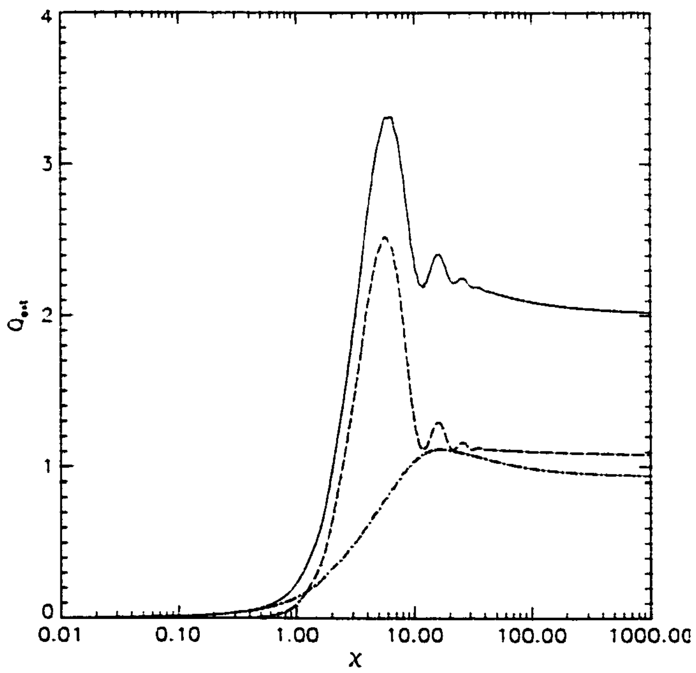

Figure 2.4 – Q_{ext} (solid), Q_{sca} and Q_{abs} as functions of the size parameter (χ) for m = 1.33 + 0.05i.

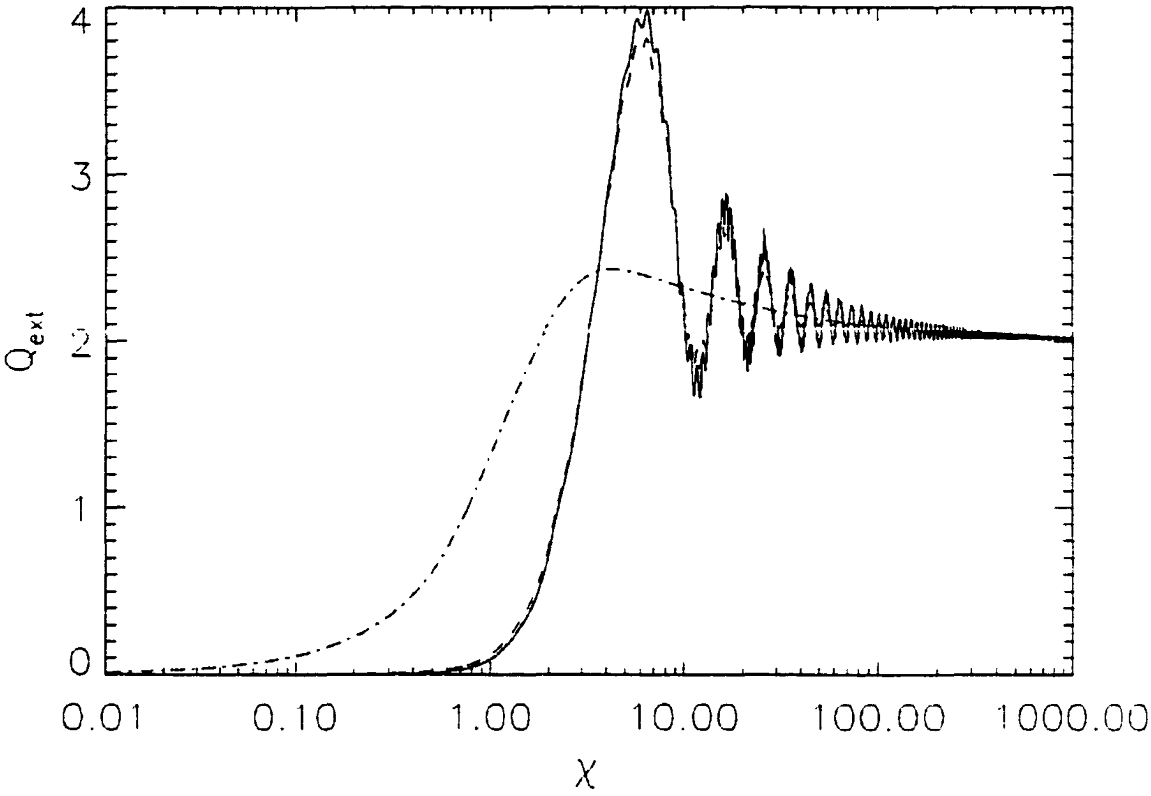

Figure 2.5 – Extinction coefficient as a function of size parameter for the following refractive indices: 1.33 + 0i (solid), 1.33 + 0.01i (dashed), and 1.33 + 0.5i (dash-dot)

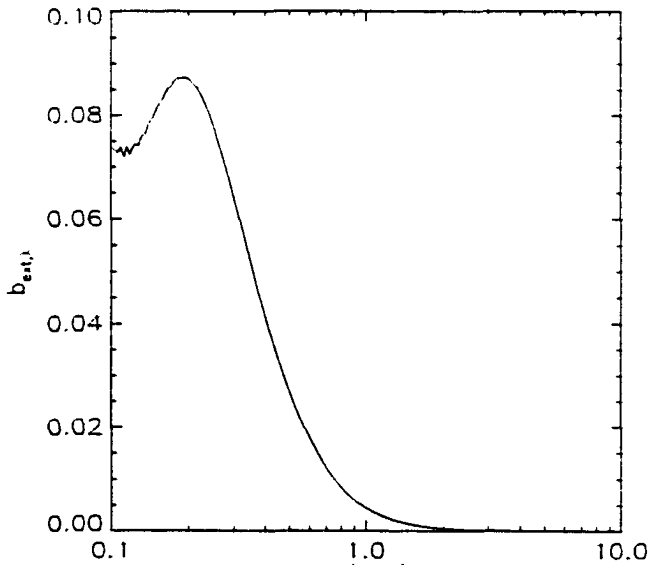

Figure 2.6 – $b_{ext,\lambda}$ as calculated for a sample aerosol size distribution from the ACE-1 field experiment

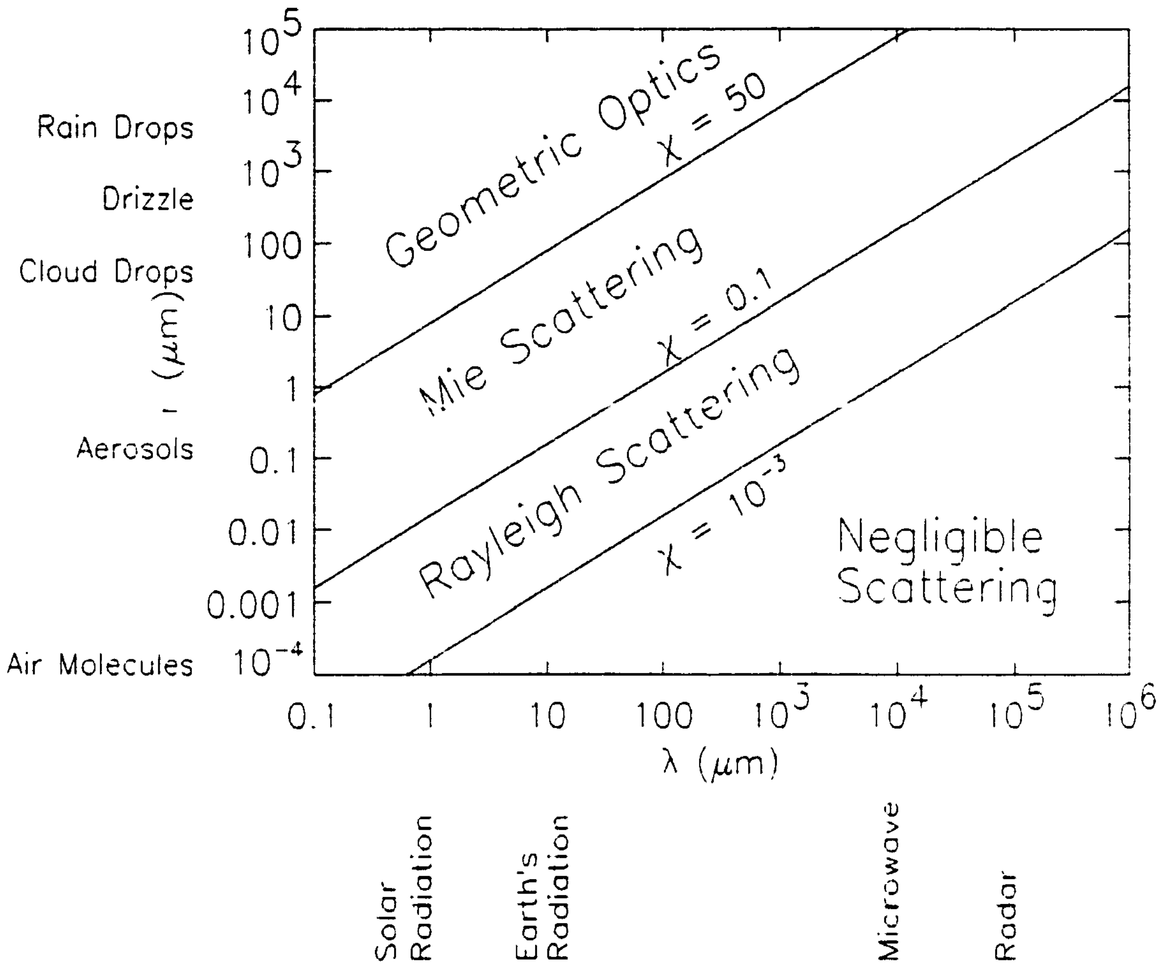

Figure 2.7 – Size parameter as a function of wavelength and particle size, delineated by scattering regimes (adapted from Kidder and Vonder Haar, 1995; Wallace and Hobbs, 1977).

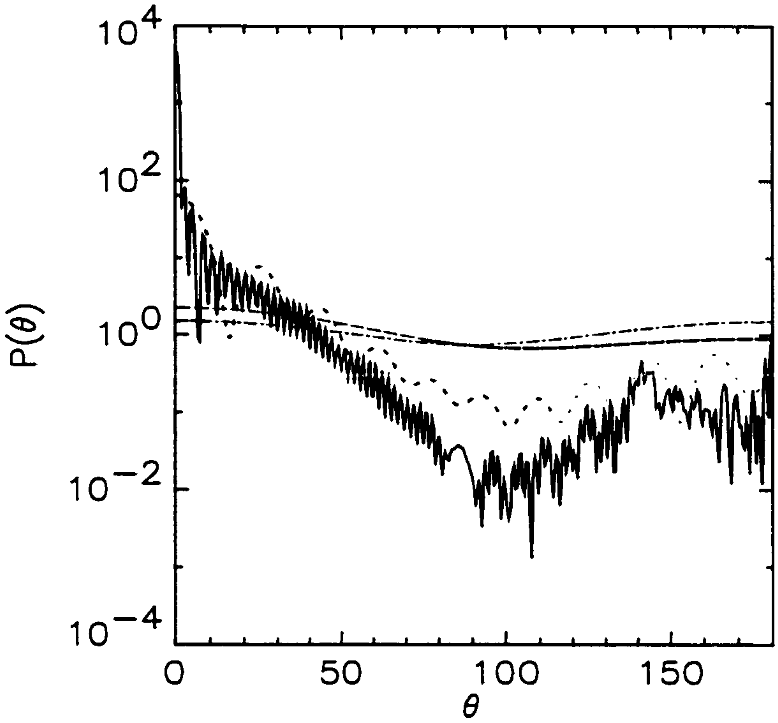

Figure 2.8 – Phase functions for monodisperse size distributions with χ = 100 (solid line), 10 (dotted), 1 (dashed) and 0.1 (dash-dot).

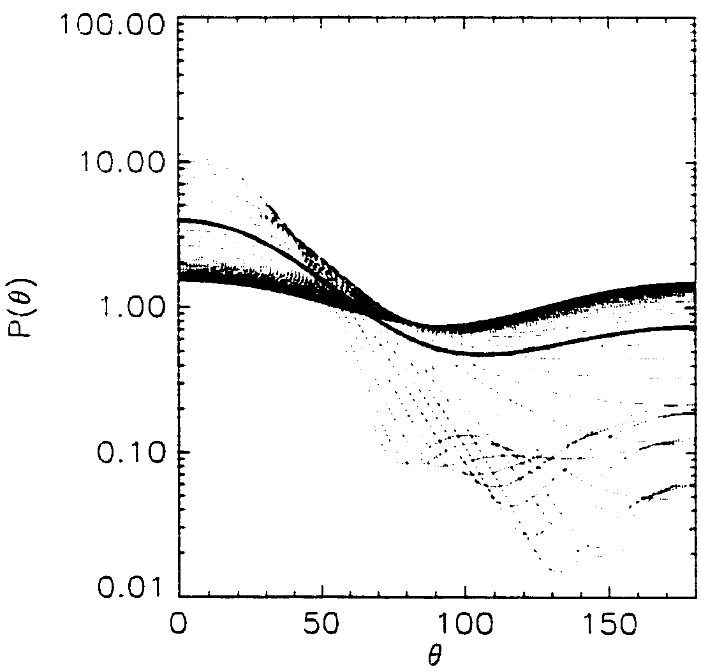

Figure 2.9 – Phase function of the ACE1 size distribution. Gray lines represent the phase function for each particle size in figure 2.1, black line represents the phase function of the distribution as calculated by Eq. 2.18, for m = 1.33 + 0.0i, λ = 0.55μm.

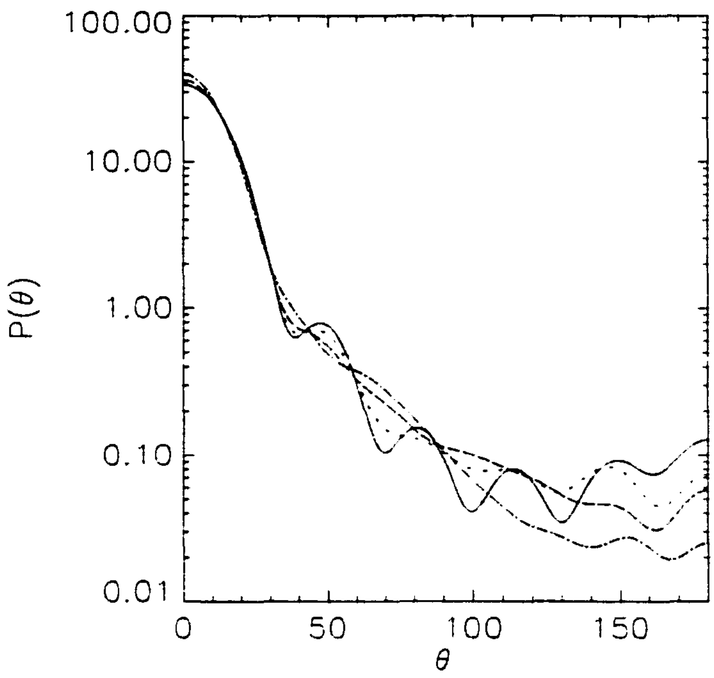

Figure 2.10 – Phase functions for monodisperse oblate spheroids, for a/b = 1.0 (solid), 1.5 (dotted), 2.0 (dashed) and 3.0 (dash-dotted), for m=1.33 + 0.0i, λ = 0.55μm and r = 0.5 (particle size is determined by equal-volume sphere).

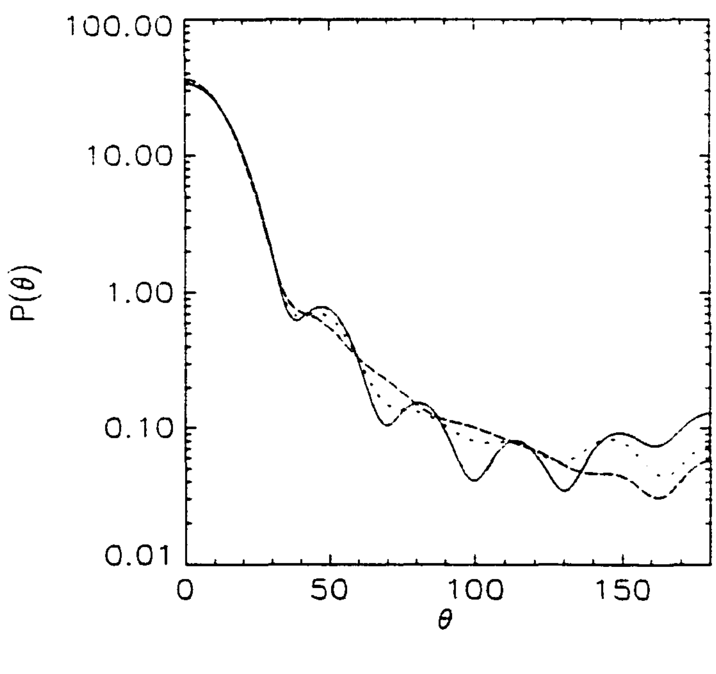

Figure 2.11 – Phase functions for monodisperse prolate spheroids, for a/b = 1.0 (solid), 0.66 (dotted), and 2.0 (dashed), for m=1.33 + 0.0i, λ = 0.55μm and r = 0.5 (particle size is determined by equal-volume sphere).

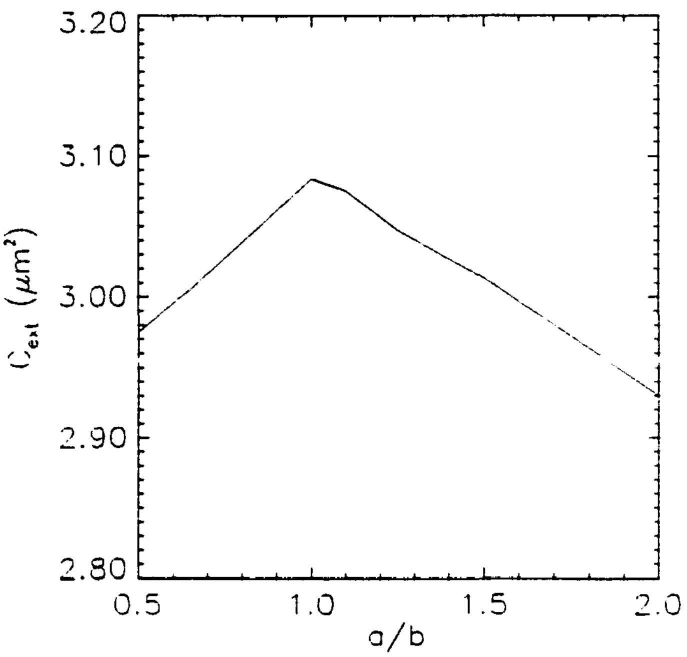

Figure 2.12 – C_{ext} as a function of the ratio of the radii in the nonspherical monodisperse particle.

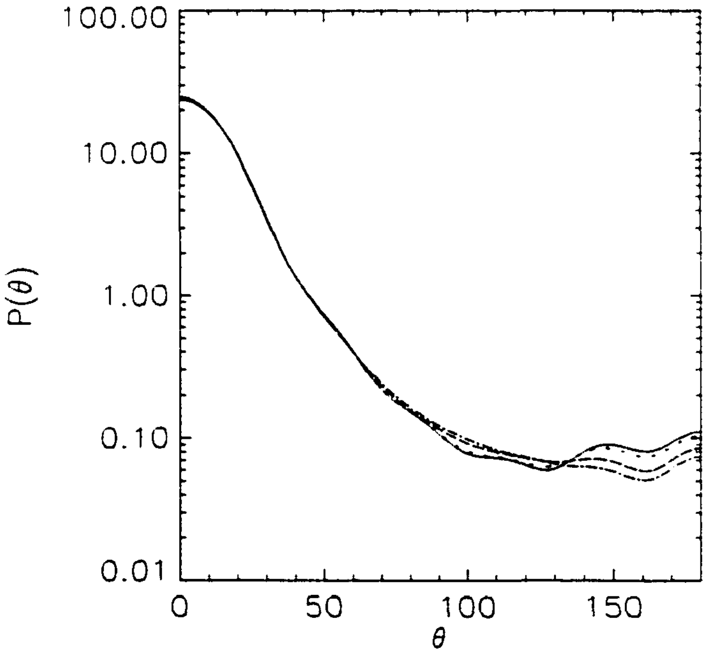

Figure 2.13 – Phase functions for a log-normal distribution of oblate spheroids, for a/b = 1.0 (solid), 1.2 (dotted), 1.5 (dashed) and 1.7 (dash-dotted), for m=1.33 + 0.0i, λ = 0.55μm and r = 0.5 (particle size is determined by equal-volume sphere).

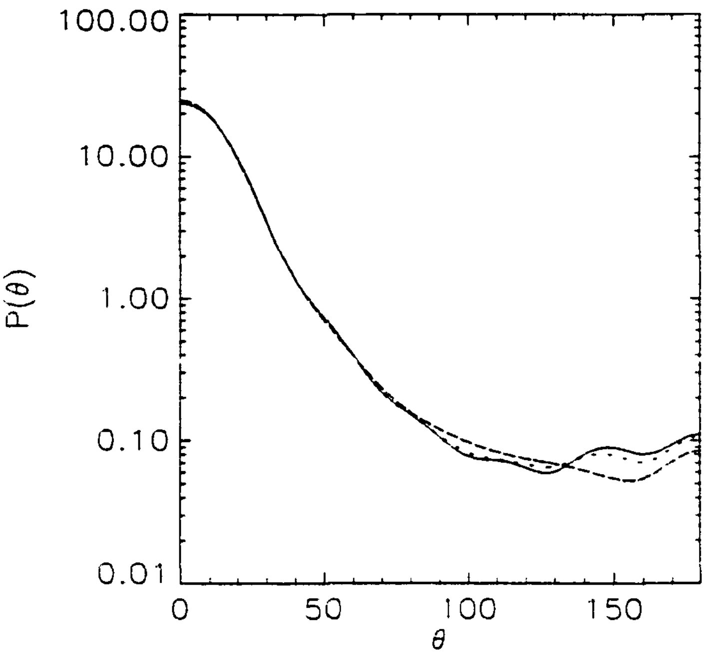

Figure 2.14 – Phase functions for monodisperse prolate spheroids, for a/b = 1.0 (solid), 0.66 (dotted), and 2.0 (dashed), for m=1.33 + 0.0i, λ = 0.55μm and r = 0.5 (particle size is determined by equal-volume sphere).

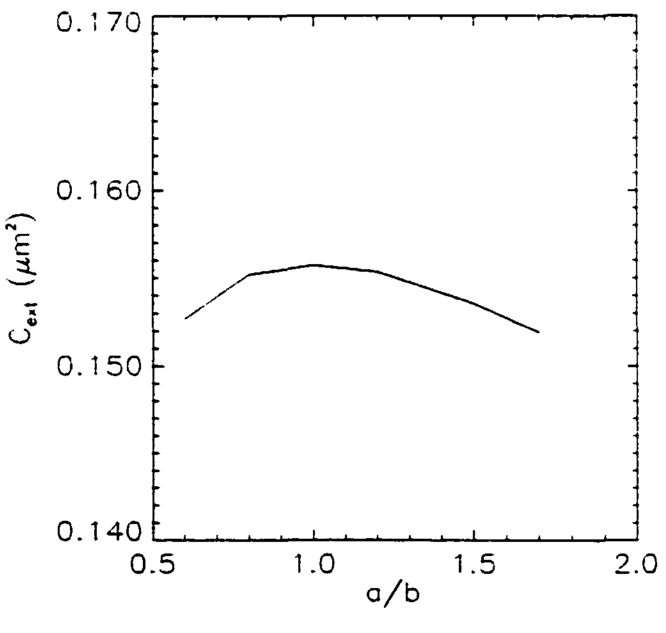

Figure 2.15 – C_{ext} as a function of the ratio of the radii in the nonspherical log-normal distribution.

3. Satellite Remote Sensing of Aerosols: 1960 - 1995

The following is a historical perspective of aerosol remote sensing from satellite. It is a review of the field from the launch of the first meteorological satellite through 1995. In that year the ATSR-2 instrument was launched (Veefkind et al., 1998) marking the beginning of a new era in aerosol remote sensing. Many satellites launched after 1995 have and will include instruments much more suitable for aerosol remote sensing. For example, the POLDER instrument which operated on the ADEOS-I satellite in 1997 will also be included on ADEOS-II. The Terra satellite has MODIS and MISR which also have channels specifically designed to measure aerosol optical properties. The next chapter will discuss the algorithms designed for these newer instruments, followed by the development and description of the GOES aerosol optical depth algorithm.

3.1 Scope

This review will attempt to concentrate on techniques of tropospheric aerosol remote sensing from passive sensors using backscattered solar radiation. There are some aerosol algorithms which have been developed which indirectly sense aerosols over land by measuring their effect on emitted infrared radiation (e.g., Legrand et al., 1988; Legrand et al., 1989; Ackerman, 1997). These techniques are still under development yet show promise of retrieving aerosol properties in the direct sensing "blind spots" – bright, homogeneous desert. In these "blind spot" areas, reflected radiation is dominated by the surface contribution with little aerosol signal. The discussion herein will concentrate on retrieval methods utilizing reflected visible radiation because it is the background for the research using the GOES-8 visible sensor.

Methods also exist for determining the vertical distribution of aerosol from satellite, such as active sensing and solar occultation. Lidars emit radiation and use the measured backscatter to assess aerosol optical properties. Lidars had been limited to use on the ground until recently when a lidar was operated from the Discovery Space Shuttle in September 1994 (www-lite.larc.nasa.gov). This was in preparation for the PICASSO-CENA (Pathfinder Instruments for Cloud and Aerosol Spaceborne Observations-Climatologie Etendue des Nuages et des Aerosols) and CloudSat missions which will fly active sensors to measure aerosol and cloud properties, respectively. While the PICASSO-CENA mission will provide important information on aerosol properties (probably most importantly, their vertical distribution in the troposphere) it is unlikely that aerosol remote sensing will be dominated by space-borne lidars in the near future, leaving passive sensors to monitor aerosols. Also, satellites measuring the occultation of the sun as they move into the Earth's shadow can also provide valuable information on the vertical distribution of aerosols in the stratosphere and upper troposphere. The second Stratospheric Aerosol and Gas Experiment (SAGE-II) has provided stratospheric aerosol observations since 1984 (www-rab.larc.nasa.gov). Since these techniques for retrieving aerosol optical properties vastly differ from the GOES-8 retrieval herein, they will not be described further.

Lastly, this review will concentrate on aerosol retrieval methods over land. Aerosol research began over oceanic areas primarily because the problem was scientifically simple: a scattering media lofted over a dark, uniformly-reflecting surface. Also, the ocean seemed like a vast, data-sparse area: "Man's knowledge of the atmosphere over the data-sparse ocean areas has increased dramatically with the application of meteorological satellites," Mayfield (1975). This is especially true of aerosols, where algorithms have been developed for many satellite sensors over the oceans. It is suggested here that the pendulum has swung and now the research and knowledge of aerosols over the ocean has surpassed that of studies over the land. Therefore, this review will attempt to concentrate on most of the previous aerosol remote sensing over land within the scope described above, except for reference to some early studies which were the beginning of satellite aerosol remote sensing.

3.2 Review of literature

The first meteorological satellite was launched in 1960 and the Advanced Technology Satellite, ATS-1 (the first geostationary weather satellite) was in orbit by 1966. The pioneer scientific reports of atmospheric aerosol detection are from the early 1970's. In general, the following review summarizes literature by the sensor used to observe aerosols; a summary of the satellite sensors is given in Table 3.1.

The likely first attempt to monitor anthropogenic aerosols over land also utilized the ATS; McLellan (1971) attempted to monitor pollution in the Los Angeles basin using ATS data (Lyons et al, 1978 referencing McLellan, 1971). Other initial aerosol reports describe Saharan dust outbreaks moving westward over the Atlantic ocean using geostationary satellite imagery. Carlson and Prospero (1972) used ATS-III visible imagery as a means of tracking the transport of Saharan dust palls. Their study tracked two dust outbreaks during the summers of 1969 and 1970 as dust was transported across the Atlantic toward the Americas. Satellite imagery supplemented aircraft observations from within the dust layer. They also discussed the development of these dust plumes in relation to tropical waves.

In 1972 the first in a series of Land Satellites (Landsat) was launched. It carried the Multi-Spectral Scanner (MSS) which was deigned to observe the earth's surface. It was also the subject of an investigation toward the possibility of aerosol monitoring from satellite data (Griggs, 1975). This research discussed many topics still relevant to the science today. The premise of the study was that upwelling shortwave radiation from the Earth was directly proportional to the atmospheric aerosol content. Radiances observed at 3 wavelengths (0.55, 0.65 and 0.75μm) over the Pacific Ocean by the MSS were compared to observations using a Volz photometer. Griggs (1975) estimated that aerosol optical depth could be retrieved to within ±10% and described the sun glitter area of an image and the adjacency effect (later described and studied by Mekler and Kaufman, 1980) with respect to retrieval uncertainty. Fraser (1976) further showed that aerosol mass retrievals of dust over the ocean were possible from MSS.

Carlson and Wendling (1977) discussed the presence of dust aerosols in Very High Resolution Radiometer (VHRR) data from 1974, where a nearly linear relationship between normalized radiances and aerosol optical depth was found. Carlson (1979) calculated radiances from ground-truth estimates of aerosol optical depth and plotted against VHRR-measured radiances. Continuous curves were then drawn by hand and used to create more highly resolved tables, thus literal look-up tables were created.

Mayfield (1975) showed visible imagery from the first Synchronous Meteorological Satellite (SMS-I) of Saharan dust over the Atlantic moving westward at 20 knots. Lushine (1975) showed similar Saharan dust imagery from SMS-I which included general haziness over the U.S. Lyons et al. (1978) tracked aerosol sulfate outbreaks over the U.S. during 1976 using SMS data. They tracked the leading edge of "smog fronts" in real-time through visual analysis of imagery using the new Man-Computer Interactive Data Acquisition System (MCIDAS) and suggested short-range forecast in support of field experiments. They further suggested that "satellite designers should realize that their systems, especially if multi-spectral, could play an important role in environmental monitoring in the 1980's." This suggestion was finally taken to heart by designers of the Meteosat Second Generation (MSG), which will have an AVHRR-like channel selection (observations at 0.6, 0.8, 1.6, 3.8 μm) increasing the ability to observe aerosols from geostationary orbit (EUMETSAT homepage: www.eumetsat.de).

Norton et al. (1980) performed aerosol optical depth retrievals of Saharan dust using SMS-1 imagery off the west coast of Africa. Retrievals were generally within 0.1 of the surface measurements with a correlation coefficient of 0.85. Likely error sources were listed as cloud contamination, satellite sensor S/N ratio, calibration and optical properties of the aerosols; these are all significant error sources in retrievals made by current sensors.

In an attempt to take advantage of the high spatial resolution of the Landsat Thematic Mapper (TM) data, Mekler and Kaufman (1980) performed theoretical analysis of the 'two-halves' field. In this case, a satellite field of a distinct surface boundary (e.g., a coastline) can be used to infer aerosol content through contrast reduction, where aerosols blur such a boundary. This approach requires multi-dimensional radiative transfer to fully quantify and was a first step toward using spatial analysis toward retrieving aerosol properties. Kaufman and Joseph (1982) explore this approach further by deriving an algorithm to retrieve either: 1) optical depth and the surface reflectance of the two surfaces types or 2) aerosol optical depth, single scatter albedo and surface reflectance of one of the surfaces (depending on the prior knowledge). This method was applied to Landsat MSS data for Saharan coastline in western Africa.

The Coastal Zone Color Scanner (CZCS) was used by Durkee (1984) and Hindman et al. (1984) to investigate aerosols off the coast of California where satellite radiances were correlated to aerosol optical depth. For maritime aerosols, the aerosol extinction in the boundary layer is correlated to the relative humidity; thus, satellite radiances are correlated with boundary layer relative humidity. This work was extended to the Advanced VHRR (AVHRR) by Durkee et al., (1986). The use of AVHRR over the ocean also allowed an estimation of the aerosol phase functions through multi-spectral measurements (Durkee et al., 1991).

Some of the first quantitative aerosol remote sensing over land from geostationary orbit was performed by Fraser et al. (1984). Aerosol optical depths were retrieved and converted to columnar aerosol mass from GOES-1 imagery using an assumed aerosol composition. These mass values were combined with 925mb wind data to investigate aerosol transport in the Eastern U.S. The retrieval method compared a hazy image to a clear image, using the clear image as the surface reflectance in a radiative transfer model. VISSR data was vicariously re-calibrated for each day a retrieval was made. In three cases, retrieved optical depths were compared to surface measurements with high accuracy. Also, Tsonis and Leaitch (1986) investigate minimum detectable pollution levels over land using GOES-1 visible imagery during 1982 and 1984. For areas near Ontario, Canada, the minimum detectable τ was approximately 0.065.

Another algorithm using aerosol contrast reduction over heterogeneous surfaces was described by Tanré et al. (1988). While Kaufman and Joseph (1982) used a distinct surface boundary (the two-halves field), this method simply uses a heterogeneous surface (e.g., agricultural planting areas). A structure function is the average change in radiance between two pixels as a function of distance between the two pixels and is related to the aerosol optical depth. The structure function measures the complexity of the surface (i.e., the heterogeneity); thus, structure function values decrease as the aerosol optical depth increases. This method was applied to Landsat TM data over Senegal (on the West Coast of Africa) where the structure function on four days was compared to the optical depth. This method can be applied to images at different wavelengths, yielding spectral optical depths. This work was extended to the Meteosat imagery by Tanré and Legrande (1991) and also showed good correlation to ground truth. Williams and Cogan (1991) suggest a similar contrast reduction method in which the total contrast of an image (brightest pixel less the darkest pixel) is used to determine the aerosol optical depth.

The absorption of aerosol particles can be estimated over land from satellite imagery. Aerosols increase the reflected radiation to space over dark surfaces and an increase in the single-scatter albedo, ω_o, which is the ratio of aerosol scattering to aerosol extinction, decreases this effect. This effect can be seen in figure 3.1 (reproduced from Kaufman, 1987). The solid and dashed lines show the increase for an aerosol with $\omega_o = 0.96$ and 0.85, respectively. Yet at large surface reflectances, aerosols can decrease the reflected radiation. For a certain surface reflectance, an aerosol has no effect on the radiation to space; this reflectance is termed the critical reflectance, ρ_c, by Kaufman (1987). In figure 3.1, $\rho_c \sim 0.27$ and 0.1 for $\omega_o = 0.96$ and 0.85 (respectively). The relationship between ρ_c and ω_o is monotonic such that ω_o might be determined from an estimate of ρ_c. Data from two satellite images can be used to determine this surface reflectance where aerosols have little effect. This method was applied to Landsat MSS data in the Chesapeake Bay region. Retrievals of ω_o were in the vicinity of 0.90 with an uncertainty of ± 0.01 (for $\lambda = 0.5\text{-}0.6\mu m$ and $0.7\text{-}0.8\mu m$).

An algorithm for the retrieval of aerosol optical depth, single-scatter albedo and effective radius from AVHRR data is described in Kaufman et al. (1990). The algorithm requires a two-halves field to derive all three optical properties. They derive an aerosol effective radius algorithm, use the aerosol optical depth algorithm described by Fraser et al. (1984), and the single scatter albedo algorithm from Kaufman (1987). This combined algorithm makes use of the knowledge of the effective radius to better estimate the aerosol phase function; so it has a more accurate optical depth retrieval. This algorithm was applied to NOAA-7/AVHRR over the Chesapeake Bay. Water pixels are used to determine optical depth and effective radius while the land pixels are used to determine optical depth and single scatter albedo.

Another method for determining aerosol ω_o is described by Kaufman et al. (1999). This used a similar technique as Kaufman (1987) except it had less uncertainty. Optically thick ($\tau \sim 2.4$) and thin ($\tau \sim 0.8$) Saharan dust plumes were viewed by Landsat and a ground-based sun-photometer over the Saharan desert. The clear-sky measurement was used to determine the surface reflectance using the surface measurement. The hazy day is used to determine ω_o by estimating the satellite radiance through the measured aerosol optical depth and varying ω_o. For this case, the aerosol absorption was nearly indistinguishable from zero (ω_o > 0.98 for λ = 0.65 – 1.5μm). These results have a reported uncertainty of $\Delta\omega_o$=±0.005, yet differ from measurements in recent literature that report more absorption in dust layers.

Perhaps the paper most relevant to current methods of aerosol remote sensing over land is published in the guise of a surface remote sensing paper. Kaufman and Sendra (1988) describe an atmospheric correction method for dense, dark vegetation (DDV). DDV areas have relatively constant surface reflectance properties. Also, DDV have a strong correlation between the reflectance in the mid-IR (e.g., 2.1μm, an area where aerosols generally have no effect) and in the visible.

This method is already (and will be) used by many instruments to detect aerosols over land. Already, the method has been applied to aerosol remote sensing from the Systeme Pour l'observation de la Terre (SPOT, translation: System for the observation of the Earth) satellite (Liu et al., 1996). The estimation of surface reflectance is used to obtain aerosol optical properties (optical depth, power of the Junge size distribution, single scatter albedo and phase function) as well as surface reflectances. The DDV method has also been applied to AVHRR imagery of north of Lake Ontario in Canada (Soufflet et al., 1997). DDV was estimated where the NDVI exceeded 0.6 and the reflectance in the red (channel 1) was dark. Aerosol optical depth retrievals ranged from 0.2 to 1.2 and were generally within ±0.1 of surface measurements.

Table 3.1 Chronological list of satellites that could/can/will detect tropospheric aerosols

Year	Satellite	Sensor	Notes
1960	TIROS 1		1st Polar orbiting weather satellite
			1st in series of TIROS series satellites
1966	ATS 1	SSR	1st geostationary weather satellite
1970	NOAA 1	APT	1st in NOAA series
1972	NOAA 2	VHRR	prelude to the AVHRR
	Landsat	MSS	high spatial resolution
1974	SMS 1	VISSR	
1975	GOES 1		1st operational Geo
1978	TIROS N	AVHRR	1st in a series of AVHRR sensors
	Nimbus 7	CZCS, TOMS	
1982	Landsat 4	TM, MSS	
1994	GOES 8	Imager	1st in series of new GOES satellites
1995	ERS 2	ATSR-2	
1996	ADEOS 1	POLDER	
1998	NOAA-15	AVHRR/3	
1999	Terra	MODIS,MISR	1st in series of EOS satellites
	The Future in aerosol remote sensing		
2000	ADEOS 2	GLI	
2000	MSG		1st Geo with numerous Shortwave channels
2003	PICASSO -CENA	Lidar A-band spectrometer	1st satellite-based lidar

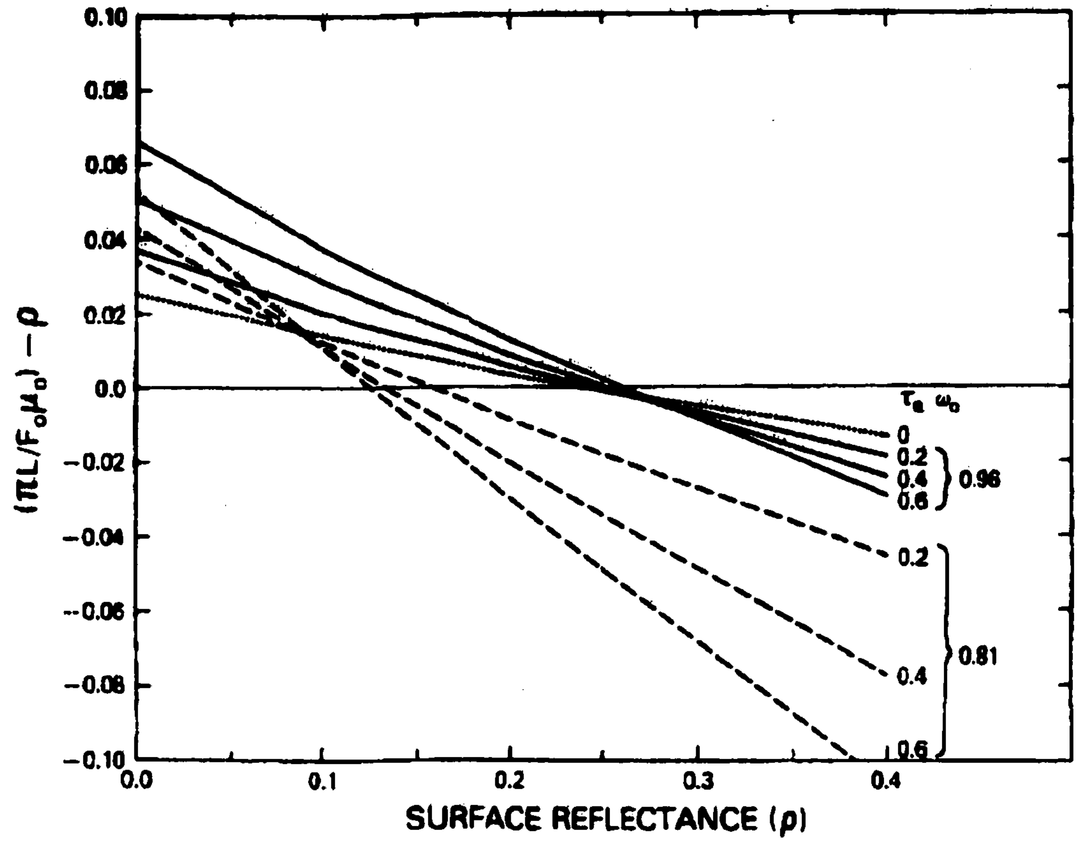

Figure 3.1 – Apparent reflectance (increase in the satellite detected reflectance) due to aerosol optical depth (τ = 0.0, 0.2, 0.4 and 0.6) and single scatter albedo (ω_o = 0.81 and 0.96) (from Kaufman, 1987)

4. Satellite Remote Sensing of Aerosols: 1995 - 2000

This chapter provides an overview of more recent aerosol optical property retrievals over land. The year 1995 was a transition period for aerosol remote sensing. With the launch of ATSR-2, aerosol remote sensing transitioned from instruments designed to observe clouds (e.g. GOES, AVHRR), land (e.g., Landsat) or ocean (e.g., CZCS) to instruments with a specific purpose to observe aerosol optical properties (e.g., MODIS or POLDER). Not only will these sensors change how aerosol retrievals are performed, but also will allow accurate estimates of optical properties other than optical depth (e.g., size, sphericity, etc.). Satellite remote sensing of aerosols can be characterized by the type of instrument used: multi-spectral, single-view (e.g., CZCS, AVHRR, TOMS, MODIS); multi-spectral, multiple view (e.g. ATSR-2, MISR); and multi-spectral and multiple-view with polarization (e.g. POLDER). While satellites prior to 1995 were limited to the single view design, the multiple view design should allow better separation of surface and aerosol contributions to the detected radiances. Also, the TOMS method is included in this discussion because it is still in the developmental stage of retrieving an aerosol property from the parameter retrieved (Herman et al., 1997a) and shows promise toward increasing the climatological understanding of aerosols over land.

It should be mentioned here that King et al. (1999) recently provided a thorough overview of aerosol remote sensing over land and ocean. The overview provided an excellent analysis of strengths and weaknesses of different algorithms. The description herein will concentrate solely on aerosol remote sensing over land; descriptions of each algorithm are summarized from publications as referenced.

4.1 The MODIS over land aerosol algorithm

The backbone of the moderate resolution imaging spectro-radiometer (MODIS) over-land aerosol algorithm is that the surface reflectance is determined at a wavelength essentially unaffected by aerosol scattering using dense dark vegetation (DDV) described by Kaufman and Sendra (1988). The algorithm is described in Kaufman et al. (1997) and summarized below.

The MODIS instrument will measure radiances with 36 channels ranging from the visible through the infrared. The MODIS over-land aerosol optical property retrieval (hereafter, MODIS-Land) algorithm establishes the surface reflectance in a vastly different method than the GOES aerosol optical depth algorithm described in chapter 8. It will also be able to distinguish between non-dust and dust aerosols by using a multi-spectral approach.

The principle of this algorithm rests in the surface reflectance relationship for dense, dark vegetation between the near-IR (λ=2.1 and 3.8μm) and the visible – at blue (λ = 0.47μm) and red (λ = 0.66μm) wavelengths. The surface reflectance at visible wavelengths is directly proportional to that in the near-IR. Specifically, the reflectance measured at 2.1 μm can be used to determine the surface reflectance in the red and blue channels. In the absence of snow, water, cloud or ice, a set of 4 criteria (Table 4.1) are used. The first criterion to be met by more than 5% of the samples in a 10$\times$10 pixel area (nominally 10×10 km^2 at nadir) is used for the entire 10×10 km^2 area. Also, the accuracy of the surface reflectance estimate decreases as the criterion increases.

The MODIS-land algorithm then retrieves the aerosol optical depth using the climatological non-dust aerosol model from the reflectances measured in the blue and the red channels. An aerosol climatology – made up of continental, biomass burning and industrial aerosols (i.e., non-dust aerosols) – is defined over the globe with spatial and temporal boundaries. A temporal distinction is made for biomass burning aerosols because burn seasons tend to follow regional dry seasons. The algorithm will also use a dust aerosol model where radiances suggest the presence of a dust aerosol. The ratio of the single scatter path radiances ($L_{ss,\lambda} = \tau_\lambda P_\lambda(\Theta)\omega_{o,\lambda}$) at the red and blue channels is used to determine the fraction of dust particles. Dust aerosols generally contain larger particles and scatter radiance in the red nearly as effectively as in the blue, causing the ratio to be near one. Conversely, the non-dust aerosols scatter radiance much more effectively in the blue, making them distinguishable from the dust. In general, for low ratios ($L_{ss,red}/L_{ss,blue} < 0.72$) the non-dust aerosol is used, whereas for $L_{ss,red}/L_{ss,blue} > 0.9$ the dust aerosol is used. These thresholds are valid for areas away from the backscatter direction, where dust becomes less distinguishable from non-dust aerosols. The aerosol models (the dust and the non-dust) are mixed for ratios that fall between the thresholds.

Finally, the preliminary τ retrieval is corrected using the optical properties of the determined aerosol model. This is performed through:

$$\tau_\lambda^{new} = \tau_\lambda^{pre} \frac{P_\lambda^{pre}\omega_\lambda^{pre}}{P_\lambda^{new}\omega_\lambda^{new}} \tag{4.1}$$

where the superscripts pre and new refer to the preliminary and new aerosol models, P_λ is the aerosol phase function and ω is the aerosol single scatter albedo. This assumes that differences in the radiances of different aerosol models are largely due to single scattering and not multiple scattering.

Finally, in some cases the aerosol optical depth will be retrieved at a sub-grid scale. If the aerosol optical depth retrieved on $10\times10km^2$ grid has a standard deviation which is more than half the average τ, then τ is retrieved on 4 sub grids, each $5\times5km^2$. This will allow better spatial distinction of aerosols near aerosol sources.

There are two studies which discuss the uncertainties in the MODIS-Land algorithm: Kaufman et al. (1997) and Chu et al. (1998). The former describes the MODIS-Land algorithm and subsequently the uncertainty, while the latter presents results from the MODIS-Land algorithm applied to the MODIS Airborne Simulator (MAS) data measured during the SCAR-B experiment. The uncertainty of the MODIS-Land aerosol optical depth retrieval is estimated as $\Delta\tau = \pm0.05$ or 20% of τ, whichever is larger.

4.2 The ATSR over land aerosol algorithm

The second Along Track Scanning Radiometer (ATSR-2) measures radiances near nadir and forward of the satellite track (view zenith angle, θ, of 55°) in the visible, near-infrared and infrared wavelengths. In a similar manner to the MODIS-land algorithm, ATSR-2 uses the surface reflectance observed at 2.21μm to estimate the surface reflectance at visible wavelengths, however it takes advantage of the multiple viewing angles. The algorithm is described by Veefkind et al. (1998).

The radiative transfer solution for a 1-layer atmosphere over a reflecting surface is assumed in the derivation of the algorithm:

$$\rho^* = \rho_a + T\frac{\rho_s}{1-\rho_s s} \tag{4.2}$$

where ρ^{*} is the satellite apparent reflectance, T is the atmospheric transmittance, ρ_s is the surface reflectance, and s is the spherical albedo of the aerosol. Equation 4.2 is valid for both the forward and nadir view of a point:

$$\begin{aligned} \rho_n^{*} &= \rho_{a,n} + T_n \frac{\rho_{s,n}}{1-\rho_{s,n}s} \\ \rho_f^{*} &= \rho_{a,f} + T_f \frac{\rho_{s,f}}{1-\rho_{s,f}s} \end{aligned} \tag{4.3}$$

where the subscripts f and n refer to the forward and nadir directions. Rearrangement of Equation 4.3 results in:

$$\rho_n^{*} - \rho_{a,n} = \frac{T_n\left(\rho_f^{*} - \rho_{a,f}\right)}{kT_f + (k-1)s\left(\rho_f - \rho_{a,f}\right)} \tag{4.4}$$

where k is a bidirectional reflectance ratio for the land surface:

$$k = \frac{\rho_{s,f}}{\rho_{s,n}}. \tag{4.5}$$

The solution derived in Veefkind et al. (1998) is:

$$\frac{\rho_n - \rho_{n,a}}{T_n} = \frac{\left(\rho_f - \rho_{f,a}\right)}{kT_f} \tag{4.6}$$

which utilizes a minor approximation. In this solution, the ρ_n and ρ_f are measured by the ATSR-2, and $\rho_{a,n}$, $\rho_{a,f}$, T_n and T_f are functions of the aerosol optical properties. An aerosol model is assumed and the aerosol optical depth is iterated to solve equation 4.6. The minor approximation of equation 4.6 is:

$$(k-1)s\left(\rho_f - \rho_{f,a}\right) \rightarrow 0 \tag{4.7}$$

The (k-1) term is a measure of the surface anisotropy, thus the more Lambertian the surface, the better the assumption. The spherical albedo, s, is linked to the aerosol optical depth, so this would work better at small optical depths. The third term (ρ_f-$\rho_{a,f}$) is smaller as the surface reflectance approaches zero. The product of these terms is generally negligible, even when one term is significant (e.g., ~0.1)

This method was tested over the Atlantic and the Eastern U.S. during TARFOX and four comparisons were made to coastal AERONET sites. Retrievals at optical depths greater than 0.3 showed results within ±0.15 (Veefkind et al., 1998).

4.3 The MISR over land aerosol algorithms

While the ATSR-2 is limited to two viewing angles, the Multi-angle Imaging Spectro-Radiometer (MISR) can view a point from nine angles: 1 nadir and four each fore-ward and aft-ward along the satellite track (θ = ±26.1°, ±45.6°, ±60.0° and ±70.5°). Measurements will be made at four wavelengths: 0.443, 0.555, 0.670 and 0.865μm. The following description of the MISR aerosol retrieval algorithm over land is a summary of Diner et al. (1996).

The instantaneous field of view (IFOV) for the nadir camera is approximately 0.2×0.25 km^2. IFOV increases with $|\theta|$, so IFOV can be as large as 0.3× 0.7km^2 for θ = ±70.5°. The algorithm uses statistics of the pixel-by-pixel observations grouped into 17.6×17.6km^2 area, which will have more pixels from nadir observations because of the smaller IFOV.

The retrieval uses aerosol models (or mixtures) to retrieve the aerosol optical depth; these aerosol models, grouped by maritime or continental, have a tri-modal log-normal distribution. Accumulation mode sea salt, sulfate aerosols and either a soot, biomass burning aerosol, a coarse mode sea salt or an accumulation mode mineral dust comprise the maritime aerosol model. Similarly, the continental aerosol model has accumulation sulfate and dust modes and one of the following: soot, biomass burning aerosol, or a coarse mode mineral dust. Radiative transfer calculations for each aerosol mode (at various viewing geometries and optical depths) are stored in the Simulated MISR Ancillary Radiative Transfer (SMART) Dataset in a manner similar to a look-up table. Reflectances from different modes of a model are combined through linear mixing where the reflectance of a mixture of aerosols is a linear combination of the reflectances of the modes of the aerosol mixture. Linear mixing allows the calculation of the reflectances of each model, rather than running a radiative transfer model for each aerosol mixture combination. Linear mixing is reported to be accurate for a wide range of viewing and solar angles as well as optical depths as large as 2 (Abdou et al., 1997). The MISR aerosol retrieval will initially use the eight aerosol models described above, but the setup of the SMART dataset allows future changes in the aerosol models.

The MISR over-land algorithm utilizes two techniques to retrieve aerosol information. The primary technique is based on the previous publications of dense dark vegetation (DDV). If the surface is not DDV, then a test is performed to determine if it heterogeneous. The heterogeneous surface algorithm uses empirical orthogonal functions to perform the retrieval. Both techniques use the multiple view angles and channels of MISR to simultaneously retrieve aerosol and surface information. No retrieval of aerosol information is performed for homogeneous, bright surfaces (i.e., surfaces that fail the tests for the above algorithms). The algorithms, which are summarized below, are fully described in Diner et al. (1996) and Martonchik et al. (1997).

4.3.1 The MISR-DDV algorithm

The first step is to determine if a surface is DDV. MISR lacks a 2.1μm (or similar) channel, thus the normalized difference vegetation index (NDVI) is used as a surrogate. The NDVI is calculated as:

$$NDVI_{\mu} = \frac{\rho_4 - \rho_3}{\rho_4 + \rho_3} \tag{4.8}$$

where ρ refers to the MISR detected reflectances at the near IR (subscript 4, 0.865μm) and red at 0.67μm (subscript 3). The subscript μ refers to the angle used to calculate the NDVI. The air mass (1/μ) defines the relative air mass between the sensor and the surface (μ = cosθ). Rayleigh scattering and aerosol extinction can severely decrease the satellite-measured NDVI by decreasing the difference between the reflectance in the two channels. The surface NDVI is estimated by using a method similar to that of a Langley plot. The NDVI calculated from the fore-pointing sensors are extrapolated to a zero air mass by quadratically fitting the NDVI vs. 1/μ relationship and extrapolating to zero. The same is performed for the aft-pointing sensors and the average of the two are used to calculate an NDVI. The surface is determined to be DDV if the NDVI > 0.8. Otherwise, tests are performed to use the heterogeneous surface technique (see following description on the heterogeneous algorithm).

The DDV algorithm retrieves aerosol optical depth from the 0.443 and 0.670μm channels and an estimate of the surface reflectance taken to be constant at both wavelengths. The surface bi-directional reflectance distribution (BRD) is important to parameterize due to the multi-angle measurements of MISR. The BRD of the DDV is assumed to vary little and is modeled using the parameterization of Rahman et al. (1993):

$$\rho_s(\mu,\mu_o,\Delta\phi)=r_o\left[\mu_o\mu(\mu_o+\mu)\right]^{k-1}\cdot\frac{(1-g^2)}{(1+g^2-2g\cos\Omega)^{3/2}}\cdot\left(1+\frac{1-r_o}{1+G}\right) \tag{4.9}$$

Where ρ_s is the surface reflectance for the $(\mu,\mu_o,\Delta\phi)$ geometry, $\mu=\cos\theta$, $\mu_o = \cos\theta_o$, $\Delta\phi$ is the difference between the solar and satellite azimuth angles, Ω is the scattering angle, G is a geometric factor and g, k, and r_o are variables used to fit different land cover types. For the MISR-DDV algorithm, g and k are fixed and r_o is allowed to vary. Through this, the shape of the BRD is fixed while the magnitude is retrieved.

The second step estimates the r_o factor from the measurements. The r_o factor, which is held constant for both channels, is calculated for each aerosol mixture and optical depth and is limited such that $0 \le r_o \le 0.03$. This r_o is then used to calculate the MISR reflectances, again for each aerosol mixture and optical depth. An optical depth is calculated for each aerosol mixture by minimizing the cost function(χ^2_{abs}):

$$\chi^2_{abs}(\tau)=\frac{1}{N\langle w_j\rangle}\cdot\sum_{l=1}^{2}\sum_{j=i}^{N_{cam}}\frac{w_j\left[\rho_{MISR}(l,j)-\rho_{model}(l,j)\right]}{\sigma^2_{abs}(l,j)} \tag{4.10}$$

where N is the number of observations, l is the channel index (1 = 0.443μm, 2 = 0.67μm), j the camera index, $\rho_{MISR}(l,j)$ and $\rho_{model}(l,j)$ are the MISR measured and modeled reflectances (respectively) from the camera j and channel l and the σ^2_{abs} is the absolute radiometric uncertainty in ρ_{MISR}. The weights, $w_j = \mu^{-1}$, weight the larger zenith angles more than the near-nadir observations and <w> is the average of the weights used. An aerosol model is deemed acceptable when $\chi^2_{abs} < 2$. Further tests are performed which weight camera-to-camera geometric differences (χ^2_{geom}) and camera-to-camera spectral reflectance ratios (χ^2_{spec}) for each aerosol model which has an acceptable χ^2_{abs}. An aerosol model is a successful match when each of these (χ^2_{abs}, χ^2_{geom}, and χ^2_{spec}) are less than or equal to 2.

The smallest $\chi^2_{abs}(\tau_i)$ value, along with the χ^2 on either side ($\chi^2_{abs}(\tau_{i-1})$ and $\chi^2_{abs}(\tau_{i+1})$), are used to calculate τ. The three χ^2 values and corresponding τ values are fit to a quadratic, from which the minimum χ^2 corresponds to the optical depth retrieval. This quadratic is also used to determine the uncertainty of the retrieval. This is performed for each model that was accepted as a possible model. A final aerosol optical depth is determined from the average of the optical depths from each possible aerosol model.

The optical depth uncertainty of the MISR DDV algorithm is reported to be 0.05 or 10%, whichever is higher. Also, about four distinct size groups between 0.1 and 20μm effective radius are expected to be retrieved in the mid-latitudes.

4.3.2 The MISR-heterogeneous algorithm

Retrieval areas (i.e., the 17.6×17.6 km^2 areas) which are not DDV are tested for the heterogeneous land aerosol retrieval method. This method uses empirical orthogonal functions to simulate surface features. First, the mean reflectance, $<\rho_{x,y}(\mu,\mu_o,\Delta\phi)>$, is subtracted from the MISR reflectances for each observation angle, wavelength and location(x,y):

$$J_{x,y}(\mu,\mu_o,\Delta\phi) = \rho_{x,y}(\mu,\mu_o,\Delta\phi) - \langle \rho_{x,y}(\mu,\mu_o,\Delta\phi) \rangle . \tag{4.11}$$

A scatter matrix is calculated from $J_{x,y}$ through:

$$C_{i,j} = \sum_{x,y} J_{x,y,i} J_{y,x,j} \tag{4.12}$$

where i,j denote the viewing geometries and $C_{i,j}$ has the dimensions $N_{cam} \times N_{cam}$. Eigenvalues (λ_n) and eigenvectors of C are used to calculate the principle components. The size of these eigenvalues relative to the instrument noise determine the information content of the imagery. The following criteria is used to test whether enough information is present for an aerosol retrieval (i.e., whether the surface is heterogeneous enough):

$$\frac{\sum_{n=1}^{N_{cam}} \lambda_n}{N_{sub} \sum_{i=1}^{N_{cam}} \left(\sigma^2_{ran,i} + \sigma^2_{pix,i} \right)} \geq 5 \tag{4.13}$$

where σ^2_{ran} is the variance of the random instrument noise, σ^2_{pix} is the variance of the pixel-to-pixel relative radiometric error and N_{sub} is the number of subregions being used . When this criteria is met, the emerging reflectances have enough information to retrieve aerosol and surface properties. Otherwise, a retrieval is not made over homogeneous bright surfaces.

A retrieval of aerosol optical depth is again performed by minimizing a cost function, this time for each eigenvalue , χ^2_N:

$$\chi^2_N(\tau) = \frac{1}{N_{chan}} \sum_{l=1}^{N_{band}} \sum_{j=1}^{N_{cam}} \frac{\left[\langle \rho_{MISR}(l,j) \rangle - \rho^{black}(l,j) - \sum_{n=1}^{N} A_n \cdot f_{j,n}(l) \right]^2}{\sigma^2_{abs}(l,j)} \tag{4.14}$$

where now the average MISR observations, $<\rho_{MISR}>$ are compared to the reflectance of an aerosol model over a black surface, ρ^{black} (from the SMART dataset) and the first N_{max} principal components. The principle components used represent 95% of the angular variance of the MISR reflectances. Again, the χ^2_N is calculated for each aerosol model and optical depth. The optical depths determined from each eigenvalue, τ_N, are then averaged:

$$\tau = \frac{\sum_{N=1}^{N_{max}} \frac{1}{\sigma^2_{\tau,N}} \cdot \tau_N}{\sum_{N=1}^{N_{max}} \frac{1}{\sigma^2_{\tau,N}}}, \tag{4.15}$$

weighted by the uncertainty of each τ_N, $\sigma^2_{\tau,N}$. The final cost function, χ^2_h is then calculated as:

$$\chi^2_h(\tau) = \frac{\sum_{i=1}^{N_{max}} \frac{\chi^2_N}{\sigma^2_{\tau,N}}}{\sum_{i=1}^{N_{max}} \frac{1}{\sigma^2_{\tau,N}}} \tag{4.16}$$

and when $\chi^2_h < 3$, the aerosol model is defined as a possible solution. Again, the optical depths from each successful model are averaged for a "best" optical depth estimate.

The expected accuracy of the MISR heterogeneous land algorithm is difficult to assess, due to the variability of surface types, and is not reported.

4.4 The POLDER over land aerosol algorithm

The Polarization and Directionality of the Earth's Reflectance (POLDER) instrument not only has multi-spectral observations at multiple viewing angles (similar to MISR) but also has polarization measurements at three of its channels. The POLDER measures top-of-the-atmosphere radiances at nadir and at ±43° and ±51°along track at the 0.443, 0.490, 0.565, 0.670, 0.763, 0.865, and 0.910 μm; oversampling allows an optimum 13 views of the same point. Polarization measurements are made at 0.443, 0.670 and 0.865μm by making three measurements with polarizers turned in 60° steps (Leroy et al., 1997). This allows the calculation of three of the Stoke's parameters: I, Q, and U. Radiance is calculated from L=I and polarized radiance from $L_p=(Q^2 + U^2)^{1/2}$. The POLDER observations are described by Leroy et al. (1997). The following is a summary of the POLDER aerosol retrieval algorithm over land (Herman et al., 1997b).

In general, Rayleigh and aerosol scattering polarize light much better than the ground. Therefore, the contribution from the ground can be assumed to vary little and is either modeled as a sandy soil (Bréon et al., 1995):

$$L_p^g(\Omega) = \frac{R_p(\Omega)}{4\mu_v}$$

or a vegetated canopy (Rondeaux and Herman, 1991):

$$L_p^g(\Omega) = \frac{R_p(\Omega)}{4(1+\mu_v/\mu_o)}. \tag{4.17}$$

which assumes an isotropic distribution of leaf orientation, and $R_p(\Omega)$ is the Fresnel reflection coefficient which depends on the refractive index of the reflecting media and the angle of the incident solar beam, Ω. The POLDER measurements are approximated as:

$$L_p(\lambda,\Theta)\cos\theta_v = L_p^g(\Theta)\cos\theta_v e^{-\tau_\lambda^R M} + \frac{\tau_\lambda^R q_\lambda^R(\Theta)}{4} + \frac{\tau_\lambda^a q_\lambda^{*a}(\Theta)}{4} \tag{4.18}$$

where q_λ^R is the polarized phase function of the Rayleigh scattering optical depth, τ_λ^R. The aerosol polarized phase function, q_λ^{*a}, is parameterized to account for multiple scattering. Aerosol information is contained in the third term on the right hand side of equation 4.18.

Aerosol optical depth and the assumed aerosol model are determined together. The aerosol optical depth is retrieved for each model at the 3 polarized channels and the 13 viewing angles by solving equation 4.18 for τ_λ^a. The aerosol model which minimizes the dispersion of τ^a is used as the aerosol model. POLDER currently uses 12 aerosol models (3 refractive indices varied over 4 Junge distributions). The estimated AOD retrieval uncertainty is 30%.

4.5 The TOMS aerosol algorithm

A unique aerosol retrieval is performed with the total ozone mapping spectrometer (TOMS) instrument; the retrieval process is described by Herman et al., (1997a) and is summarized below. TOMS measures TOA reflected radiation at 0.313, 0.318, 0.313, 0.340, 0.360, and 0.380μm; there is a nearly continuous record of TOMS data from 1978 (the first TOMS launched on Nimbus 7) to the present. The three longest wavelengths were provided to test different methods of producing the observed wavelength dependence of reflected radiation from different atmospheric models. Rayleigh and Mie scattering (including aerosols and clouds) and a surface reflectance contribute to this wavelength dependence. The Dave (1978) code reproduced the radiances quite well for many conditions using a Rayleigh atmosphere and a Lambertian surface reflectance, R. R is calculated by requiring:

$$L_{meas}(0.38\mu m) = L_{calc}(0.38\mu m) \tag{4.19}$$

Where subscripts meas and calc refer to the measured and calculated radiances, respectively. Radiances can then be calculated for other wavelengths and compared to measurements. This results in a residue (ΔN_λ):

$$\Delta N = -100\log_{10}\left[\frac{L_{meas}(0.34\mu m)}{L_{calc}(0.34\mu m)}\right] \tag{4.20}$$

This residue parameter, ΔN, can be used as a measure of the presence of UV-absorbing aerosols. UV-absorbing aerosols attenuate the Rayleigh scattering in and below the aerosol layer which affects the ΔN. Cloud contamination can be a problem. While the spectral signature of clouds can be used as a mask, the large IFOV (from 50×50 km^2 at nadir to 150×250km^2 at ends of the swath) likely misses smaller sub-pixel clouds. ΔN is also very sensitive to aerosol properties which limits the ability to use ΔN as an optical depth retrieval. Table 4.2 (reproduced from Herman et al., 1997a) shows the residue sensitivity to aerosol particle size, absorbing index (i.e., the imaginary part of the refractive index), aerosol layer height and optical depth. It can be seen that varying τ by 0.9 changes ΔN by 1.52; changes in other parameters can produce a similar change in ΔN. For this reason, aerosol information from the TOMS instruments remain as ΔN and research is ongoing toward retrieving a more meaningful parameter.

Table 4.1 – Criteria for retrieving τ for the MODIS land algorithm with the equations for calculating the surface reflectance at 0.47 and 0.66μm (from Kaufman et al., 1997)

Criteria	Near IR range	$\rho_{s,0.47}$	$\rho_{s,0.66}$
1	$0.01 \leq \rho_{2.1} \leq 0.05$	$\rho_{2.1} / 4$	$\rho_{2.1} / 2$
2	$\rho_{3.8} \leq 0.025$	0.01	0.02
3	$0.01 \leq \rho_{2.1} \leq 0.10$	$\rho_{2.1} / 4$	$\rho_{2.1} / 2$
4	$0.01 \leq \rho_{2.1} \leq 0.15$	$\rho_{2.1} / 4$	$\rho_{2.1} / 2$

Table 4.2 – Sensitivity of ΔN to varying particle size, absorbing index, aerosol layer height and aerosol optical depth (from Herman et al., 1997a)

$k = 0.04$, $\tau_{0.38} = 1.$ $h = 2.9km$		$r_{eff} = 0.1$, $\tau_{0.38} = 1.0$ $h = 2.9km$		$k = 0.04$, $\tau_{0.38} = 1.0$ $r_{eff} = 0.1$		$r_{eff} = 0.1$, $k = 0.04$ $h = 2.9$	
Particle Size (μm)	ΔN	Absorbing Index k	ΔN	Height km	ΔN	$\tau_{0.38}$	ΔN
0.1	2.06	0.02	0.71	1.4	0.94	0.1	0.54
0.2	3.03	0.04	2.06	2.9	2.06	0.5	1.32
0.8	5.07	0.06	2.97	5.8	4.18	1.0	2.06

5. Radiative Transfer

Aerosols scatter and absorb solar radiation in the Earth's atmosphere. The Discrete Ordinate Radiative Transfer (DISORT, Stamnes and Swanson, 1981) model is used to model these radiative effects and is developed to model the radiances observed by the GOES-8 Imager visible channel. The GOES-8 Imager is described in the following chapter.

Accurate modeling of the radiative properties in the atmosphere is necessary in remote sensing from satellite. The second simulation of the satellite signal in the solar spectrum (6S, Vermote et al., 1997) has been widely used for aerosol work from satellite (e.g., Stroeve et al., 1997; Sandmeier and Itten, 1997). 6S is the second generation of a model that uses the successive orders of scattering to simulate the satellite signal. It is a well-developed model with user-friendly options for choosing different bidirectional reflectance functions, sensor spectral responses, aerosol optical properties, gaseous atmospheres, etc.

While this model provides many useful routines for simulating atmospheric and surface properties, its method of solution is its weakness. The model solution was tested using a simple Rayleigh atmosphere (completely scattering with no gaseous absorption). The Rayleigh optical depth was varied from 0 to 2.5 and compared to the same solution from the discrete ordinate radiative transfer (DISORT) model (Stamnes et al., 1988). The results (shown in Figure 5.1) compare well for optical depths less than

0.5 with differences less than 2%. However, as the optical depth increases the difference increases more then 35%.

Therefore, the discrete ordinate radiative transfer (DISORT) model is used here to calculate the scattering and absorption of radiation in the atmosphere. DISORT is a widely accepted solution for radiative transfer and has been incorporated into other models such as MODTRAN, LOWTRAN and SBDART.

5.1 DISORT input and output

The DISORT model can calculate radiances at numerous levels in the atmosphere. The scattering parameters required for each model level include: optical depth (τ), single scatter albedo (ω_o), and the coefficients of the Legendre polynomial expansion of the phase function for the layer (P_L). Atmospheric radiative effects are generally described in three ways: Rayleigh scattering (for gases), Mie scattering (for aerosols) and gaseous absorption. These effects must be combined for each layer, so effective τ_{eff}, $\omega_{o,eff}$ and $P_{L,eff}$ are calculated following Greenwald and Stephens (1988):

$$\tau_{eff} = \tau_R + \tau_A + \tau_G$$

$$\omega_{o,eff} = \frac{\omega_{o,R}\tau_R + \omega_{o,A}\tau_A + \omega_{o,G}\tau_G}{\tau_{eff}}$$

$$P_{L,eff} = \frac{\omega_{o,R}\tau_R P_{L,eff} + \omega_{o,A}\tau_A P_{L,eff} + \omega_{o,G}\tau_G P_{L,eff}}{\omega_{o,R}\tau_R + \omega_{o,A}\tau_A + \omega_{o,G}\tau_G}$$

where subscripts R, A, and G represent Rayleigh, aerosol and gaseous effects. The equation is simplified using a fully absorbing gas, $\omega_{o,G} = 0$, and conservative Rayleigh scattering, $\omega_{o,R} = 1$:

$$\tau_{eff} = \tau_R + \tau_A + \tau_G$$

$$\omega_{o,eff} = \frac{\tau_R + \omega_{o,A}\tau_A}{\tau_{eff}}$$

$$P_{L,eff} = \frac{\tau_R P_{L,eff} + \omega_{o,A}\tau_A P_{L,eff}}{\tau_R + \omega_{o,A}\tau_A}$$

The derivation of these parameters are described in the following sub-sections. These optical properties are calculated by Mie code and other routines at a desired wavelength. Thus, the wavelength of radiation is not input directly into DISORT, but is inherently dependent upon wavelength through the calculation of the optical properties by other routines.

Other parameters are also required to operate DISORT. The incident solar irradiance at the top of the atmosphere is described by its intensity and the solar zenith angle (θ_o). The solar spectral irradiance at the wavelength for which the optical properties were calculated is used to simulate the radiance reflected to space. DISORT calculates view angle-dependent radiances. Thus the satellite zenith angle (θ) and azimuth angle relative to the solar azimuth angle ($\Delta\phi$) are also input. The spectral radiances are then weighted by the satellite sensor to determine a satellite-detected radiance, L^*, for a given geometry.

A Lambertian surface is used to describe the reflectance of the Earth. While most land surfaces are not Lambertian, the GOES views a specific scene from very limited geometry. Only the solar declination angle varies on a daily basis; over the course of a month, this change can be as large as 10° (Houghton, 1985). This change is relatively small because bidirectional reflectances tend to be smooth functions, as shown by measurements of surface bidirectional reflectance distributions over different surfaces by Tsay et al. (1998). The uncertainty of the assumption of a Lambertian surface is discussed in chapter 8.

DISORT solves the radiative transfer equation for a plane-parallel atmosphere through the discrete ordinate method. Thus the accuracy of angular dependence of L^* is dependent upon the number of streams, N_s, used. The accuracy of the model increased as N_s doubles, but so does computation time. Two model runs were computed: $N_s = 64$ at 57 wavelength bands and 16 streams at 8 wavelength bands. Figure 5.2 shows the percent differences in L^* as a function of viewing angle (positive is toward the Sun) for different scattering media. Larger differences are seen at large viewing angles. Differences are small when gaseous absorption is excluded. When gaseous absorption is included, the differences can be as large as 3% near the horizon. Thus, the $N_s = 16$ case is used to calculate τ, but viewing and solar zenith angles are limited to less than 50° to keep the error of 16-streams to a minimum. This also excludes zenith angles where the plane-parallel assumption is invalid (Houghton, 1985).

5.2 Spectral and vertical resolution

The GOES visible sensor has a broad spectral response, encompassing 0.525 to 0.725μm (width at half maximum) with a maximum response at 0.6μm (details of the GOES Imager characteristics are discussed in chapter 5). The spectral response is shown in figure 5.3, where the response has been normalized by:

$$1 = \int_{0.45\mu m}^{1.01\mu m} W(\lambda) d\lambda$$

where 0.45 and 1.01μm are the bounds on the GOES spectral response. Computing L^* at each wavelength is computationally expensive, so the response function between 0.5 and 0.85μm was binned into 8 wavelengths ($\Delta\lambda = 0.05$). This is shown by the solid line in Figure 5.3. It reasonably recreates the GOES spectral response and was shown in figure 5.2 to incorporate little error. Aerosol , Rayleigh and gaseous optical properties for the eight wavelength bands are listed in Table 5.1. In general, τ_R and τ_A decrease with wavelength, whereas τ_G is variable with wavelength because of the spectral absorption bands of different gases.

The DISORT model was also tested for the number of layers required to accurately simulate the aerosol, Rayleigh and gaseous vertical distributions. Aerosol and gaseous data are available at 33 layers from McClatchey atmospheric profiles (McClatchey, 1971) and MODTRAN aerosol profiles (respectively). The vertical extinction coefficient for gaseous particles is shown in figure 5.4 for a tropical atmosphere. The Rayleigh and gaseous extinction coefficients are calculated using 6S-generated transmittance. The GOES visible imagery is sensitive to the oxygen-A band, water vapor and ozone absorption bands. The vertical extinction coefficient, b_{ext} for gaseous absorption and Rayleigh scattering is shown in figure 5.4. Rayleigh and oxygen b_{ext} monotonically decrease with height. The water vapor and ozone b_{ext} follow their respective distributions in the atmosphere, with water vapor peaking at the surface and ozone peaking in the stratosphere. The aerosol vertical distribution is shown in figure 5.5. Most of the aerosols are limited to the boundary layer, with a secondary maximum in the stratosphere. To save computational time, the atmosphere was grouped into six layers (solid line in figure 5.5). Table 5.2 shows calculated reflectances for the full 33-layer simulation compared to 1-layer (i.e., "slab" model) and 6-layer simulations. These simulations were performed for different scattering and absorption conditions. The 1-layer model is the DISORT simulation most similar to the 6S solutions. In general, the differences are less than 1%. However, the 1-layer difference increases more rapidly with optical depth than the 6-layer. Therefore, the 6-layer model is used to simulate atmospheric reflected radiation. Retrieving aerosols is performed by inserting aerosols into the lowest layer (0-2 km). The error in the uncertainty of the aerosol height is discussed in section 8.2.3.

5.3 Aerosol scattering and absorption

Calculations of aerosol optical properties are made at the center of the 8 wavelength bands. The Legendre polynomials of the phase function are calculated for an aerosol size distribution using MIESCAT Fortran code, which was obtained from K. Frank Evans of the University of Colorado. The optical properties were calculated for the four aerosol model described in Table 2.1. The refractive index for all is assumed m = 1.53 + 0.0035i.

The calculation of aerosol spectral extinction coefficients are shown in Figure 5.6 (the Rayleigh spectral scattering coefficients are also included, dash-dot-dotted line). It is clear that the dust model (dash-dotted line) has the least spectral dependence, while the continental (solid), industrial (dashed) and biomass burning (dotted) have similar dependence. Because the spectral signature is determined solely by the aerosol model, the wavelength at which the aerosol optical depth is retrieved is relatively unimportant (except for comparison to ground truth). Thus, the optical depth retrieval is defined at $\lambda = 0.5\mu m$.

Table 5.1 – Spectral information used in the GOES-AOD RT model.

Wavelength Range (μm)	0.5-0.55	0.55-0.60	0.60-0.65	0.65-0.70	0.70-0.75	0.75-0.80	0.80-0.85	0.85-0.90
Sensor Response	0.034	0.24	0.26	0.22	0.15	0.072	0.017	0.002
$\tau/\tau_{0.5\mu m}$	1.00	0.86	0.75	0.67	0.59	0.53	0.48	0.44
Rayleigh τ	0.12	0.092	0.065	0.048	0.036	0.027	0.022	0.014
Gas τ	0.011	0.024	0.041	0.030	0.13	0.25	0.026	0.33

Table 5.2 – Sensitivity of reflectance to vertical resolution of the model.

Atmosphere type	33-layer Reflectance	1-layer % Difference	6-layer % Difference
Rayleigh Scattering	0.106612	0.0075	0.0
Aerosol Extinction	0.193738	0.0	0.0
Ray. + Gas	0.094218	2.98	-0.0096
Ray + Aer	0.210448	25.9	0.018
Gas + Aer	0.179736	0.40	0.082
Ray + Aer + Gas			
$\tau_{aer} = 1$	0.195508	-0.078	-0.055
$\tau_{aer} = 2$	0.274972	-0.91	-0.077
$\tau_{aer} = 3$	0.332758	-1.2	-0.091

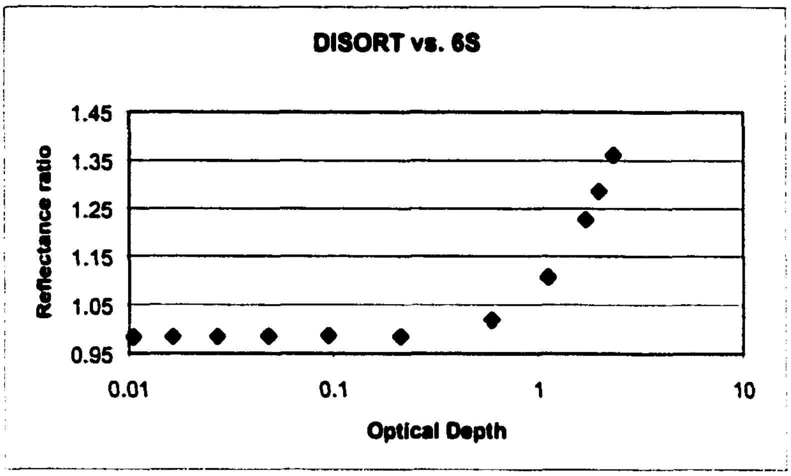

Figure 5.1 – Ratio of 6S to DISORT calculations of satellite-detected radiance for varying Rayleigh optical depths.

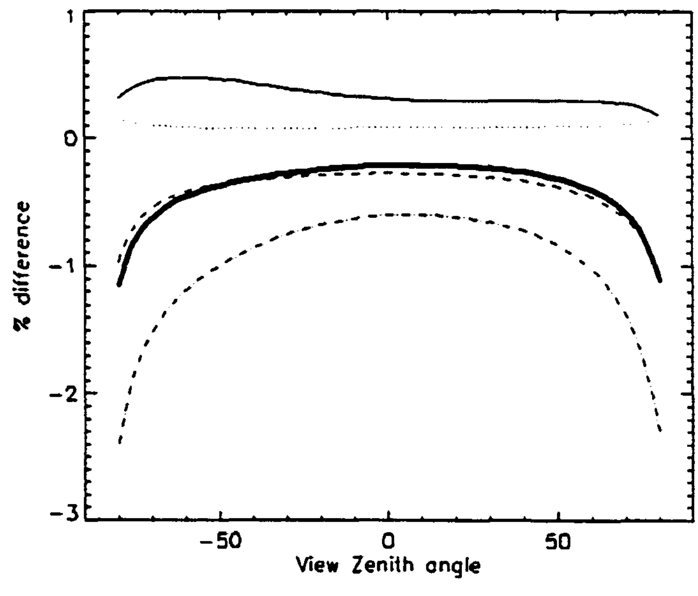

Figure 5.2 – Percent difference for two DISORT calculations for atmospheres scatterers and absorbers: aerosols (thin solid), Rayleigh (dotted), aerosol + gaseous (dashed), Rayleigh + gas (dot-dashed) and aerosol + Rayleigh + gas (thick solid)

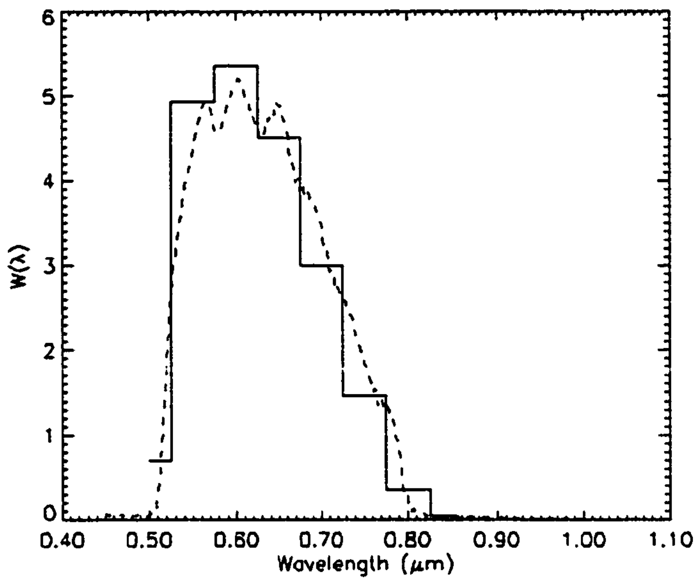

Figure 5.3 – GOES-8 normalized spectral response, W(λ), as a function of wavelength (dashed line). GOES-8 spectral response used at the RT wavelengths for the GOES-AOD algorithm (solid line). Spectral range encompasses 99.5% of the GOES-8 spectral response.

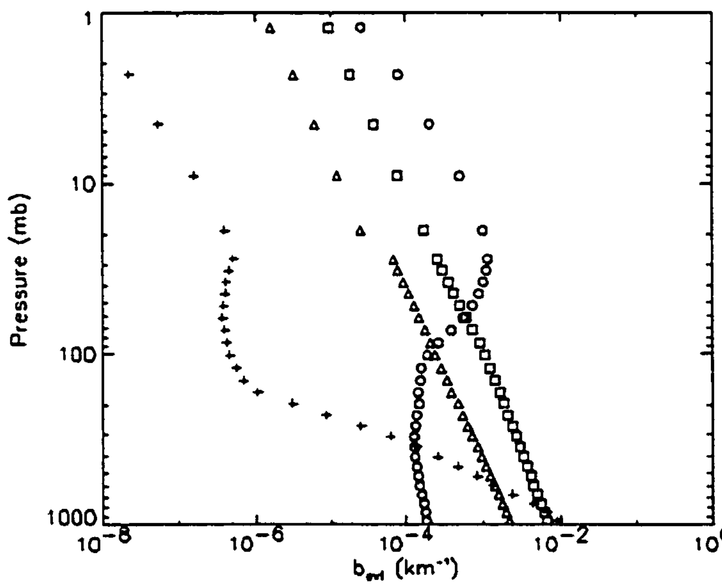

Figure 5.4 – Vertical distribution of the effective extinction coefficient (b_{ext}) for the GOES-8 Imager visible wavelength for water vapor (+), ozone (o), Rayleigh scattering (□) and oxygen (Δ).

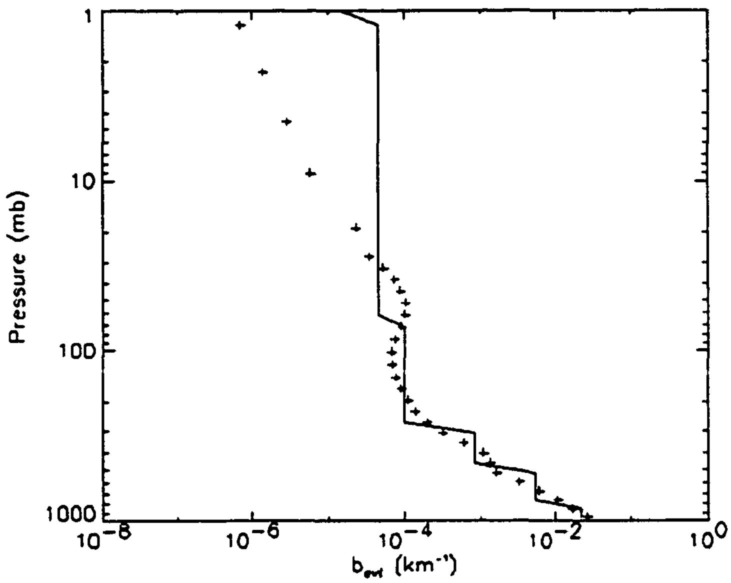

Figure 5.5 – Vertical distribution of the aerosol extinction coefficient (b_{ext}). Solid line uses six atmospheric layers.

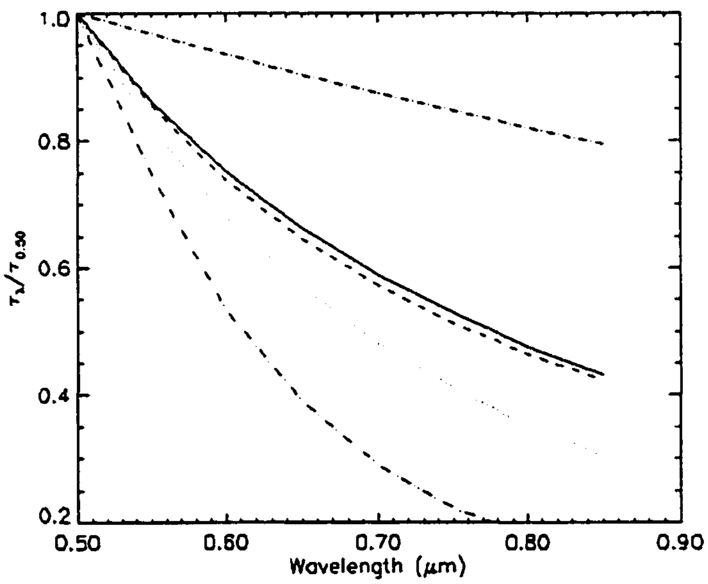

Figure 5.6 – Aerosol spectral optical depth (normalized by τ at λ = 0.5μm) for the continental (solid line), biomass burning (dotted line), industrial (dashed) and dust (dash-dotted) aerosol models. The normalized Rayleigh spectral optical depth is also included (dash-dot-dotted line).

6. Instrumentation

As described above, aerosols have the largest radiative effect – thus, are best detected – in the visible region of the EM spectrum. The following describes the two primary data sources used in this dissertation. The GOES-8 Imager is calibrated in the next chapter. The GOES-AOD algorithm is then developed in chapter 8; the AERONET observations are used as "ground-truth" in chapter 9 to validate the GOES-AOD retrievals.

6.1 The GOES satellite

As described in chapter 3, the first geostationary weather satellite – the ATS-1 – was launched in 1966. The primary imaging instrument was the Spin Scan Radiometer (SSR), which had an infrared and visible channel. Later the SMS-1 was launched with an improved version of the SSR (VISSR) and finally the first operational weather satellite in geostationary orbit was launched in 1975 – the Geostationary Operational Environmental Satellite (GOES-1). For the next 24 years, the primary design of the following GOES series satellites went unchanged. GOES-8, however, was the first in a series of improved geostationary sensors. The reader is referred to Menzel and Purdom (1994) or Ellrod et al. (1998) for more detailed descriptions of the improvements of GOES-8 over the previous GOES-series of satellites. The following is a description of the GOES-8 and specifically the visible channel of the Imager.

6.1.1 Imager spectral characteristics

The Imager has five channels that measure radiation reflected by or emitted from the Earth. Table 6.1 shows the wavelength ranges and observable phenomena for each channel. The size parameter ($\chi = 2\pi r/\lambda$) is listed for the central wavelengths of each channel in Table 6.2 Also, the Mie extinction efficiency (Q_{ext}) for an aerosol particle (with r = 0. 25 and m=1.43+0i) is shown for the central wavelength. It can be seen that the visible channel is the primary channel available for aerosol observation. Also, the mid-IR channel (channel 2) has some sensitivity to aerosols. Thus, optically thick dust can have an observable effect on infrared radiation

6.1.2 Imager visible calibration

Upon launch of GOES-9 in 23 May 1995 (405 days after the GOES-8 launch), visible images were compared to those from the GOES-8 Imager. The GOES-8 imagery was noticeably darker, suggesting a decrease in the response of the instrument. M. Weinreb of NESDIS found a 15% difference between the reflectances calculated from the two instruments (personal communication) suggesting a departure from the pre-launch calibration coefficients. NESDIS researched the problem, but is yet to perform operational calibrations, thereby leaving it up to the user. The GOES-8 calibration is described in the following chapter (also, Knapp and Vonder Haar, manuscript accepted to the *Journal of Atmospheric and Oceanic Technology*).

6.1.3 Imager characteristics

The Imager visible channel has a 1 × 1 km^2 IFOV, thus one pixel corresponds to 1 km^2 at nadir. This roughly corresponds to 1.2 × 1.2 km^2 at 30°N and 1.5 × 1.5 km^2 at 45°N because of the curvature of the Earth.

The Imager observes the Earth on a flexible schedule. In general, the continental U.S. is viewed every 15 minutes, the Northern Hemisphere is viewed every 30 minutes and the full disk of the earth is viewed at least every three hours. This schedule is often interrupted for rapid-scan imagery which allows the observation of small areas at 1 minute intervals. This has lead to spectacular satellite loops of severe storm development and cloud motions in a hurricanes eye. However, these scans are often taken at the expense of observations of the Southern Hemisphere.

6.1.4 Data processing

The signal-to-noise ratio (S/N) of the visible instrument can be determined empirically from satellite imagery. The S/N is determined by measuring the same radiance numerous times. This is performed when the sensor views space. The statistics of a GOES-8 view of a 400×400 pixel sector of space is 29 ± 2.71 counts (1σ), which is similar to ±8 counts (3σ) reported in Menzel and Purdom (1994). This S/N is somewhat low, as the satellite signal of aerosols over land can be less than 8 counts. Thus, spatial averaging is performed in this research to provide a better estimate of that actual count value measured.

6.2 The Aerosol Robotic Network (AERONET)

The Aerosol Robotic Network (AERONET) is a federation of sun-photometers with a centralized data processing site that allows fast dissemination of AERONET measurements. The data are made available through the web site: http://aeronet.gsfc.nasa.gov:8080/. The reader is referred to Holben et al. (1998) for a thorough description of the AERONET; a summary of details relevant to this work is given below.

6.2.1 Radiative measurements

The CIMEL (a French manufacturer) sun-photometers measure direct solar radiance at 8 spectral bands; standard wavelengths include: 0.44, 0.67, 0.87, 0.94 and 1.02μm. Other measurements (which vary with site) include 0.50μm and polarization at 0.87μm. Radiance measurements at each spectral band are taken looking directly at the sun or sky.

In addition to measurements of the direct solar beam, the photometer performs measurements through the almucantar, and principle plane. An almucantar scan is a set of measurements that starts with the photometer measuring the direct beam, then scans through the full azimuth (holding the elevation angle constant). This provides sky radiance measurements at numerous scattering angles from the Sun. Conversely, a principle plane scan observes through elevation angles, holding azimuth constant. These two measurements techniques provide sky radiances at numerous scattering angles and wavelengths that can be used to estimate aerosol optical depth, phase function and size distribution.

Calibration is a three step process. First, a reference instrument is calibrated using an integrating sphere at Goddard Space Flight Center. This results in a gain which is used to convert digital output from the instrument to radiance units (W m^{-2} μm^{-1}). The accuracy of this calibration is less than ±5.5%. Second, the reference instrument is stationed at Mauna Loa. Mauna Loa is the Earth's optimum location for the calculation of V_0 (because of the pristine atmosphere, high elevation and low latitude). The reference instrument is used to create Langley plots, which are used to determine the instruments extra-terrestrial solar constants. Third, the reference instrument is returned to GSFC after 6 months where it is used to transfer its calibration information to other photometers. Field photometers are then calibrated with the reference photometers at 6-

month intervals. The overall calibration uncertainty, expressed in aerosol optical depth, is $\Delta\tau \sim 0.01$ for wavelengths greater than 0.44μm.

6.2.2 Instrument characteristics

An interesting aspect of this network is that while temporal measurements are defined at specific air mass intervals, the locations of the instruments is defined solely by the owner of the instrument. Thus, AERONET are reliable when you know where they are and spotty if you need data at a certain location and time period. The temporal distribution of sites is shown in Table 6.3. In general, the number of sites has increased since the first few sites operational in 1995. The decrease in the number of sites for 1999 is because of the time lag of 6 months to a year required for reprocessing and re-calibration of Level 1 data. The distribution of sites is shown in Figure 6.1. In general, measurements are concentrated over the US, with numerous sites on other continents and less in oceanic areas.

6.2.3 Data Processing

The processing of the AERONET data is well documented by Holben et al. (1998) and is summarized here. The AERONET database contains two primary data levels. Level 1 consists of the measurements as reported directly from the instrument. The level 2 data set is the processed version of the level 1 data. The processing for level 2 includes cloud screening and post-calibration. Each radiance measurement by the instrument is performed in triplets – three individual measurements at 15 second intervals. Significant variation in these triplets is assumed to be cloud contamination and is filtered by the Level 2 processing algorithm. Also, an instrument needs to be re-calibrated every 6 months to be processed at level 2. This provides a higher accuracy radiance measurement, because filter throughput (transmittance) decays with time.

6.3 Polar Orbiting Instrument Aerosol Retrieval Simulation

The ability of a polar orbiting satellite to retrieve an optical depth characteristic of the daily optical depth can be investigated using the AERONET data. A polar orbiting satellite instrument generally has one sunlit observation per day per Earth location. The time of this observation is determined from the satellite orbital characteristics – primarily, the equator crossing time. Satellite observations should be representative of the daily average aerosol optical depth for these once-per-day observations to be useful.

AERONET data was averaged to provide daily average aerosol optical depths and compared to instantaneous observations at specific times of day. This was performed for two simulations: 1) SCAR-B, where only Level 2 AERONET data from the SCAR-B experiment was used (10 sites) and 2) All level 2 AERONET data from 1997 (32 sites). The spatial coverage of the SCAR-B simulation is primarily South America. The second simulation extends this to most parts of the world. The daily average τ is compared to the optical depth at a certain time of day, τ_H, where H represents the departure from 12:00 local time (LT). For example, τ_{-2} would represent the observation nearest 10:00 local standard time. This is characteristic of a morning polar orbiter. Figure 6.2a shows the SCAR-B simulation; the relationship is highly correlated with bias of only 0.01 and the RMS is 0.125. However, the statistics are largely affected by the observations of smoke-free sky. Figure 6.2b shows the same comparison for optical depths larger than 1. In this case, a significant bias emerges (0.21) with a large RMS (0.42). A similar analysis on a global scale (simulation 2) is shown in figure 6.3. Therefore, for optical depths less than one, an observation from one time of day is generally characteristic of the entire day. However, when the optical depth is large, more than one measurement is required to estimate the daily average τ.

Also, clouds can significantly decrease the number of aerosol optical depth retrievals from a polar orbiting instrument. For simulation 1, 48% of the days had a missing observation at 10:00 LT yet had at least one aerosol observation at some other time of that day. On a global scale, a polar orbiter will miss 40% of observations at 10:00 LT. Table 6.4 shows the percentages of aerosol observations missed for numerous observation times. In general, the best case scenario is a satellite observing near 8:00 LT, thus missing only 37.1% of the days. Daily observations may be less important to climatological observations, where monthly averages are compiled, but military applications and fire monitoring require constant monitoring of regional aerosol trends.

Table 6.1 – Spectral characteristics of the GOES-8/Imager with examples of observable phenomena (from Menzel and Purdom, 1994)

Channel	λ range (μm)	Observable phenomena
1	0.52-0.72	Clouds, aerosols
2	3.78-4.03	Discrimination of fog at night, fire detection, Ice/Water cloud discrimination
3	6.47-7.02	Upper-tropospheric water vapor
4	10.2-11.2	Thermal radiances
5	11.5-12.5	Low-level water vapor, sea surface temperature and airborne dust and volcanic ash

Table 6.2 – Aerosol extinction efficiency (Q_{ext}) as calculated by Mie code for a particle with r = 0.25 μm with m = 1.43 + 0.0i.

Channel	Central λ (μm)	Size Parameter	Q_{ext}
1	0.7	2.24	1.65
2	3.9	0.40	4.7×10^{-3}
3	6.7	0.23	5.4×10^{-4}
4	10.7	0.15	5.8×10^{-5}
5	12.0	0.13	5.2×10^{-5}

Table 6.3 – Number of Level 1 and 2 data sites grouped by year.

Year	Number of Level 1 Data Sites	Number of Level 2 Data Sites
1993	19	16
1994	48	31
1995	57	37
1996	67	44
1997	64	32
1998	77	25
1999	99	14

Table 6.4 – Simulated percent of days observed by a polar orbiting instrument with observation time H.

H	Local Time	% observed
-4	08:00	72.9
-3	09:00	59.4
-2	10:00	60.2
-1	11:00	62.4
0	12:00	65.7
1	13:00	65.5
2	14:00	64.8
3	15:00	60.3
4	16:00	62.0

Figure 6.1 – Level 2 AERONET site locations around the world (from Brent Holben, http://aeronet.gsfc.nasa.gov:8080/).

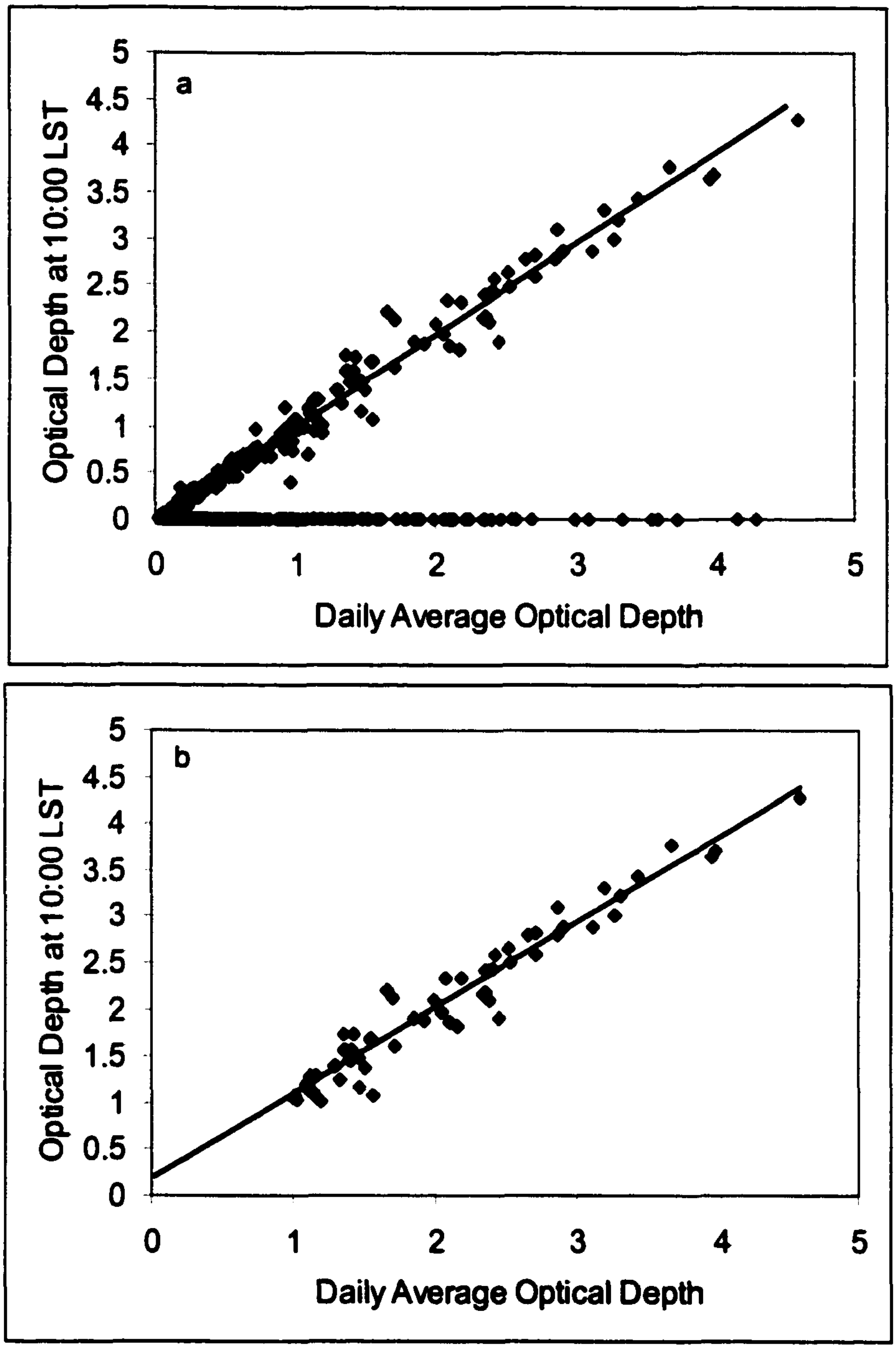

Figure 6.2 – a) Comparison of daily average τ with that observed at 10:0 LST for SCAR-B AERONET sites. The solid line is the linear regression with y = 0.9857x, r^2 = 0.98. b) the same as part a excluding τ = 0. and τ < 1. The linear regression equation is y = 0.9167 + 0.1788, r^2 = 0.94.

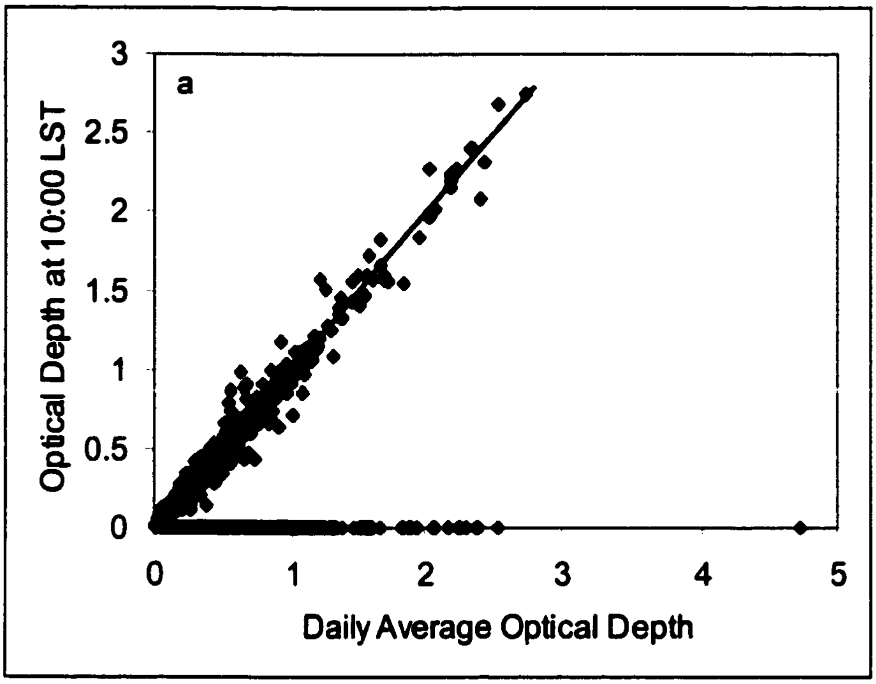

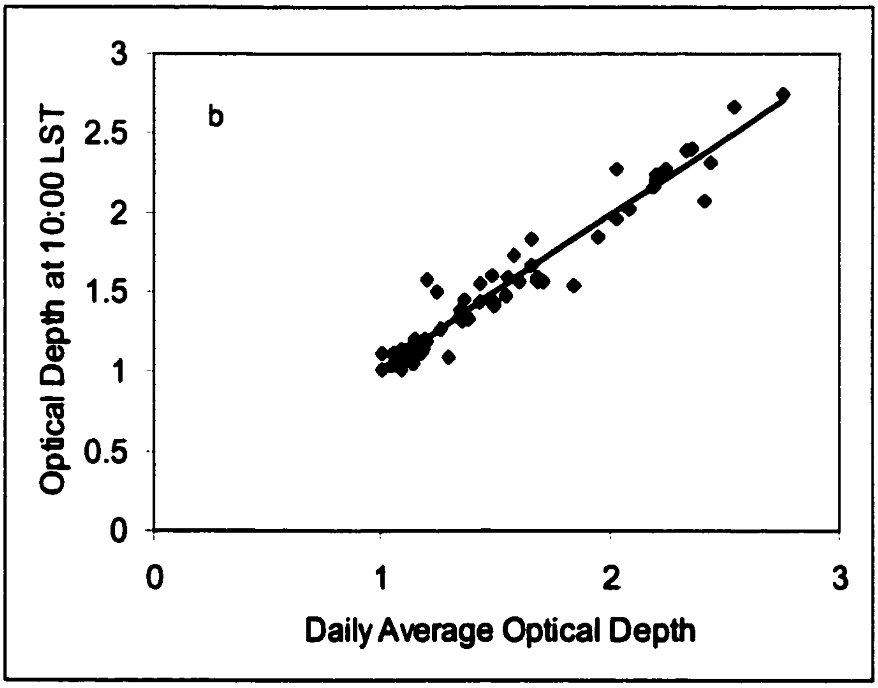

Figure 6.3 – a) Comparison of daily average τ with that observed at 10:0 LST for all 1997 level-2 AERONET sites. The solid line is the linear regression with y = 0.991x, r^2 = 0.98. b) the same as part a excluding τ = 0. and τ < 1. The linear regression equation is y = 0.970 + 0.04, r^2 = 0.94.

7. GOES-8 Visible Calibration

The GOES-8 imager visible sensor (described above) is calibrated in this chapter. The new calibration coefficients are used to derive aerosol optical depth in chapters 8 and 9.

7.1 Introduction

The GOES-8/Imager has provided scientifically valuable images of weather phenomena since its launch on 13 April 1994. The Imager views the earth at a higher spatial (1km at nadir) and temporal (about 1 minute in rapid scan mode) resolution than its predecessor, the Visible Infrared Spin-Scan Radiometer (VISSR) (Menzel and Purdom, 1994). This high temporal resolution imagery has contributed to the understanding of rapidly-developing weather systems (e.g., thunderstorms and hurricanes). The reader is referred to Menzel and Purdom (1994) or Ellrod et al (1998) for further description of the improvements from GOES-7 to GOES-8 imagery. Also, the GOES-series of satellites has made significant contributions to cloud climatology through the International Satellite Cloud Climatology Project (ISCCP) – a database of cloud observations where clouds are classified by cloud-top temperature (an infrared observation) and optical depth (a visible observation).

The GOES-8/Imager visible channel (centered on 0.6μm with 0.52-0.72μm full width at half maximum) provides qualitative images of weather phenomena.

Quantitatively, it provides visible radiance data, however, little calibration information is available beyond that provided by the manufacturer. Upon the launch of GOES-9 in 1995, a 15% difference was noted between the satellite-detected reflectances of the new GOES-9/Imager visible data and the older GOES-8/Imager (M. Weinreb, 1995 personal communication). Since this observation, researchers using the GOES-8/Imager visible data have performed their own independent calibrations. This work summarizes these previous calibration efforts in order to quantify the calibration uncertainty for the GOES-8 visible channel.

The calibration method proposed here is similar to the method described by Fraser and Kaufman (1986). Fraser and Kaufman (1986) calibrate GOES/VISSR imagery using clear-sky observations of the North Atlantic Ocean. These ocean observations are correlated to theoretical reflectances computed by a radiative transfer model, from which a measure of sensor response is derived. The calibration method herein, is similar, comparing GOES-8 ocean observations to simulated reflectances. However, this method is an improvement over Fraser and Kaufman (1986) in that 1) the Southern Pacific Ocean is used, which has less aerosol than the Northern Atlantic Ocean, and 2) ocean anisotropic reflectance is simulated using wind speed estimates from the Special Sensor Microwave/ Imager (SSM/I). The calibration of the GOES-8/Imager visible channel was performed at 6-month intervals from August 1995 through August 1999. These calibration results are compared to previous calibration efforts. Studies of clouds (e.g., Minnis and Smith, 1998, Greenwald et al., 1997) and aerosols (e.g., Knapp and Vonder Haar, 2000) can benefit from these calibration results.

Henceforth, references to the visible channel imply the GOES-8/Imager instrument, since neither the visible sensor of the GOES-8 Sounder nor other GOES-series sensors were calibrated in this work. Section 7.2 provides a summary of visible channel calibration and a review of recent calibration studies of GOES visible imagery. The calibration method is described in section 7.3, and results are presented in section 7.4.

7.2 Background

7.2.1 Calibration review

The visible channel measures radiance of reflected sunlight with eight independent detectors. These detectors convert sensed radiance to voltage, which is then digitized to 10-bit quantized data (that is, given values from 0 through 1023). For GOES-8, the relationship between radiance (L) and digital counts (DN) is a linear one:

$$L = DN \bullet m + b. \tag{7.1}$$

The values of slope, *m*, and intercept, *b*, are unique for each detector. The output from all the detectors are now normalized to detector #6 to prevent image striping; the calibration coefficients of detector #6 are m = 0.5522 W m^{-2} ster^{-1} μm^{-1} DN^{-1} and b = -15.27 W m^{-2} ster^{-1} μm^{-1}. Satellite-detected reflectance (ρ_{sat}) is obtained by normalizing L by the solar output weighted by the instrument spectral response (F_o) by:

$$\rho_{sat} = \frac{\pi L}{\delta(D)\mu_o F_o}, \tag{7.2}$$

where μ_o is the cosine of the solar zenith angle, π comes from the conversion to an equivalent Lambertian reflectance and δ is the Earth-Sun distance correction factor for the day of the year, D. F_o is computed from:

$$F_o = \frac{\int_0^\infty S(\lambda)W(\lambda)d\lambda}{\int_0^\infty W(\lambda)d\lambda} = 1628\,\mathrm{W\,m^{-2}ster^{-1}\mu m^{-1}},$$

where $S(\lambda)$ is the top of the atmosphere solar spectral flux and $W(\lambda)$ is the spectral response of the instrument. Equations 7.1 and 7.2 are combined to form:

$$\rho_{sat} = \frac{1}{\delta(D)\mu_o}\frac{DC - C_o}{\gamma}, \qquad (7.3)$$

where C_o (= -b/m) represents the GOES offset (the DN value when viewing space) and γ is the calibration coefficient. For pre-launch conditions, $\gamma = F_o/(m\pi) = 938.4$ DN.

7.2.2 Previous calibration efforts

Previous researchers have used the GOES-8 visible channel for quantitative scientific research, each making corrections to the calibration using methods suitable to their needs. The methods are discussed below and a summary of the results is shown in Figure 7.1.

Greenwald et al. (1997) calibrate the GOES-8 visible sensor by matching a histogram of reflectance to that of co-located GOES-9 data (asterisk, Figure 7.1). Bremer et al. (1998) find that the star-sense radiance measurements (which are used in determining the satellite attitude) have decreased since launch at an average rate of 7.6% per year (dashed line, Figure 7.1) over a period from January 1995 through January 1998. Ellrod et al. (1998) note a one-time 9% drop in responsivity shortly after launch (square, Figure 7.1). Minnis and Smith (1998) co-locate NOAA-14/ AVHRR channel-1 data with GOES-8 imagery, resulting in $\gamma = 768$ DN for 9 April through 9 May 1996 (triangle, Figure 7.1).

Unpublished studies from the National Environmental Satellite, Data, and Information Service (NESDIS) have shown a significant ongoing decrease in the GOES-8 detector responsivity. The 15% decrease noted by M. Weinreb is denoted by × in Figure 7.1. N. Rao (1998, personal communication) collected data over the Sonoran Desert from November 1994 through October 1997 which indicated a degradation trend of about 4.5% per year (solid line, Figure 7.1). Note: the results of Rao (1998) and Bremer et al. (1998) are trends and thus are plotted in figure 7.1 relative to Ellrod et al. (1998).

7.3 Calibration Method

Calibration of a radiation sensor is generally performed under conditions where the instrument is viewing a source of known radiance. However, vicarious calibration is required when the instrument is in orbit and no calibration is available. In some cases, radiance observations of an earth location from one sensor are transformed to another sensor (e.g., Minnis and Smith. 1998); another method is to compare observations to modeled results. In the latter, a region where the surface and atmospheric characteristics are well-known is required. Radiative transfer models also allow the investigation of calibration sensitivity to different atmospheric and surface parameters, such as ocean roughness and aerosol optical depth. Unfortunately, there are relatively few locations around the globe where aerosol optical depth, atmospheric temperature and humidity and surface reflectance are measured routinely.

Therefore, clear-sky ocean observations are used to calibrate the GOES-8. The full disk image time nearest to local noon for GOES-8 (17:45 UTC) was chosen for calibrations. For this condition, the Earth-Sun-satellite geometry is primarily back scattering and the sensitivity of ρ_{sat} to τ is at a minimum ($\partial\rho_{sat}/\partial\tau$, Figure 7.2). Each full resolution GOES-8 image was broken into 16×16 pixel sectors (N=256), which constitutes two passes of the eight-detector array. Sectors with a standard deviation near the noise level of the sensor were used as calibration points; this effectively filtered out all land and cloudy pixels. The Southern Pacific Ocean was chosen as a suitable calibration area because aerosol optical depths are low in this region and the ocean surface reflectance can be characterized by only a few parameters. The heavy lines in figure 7.2 denote the calibration region, bounded by 15°S, 90°W and a satellite view angle less than 65°. All sectors located within the defined region in Figure 7.2 which satisfied the noise criteria were used as calibration points for each day. For each ocean calibration point, four space views were used to define the offset (C_o).

7.3.1 Simulating ρ_{sat}

The radiative transfer model used herein was the Second Simulation of the Satellite Signal in the Solar Spectrum (6S) described by Vermote et al. (1997). Aerosol optical depth is input at 0.55µm. Using the aerosol optical properties of the maritime aerosol model (WMO, 1983), 6S calculated scattering properties at 10 wavelengths between 0.4 and 3.75µm. The aerosol scattering was then interpolated to the resolution at which the gaseous transmittance is calculated, 0.0025µm. The top-of-the-atmosphere (TOA) radiance was then calculated using the successive orders of scattering solution method at the gaseous spectral resolution. Finally, the ρ_{sat} was simulated by weighting the spectral TOA reflectances by $W(\lambda)$.

For ocean observations, the ρ_{sat} is dependent upon ocean reflectance parameters as well as atmospheric absorption (primarily due to ozone and water vapor) and scattering (molecular and aerosol scattering) characteristics. The ocean surface reflectance is a function of wind speed and direction, ocean salinity and the pigment concentration. 6S simulates the ocean reflectance with a bidirectional distribution function summarized by Vermote et al. (1997) which accounts for the contribution of: whitecaps, sun glint, Fresnel's reflection and also the reflectance emerging from sea water.

7.3.2 Sensitivity of ρ_{sat} to model parameters

A sensitivity study was performed to determine the influence of different atmospheric and oceanic parameters on the calibration method. Surface, atmospheric and oceanic parameters were varied to determine their contribution to the calibration uncertainty; the parameters studied include: surface wind speed and direction, aerosol optical depth (τ), atmospheric model (which defines column water vapor and ozone amounts), Rayleigh optical depth and the ocean pigment and salinity. The default values for each parameter and the amount that each was varied are presented in Table 7.1. Atmospheric transmission was calculated for each model atmosphere, the largest difference being between the sub-arctic winter and the tropical model (the atmospheres used in 6S are defined by McClatchey et al., 1971). Also, a 1.6% uncertainty estimate in the 6S model (Vermote et al., 1997) is included. The range in DN (ΔDN) was calculated by differentiating equation 7.3:

$$\Delta DN = \frac{dDN}{d\rho_{sat}}\Delta\rho_{sat} = \gamma\Delta\rho_{sat}, \tag{7.4}$$

where the pre-launch γ value is used and μ_o and $\delta(D)$ are ignored in these sensitivity studies. Changes in aerosol optical depth and surface wind speed resulted in the largest change in ρ_{sat}. Other errors suggest less than 1 DN uncertainty assuming that one can estimate their value near the monthly average. Thus, greater effort was made toward estimating the surface wind speed and τ. Further, the sensitivity of the calibration to τ was illustrated by plotting values of $\partial\rho_{sat}/\partial\tau$ (Figure 7.2). Values increase toward the horizon (as path length increases) and become negative in the sun glint region (where the specular reflectance is large and a differential increase in τ abates this effect). In general, values in the calibration region are less than 0.15, so an error in τ of 0.01 results in an error in ρ_{sat} of 0.0015 or less.

7.3.3 External data

The Special Sensor Microwave Imager (SSM/I) data archive provides estimates of surface wind speeds from retrievals at microwave frequencies (Wentz, 1997). Monthly wind speed maps were created from SSM/I-retrieved daily wind speed data. Clouds were filtered by removing SSM/I pixels having cloud liquid water amounts greater than 0.075mm prior to computing the monthly average to create an average cloud-free wind field. The results of the cloud filtering procedure effectively removed the higher wind speeds generally associated with the presence of clouds.

Aerosol optical depth estimates from the NOAA/AVHRR Pathfinder data set were employed in the calibration. Data from Husar et al. (1997) show that the Southern Pacific has the lowest aerosol burden of all the oceans of the world. Monthly-mean values of τ from the Pathfinder Atmospheres dataset (Stowe et al., 1997) for the Southern Pacific Ocean were computed as 0.04 and 0.10 for the months of August and February, respectively, and were used in the 6S simulations of ρ_{sat}. Uncertainty in γ resulting from this assumption will be discussed in the results section to follow.

7.4 Results

Daily comparisons of modeled ρ_{sat} and observed DN were used to calculate γ. An example of this method is shown in Figure 7.3. Figure 7.3a shows the location of the calibration points. The solid line in Figure 7.3b shows the pre-launch calibration. All 480 calibration points are below this line, suggesting a degradation in instrument response. The calibration coefficient, γ, is calculated through linear regression of the calibration points (including the space views) and 6S-simulated ρ_{sat}. The average number of ocean calibration points was 500 per day (ranging from 150 to 824 per day).

Monthly-averaged γ values are plotted together with those of previous research in Figure 7.4 as plus signs. The current estimates of γ compare well with those of previous work. Linear regression of the monthly values (Figure 7.4) suggests a decrease in γ of 52.5 per year (5.6% per year). The vertical extent of the plus signs represent the 99% confidence limit; these values are on the order of 2% of γ. However, the degradation need not be linear. Specifically, the change between August 1997 and February 1998 departs from the linear fit. This non-linearity may be due to variations in the aerosol optical depth or could be related to changes in the instrument optics.

For analysis purposes, γ can be approximated by linear regression with a fixed intercept. In this case, γ becomes:

$$\gamma \approx \frac{\overline{DC \pm \sigma_G} - \overline{C_o \pm \sigma_G}}{\overline{\rho_{sat} \pm \sigma_\rho}},$$

where barred quantities are averages of the calibration points and σ represents the standard deviation of the GOES and 6S (subscripts G and ρ, respectively). The resulting relative calibration uncertainty, σ_γ/γ, is then:

$$\frac{\sigma_\gamma}{\gamma} \approx \pm\sqrt{\left(\frac{\sigma_G\sqrt{2/N}}{\overline{DN} - \overline{C_o}}\right)^2 + \left(\frac{\sigma_\rho}{\overline{\rho_{sat}}}\right)^2} \tag{7.4}$$

This assumes that the random uncertainty in DN and C_o is decreased by N measurements, while the 6S uncertainty is likely a bias and is not decreased by spatial averaging. Temporal averaging will decrease σ_γ by decreasing σ_ρ because monthly means were used for τ and wind speed. Therefore over the course of a month, the uncertainty of monthly-average γ can be estimated from Equation 7.4 as:

$$\frac{\sigma_\gamma}{\gamma} \approx \pm\sqrt{\frac{1}{N_d}\left[\left(\frac{\sigma_G\sqrt{2/N}}{DN - C_o}\right)^2 + \left(\frac{\sigma_\rho}{\rho_{sat}}\right)^2\right]}, \tag{7.5}$$

where N_d is the number of γ calculations for the month. The first term on the right hand side of Equation 5 represents the GOES uncertainty. For characteristic values ($DN\text{-}C_o$ ~ 25, σ_G ~3 and $N=16^2$) it contributes ~0.01^2. σ_ρ is estimated from Table 7.1 as 0.01, therefore the second term in equation 5 contributes ~0.33^2 (assuming a minimum ρ_{sat} = 0.03). Then, $\sigma_\gamma/\gamma \sim 0.06$, for the monthly-mean γ with N_d = 25 days.

However, a bias is still possible due to the assumed aerosol model. Calculations (shown in Table 7.3) for a log-normal distribution, modified-Junge distribution (Stowe et al. 1997), and continental aerosol (WMO, 1983) show variations as large as 8%. Thus, the aerosol optical property uncertainties result in σ_ρ/ρ_{sat} ~ 0.08. Because σ_γ/γ is dominated by σ_ρ/ρ_{sat}, the resultant possible bias in the calibration is ±8%.

7.5 Conclusions

The visible channel of the GOES-8/Imager instrument was calibrated vicariously using a radiative transfer model as a source. Visible observations of the Southern Pacific Ocean were related to theoretical calculations and a calibration coefficient (γ) was derived daily for one-month periods. Calibrations were performed at 6-month intervals beginning in August 1995 continuing through August 1999.

The calibration results compare well with previous work using different calibration methods, which is encouraging for two reasons. First, the current technique uses only a dark surface (the ocean). The range of reflectances measured by the satellite for this calibration were less that 0.1. Other techniques (e.g., Greenwald et al., 1997) used cloud tops and other surfaces which generally have brighter reflectances (e.g., 0.05 <

$\rho_{sat} < 0.4$). This suggests that the values of γ computed here are representative of the dynamic range of the instrument response.

Second, this calibration procedure is theoretically-based. Other efforts compared the GOES-8/Imager visible channel to observations from other satellites (e.g. GOES-9/Imager or NOAA/AVHRR). In such studies, the calibration of GOES-8 depends implicitly on the accuracy of the calibration of the reference instrument. In the present work, the calibration depends primarily on the ability of the 6S model to reproduce reasonably the radiance of the atmosphere-ocean system.

The results suggest a 5.6% annual decrease in response, with a current (as of August 1999) instrument response of $\gamma = 572 \pm 8$ DN (with 99% confidence). Additional research is needed to understand the cause of this significant degradation, especially the nonlinear 7.6% decrease shortly after launch. Also, a calibration source should be included on future geostationary satellite visible instruments. Such calibrated measurements would increase the ability of scientists to remotely sense the Earth-atmosphere system accurately, thus maximizing the utility of geostationary data.

Table 7.1 – Sensitivity of the GOES/Imager visible sensor to different atmospheric and oceanic parameters.

Parameter	Default	Range	$\Delta\rho_{sat}$	ΔDN
τ (at 0.55μm)	0.05	0.01 – 0.09	0.0079	7.5
Wind Speed	5 m s^{-1}	1 – 13 m s^{-1}	0.0061	5.7
Wind Direction	Easterly	0-360°	0.0022	2.1
Pigment	0.05 mg m^{-3}	0.001 – 2.0mg m^{-3}	0.0019	1.8
Atmosphere	US1962	All	0.0013	1.2
6S Uncertainty (1.6%)			0.0005	0.5
Rayleigh Optical Depth (defined by surface pressure)	1013mb	1000 – 1026mb	0.00003	0.03
Salinity	34.3 ppt	30 – 37ppt	0.00002	0.02

Table 7.2 – Monthly calibration results, standard deviation and the 99% confidence limits (CL)

		γ	σ_γ (%)	99% CL
1995	Aug	806.3	27.9 (3.4)	±16
1996	Feb	760.7	18.7 (2.4)	±9
	Aug	760.7	31.9 (4.2)	±13
1997	Feb	681.2	23.9 (3.5)	±12
	Aug	683.3	24.8 (3.6)	±10
1998	Feb	675.2	27.7 (4.1)	±11
	Aug	653.0	23.2 (3.6)	±9
1999	Feb	618.8	22.0 (3.6)	±10
	Aug	571.7	20.4 (3.6)	±8

Table 7.3 – Sensitivity of the calibration to the aerosol model used, where P is the aerosol phase function at the scattering angle of 161°

Aerosol type	$P(\Theta = 161°)$	ω_0	ρ_{sat} $\tau = 0.04$	ρ_{sat} $\tau = 0.10$
Maritime	0.296	0.990	0.0443	0.0521
			$\frac{d\rho_{sat}}{\rho_{sat}}$ (%)	
Log-normal	0.198	1.00	4.0	8.1
Modified Junge	0.287	1.00	0.7	1.0
Continental	0.253	0.887	3.0	6.5

Note: The geometry was chosen for a calibration point at 20°S and 105°W.

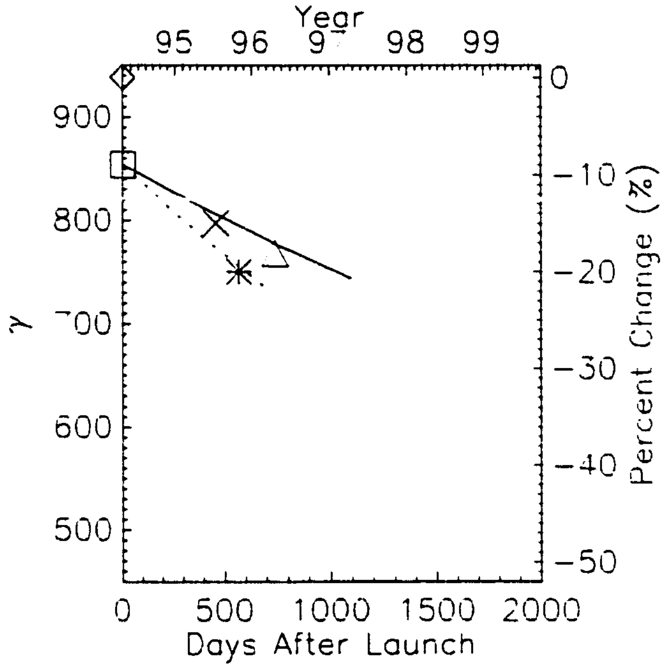

Figure 7.1 – Summary of the calibration of the GOES-8/Imager visible sensor. The calibration coefficient, γ, as a function of days after launch: open diamond -Pre-launch value, open square - Ellrod et al. (1998), solid line - Rao (personal communication, 1998), dashed line - Bremer et al. (1998), x - Weinreb (personal communication, 1995), asterisk - Greenwald et al. (1997), and open triangle - Minnis and Smith (1998). Note: Bremer et al., 1998 and Rao (1998) are degradation trends, thus they are plotted relative to the Ellrod et al. (1998) value.

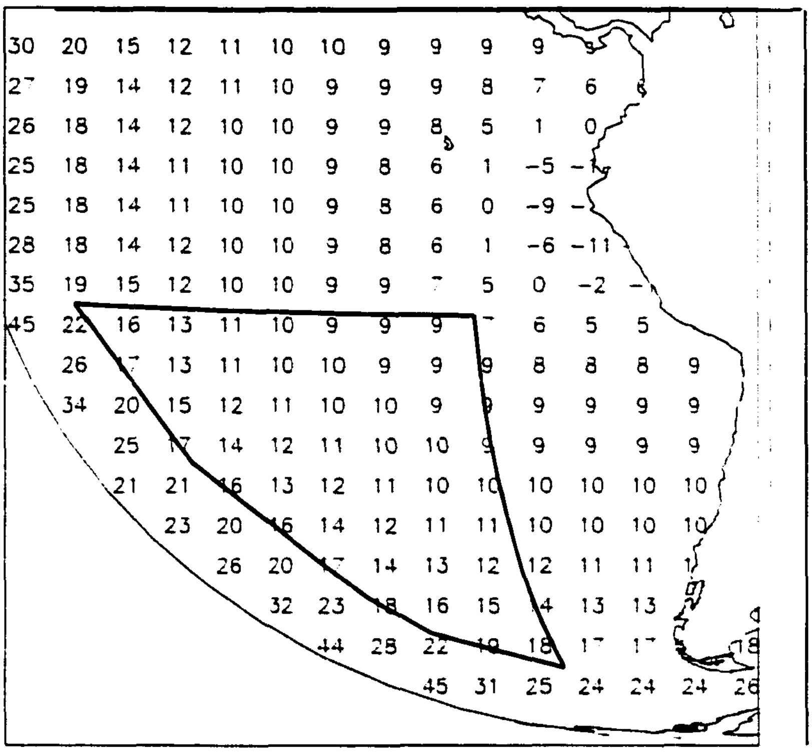

Figure 7.2 – Sensitivity of ρ_{sat} to τ ($\partial\rho_{sat}/\partial\tau \times 100$) for the Southern Pacific for GOES-8 at 17:45 UTC. The heavy solid line denotes the calibration area: west of 90°W, south of 15°S and a satellite viewing angle less than 65°.

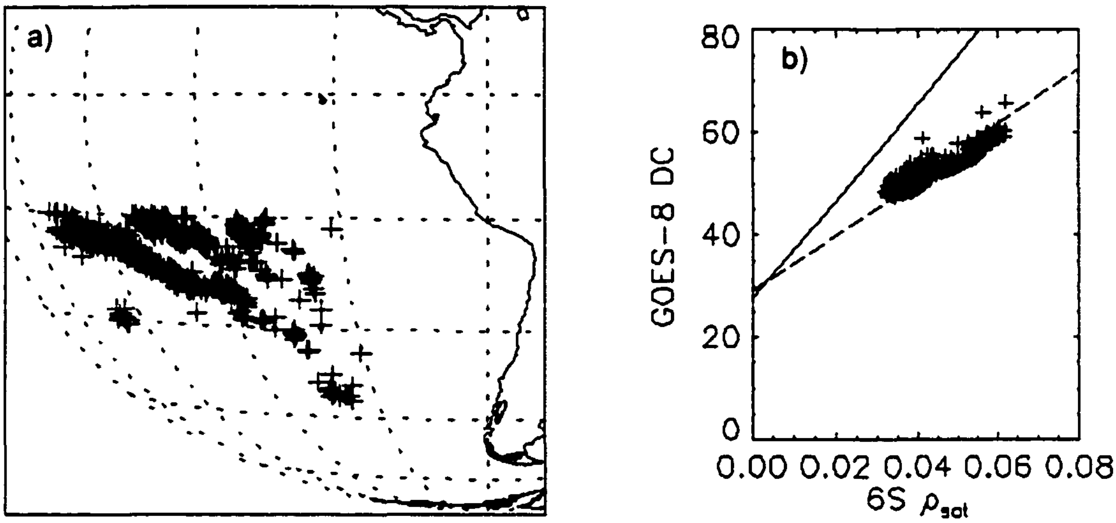

Figure 7.3 – Example of a calibration plot with 480 ocean calibration points. a) location of calibration points. b) Measured visible count values plotted versus modeled ρ_{sat} values. Solid line is the pre-launch calibration (y=938x+28.8); dashed line is the fixed-intercept linear regression (y = 544x + 29.2).

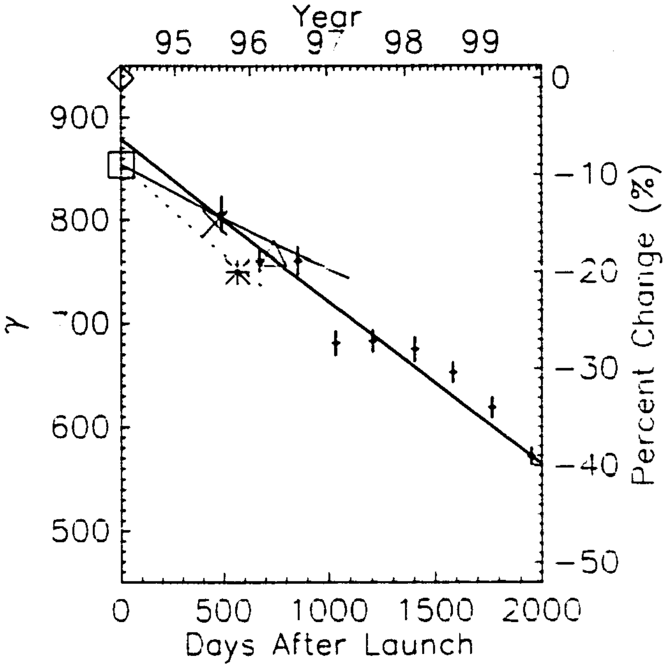

Figure 7.4 – Same as Figure 7.1, but including the current results of the GOES-8/Imager visible calibration (+), where its vertical extent represents the 99% confidence limit. The heavy solid line is the linear regression of monthly-averaged γ.

8. The GOES Aerosol Optical Depth (GOES-AOD) Algorithm

This chapter provides a description of the GOES aerosol optical depth (GOES-AOD) retrieval algorithm. The algorithm uses the radiative transfer model described in chapter 5 and the GOES Imager instrument in chapter 6 to sense aerosols over land. The next chapter provides the GOES-AOD validation efforts.

8.1 The GOES-AOD algorithm

Retrievals using the GOES Imager visible channel incorporate a three step process. The first step is the creation of a mosaic, where for each observation time, the darkest pixel is chosen to represent "background" (or clear-sky) conditions. Second, atmospheric correction is performed to transform the "background" radiance to a surface reflectance. Last, satellite-detected radiances from other days are used to retrieve aerosol optical depth using the surface reflectance obtained in the previous step. These processes are discussed in detail below.

8.1.1 Step 1 – Creation of the composite background

The backbone of this approach is the creation of a background image from a time-series of satellite images. A background image is created for each satellite observation time; during 1995 these occur at 11:45, 14:45 and 17:45 UTC. The frequency of images increases to 30 minutes for the 1998 study (due to a change in the archiving process at CIRA).

The darkest GOES-8 visible pixel for each Earth location is chosen for the background composite. This requires the correction for such effects as variations in the image navigation and cloud shadows. Small variations in the instrument attitude with respect to the Earth can cause significant errors in the location of surface features from image to image. Therefore, images were corrected for these variations such that when visibly looped, the surface features showed little movement. Also, while choosing the darkest pixel removes most cloud contamination, cloud masking is required to remove cloud shadows that can occur at large solar zenith angles. These shadows have a darker appearance than a normal scene which can contaminate the background image.

An example of a composite background scene is presented in Figure 8.1a for a sector over Brazil during August of 1998 (at 15:45 UTC). Clouds are masked using channel 4 (10.7μm) of GOES-8; cloud shadows are then masked by locating areas near clouds. For this work, a period of two months was used to perform the background compositing. This provides about 40-60 opportunities for a clear sky observation of a pixel, similar to previous studies (Jankowiak and Tanré, 1992). Uncertainty caused by temporal variation in the surface reflectance during the two months is discussed later.

Figure 8.2 shows the percentage of pixels from each day in August which contribute to the background image. It can be seen that more than 70% of the background is compiled using only three days (from 1, 2, and 15 August). The probability distribution function (PDF) of the GOES DN values are shown in figure 8.3. In general, there is a definite minimum near 72 below which few observations are measured. This clear-sky observation, however, is not completely free from atmospheric and aerosol extinction; these effects are removed using atmospheric correction.

8.1.2 Step 2 – Atmospheric correction of the composite background

The second step of the algorithm removes atmospheric effects on the satellite-detected radiance using the radiative transfer model described in chapter 5. The background image from step 1 is calibrated to radiance values using the results of the calibration (chapter 7). Atmospheric effects including gaseous absorption, molecular scattering and aerosol extinction are removed via inversion of the satellite-detected radiance for a surface reflectance estimate. This step requires assumptions regarding the state of the atmosphere on the day with the darkest pixel. The assumed variables are: column amounts of the gaseous absorbers (specifically water vapor and ozone), background aerosol optical depth (τ_b) and the optical properties of the aerosols in the atmosphere.

The surface reflectance retrieved for each time period requires some definition. It is not an albedo; an albedo suggests some sort of angular integration to determine the total reflectance at all viewing angles. Therefore, it is an anisotropic reflectance which is dependent upon Sun-Earth-satellite geometry. Retrievals are made using only the anisotropic reflectance from the same time period as the image ($\pm$7 minutes), which fixes the Sun-Earth-satellite geometry. This decreases the need for using a surface bidirectional reflectance model. Since only the anisotropic surface reflectance is retrieved, ρ_s will be referred to as the surface reflectance. Also, the GOES-8 sensor actually observes the ground at numerous wavelengths weighted by the instrument response, thus the surface reflectance retrieved is an estimate of the surface reflectance at the central wavelength of the sensor, 0.6μm.

The surface retrieval for the background image in figure 8.1a is shown in Figure 8.1b. Surface reflectances range from 5 to 10%. These 500×500 km sectors are centered on the AERONET sites for 1995. For 1998, sectors were chosen to give a more spatially uniform retrieval. The surface reflectance for 17:45UTC August 1998 is shown in Figure 8.4.

8.1.3 Step 3 – Retrieval of Aerosol Optical Depth

The third step compares imagery from other days of the month to the surface reflectance from step 2. The change in radiance is assumed to be due to an increase in the aerosol amount. A look-up table is compiled by varying surface reflectance and optical depth. For each pixel, the surface reflectance is determined from step 2, so the look-up table is first interpolated for surface reflectance. Then, a retrieval is performed by finding the radiance in the table that matches the satellite observed radiance. The retrieved AOD (GOES-AOD) is valid at 0.50 μm, because this is the value used as input to the radiative transfer model. This wavelength was chosen because it is also observed by AERONET.

GOES imagery from 30 August 15:45 UTC is plotted in figure 8.1c; the PDF of this image is shown in figure 8.5. Figure 8.1c has the same gray scale as 8.1a. In general, the image is brighter, with larger DN values. The PDF (figure 8.5) is notably wider and the values are much larger. Fire plumes are visible in the GOES image (figure 8.1c); the corresponding GOES-AOD retrieval image is shown in 8.1d. The smoke plumes are again visible and the cloud in the northeast corner saturates the color scale. A retrieval for 28 August 1998 at 17:45UTC is also shown in Figure 8.6.

8.2 Sensitivity Study

Aerosol information (whether chemical, optical or other properties) is convoluted in satellite-detected reflectances of solar radiation (Twomey, 1977). Therefore, aerosol optical property retrievals include some level of uncertainty. This section attempts to realistically calculate the uncertainty of the GOES-AOD algorithm. The results of these sensitivity studies are important when evaluating comparisons to ground truth (which is in the following chapter).

In the following simulations, there are two measured variables, numerous assumed parameters and two retrieved variables. The measured variables are the observed background count, DN_0, and observed aerosol count, DN. DN_0 is the darkest pixel obtained from the retrieval algorithm step 1. The second measured variable is the GOES-8 observation, DN, used to retrieve τ. The assumed parameters are those not retrieved, yet are required by the radiative transfer model during the retrieval. These include:

- the assumed background optical depth (τ_b) from step 2,
- aerosol optical properties - e.g., ω_0, n(r), sphericity, and
- atmospheric variables – e.g., surface pressure, column water vapor amount, column ozone amount.

These quantities have varying affects on the radiative transfer, some larger than others, which is analyzed below. Finally, two parameters are retrieved: surface reflectance (ρ_s) and aerosol optical depth (τ). These parameters are dependent not only on the measured variables but also the assumed parameters.

A different approach to determining sensitivity to retrieval uncertainties was used in assessing the uncertainty of the GOES-AOD algorithm. Often in reports of satellite retrieval algorithms, the parameters are systematically varied for each retrieval degree of freedom (e.g., Tanré et al., 1997, Nakajima and Higurashi, 1997). For instance, the GOES-AOD algorithm can have nearly 16 degrees of freedom. If each degree were varied over 3 values, the total calculations would be 3^{16} (or 4.3×10^{7}). Further, if the uncertainty of each assumed retrieval parameter were included (e.g., optical properties, satellite radiance measurements, etc.) the total calculations would increase to ~ 3^{19} (~10^{9}). Thus to accurately describe the uncertainty with respect to each value for all conditions would require a large number of retrievals – as well as thousands of graphs or dissertation pages. Also, this systematic approach does not account for the interaction of differing values of uncertainty – such as in cases where errors may either cancel or increase the retrieval error. Rather, a general description of the uncertainty in all conditions is desired.

To reduce the number of satellite retrieval simulations needed to describe the uncertainty estimates as well as to understand the interactions of retrieval uncertainties, a pseudo-"Monte Carlo" approach was used. In short, the retrieval degrees of freedom were randomly varied over their expected range of values in the forward calculation of satellite detected radiances. This allowed the calculation of retrieval error for a large variety of conditions. The uncertainties in assumed parameters were varied using a normal distribution of error. Retrieval errors can then be compared to the parameter errors and relationships between both can be found. This approach to retrieval uncertainty, however, does not lend itself to all areas of algorithm investigation. Specifically, calculations with respect to aerosol vertical distribution, aerosol sphericity, bidirectional reflectance uncertainty, temporal reflectance uncertainty and NO_2 absorption contamination are presented separately.

8.2.1 The pseudo-"Monte Carlo" approach to retrieval uncertainty

Forward Model

First, the forward model uses random conditions to simulate an observed GOES radiance. This is performed using the variables listed in Table 8.1: the Sun-Earth-satellite geometry, surface reflectance, background optical depth and aerosol parameters. A random number generator (RNG) is used to generate random numbers (RND) to determine the parameter value via:

$$p = p_{\min} + (p_{\max} - p_{mian})RND \quad (8.1)$$

where p is a parameter used in the forward model and subscripts max and min represent the maximum and minimum values of the parameter p (defined in Table 8.1). The input optical depth (τ_{in}) was varied between 0.03 and 1.5, thus simulating a large range of optical depths. As will be shown in the following chapter, this range is smaller than the range of optical depths used in validation, yet is useful for the uncertainty estimate. The solar zenith angle (θ_o) was varied between 1 and 50° while the satellite zenith angle was varied between 1 and 60°. Also, the relative azimuth ($\Delta\phi$), which is the difference in the azimuth angles of the satellite and the Sun, was varied between 0 and 180°. This represents a large range of scattering angles. While the angles for retrievals in the next chapter are limited to South America, varying the angles over these large ranges allows the analysis of how the retrieval accuracy is dependent upon the Sun-Earth-satellite geometry. The surface reflectance, ρ_s, was varied between 0 and 0.12 and the background optical depth, τ_b (used in the atmospheric correction) was varied from 0.01 to 0.05. Also, the aerosol model index (IAER) was allowed to vary in one case study between 1 and 4 – representing the four aerosol models described by Kaufman et al., 1997. These conditions are used in a forward model to simulate the satellite-detected radiance for an aerosol layer, DN, as well as the clear-sky background condition, DN_o.

Introduction of Noise

Second, assumed retrieval parameters are varied to simulate noise. A method was derived to convert random numbers (RND) generated by the RNG to a normal distribution. The RNG produces random numbers less than one and greater than or equal to zero. A probability distribution function (PDF) of the first 1500 random numbers provided by the RNG is shown in figure 8.7 (grouped into bins of width 0.1); the numbers are evenly distributed between zero and one. However, satellite noise, aerosol optical properties errors and other assumptions are often distributed about a mean by some standard deviation (σ_p). So, it is assumed that the error distribution is normal, in which case the distribution (y) can be described by:

$$y = \frac{1}{\sigma_p \sqrt{2\pi}} \exp\left[-\frac{1}{2} \left(\frac{p}{\sigma_p} \right)^2 \right] \tag{8.2}$$

The integral of equation 8.2 evaluated from negative infinity to positive infinity is one. Thus integrating from negative infinity to some real number (e.g., zero) results in a value between zero and one. Therefore, the inverse of this integration, Norm(x), maps a number between zero and one to the range of negative infinity and positive infinity. This is graphically shown in figure 8.8; for example, for RND = 0.103 corresponds to Norm(RND) = -1.26. The bounds on Norm(x) used in the error study are –5 to 5, which only excludes 0.00034%. The resulting distribution is a normal distribution with a mean of zero and a standard deviation of one. For the example in figure 8.7, the resultant normal distribution has a mean of -0.03 and a standard deviation of 0.999.

These normally-distributed "random numbers" can then be used to simulate noise in the retrieval method. The Norm function output is the z-score, which represents a normalized error by:

$$z = \frac{p - \bar{p}}{\sigma_p} \tag{8.3}$$

where the parameter has a mean of $\bar{p}$ with a standard deviation σ_p. The retrieval parameters which are assumed by the GOES-AOD algorithm are varied by a normal distribution. Errors were simulated by:

$$\Delta p = \mathrm{Norm}(\mathrm{RND})\sigma_p \tag{8.4}$$

where $\Delta p = p - \bar{p}$ and represents the error used in the retrieval. Values of σ_p for each retrieval parameter are shown in Table 8.2 for four cases. An example of the simulated noise is shown in figure 8.10 for the uncertainty in the GOES observation ($\sigma_p = 0.5$). The four cases of retrieval uncertainty represent: Case A – single parameter analysis, Case B – retrieval with known aerosol type, Case C – retrieval with spatially varying aerosol type (near source) and Case D – retrieval with completely unknown aerosol. For all cases, the estimated errors are assumed unbiased ($\bar{p}$ = 0). The satellite instrument uncertainty (ΔDN) was simulated by ±0.5 uncertainty; the GOES estimate for the background composite was similarly simulated (ΔDN_0 = 0.5). The aerosol optical properties were varied using two estimates of property uncertainty: $\Delta\omega_0$ = 0.02 and 0.04, refractive index, Δm= 0.06 and 0.1, mean radius, Δr_m, (which randomly varied the aerosol mean radius for each log-normal mode in the aerosol model) by 20 and 30% and $\Delta\tau_b$ = 0.02 and 0.04. Also, an uncertainty in the calibration coefficient, $\Delta\gamma$, was simulated.

Retrieval parameters changed by the pseudo-noise are then used to retrieve the AOD from the simulated radiances. The retrieved AOD,τ_r, differs from the input AOD,τ_{in}, by:

$$\tau_e = \tau_r - \tau_{in}.$$

A surface reflectance error, $\rho_{s,e}$, is calculated in like manner. This error represents the GOES-AOD algorithm error for some random condition with normally-distributed noise when a "clear" scene is observed. If no clear-sky pixel with low optical depth is observed, then the atmospheric correction would use an incorrect τ_b; this case is described in section 8.2.8. The uncertainty analysis was performed 1500 times for each case (except case A). Not only does this significantly decrease the retrievals needed to fully describe the error characteristics (roughly 10^9 fewer retrievals, as estimated above) but also accurately describes how interacting uncertainties can increase or decrease the error.

8.2.2 Retrieval uncertainty results

First, a study was performed where a set of retrievals were performed with only one assumed retrieval parameter varied – Case A. In this way, the uncertainty as a function of each parameter can be described. Seven sets of 500 retrievals were performed. The results are listed in Table 8.4 for the entire set and also grouped by aerosol type. The slope of the line ($d\tau/dp$) describes the sensitivity of the aerosol retrieval to the parameter p. Clearly, each parameter is strongly correlated with the retrieval error. The parameters m and r_m affect the phase function of the retrieval. This phase function varies with Sun-Earth-satellite geometry (which determine Θ), lowering the correlation for these parameters. The slopes also vary for each model, so correlation increases when grouped by aerosol model. This suggests a sensitivity of the retrieval to ω_0 and the size distribution, which are the primary difference in the models. Also, the comparisons of τ_e with r_m uncertainty are not described separately because each aerosol model had a specific number of modes by which each mode was specifically varied. Also, it is not appropriate to compare the uncertainty with each mode because each mode of each model had a different mean radius.

These slopes can be converted to an uncertainty for each parameter using the σ_p values given in Table 8.2. The uncertainty of the retrieval can estimated from the uncertainty due to each parameter through:

$$\sigma_{\tau,p} = \sqrt{\sum \sigma^2} = \sqrt{\sum \left(\sigma_p \frac{d\tau}{dp} \right)^2} \qquad (8.5)$$

where $\sigma_{\tau,p}$ is the parameterized uncertainty and error sources are assumed independent. This analysis will be compared to the full pseudo-Monte Carlo analysis (Case C) later.

Cases B, C and D allow the study of the interaction of the retrieval parameter errors. Uncertainties in Case B describe a retrieval where the aerosol properties are well-known. Case C represents a more realistic scenario, where the aerosol type is understood, but the optical properties remain somewhat uncertain and Case D represents the extreme: a retrieval where absolutely nothing is known about the aerosol. Results of these cases are shown in Table 8.4 where the retrieval error, τ_e, for each case is correlated to parameter error (Δp) and the retrieval error characteristics. Two uncertainty estimates are shown. The standard deviation of τ_e, σ_τ, shows the dispersion of τ_e, but is sensitive to outliers. Thus an equivalent standard deviation, s_τ, is calculated. This parameter is calculated by integrating the τ_e probability distribution function (PDF) outward from the mean until 68% of the area is found. For a normal distribution, $\pm 1\sigma$

encompasses 68% of the distribution. Thus where $\sigma_\tau > s_\tau$, the distribution is likely biased to one side of the mean.

Although no biases were used ($\bar{p} = 0$) in simulating retrieval uncertainty, a bias appears in the τ_e analysis for two reasons. First, some retrieval parameters which were not simulated as a pure normal distribution. ω_o and τ_b were limited to realistic values; such that $\omega_o < 1$ and $\tau_b > 0$. This affected the $\Delta\omega_o$ distribution, as seen in figure 8.11. For the continental aerosol model ($\omega_o = 0.96$), $\Delta\omega_o$ was not allowed larger than 0.04, partly causing the slight bias results in the error analysis. Similar trends also appear in a τ_d frequency distribution. Second, the larger biases are positive (Figures 8.12, 8.13 and 8.14) meaning that the τ_r is overestimated. When τ_r largely underestimates τ_{in}, the retrieval fails because $\tau_r < 0$; in such cases $\tau_r = 0$. This is also evident in figure 8.15. This limits negative errors to 100%, with no such limit on positive errors. This is also shown through the median of τ_e, which in all cases is zero.

Also from figure 8.15, τ_e increases with τ. This is more clearly seen in figure 8.16 where σ_τ and s_τ are plotted against τ for case B (also, for case C and D in figures 8.17 and 8.18 , respectively). In general, the $s_\tau < \sigma_\tau$, suggesting evidence of retrieval outliers. Since σ_τ is less correlated with τ due to the random appearance of outliers, the s_τ parameter will be used to describe the uncertainty as it less sensitive to outliers. For Case B (the well-known aerosol), the uncertainty is 18% of the optical depth. The uncertainty increases in Cases C to 34% due to increased uncertainty in aerosol optical properties. Case D, while having similar uncertainty values to Case B, has an overall uncertainty (33%) which is similar to Case C because the aerosol model was allowed to vary.

ω_0 and m are clearly the most significant parameters when retrieving aerosol (for the uncertainties prescribed). τ_e remains strongly dependent upon ω_0 and m for all cases (explaining 16 to 25% of the variance in Table 8.3) while other parameters are generally uncorrelated with it.

The retrieval uncertainty is also a function of surface reflectance, ρ_s, where τ_e increases linearly with ρ_s (figure 8.19). The minimum uncertainty is 0.19 for ρ_s = 0.0-0.01 with s_τ increasing 0.012 for each percent increase in ρ_s (which is $\rho_s \times 100$), for Case C. The uncertainty decreases for Case B to a minimum of 0.10 and an increase of s_τ = 0.008 per ρ_s (%). Again, Case D (not shown) has a similar relationship to Case C, with s_τ increasing 0.012 per ρ_s (%) and a minimum of 0.18 over a black surface.

Analysis of case D also emphasizes the importance of correctly estimating the aerosol model. For case D, the forward model and retrieval both used random aerosol models. Thus, in some retrievals the correct model was used in the retrieval, but not in others. This results in uncertainties and biases based on the assumed and true aerosol model (see Tables 8.5 and 8.6). Also, case D included similar retrieval parameter errors as Case B, which provide comparison to Case B results. The results show conclusively that GOES-AOD is much more accurate when using the correct aerosol model (diagonal values in table 8.5 are small with biases near zero in Table 8.6). When the aerosol model is unknown, the best guess would be assuming an industrial model. This should result in an overall uncertainty of 0.21 and a bias near zero. Conversely, incorrectly assuming a dust aerosol can cause large errors: s_τ = 0.44 with a bias of 0.44.

The retrieval simulations from Case B, C, and D also produce an error in the retrieved surface reflectance. The PDF of surface retrieval errors for case C is shown in figure 8.20. In general, this error is small and independent of the case (σ_ρ values in Table 8.4). $\rho_{s,e}$ is more dependent on instrument uncertainties than aerosol uncertainties. This is seen in a plot of surface retrieval error vs. τ_b (figure 8.21) and γ (figure 8.22). The errors are uncorrelated with τ_b but are strongly correlated to calibration uncertainty (figure 8.22). It should also be mentioned that a simulation of noise for the calibration (with bias = 0) might be unrealistic, as an error in γ would most likely be a bias error. Yet, as shown in Table 8.2, a relative error in γ of 2% results in τ_e ~ 0.02.

The uncertainty of τ_e is plotted as a function of scattering angle in figure 8.23 where a scattering angle of 180° is complete back scattering. In general, the retrieval uncertainty is proportional to scattering angle except for angles nearest the backscatter direction (170-180°). This suggests that retrievals with lower scattering angles should be more accurate.

Finally, the uncertainty, s_τ, calculated for Case C can be compared to an independent uncertainty estimate from equation 8.5. Using σ_p from Table 8.2 for Case C and slopes from Table 8.3; $\sigma_{\tau,p}$ = 0.60 which is twice the s_τ value (0.24) yet is close to σ_τ (0.69). This would suggest that the estimate of uncertainty using equation 8.5 overestimates the uncertainty by significantly weighting the retrieval outliers. This is significant, because error studies in literature generally use a method similar to equation 8.5 to estimate retrieval error. This also suggests that the interacting uncertainties tend to lower (or cancel out) uncertainty rather than increase the uncertainty.

8.2.3 Aerosol layer height uncertainty

Absorption in the atmosphere can cause a sensitivity in the top of the atmosphere reflectances to the aerosol vertical distribution. The variation of the aerosol layer height is somewhat cumbersome to change, thus, it was not incorporated into the pseudo-Monte Carlo uncertainty study.

The vertical distribution of the aerosols in GOES-AOD, shown in figure 5.5, was adapted from the MODTRAN radiative transfer model. The altitude of maximum b_{ext} is varied for this sensitivity study from the surface to the stratosphere to simulate an aerosol layer at different altitudes. Reflectances are then calculated using this new aerosol vertical distribution with τ = 0.3 and 1.0 (figures 8.24 and 8.25, respectively) representing thin and thick aerosol layers. Reflectances are normalized to the reflectance calculated for the maximum of aerosols at the surface. In this way, a change in height refers to transporting an aerosol layer to a different height. The solid line in figure 8.24 represents an aerosol only calculation, i.e., no Rayleigh scattering or gaseous absorption. It can be seen in the absence of these effects, the reflectance is constant with height. The dotted and dashed lines represent an aerosol with ω_o = 1.0 and 0.96 (respectively) in the presence of Rayleigh scattering. This could represent the effect of height in atmospheric windows void of gaseous absorption. In such a case, increasing the aerosol height increases the reflectance by 2% in the troposphere – from 1.0 at the surface to 0.98 at 100mb. For aerosol scattering with Rayleigh scattering and gaseous absorption (Figure 8.24, ω_o = 1.0 – dash-dot, and 0.96 – dash-dot-dot), the reflectance decreases with height. This effect is significant over the depth of the atmosphere, but realistically is at most 4% in the troposphere for both τ = 0.3 and 1.0. Since the GOES-AOD algorithm assumed an aerosol distribution with a maximum at the surface, errors could occur when the aerosol layer is lofted. Mis-location of the aerosol layer overestimates the radiance reflected by the layer, thus causing the GOES-AOD to underestimate the aerosol optical depth.

The error is most sensitive near the surface, where a variation of the layer from the surface to 600mb can decrease the reflectivity by 2.5%. This change is relatively constant with aerosol absorption (ω_o = 0.96 or 1.0) and aerosol optical depth (τ = 0.3 or

1.0). A 2.5% decrease in the GOES observation for DN = 100 (estimated from figure 8.5) is $\Delta DN = -1.8$. This is equivalent to an error in τ of -0.066 (using $d\tau/dDN$ from table 8.3). Similar errors are also found for an optical depth of 1.0 (figure 8.25).

8.2.4 Aerosol sphericity

The non-spherical T-matrix scattering method, described by Mishchenko et al. (1996), was used to calculate phase functions and b_{ext} for non-spherical particles. The calculations are made for $\lambda = 0.55\mu m$ with m=1.33 + 0.0i. Figures 2.10 through 2.15 show the evolution of scattering from a spherical to non-spherical particle. In general, the phase functions become more forward scattering and C_{ext} decreases as the particle becomes less spherical. Nonspherical particles decrease the amount of radiance reaching a sensor, thus fewer spherical particles are needed to simulate L^*, underestimating the aerosol optical depth. Also, Mishchenko et al. (1995) suggest that these errors can reach 100% but are less near a scattering angle of 150°. Therefore, assuming spherical particles for non-spherical particles underestimates the retrieved optical depth.

8.2.5 Bidirectional Reflectance Contamination

The GOES observations are limited in viewing geometry, yet are somewhat affected by the bidirectional reflectance of the surface. The DISORT model does not yet incorporate surface bidirectional effects, therefore the 6S model is used to estimate uncertainties.

The Cloud Absorption Radiometer (CAR) measured the bidirectional reflectance distribution function (BRDF) for dense forest and cerrado areas of South America; the measurements are described in Tsay et al. (1998). Figure 8.26 shows the BRDF for

0.675 μm measured at 600m altitude from the C-131A aircraft. The BRDF is modeled using the BRDF described by Rahman et al. (1993) (Eq. 4.9). The resulting fit is shown in figure 8.27; the surface reflectance differs from a Lambertian surface. The BRDF effect on the top of the atmosphere reflectance is shown in figure 8.28. The differences over the forest are smaller than that of the cerrado, because the forest is darker. The difference over cerrado is significant in the back scattering direction (θ_0 = -30 and θ = -30), also termed the "hot-spot" effect. The differences decrease with increasing optical depth; at τ = 2, the differences over both surfaces is negligible.

However, the BRDF effect on the retrieval of τ seems to be large. The following steps describe the method used to simulate the BRDF contamination:

1. Forward Model – Simulate top of the atmosphere reflectances using the Rahman BRDF
2. Surface retrieval – Retrieve the Lambertian surface reflectance
3. τ retrieval – Retrieve τ using the Lambertian surface and the reflectance from step 1.

This was performed for 3 conditions over the forest BRDF. Results are shown in figure 8.29. In general, the uncertainties are large; maximum values range from 51% for θ_0 = 60° to 80% for θ_0=30° and τ=1.5. In general, errors are lower for large zenith angles and error also decreases as θ_0 increases. Results are even larger for the cerrado BRDF (figure 8.30) where uncertainties are as high as 100% in the hot-spot region.

These results suggest either: 1) the BRDF is extremely important to simulate during the retrieval and large errors result when ignored or 2) the 6S model is overestimating the BRDF effect. The retrievals in the following chapter show no significant bias (at least none approaching a 45% to 80% bias) which suggest that the 6S model is overestimating the BRDF contamination.

8.2.6 Temporal Surface Reflectance Contamination

The composite background (Step 1 in the GOES-AOD retrieval) is determined from a 2-month composite of visible imagery. This composite can be contaminated by surface reflectance variations during this time period. Possible sources of contamination include the growing season of vegetation or rainfall changing the reflectivity of soil. Csiszar and Gutman (1999) estimate the broadband albedo on a monthly basis from AVHRR data at a 0.15° resolution. The monthly albedo for the AERONET validation sites is provided in figure 8.31. The albedo is a maximum in December and January and a minimum around June and July for most locations. The values for Alta Floresta and Los Fieros are constant because the albedo was held constant for areas with very high NDVI values (Csiszar and Gutman, 1999). The Campo Grande site has the largest reflectance during the entire time period, as it is located in the cerrado region of South America. Also, Brasilia is an urban location, yet has a similar trend to the more forested sites of Cuiaba and Concepcion.

Values for each site during the study period months are provided in Table 8.7. The change from August to September seems to be larger than from July to August. The change is almost 1% in albedo from August to September, however, this is a change in the broadband albedo which includes the significant vegetation reflectance in the near IR. Therefore, these changes are likely larger than the GOES visible channel would observe, because it strongly truncates the reflectance from the near IR. Thus, the magnitude of the uncertainty can not be estimated from the albedos, yet they do suggest when the surface reflectance changes are more likely. Errors should be larger for the retrievals in 1995, which composite imagery during from August and September. The 1998 composites (from July and August) are likely more accurate.

8.2.7 NO_2 Absorption Contamination

NO_2 absorbs radiation in the visible spectrum, yet was not incorporated into the DISORT because its concentrations are not measured and its affect is small. Figure 8.32 shows the vertical distribution of NO_2 for three atmospheres: U.S. Standard (McClatchey, 1971), biomass burning and an urban atmosphere. The biomass burning atmosphere is simply the US Standard with the concentration in the lowest 5 km increased to 4 ppbv. The urban atmosphere is the US Standard atmosphere with the concentration in the lowest 2 km increased to 120 ppbv, representing a heavily polluted boundary layer. The NO_2 spectral optical depths for these atmospheres is plotted in figure 8.33 (along with the GOES spectral response for reference). The absorption peaks near 0.4μm, outside the GOES spectral response. The largest values are for the urban atmosphere with a peak optical depth of 0.45 at 0.4μm. However, the GOES optical depth (τ_λ weighted by $W(\lambda)$) is much less (Table 8.8). Again, the urban atmosphere has a significant optical depth near 0.02. The absorption in the biomass burning atmosphere is well below the uncertainty in the GOES-AOD retrieval caused by other assumptions. Therefore, the NO_2 absorption uncertainty is negligible.

8.2.8 Incorrect τ_b contamination

The length of time used in the composite method is a balance of errors. By using a time period which is too long, the surface reflectance is likely changing as discussed in section 8.2.6. Conversely, by using too short of a time to composite, the likelihood of a clear-sky observation decreases. For instance, the optical depth during August near the biomass burning sites (such as Alta Floresta) does not decrease below 0.5. Therefore, a special Monte Carlo error simulation was performed where only the uncertainty in τ_b was varied. The simulations varied the assumed τ_d between 0.02 and 0.5. The actual τ_b was similarly varied, which allowed for errors in τ_b as large as 0.48. The resulting surface reflectance error is shown in figure 8.34a. As the τ_b is underestimated, less aerosol scattering is removed from the image, leaving the surface reflectance too large. This error propagates as an underestimate in the optical depth retrieval (figure 8.34b) because the surface reflectance contribution is too large. The effect is largely independent of solar geometry or other conditions. The correlation of τ_e to τ_b error is 0.96 with a slope of 0.67. This suggests that the uncertainty is related by: $\tau_e = 0.67\ \tau_{b,e}$. So an error in τ_d can significantly bias the retrieval.

8.3 Conclusions

The GOES-AOD algorithm is described here and validation follows in the next chapter. The sensitivity study investigated general algorithm uncertainty and specifically looked at aerosol layer height and sphericity effects. The overall uncertainty of the GOES-AOD algorithm is ±33% of τ. This varies with optical depth and surface reflectance, where uncertainty is lowest for dark surfaces.

Primary conclusions include:

- Overall uncertainty is $\Delta\tau = \pm 0.34\tau$ (34%) for an aerosol with unknown characteristics or if the aerosol model is completely unknown.
- Uncertainty decreases to $\Delta\tau = \pm 0.18\tau$ (18%) when the aerosol characteristics are relatively well-known
- The retrieval uncertainty also increases as ρ_s increases.
- Retrieval uncertainty varies with aerosol type and is largest for the mineral dust aerosol model.

- If the aerosol model is completely unknown, it is best to guess the industrial aerosol, which results in an overall uncertainty of approximately ±0.21 and relatively no bias (for random aerosol distributions).
- A bias is likely to occur if the aerosol model is incorrectly estimated. Again, bias errors are largest when incorrectly assuming a dust aerosol.
- Retrievals are most sensitive to the assumed single scatter albedo and refractive index and less to the calibration
- Conversely, the retrieved ρ_s is more sensitive to calibration than to aerosol optical properties.
- Independently estimating the sensitivity of the retrieval to each parameter, then combining these sensitivities using the sum of the squares overestimates the retrieval uncertainty
- Uncertainty increases with scattering angle.
- Error in the height of the aerosol layer causes an AOD retrieval error less than 0.06.
- Nonspherical particles can cause a negative bias in the GOES-AOD algorithm.
- NO_2 absorption causes negligible error in the GOES-AOD retrieval of biomass burning areas, yet becomes important in heavily polluted urban environments.
- The 6S simulation suggests the Lambertian surface reflectance assumption error can be large, especially for brighter cerrado regions.
- The temporal changes in surface reflectance during a two month composite should be small, but could still affect the retrieval accuracy.

Table 8.1 – Parameters randomly varied in the error study

Parameter (p)	p_{min}	p_{max}
τ	0.03	1.5
SZA	1	50
VZA	1	60
Azimuth	0	180
ρ_{sfc}	0.0	0.12
τ_b	0.01	0.05
IAER[1]	1	4

[1] – IAER, which selects one of the 4 aerosol models, is an integer varying from 1 to 4

Table 8.2 – Parameters varied in the error study using a normal distribution and their uncertainty (σ_p) for the four sensitivity cases.

Parameter (p)	σ_p Case A Individual	Case B Known	Case C Unknown	Case D No information
DN	0.5	0.5	0.5	0.5
DN_o	0.5	0.5	0.5	0.5
ω_o	0.04	0.02	0.04	0.02
τ_b	0.04	0.02	0.04	0.02
m	0.1	0.06	0.1	0.06
γ	0.022	0.022	0.022	0.022
r_m	0.3 (30%)	0.2 (20%)	0.3 (30%)	0.2 (20%)
Aerosol Model	n.v.	n.v.	n.v.	Varied

n.v. = not varied, i.e. aerosol model assumed correct

Table 8.3 – The relationship of model parameter noise (Δp) and retrieval error (τ_e) expressed through slope and correlation coefficient for Case A. The relationships are also broken down by aerosol type.

		aerosol model $\frac{d\tau_e}{dp}$ and r			
p	$\frac{d\tau_e}{dp}$ (r)	continental	biomass burning	industrial	mineral dust
DN	0.037 (0.91)	0.027 (0.96)	0.042 (0.90)	0.030 (0.94)	0.048 (0.94)
DN_o	-0.029 (-0.86)	-0.020 (-0.95)	-0.035 (-0.93)	-0.025 (-0.94)	-0.039 (-0.85)
ω_o	-5.9 (-0.72)	-5.7 (-0.71)	-5.1 (-0.74)	-6.2 (-0.79)	-6.8 (-0.69)
τ_d	0.66 (0.95)	0.70 (0.97)	0.66 (0.96)	0.62 (0.95)	0.72 (0.94)
m	-2.1 (-0.49)	-1.3 (-0.83)	-0.90 (-0.81)	-1.0 (-0.84)	-5.6 (0.64)
γ	-1.7 (-0.84)	-1.2 (-0.88)	-1.8 (-0.89)	-1.2 (-0.88)	-2.4 (-0.87)

Table 8.4 – Correlation (expressed as the correlation coefficient, r) between retrieval parameter error (Δp) and retrieval error (τ_e) for the four sensitivity cases as well as the overall uncertainty in the surface reflectance and optical depth retrievals expressed through average, median, standard deviation (σ) and equivalent standard deviation (s_τ).

Parameter (p)	Case A Individual	Case B Known	Case C Unknown	Case D no information
DN	0.91	0.07	0.02	0.00
DN_0	-0.86	-0.09	-0.06	-0.02
ω_0	-0.72	-0.41	-0.42	0.02
τ_d	0.95	0.03	0.02	0.05
m	-0.49	-0.48	-0.43	-0.32
γ	-0.84	-0.12	-0.09	-0.09
$\rho_{s,e}$ average	n.a.	0.000	-0.001	0.00
σ_ρ	n.a.	0.003	0.003	0.003
τ_e average	n.a.	0.03	0.10	0.07
τ_e median	n.a.	0.00	0.00	0.00
σ_τ	n.a.	0.27	0.69	0.46
s_τ	n.a.	0.14	0.24	0.24

n.a. = not applicable

Table 8.5 – Retrieval uncertainty (s_τ) for case D – retrievals performed when assumed aerosol model is not necessarily correct.

Assumed aerosol model	actual aerosol model: continental	biomass burning	industrial	mineral dust	correct model	incorrect model
Continental	0.10	0.18	0.12	0.22	0.10	0.17
Biomass burning	0.35	0.11	0.23	0.23	0.11	0.28
Industrial	0.17	0.15	0.10	0.18	0.10	0.21
Mineral dust	0.54	0.36	0.40	0.17	0.17	0.44

Table 8.6 – Retrieval bias for case D – retrievals performed when assumed aerosol model is not necessarily correct.

Assumed aerosol model	actual aerosol model: continental	biomass burning	industrial	mineral dust	correct model	incorrect model
Continental	0.02	-0.21	-0.12	-0.27	0.02	-0.2
Biomass burning	0.40	0.03	0.19	-0.03	0.03	0.17
Industrial	0.16	-0.12	-0.02	-0.15	-0.02	-0.04
Mineral dust	0.60	0.28	0.44	0.02	0.02	0.44

Table 8.7 – Broadband albedo values for the AERONET validation sites for the months used in the validation: July, August and September

	Broadband Albedo		
Site	July	August	September
Cuiaba	10.1	11.5	13.4
Alta Floresta	11.3	11.3	11.3
Brasilia	9.9	10.8	12.1
Campo Grande	12.0	12.0	13.2
Concepcion	10.4	10.8	12.9
Los Fieros	10.0	10.0	10.0

Table 8.8 – GOES-8-weighted visible NO_2 optical depths for three atmospheres.

Atmosphere	Optical Depth
US Standard	0.00019
Biomass burning	0.0013
Polluted Urban	0.020

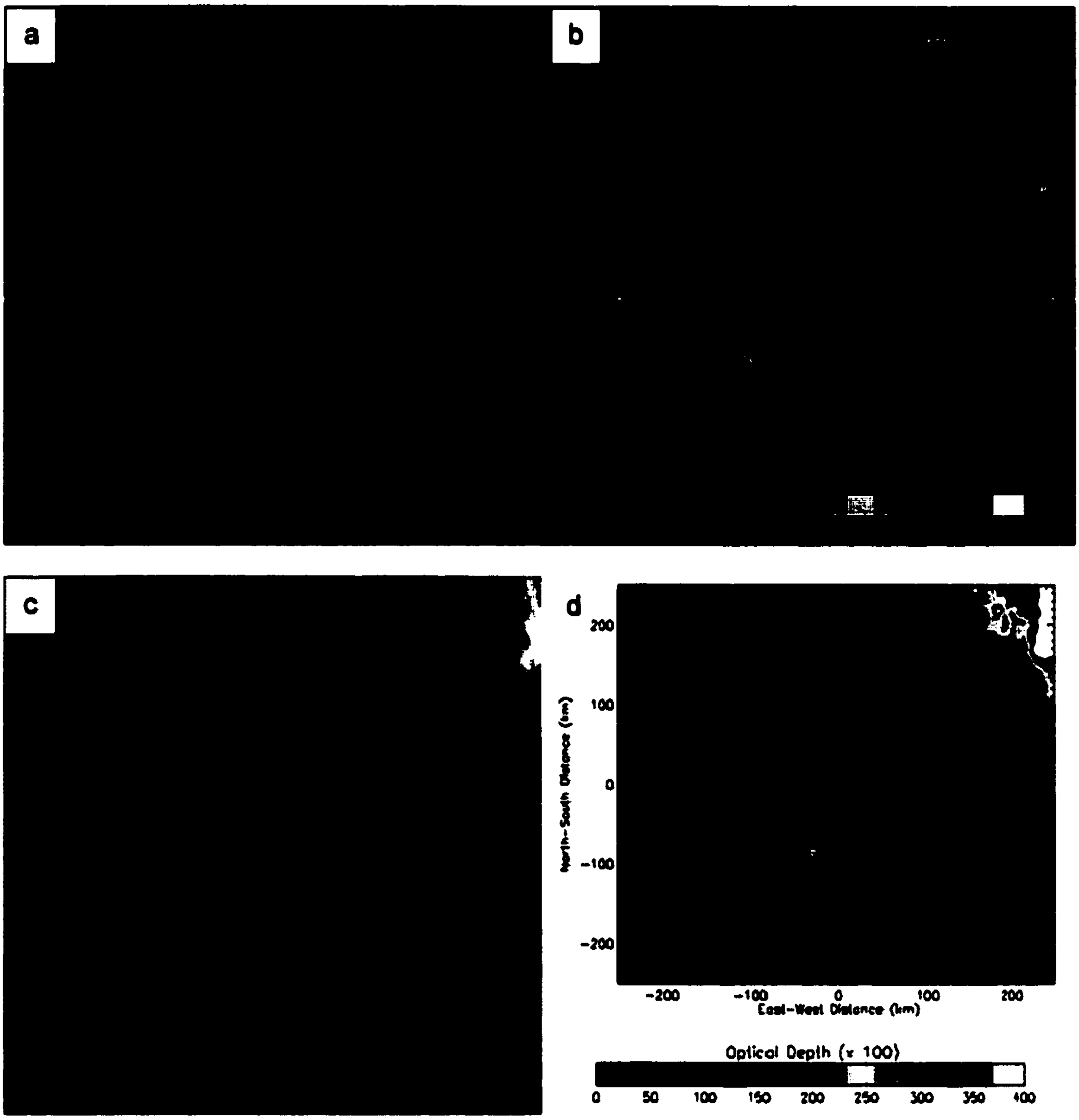

Figure 8.1 – a) Background image from Sector 3 during August 1998 for 15:45 UTC. b) Surface reflectance of the background image in part a. c) GOES data from 30 August 1998 at 15:45 UTC (same gray scale as part a). d) GOES-AOD for image in part c using surface reflectances in part b.

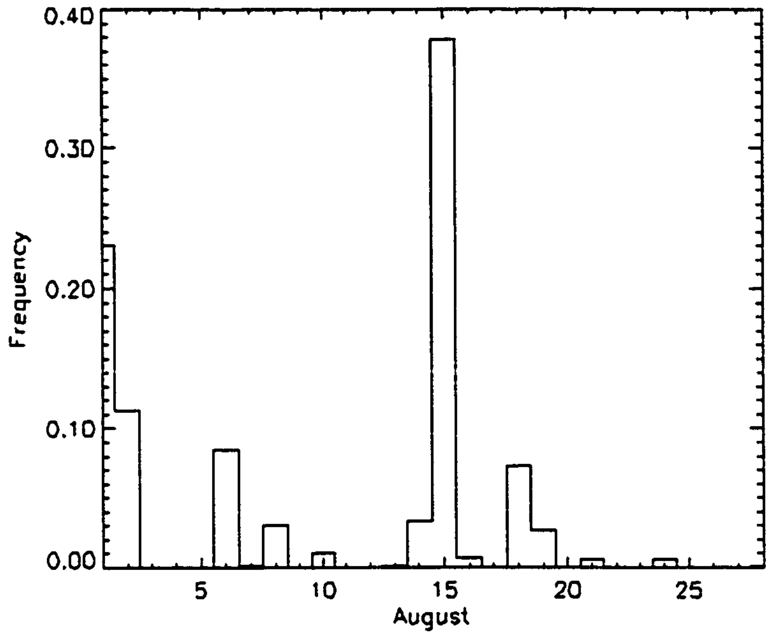

Figure 8.2 – Frequency of pixels from each day in August which are used in the background image. 72% are from 3 days – 1, 2, and 15 August.

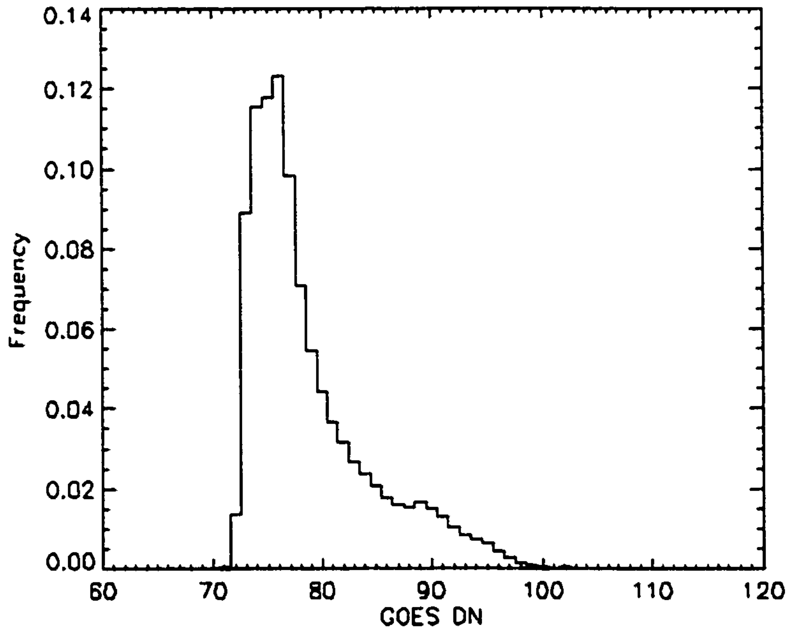

Figure 8.3 – PDF of GOES-8 DN for background image in figure 8.1a.

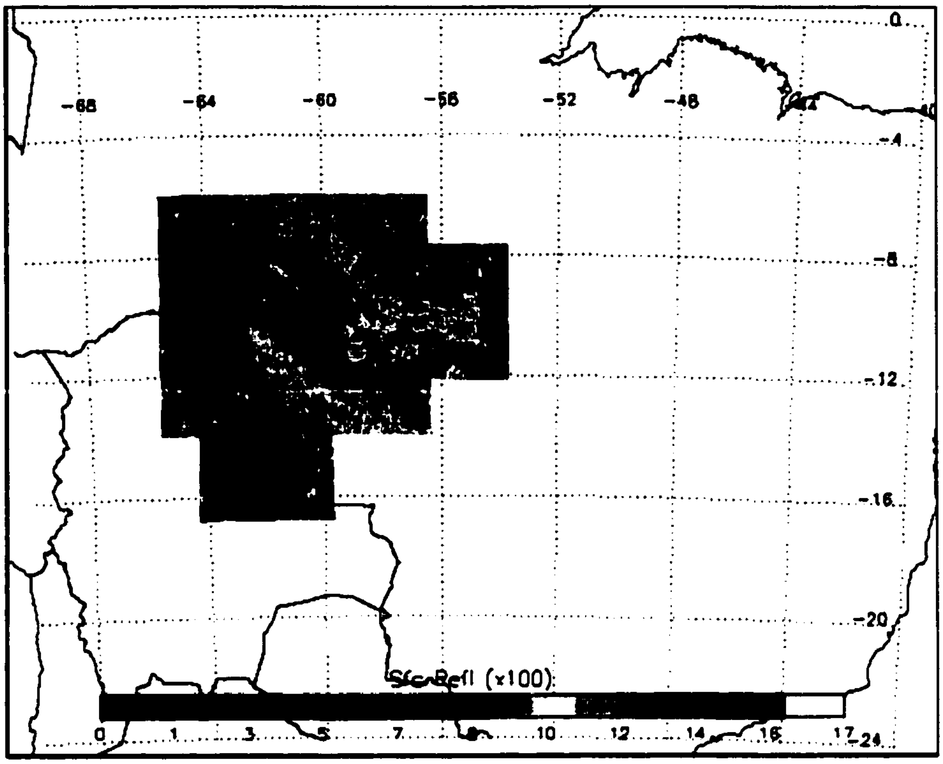

Figure 8.4 – Surface reflectance retrieval for August 1998 at 17:45 UTC.

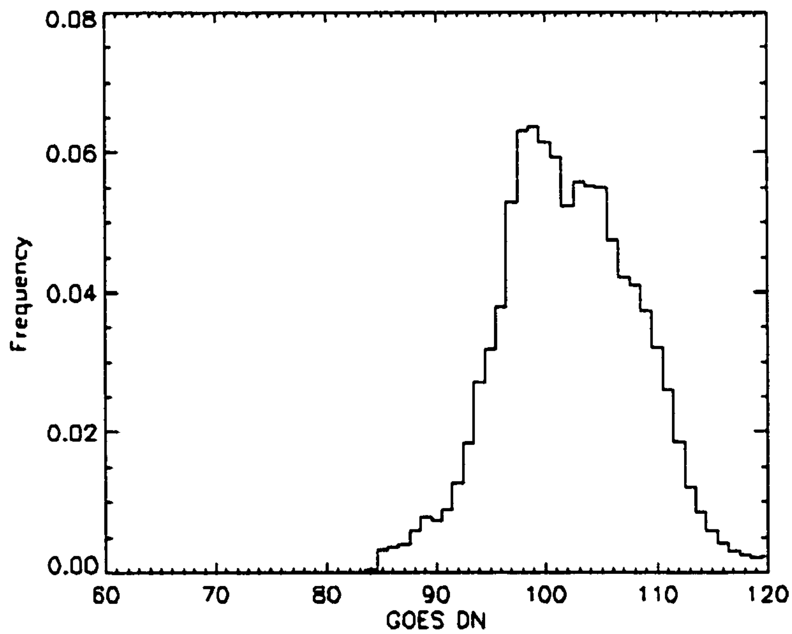

Figure 8.5 – PDF of the GOES image (figure 8.1c) used in the GOES-AOD retrieval in figure 8.1d.

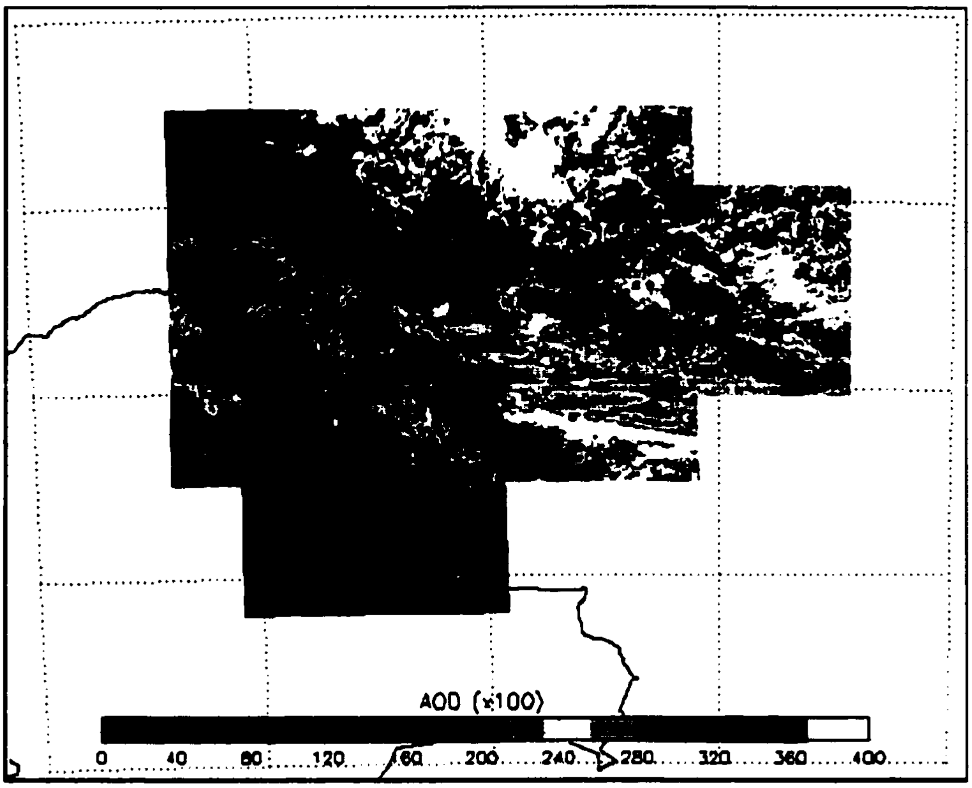

Figure 8.6 – GOES-AOD for 28 August 1998 at 17:45UTC (using surface reflectance shown in figure 8.4).

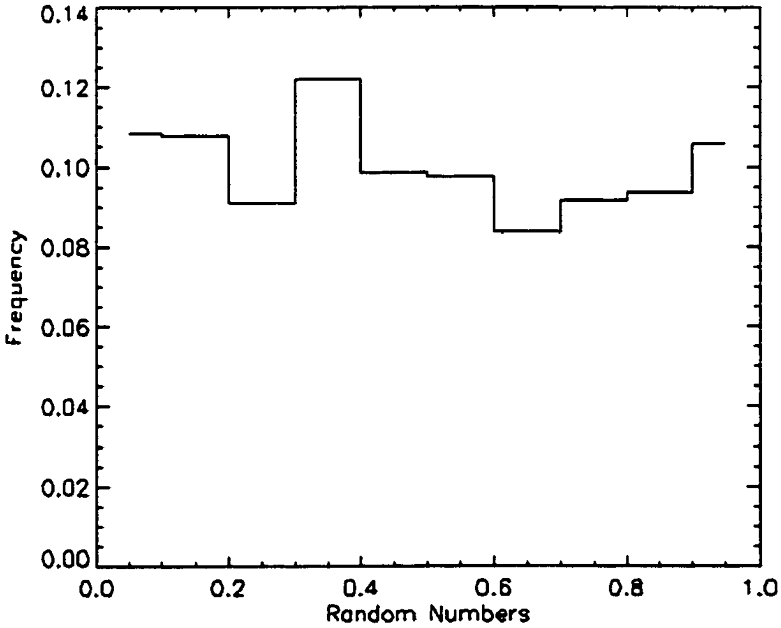

Figure 8.7 – Example PDF of random numbers used in the error study (bin width is 0.1).

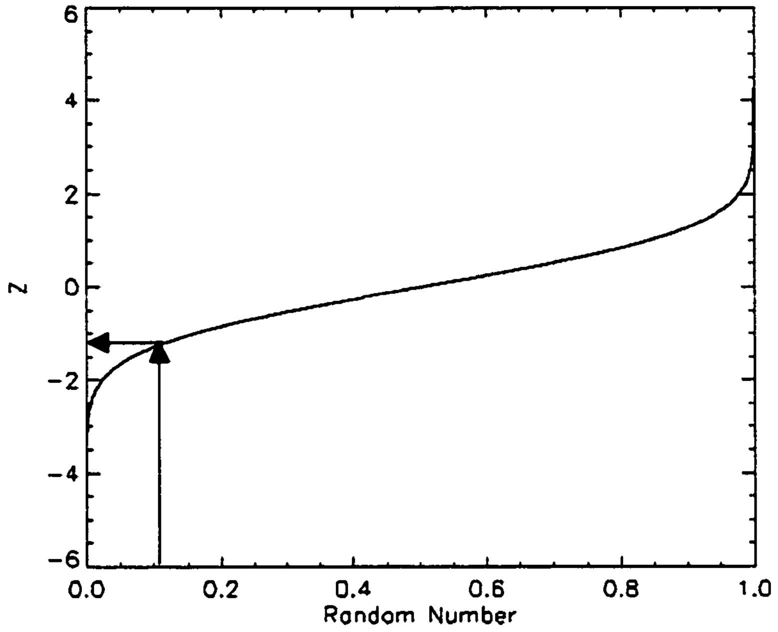

Figure 8.8 – The function used to convert random numbers ranging from 0 to 1 to a normal distribution (represented here by the z-score). Arrows represent the mapping of 0.103 to –1.26.

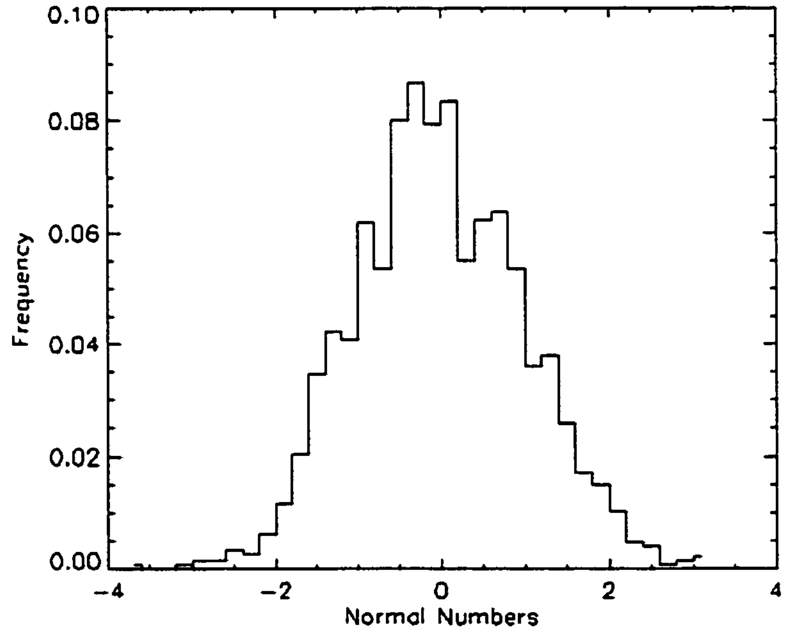

Figure 8.9 – Example PDF of normal numbers calculated from the random numbers in figure 8.7 and equation 8.4 used in the error study. The mean and standard deviation are -0.03 and 0.999, respectively.

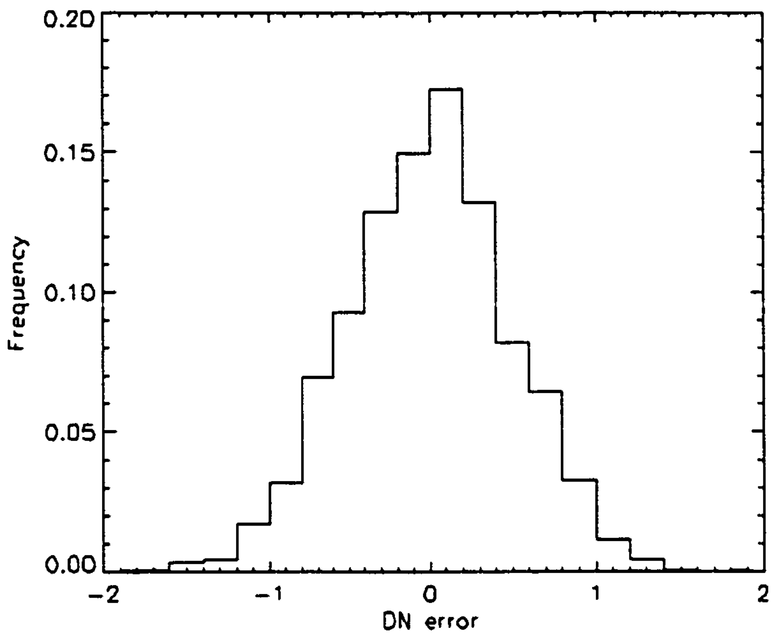

Figure 8.10 – Distribution of simulated GOES digital count errors (DN) . The mean and standard deviation are -.019 and 0.502 (simulating an uncertainty of 0.5), respectively.

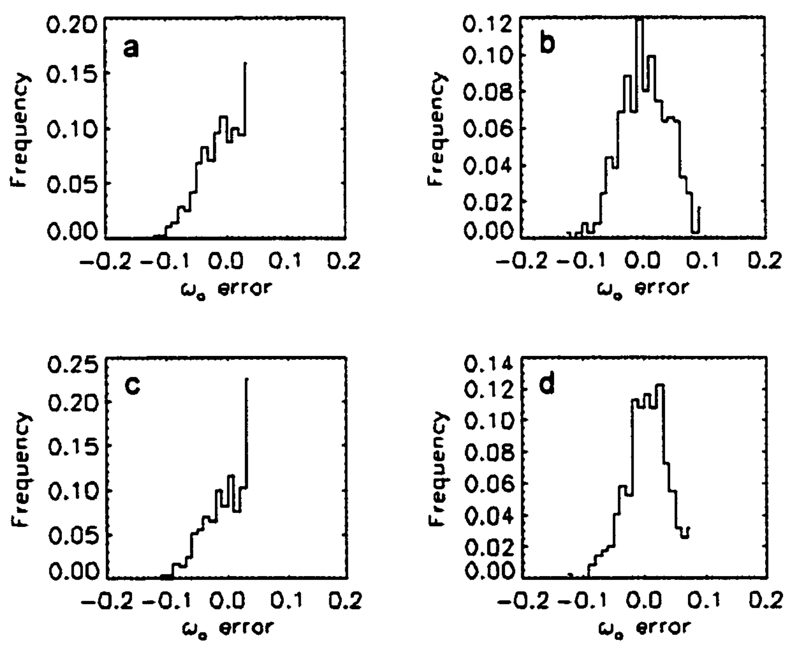

Figure 8.11 – Frequency distribution of the simulated ω_0 error showing the effects of limiting ω_0 to 0.9999 or less (the distribution is not a normal distribution) for a) continental, b) biomass burning, c) industrial and d) mineral dust aerosol models.

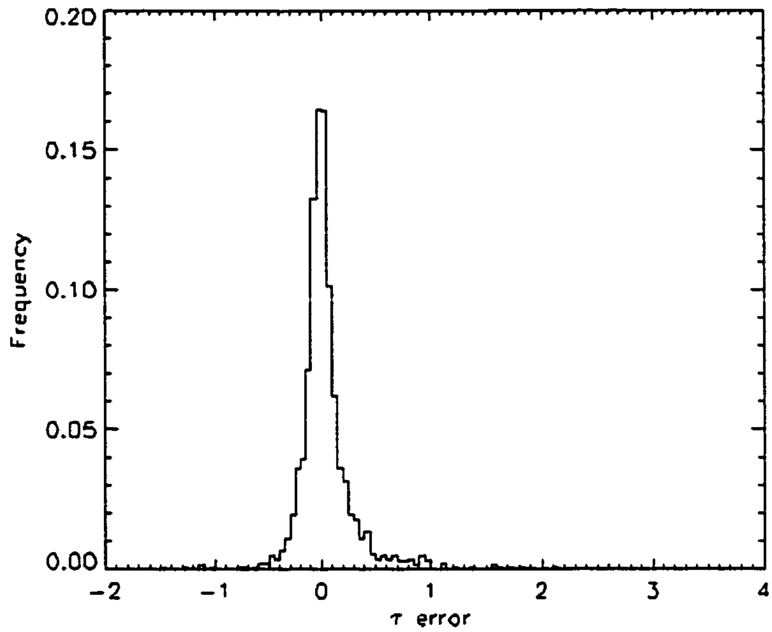

Figure 8.12 – τ retrieval error PDF for error study case B (known aerosol).

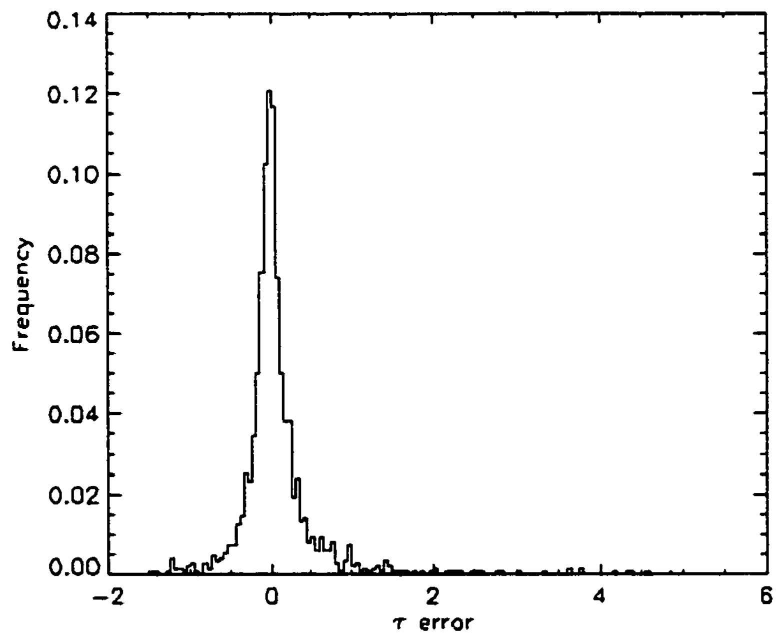

Figure 8.13 – τ retrieval error PDF for error study case C (unknown aerosol).

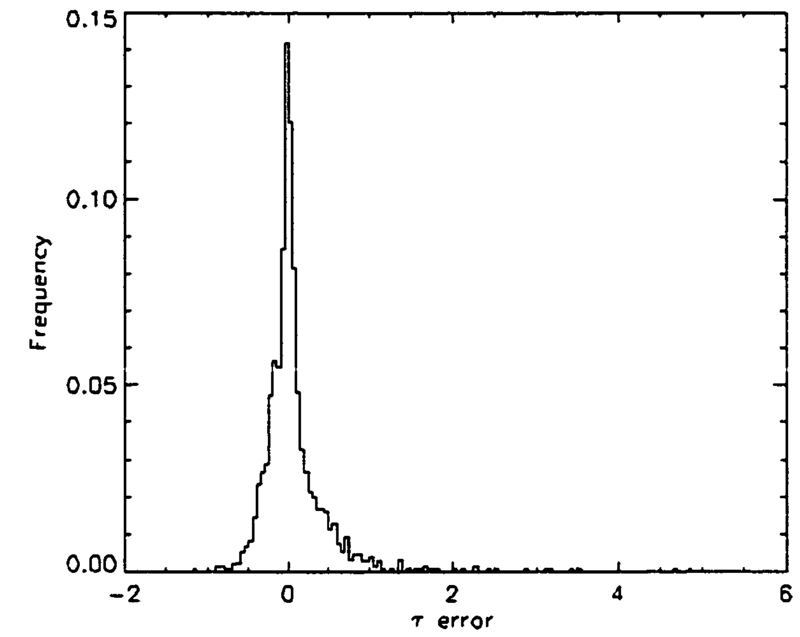

Figure 8.14 – τ retrieval error PDF for error study case D (completely unknown aerosol model).

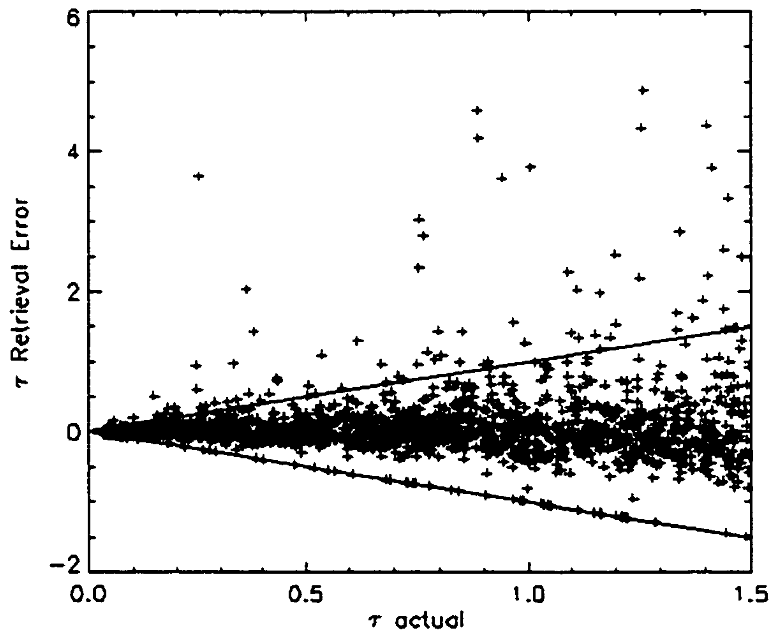

Figure 8.15 – Retrieval error, τ_e, as a function of τ_{in}. The solid line represents ±100% error.

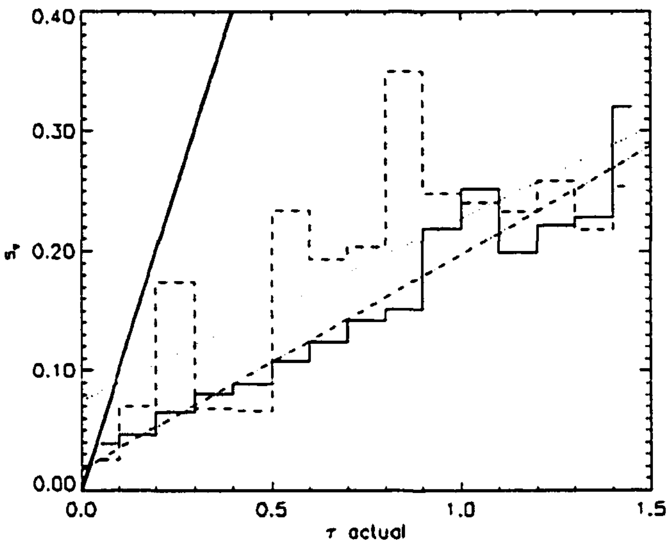

Figure 8.16 – Standard deviation of the retrieval error as a function of actual τ for case B (dashed line) with linear regression line (dashed): $\sigma_\tau = 0.15\tau + 0.07$ ($r = 0.75$). The thin solid line represents the approximate standard deviation (s_τ) with linear regression line (dash-dotted): $s_\tau = 0.18\tau + 0.02$ ($r = 0.96$). The heavy solid line represents the one-to-one line.

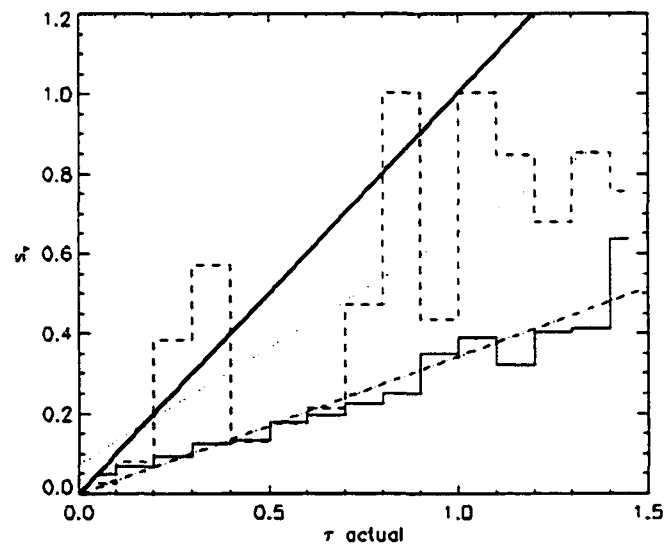

Figure 8.17 – Standard deviation of the retrieval error as a function of actual τ for case C (dashed line) with linear regression line (dashed): $\sigma_\tau = 0.58\tau + 0.07$ ($r = 0.77$). The thin solid line represents the equivalent standard deviation (s_τ) with linear regression line (dash-dotted): $s_\tau = 0.34\tau + 0.0$ ($r = 0.95$). The heavy solid line represents the one-to-one line.

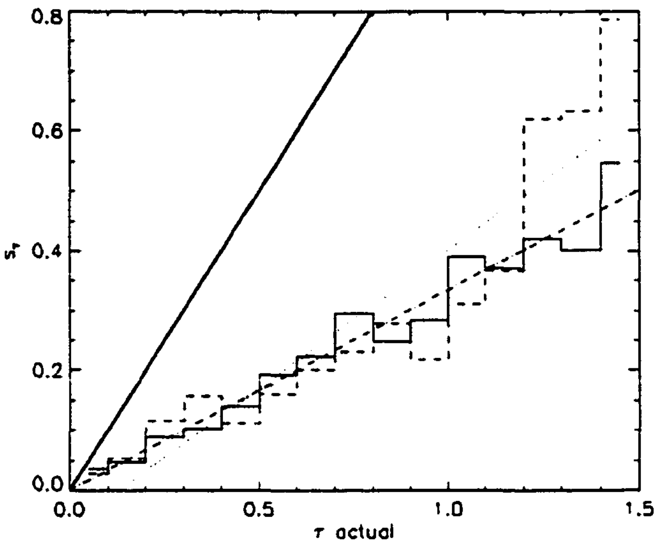

Figure 8.18 – Standard deviation of the retrieval error as a function of actual τ for case D (dashed line) with linear regression line (dashed): $\sigma_\tau = 0.46\tau - 0.06$ ($r = 0.91$). The thin solid line represents the equivalent standard deviation (s_τ) with linear regression line (dash-dotted): $s_\tau = 0.33\tau + 0.0$ ($r = 0.98$). The heavy solid line represents the one-to-one line.

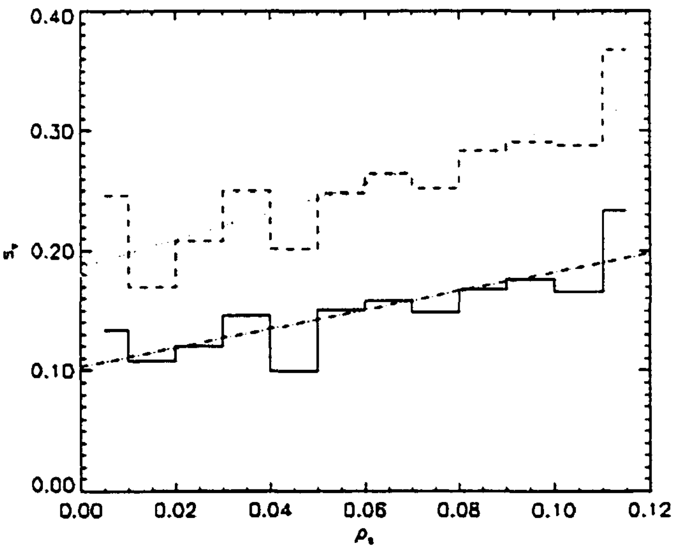

Figure 8.19 – s_τ, of the retrieval error as a function of ρ_s for case C (dashed line) with linear regression line (dotted): $s_\tau = 1.16\rho_s + 0.19$ ($r = 0.81$) and for case B (solid line) with linear regression (dash-dotted): $s_\tau = 0.80\rho_s + 0.10$ ($r = 0.81$).

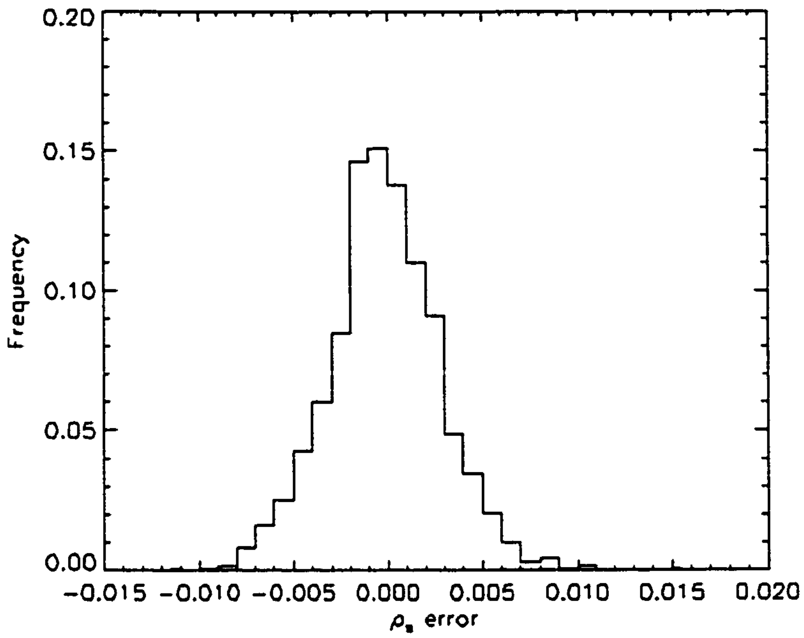

Figure 8.20 – PDF of surface reflectance error ($\rho_{s,e}$) as retrieved in step 2 of the GOES-AOD algorithm.

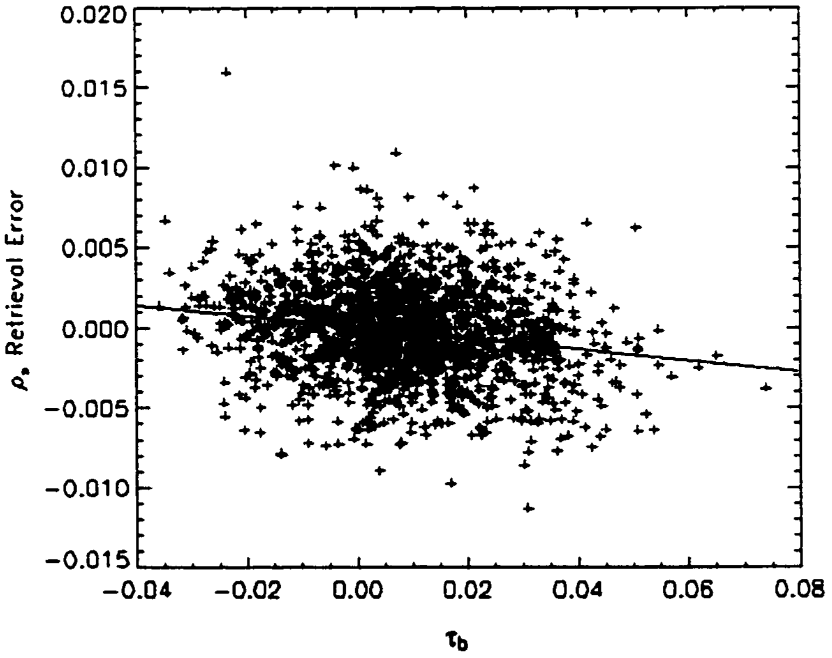

Figure 8.21 – $\rho_{s,e}$ as a function of τ_b error. The equation for the linear regression line is: $\rho_{s,e}$ = -0.03$\Delta\tau_d$ with r = -0.19

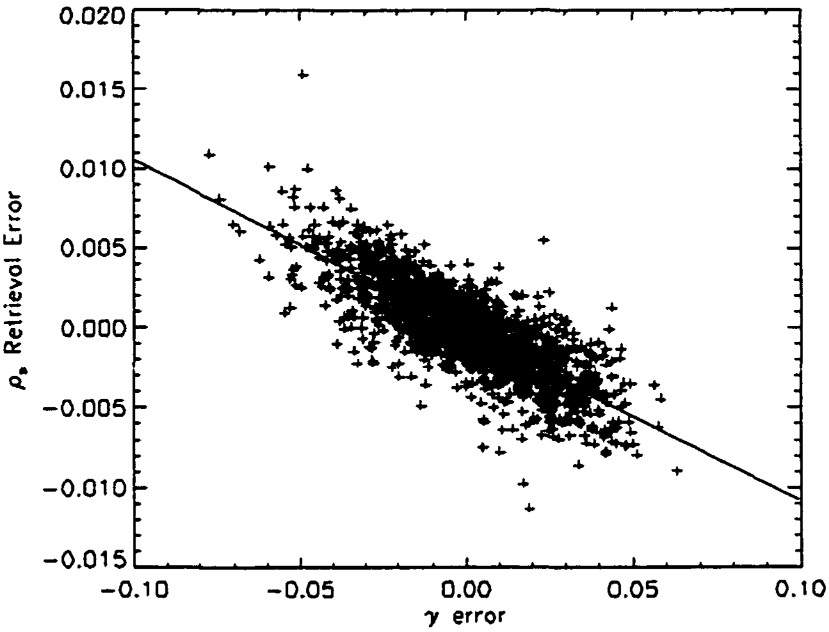

Figure 8.22 – $\rho_{s,e}$ error as a function of γ. The equation of the linear regression line is: $\rho_{s,e}$ = -0.11$\Delta\gamma$ with r = -0.80.

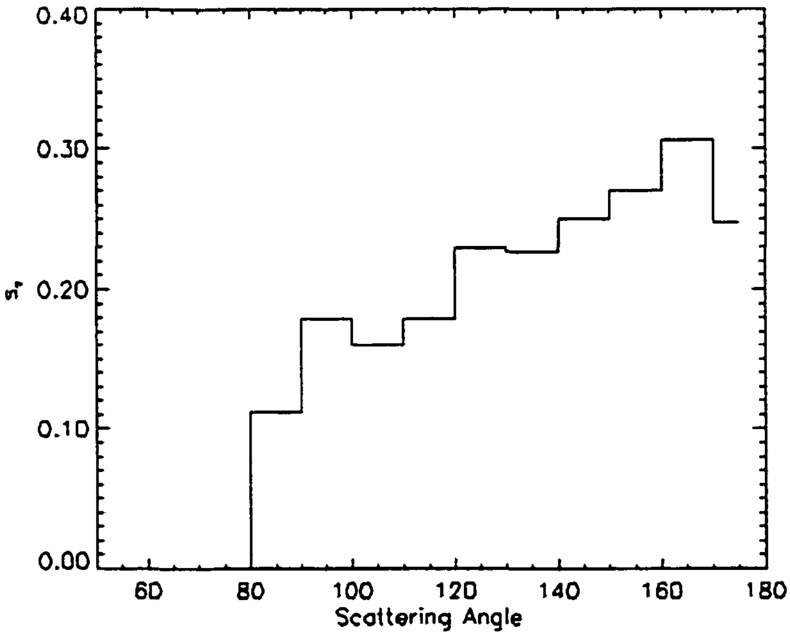

Figure 8.23 – s_τ as a function of scattering angle.

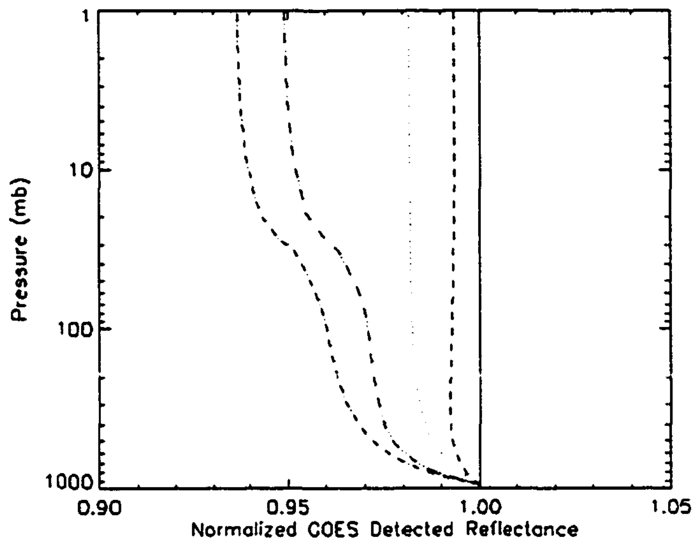

Figure 8.24 – Change in GOES reflectance (calculated by DISORT) as a function of aerosol layer height for different atmospheric conditions, normalized by the radiance when the aerosol (τ = 0.3) is concentrated in the lowest layer. Solid line – aerosol only (ω_0 = 0.96 and 1.0), dotted line – Aerosol (ω_0 = 1.0) and Rayleigh scattering, dashed line – Aerosol (ω_0 = 0.96) and Rayleigh scattering, dash-dotted line – Aerosol (ω_0 = 1.0) and Rayleigh scattering and gaseous absorption, dash-dot-dotted – Aerosol (ω_0 = 0.96) and Rayleigh scattering and gaseous absorption.

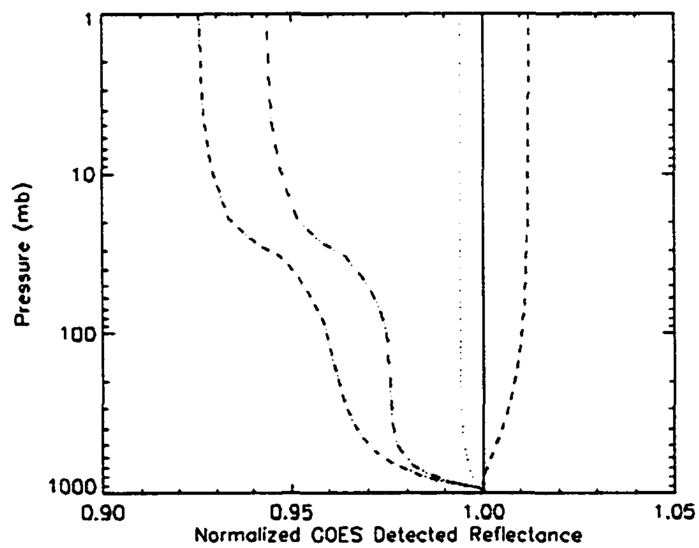

Figure 8.25 – Same as figure 8.24 except for τ = 1.0.

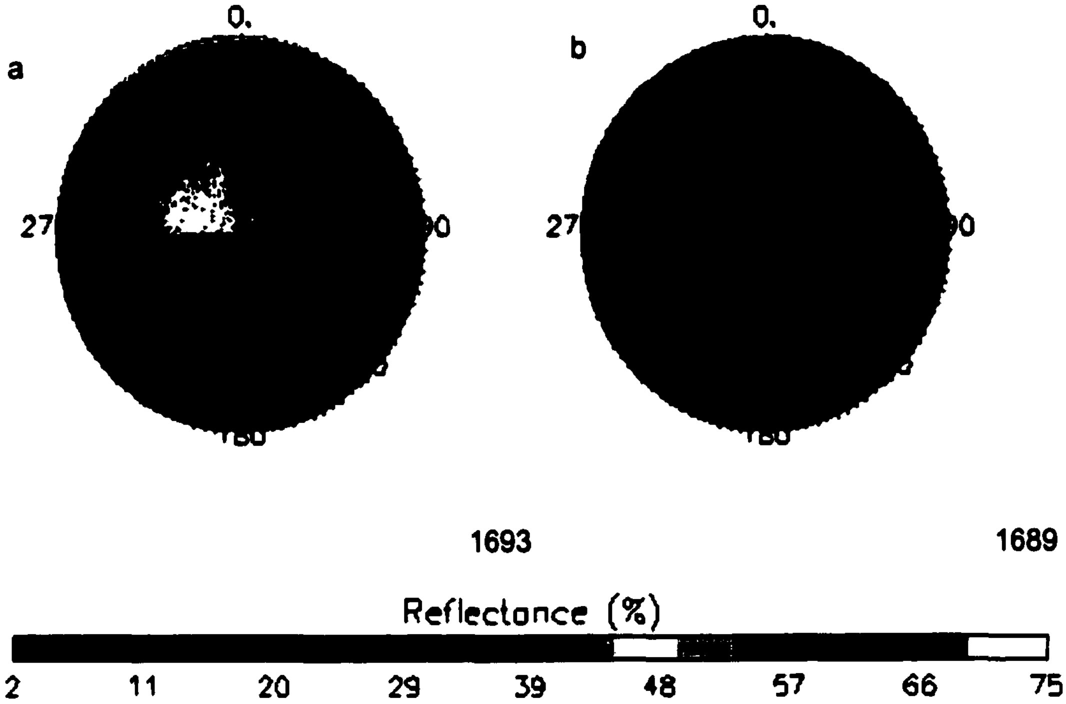

Figure 8.26 – BRDF measured during SCAR-B at 0.675 μm for a) forest and b) cerrado land cover.

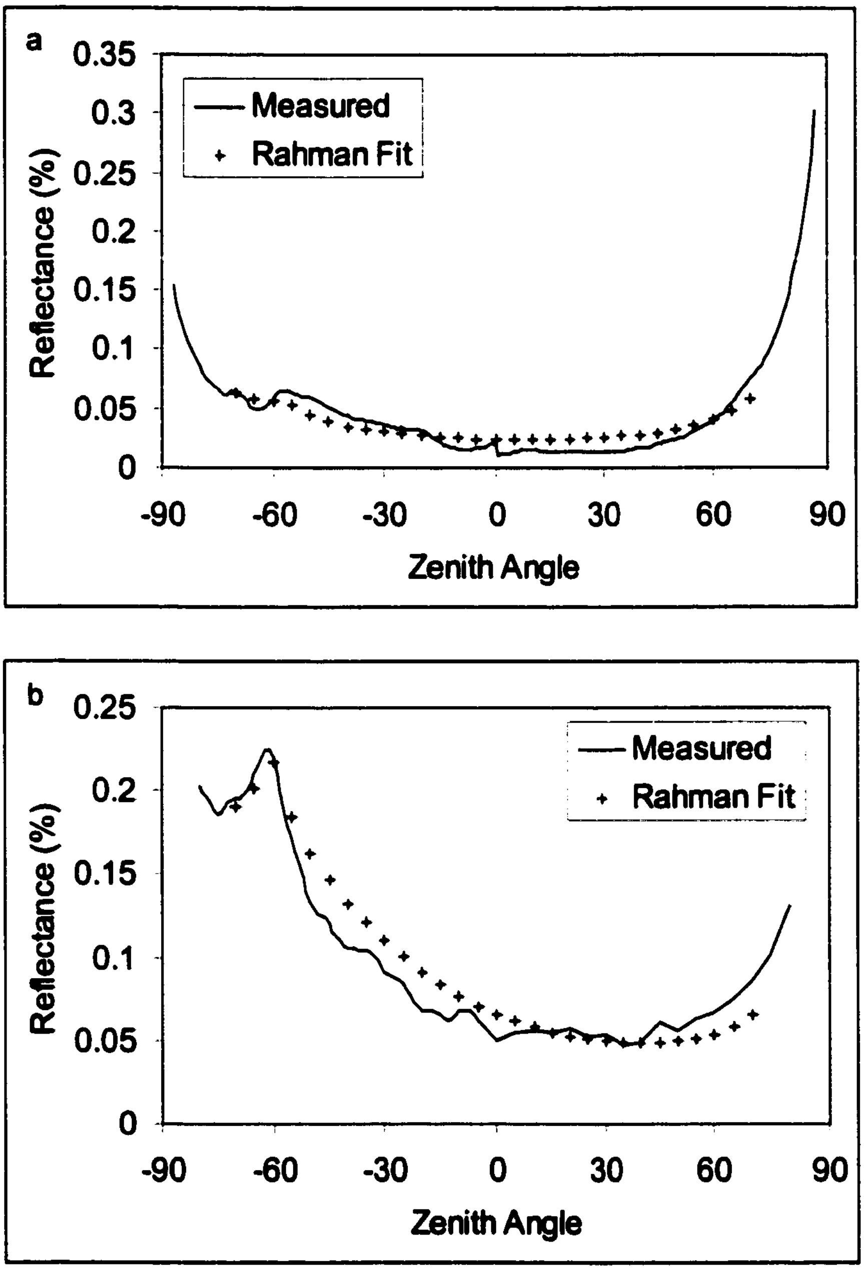

Figure 8.27 – SCAR-B BRDF measurements through the principle plane for a) forest and b) cerrado with the Rahman BRDF best fit.

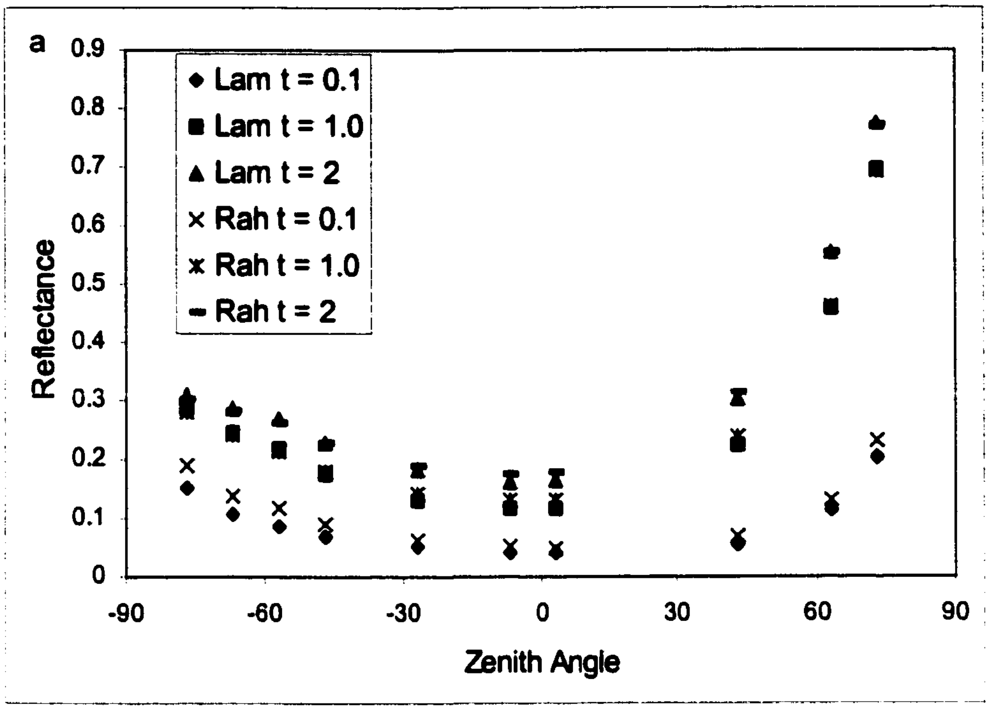

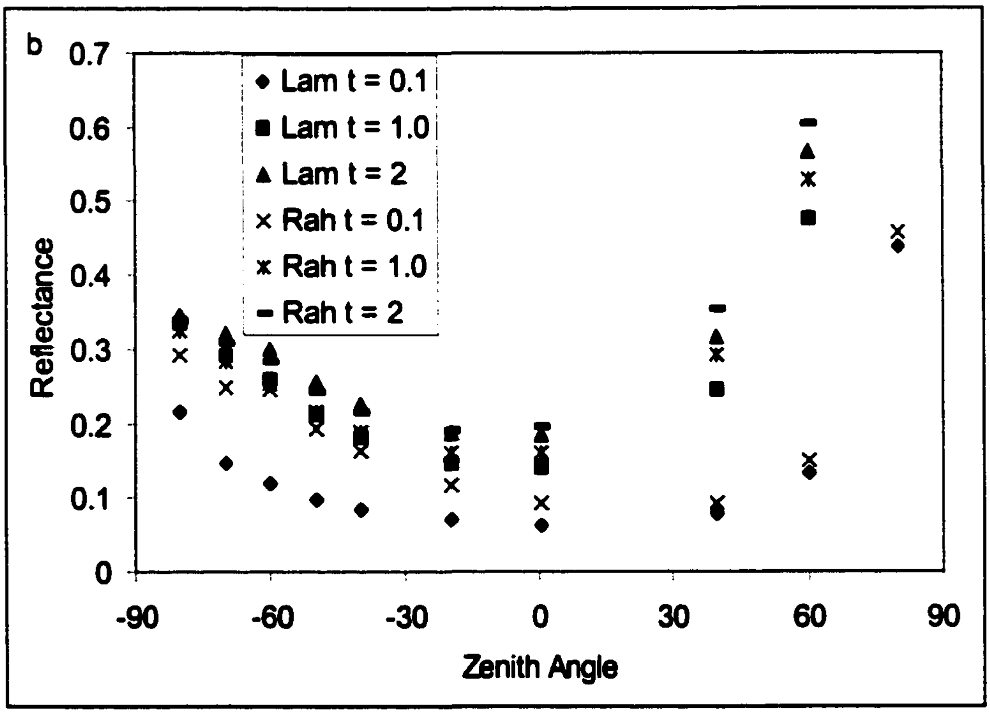

Figure 8.28 – Top of the atmosphere reflectances for a) forest and b) cerrado using the Lambertian (Lam) and an estimated Rahman BRDF (Rah) surface for varying optical depths.

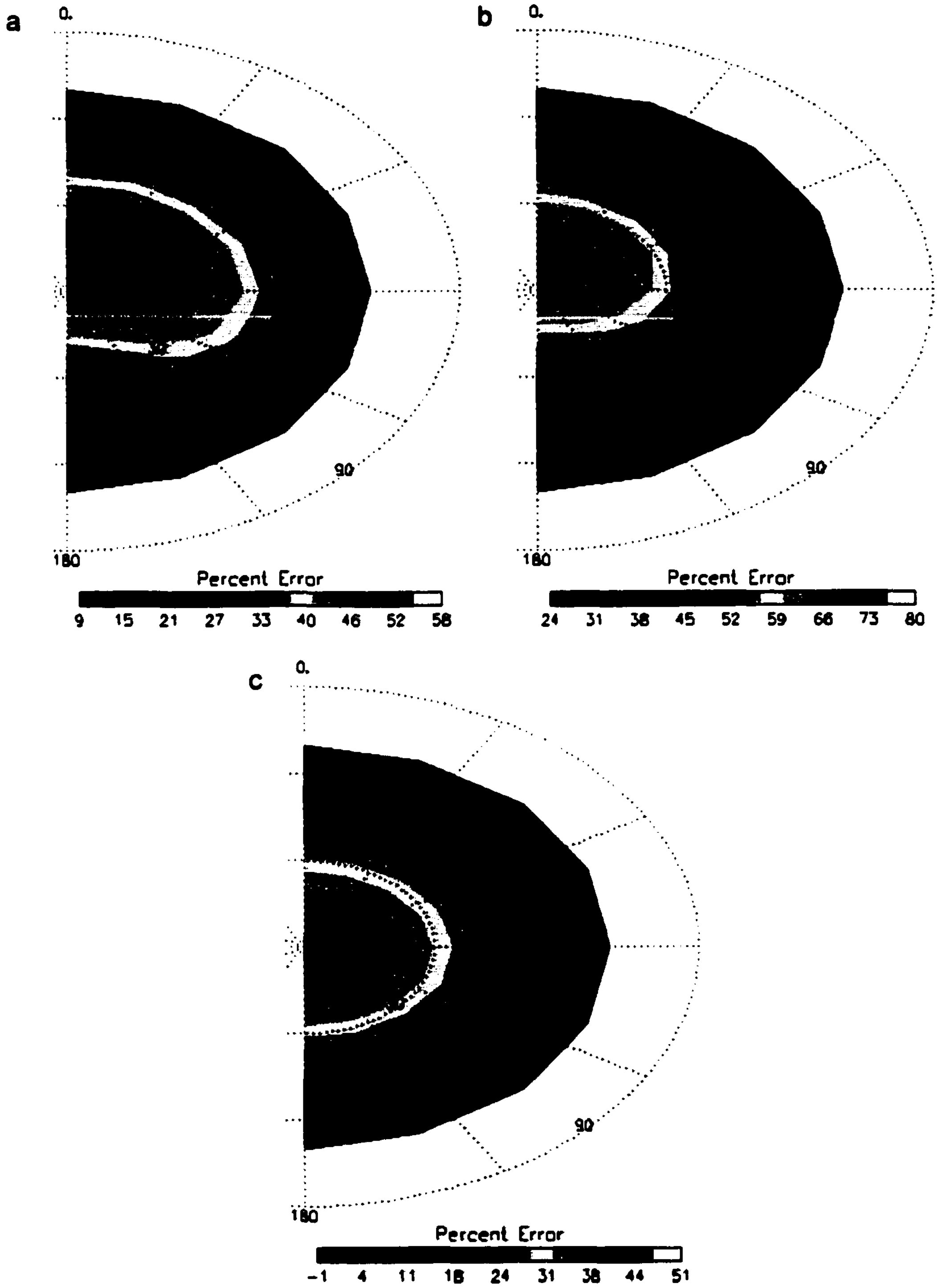

Figure 8.29 – GOES-AOD percent error for neglecting the BRDF of a Forest with the sun at θ_0 = 30° and ϕ=180° for a) τ = 0.2 and b) τ = 1.5 and c) sun at θ_0 = 60° and ϕ=180° and τ = 1.5.

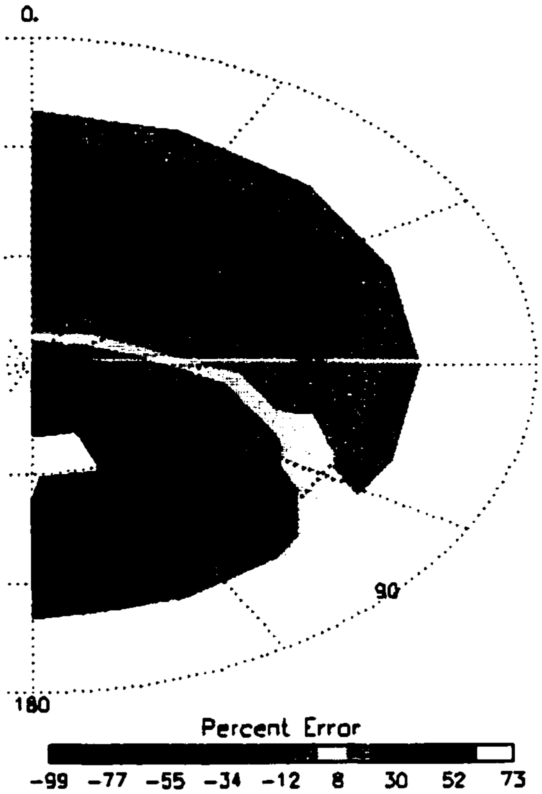

Figure 8.30 – GOES-AOD percent error for neglecting the BRDF of cerrado with the sun at θ_o = 30° and ϕ=180° and τ = 0.2.

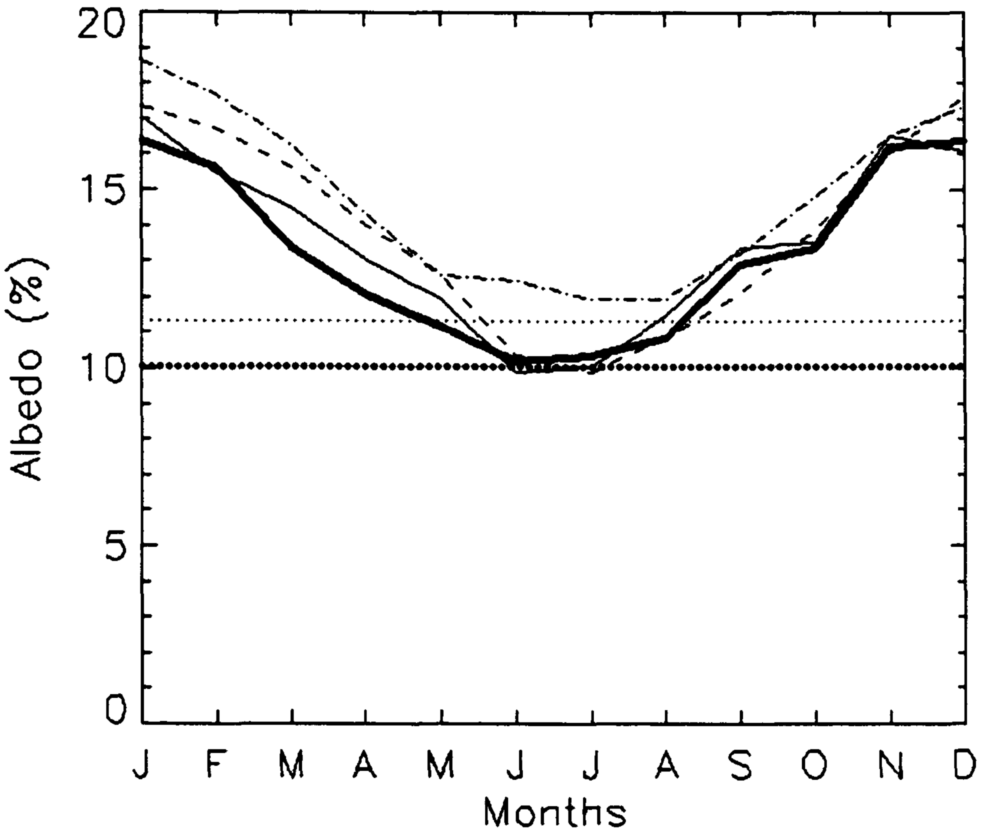

Figure 8.31 – Temporal Variation of the broadband albedo at the six sites used for ground validation in this study: 1995 (thin lines) – Cuiaba (solid), Alta Floresta (dotted), Brasilia (dashed), Campo Grande (dash dotted) and 1998 (thick lines) – Concepcion (solid) and Los Fieros (dotted).

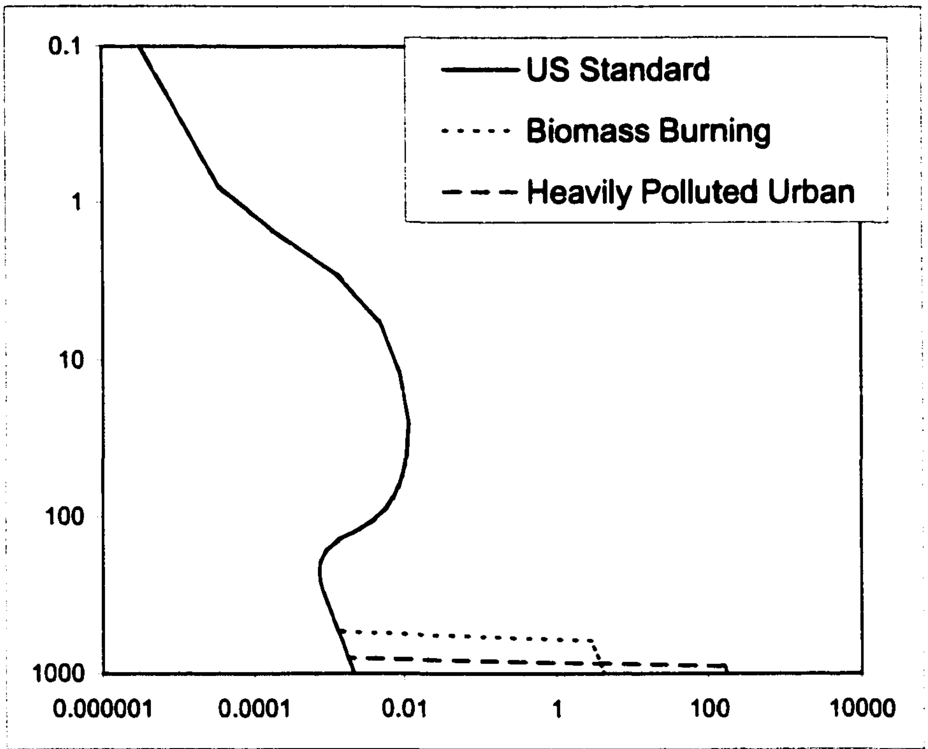

Figure 8.32 – Vertical distribution of three atmospheres: US Standard (solid), Biomass burning (dotted) and a heavily polluted urban (dashed).

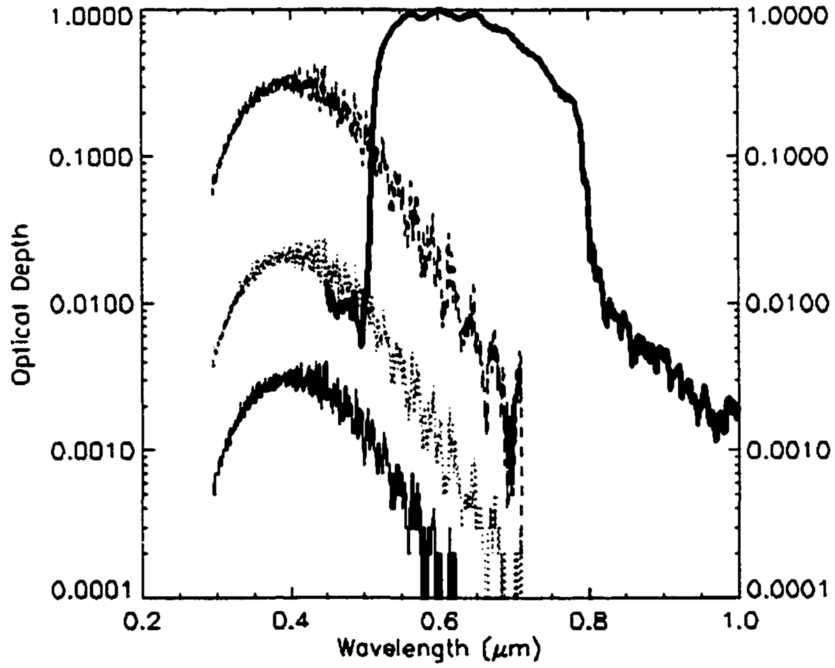

Figure 8.33 – Spectral optical depth of NO_2 absorption for a U.S. Standard (thin solid line), biomass burning (dotted line) and heavily-polluted urban atmospheres (dashed). The GOES-8 visible spectral response is also provided for reference (thick solid line).

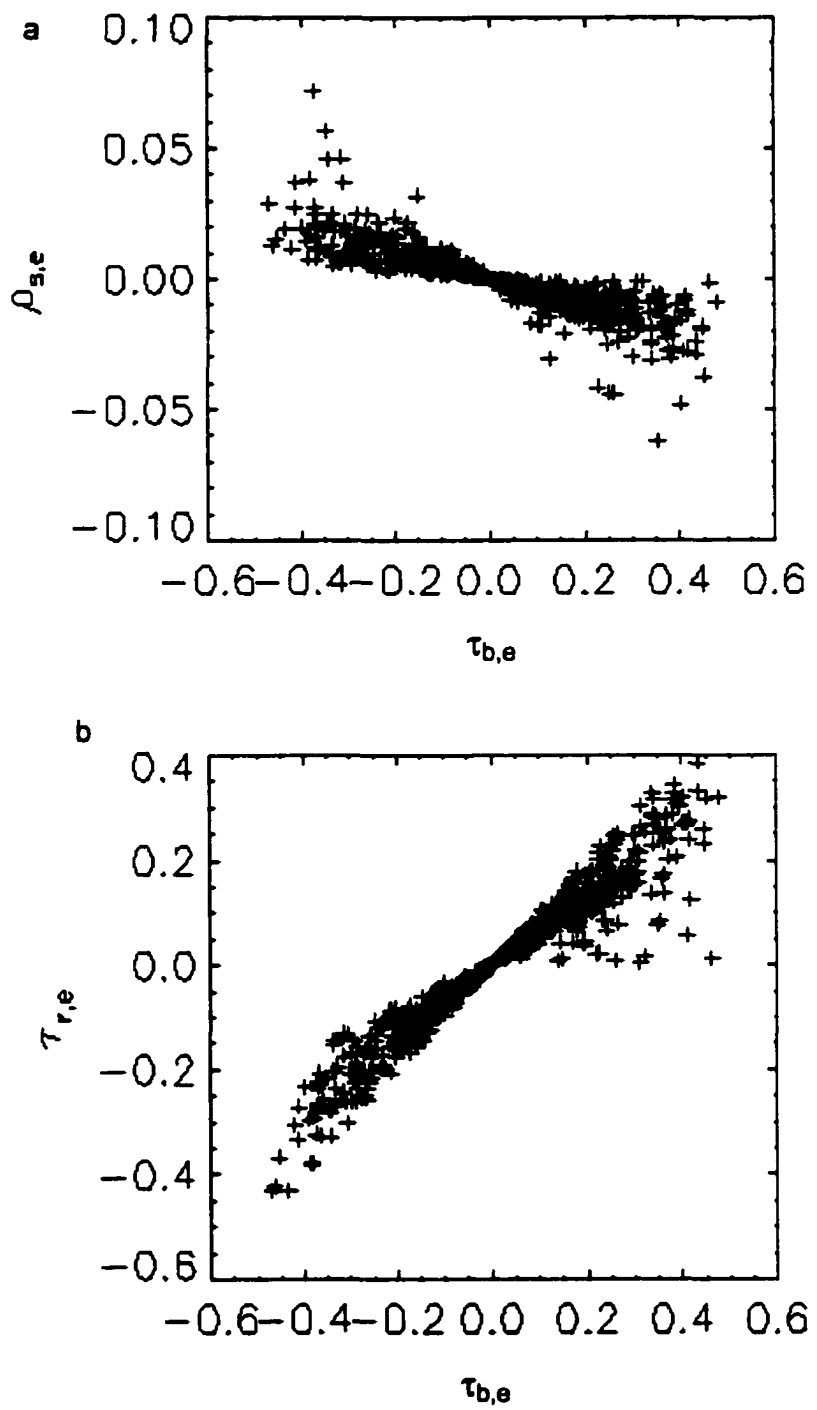

Figure 8.34 – a) Surface reflectance error as a function of background optical depth error and b) Aerosol optical depth error as a function of background optical depth error.

9. Validation of GOES-AOD

The GOES-AOD algorithm is validated against two aerosol optical depth estimation data sets. The first dataset is the AERONET aerosol observations which is described in chapter 6 and has an accuracy of $\Delta\tau = \pm 0.01$. This is much higher than the accuracy of the GOES-AOD and is considered "ground truth." The second dataset consists of aerosol optical depth retrievals made using the MODIS Airborne Simulator (MAS-AOD) provided by Rong-Rong Li of NASA-GSFC. This is beneficial for comparing the ability of the GOES-AOD to the MODIS-AOD.

The comparisons show that the GOES-AOD can accurately retrieve aerosol optical depth in the biomass burning regions of South America. The results of the retrievals verified in this chapter are used to investigate aerosol climatic effects in chapters 10 (the radiative direct effect) and 11 (estimating aerosol mass emission rates from fire sources).

9.1 The SCAR-B Field Experiment

The Smoke, Clouds, And Radiation – Brazil (SCAR-B) field experiment provided a thorough study of aerosols emitted from biomass burning (e.g., the burning of the tropical forest in South America). In situ measurements allowed the characterization of numerous aerosol optical and physical properties. Of the many instruments in the area, the AERONET observations of aerosol optical depth are most valuable to the validation of AOD retrievals; AERONET sites are shown in figure 9.1. Results from SCAR-B are described by Kaufman et al. (1998) and the following special section in the *Journal of Geophysical Research*. The MAS flew on the NASA/ER-2 on 12 flights; results from six of these are compared to GOES-AOD.

The burn season in central South America generally begins in late July or early August and continues through October (Prins et al., 1998). During this time, the aerosol optical depth increases as the smoke palls collect over Brazil, until transported south and eastward over the South Atlantic. The time series of τ at six of the SCAR-B AERONET sites used for validation are shown in figure 9.2. The sites nearer the burning – Cuiaba and Alta Floresta – have large optical depths. Alta Floresta is in the heart of the burn area; optical depths here are the largest, with τ rarely less than 0.5 in August. Campo Grande – in a grassland region of southern Brazil – has lower optical depths. Cuiaba and Campo Grande have similar trends as smoke palls periodically advect over the sites. Also, Brasilia is included which is located far from the burn areas, thus aerosols there likely have different optical properties than the sites nearer the burn area. Yet, it shows a significant aerosol optical depth increase in mid and late September. Two other AERONET sites – Ji Parana and Potosi Mine – have limited measurements, but still provide enough points to draw some conclusions. Other AERONET sites are shown in figure 9.1 but have few measurements, yielding no comparison to GOES-AOD.

The SCAR-B study affords numerous datasets for use with optical depth retrievals. The GOES-8 automated biomass burning algorithm (ABBA) uses multi-spectral GOES imagery to detect pixels containing fires. For such pixels, the fire temperature and fire area are estimated. The algorithm is described by Prins et al. (1998), which also summarize the algorithm results during the SCAR-B experiment. Also, the MODIS Airborne Simulator (MAS) flew more than a dozen flights during the experiment. The data from such flights have been processed by NASA to retrieve aerosol optical depth in a similar manner to the MODIS-Land algorithm.

Two AERONET sites from 1998 are also included in this validation. Retrievals during 1998 have significant advantages over those in 1995: 1) A change in the CIRA archival process allowed retrieval at half hour intervals (increased from the 3-hour intervals of SCAR-B) and 2) the CERES instrument was operational during August 1998, allowing for comparisons between GOES-AOD retrievals and CERES shortwave flux estimates. The 1998 AERONET sites are Los Fieros and Concepcion.

9.2 GOES vs. AERONET

Sun photometers provide the best information available for validation of satellite retrievals of AOD. The photometer observes the light extinguished from the direct solar beam and calculates the optical depth from the Beer-Lambert Law. The AERONET observations have uncertainties of ±0.01 (Holben et al., 1998).

Yet another uncertainty in the validation can exist. The photometer measures the extinction along a path from the photometer to the sun. The measured volume of air is a small cone from the sensor to the theoretical top of the atmosphere (TOA). The effective volume of the GOES-AOD is a combination of a $1 \times 1 km^2$ column extending upward toward the satellite from the ground point as well as a similar column extending from the satellite footprint toward the sun. Thus, a sun photometer observes aerosol over a volume about one-sixtieth that of the GOES-AOD sampled volume. This requires a horizontally homogeneous aerosol mass for comparisons of the two measurements.

Comparisons between GOES-AOD and AERONET observations of AOD are made during August and September of 1995 (the SCAR-B field experiment) and August 1998. Imagery during 1995 is available at 3-hour intervals, while imagery from 1998 is available at 30 minute intervals. The difference in temporal resolution is due to an archival process change, rather than any improvements in the satellite observations. Subsequently, there are about 18 retrievals per day available for validation in the 1998 data, compared to 3 observations per day for 1995. First comparisons are made for instantaneous observations, then daily average optical depths are compared.

9.2.1 Co-located ground truth

The number of level 2 AERONET observations are limited during SCAR-B, so, the validation is limited to Alta Floresta (ALT), Brasilia (BRA), Campo Grande (CAM), Cuiaba (CUI), Ji Parana (JIP) and Potosi Mine (POT) for 1995. Results of the comparisons are grouped by AERONET site. Statistics are shown in table 9.1 and GOES-AOD error, τ_e, is correlated with various parameters in Table 9.2. The bias and root-mean-square (RMS) parameters are calculated from:

$$\mathrm{RMS} = \sqrt{\frac{\sum(\tau_r - \tau_A)^2}{N}}$$

and

$$\mathrm{bias} = \frac{\sum(\tau_r - \tau_A)}{N}$$

where N is the number of comparison points per site, τ_r is the GOES-AOD retrieval and τ_A is the AERONET observation. Also, the standard deviation of the τ_e, σ_τ, is calculated because the RMS is affected by the bias as well as the noise. The percent error is then the ratio of σ_τ to the mean optical depth times 100. This value should be approximately 0.35, as determined by the sensitivity study. Both τ_r and τ_A are reported at λ=0.5μm. τ_r, is compared to τ_A if all of the following conditions are met:

1) $\tau_r > 0$

2) $\sigma_\tau < 0.25$, which is a threshold value used to filter for cloud contamination and spatial homogeneity

3) AERONET observation is valid ($\tau_A > 0.$)

4) AERONET observations exist before and after the τ_r (within 2 hours)

5) AERONET observations before and after the τ_r less than 1.

Criteria 1 through 3 assure valid aerosol observations. The comparison was performed when the time of the AERONET observations bounded τ_r. This was done so AERONET observations could be interpolated to the GOES observation time, limiting temporal difference problems, thus criterion number 4.

Comparisons for each site are plotted τ_r (GOES-AOD) vs. τ_A (AERONET AOD), (figures 9.3, 9.5, 9.7, 9.9, 9.11 9.12, 9.13, and 9.15,). Each plot consists of the scatter plot, a solid line representing the one-to-one correlation and a dashed line representing the linear regression (LR). Also, retrieval error (denoted τ error in graphs) is compared to various parameters to allow better analysis of the retrieval error (excluding Ji Parana and Potosi Mine which had few comparisons). The following describes the error analysis graphs of figures 9.4, 9.6, 9.8, 9.10, 9.14, and 9.16, where letters refer to the same scatter plot types in each graph.

The relationship between τ_e and different parameters allows insight toward the cause of any noise or bias in the retrieval validations. τ_e is compared to τ_A (A graphs). Any correlation between τ_e and τ_A would suggest an error in the aerosol model, i.e. incorrect ω_0. Also, τ_e would be correlated to time of day if the aerosol phase function (and thus the aerosol size distribution) is incorrect (B graphs).

Surface reflectance changes would appear as a trend in the τ_e vs. day of year plot (C graphs). Errors correlated with water vapor (D graphs) could suggest change in particle characteristics (absorption of water vapor).

A discussion of the validation at each site follows. For each site, σ_τ is compared to the mean observed optical depth (which should be ~34% from the sensitivity study).

Cuiaba

The comparison of GOES-AOD with AERONET AOD for Cuiaba is quite good (Figure 9.3). The correlation is 0.92 for 60 points with an LR slope near 1. The bias of 0.04 is small, but the RMS is large at 0.35; the percent error is 27%. Errors are largely uncorrelated (figure 9.4).

Alta Floresta

Retrievals at Alta Floresta are also encouraging. Correlation is still large – explaining 86% of the variance – and the LR slope is 0.96 (figure 9.5). Strong correlation exists between the τ_e and τ suggesting a problem with the aerosol model. There is little correlation of error with other parameters (figure 9.6) but the variance does seem to increase during the day (figure 9.6b). The percent error is 20%.

Campo Grande

While the range of optical depths at Campo Grande was smaller than the previous two comparisons, τ_r was nearly as well correlated – r = 0.83 (figure 9.7).The correlations with respect to different parameters are small (table 9.2) yet there is a large trend in error with time of day (9.8b). Significantly, this site is in the cerrado region. This represents two sources of error: 1) the surface reflectance is brighter in this region and 2) the BRDF effect is much stronger. This causes the percent error to be larger then most other sites, 45%.

Brasilia

The correlation at Brasilia is also quite large in spite of the small range of aerosol optical depth. Again, an interesting trend occurs in the error versus time of day (figure 9.10b) suggesting BRDF effects or an error in the aerosol model. Brasilia is an urban region, located far from the biomass burning regions. It is likely that aerosols in Brasiilia are not primarily biomass burning and those that are have likely undergone significant changes in the transport. Also, a trend exists in the error versus day (figure 9.10c), suggesting changes in the surface reflectance during the time period. Nonetheless, the slope is still near one, with a bias of only 0.1.

Ji Parana and Potosi Mine

The comparisons at Ji Parana and Potosi Mine show similarly retrieval success. Ji Parana has more comparisons (19), yet the RMS is also large (0.73). However, the RMS relative to the average τ is similar to the previous sites, 0.31. Potosi Mine shows very high correlation (0.93) and low RMS (0.07). Yet the number of comparisons is again low. No estimate of cause of error is possible from these sites due to the small number of comparisons.

Concepcion

The correlation at Concepcion, r = 0.94, is quite good (figure 9.13); the RMS is 0.18 with a bias of 0.16 (Table 9.3).There is some correlation between optical depth and retrieval error (figure 9.14a). Also, the variance in the error (figure 9.14b) is lower when the solar zenith angle is higher (sun approaching horizon).

Los Fieros

The Los Fieros site has a similarly high correlation, yet the bias is 0.04 (figure 9.15). Similar to Concepcion, the error is a strong function of τ. (figure 9.16a).

9.2.2 Daily average optical depth comparisons

Comparisons at Los Fieros and Concepcion provide an opportunity to compare daily average estimates of aerosol optical depth. The daily average τ_r compares very well with the daily average τ_A (Figure 9.17). The numbers plotted in figure 9.17 represent the number of GOES observations for that value. The correlation for the daily average comparison increases from the instantaneous comparisons (Table 9.3). Also, the outlier in figure 9.17 is an average of only two GOES-AOD retrievals. Figure 9.18 compares the number of daily AERONET observations (solid line) to the number of daily GOES observations (dashed line). In general, the range of GOES observation is between 15 and 20, except for cases where imagery was limited. Similar results are obtained at Concepcion, with a correlation of 0.96 (figure 9.19), showing that the daily average optical depth retrieval is more accurate than individual comparisons. Again, outliers had fewer GOES observations. Yet while the RMS and σ_τ for the daily average are lower than those of the instantaneous comparisons, the percent error (or noise estimate) is still 20 and 27% (table 9.3).

The numerous comparisons allows the linear regression comparison for each time of day. Figure 9.20 shows the time series of correlation and the linear regression slope. The correlation at each time of day are generally constant and larger than 0.9 (with the exception of one point affected by cloud). The slopes, however, vary substantially through the day. The trends have some similarity, yet diverge when the solar zenith angle is extremely large, suggesting that either the aerosol model wrong, causing the phase function to be incorrectly modeled, or the BRDF is affecting the retrieval. It is likely the former, since the BRDF is smaller over these forested sites.

The number of daily τ observations are compared in Tables 9.4 and 9.5. In general, both AERONET and GOES observations occurred 66% and 77% of the time, at

Concepcion and Los Fieros (respectively). However, of the 51 days with AERONET observations, the GOES observations are missing from only 7, which is primarily due to archival losses. This loss rate of 14% is much less than the expected loss rate of τ observations from a polar orbiting satellite of 30-40% (as described in section 6.3).

9.3 GOES vs. MAS AOD

During SCAR-B, the MODIS Airborne Simulator (MAS) flew 12 flights over the biomass burning regions of central South America collecting data. This provided an excellent test-bed for the MODIS algorithm. The results of the MODIS-Land algorithm (compared to AERONET sites during SCAR-B) are described by Chu et al. (1998). The results show a strong correlation with a linear regression near the one-to-one relationship. The frequency of the MAS flights also allow an opportunity to inter-compare the retrievals of aerosol from MODIS-AOD with the GOES-AOD results. However, prior to comparing GOES-AOD with MODIS-AOD, the ER-2 flight pattern on 4 September allowed an intra-comparison of the MODIS-AOD data.

On 4 September 1995, the MAS instrument measured the same biomass burning plume twice, within 27 minutes. The NASA-ER-2 flew a path over a plume, then retraced its flight path over the same plume. The aerosol optical depth retrievals for these flights, leg number 12 and 13, are shown in Figures 9.21 and 9.22 (respectively). These retrievals are collocated and compared in Figure 9.23, It can be seen that the results are generally within 10% of each other, with no points beyond 25% (dashed line). This is not an error with regard to the MODIS-AOD algorithm, but shows an uncertainty in comparing two images of a smoke plume at different times. Thus, when comparing GOES-AOD and MODIS-AOD at times more than 10 minutes apart, a large portion of the variance can be explained by the difference in the observation time of each data set.

It also should be noted here that this comparison does not validate the GOES-AOD algorithm as much as it will show the ability of the GOES-AOD algorithm in comparison to the MODIS-Land algorithm. Here, the MODIS algorithm represents the "state-of-the-art" in aerosol remote sensing, whereas the GOES-AOD algorithm represents the ability of previous sensors. Any correlation of the two does not prove further accuracy, but would imply some comparative ability of the two algorithms.

There are fifteen flight legs which are co-located with GOES-AOD retrievals, which are summarized by Table 9.6. In general, the flights are within ±30 minutes of the GOES image observation. The comparisons are shown in figures 9.24 through 9.28 with a summary of the statistical comparison in Table 9.7. For each comparison, a point-by-point comparison is shown along with a PDF of the percent error. Many of the comparisons are highly correlated – nine of 15 explaining more than 50% of the variance. Two comparisons had very low optical depths (cases 1 and 9). The correlation for these comparisons is low, likely emphasizing the differences in the surface reflectance estimates. The standard deviation between the two retrieval estimates ranges from 0.07 to 0.36. This is well within the range of uncertainty calculated in chapter 8. The results also have significant bias differences – eight positive biases and seven negative biases. This suggests further differences in the retrieval methods. Overall, the comparison shows similar ability between the retrieval methods.

9.4 Conclusions

- Comparisons to eight AERONET sites show high correlation. Correlations ranged from 0.78 to 0.97. These high correlations occurred for both the 1995 SCAR-B comparisons as well as the two observation sites in 1998.

- Relative errors were less than 38% with the exception of Brasilia and Campo Grande. The larger Brasilia error was due to low optical depths and an aerosol not well represented by biomass burning. The Campo Grande site provided larger error because the albedo in the region was higher and the region was cerrado. As shown in chapter 8, the uncertainty of assuming a Lambertian surface in the cerrado regions is larger.
- Relative uncertainties were generally within those estimated from the sensitivity study presented in chapter 8.
- Comparisons were biased; seven of eight sites showed a positive bias. This bias could result from an incorrect aerosol model, particularly the single scatter albedo. The bias was weakest at Alta Floresta, a site located close to the burning regions. Sites further away would encounter aged smoke, which would have a larger single scatter albedo, thus biasing the measurements high.
- Diagnostic analysis of the retrieval error provided insight to the cause of some discrepancies. The error at Los Fieros and Concepcion showed correlation between the error and optical depth, suggesting a different aerosol model would be more accurate or possibly a calibration error. A significant trend in the error at Campo Grande as a function of time of day suggests either an incorrect aerosol phase function, or significant BRDF contamination.
- Daily averaging of comparisons significantly decreases the retrieval noise. Hundreds of comparisons were averaged for 46 and 55 daily comparisons at Concepcion and Los Fieros, respectively. In both cases, the standard deviation and relative error decreased. Also, the correlation increased for daily averaging.
- Comparisons grouped by time of day showed significant trends. While the correlations were high, the slope of the comparisons ranged from 0.8 to 1.4. This

suggests either an error in the aerosol size distribution (causing the phase function to be incorrect) or contamination from the BRDF of the forest.

- The GOES imager provides numerous images of a smoke plume per day. The number of observations ranged from a minimum of at least four to as many as 20 (with half hour temporal resolution).
- The GOES-AOD performed retrievals with a much lower "loss rate" than a polar orbiter. The GOES-AOD missed 14% of the days on which an AERONET observation was made. This is a large increase from the 60-70% loss rate possible from a polar orbiting instrument. The loss of the 14% is due to either 1) days where data was not archived or 2) days where fewer images were available.
- The GOES-AOD retrieval showed comparable ability to the "state-of-the-art" retrieval performed using the MODIS Airborne Simulator. Comparisons between GOES-AOD and MAS-AOD showed large correlations and low standard errors. Nine of fifteen comparisons had correlations larger than 0.71.

Table 9.1 – Statistical values for the comparison of AERONET to GOES-AOD including number of points (n), correlation coefficient (r), bias, RMS, σ_τ, and relative error ($\sigma_\tau/\bar{\tau}$).

parameter	CUI	ALT	CAM	BRA	JIP	POT
n	60	48	34	45	19	6
r	0.92	0.93	0.83	0.87	0.78	0.93
Bias	0.14	-0.07	0.23	0.10	0.25	0.07
RMS	0.29	0.29	0.35	0.13	0.73	0.17
σ_τ	0.25	0.29	0.27	0.09	0.71	0.17
$\sigma_\tau/\bar{\tau}$	0.27	0.20	0.45	0.52	0.31	0.08

Table 9.2 – Correlation coefficients of the comparison of GOES-AOD error vs. various parameters for the 6 AERONET sites* and altitude and land cover.

parameter	CUI	ALT	CAM	BRA	CON	LOS
τ	0.01	-0.10	0.06	0.17	-0.24	-0.46
time	-0.06	-0.08	-0.03	0.48	0.01	0.03
day	0.23	-0.01	0.16	0.15	0.03	-0.25
H_2O	-0.06	0.20	-0.04	0.25	-0.04	0.02
Altitude (m)	250	175	500	1100	500	170
Land Cover	Forest	Forest	Cerrado	Urban	Forest	Forest

*Ji Parana and Potosi Mine are excluded from this comparison because of the limited number of comparisons.

Table 9.3 – Same as table 9.1 except for comparisons at Concepcion and Los Fieros during 1998.

	Instantaneous		Daily Average	
parameter	CON	LOS	CON	LOS
n	377	646	46	55
r	0.94	0.97	0.96	0.98
Bias	0.16	0.04	0.19	0.04
RMS	0.18	0.17	0.23	0.14
σ_τ	0.18	0.17	0.14	0.14
$\sigma_\tau/\bar{\tau}$	0.38	0.28	0.27	0.20

Table 9.4 – Comparison of GOES-AOD observations to the AERONET observations at Concepcion.

		AERONET Observations?		
		Yes	No	Totals
GOES Observations?	Yes	20	0	20
	No	2	9	11
	Totals	22	9	31

Table 9.5 – Comparison of GOES-AOD observations to the AERONET observations at Los Fieros.

		AERONET Observations ?		
		Yes	No	Totals
GOES Observations?	Yes	24	0	24
	No	5	2	7
	Totals	29	2	31

Table 9.6 – List of GOES-AOD vs. MAS-AOD comparisons with observation times of each retrieval. MAS observation time is relative to the GOES image time.

Comparison	Day	MAS Flight Leg	GOES Image time – sector (UT)	MAS time (UT)	MAS time (min)
1	16 Aug	3	15:01 – BRA	14:40-14:57	-21 to -4
2	23 Aug	10	18:01 – JIP	17:29-17:42	-32 to -19
3	23 Aug	11	18:01 – JIP	17:43-17:48	-18 to -13
4	23 Aug	12	18:01 – POT	17:49-18:06	-12 to +5
5	23 Aug	12	18:01 – JIP	17:49-18:06	-12 to +5
6	30 Aug	2	15:01 – CUI	14:51-15:13	-10 to +12
7	1 Sep	8	15:01 – CUI	14:29-14:48	-32 to -13
8	1 Sep	11	15:01 – CUI	15:04 15:29	+3 to +28
9	4 Sep	1	15:01 – CUI	14:43-15:06	-18 to +5
10	4 Sep	12	18:01 – POT	17:31-17:42	-30 to -19
11	4 Sep	13	18:01 – POT	17:50-17:58	-11 to -3
12	4 Sep	15	18:01 – POT	18:04-18:25	+3 to +24
13	7 Sep	1	15:01 – CUI	14:53-15:11	-8 to +10
14	7 Sep	12	18:01 – JIP	17:31-17:57	-30 to -4
15	7 Sep	12	18:01 – POT	17:31-17:57	-30 to -4

Table 9.7 – Statistics of each GOES-AOD vs. MAS-AOD comparison.

Comparison	τ range	r	Bias (τ_{MAS}-τ_{GOES})	σ_{diff}
1	0.01-4.5	0.50	-0.16	0.07
2	2.5-4.0	0.78	-0.32	0.22
3	1.6-2.9	0.62	-0.02	0.20
4	1.5-2.2	0.07	-0.14	0.17
5	1.4-2..2	0.84	0.07	0.11
6	2.4-4.0	0.01	0.19	0.36
7	0.53-2.3	0.80	0.14	0.19
8	0.48-2.6	0.95	0.32	0.15
9	0.41-1.1	0.28	0.22	0.17
10	1.9-4.1	0.85	-0.12	0.32
11	2.1-4.1	0.94	-0.12	0.22
12	2.0-3.7	0.54	-0.07	0.22
13	0.47-2.1	0.93	0.08	0.14
14	2.0-4.1	0.95	0.11	0.18
15	2.0-3.9	0.92	0.15	0.17

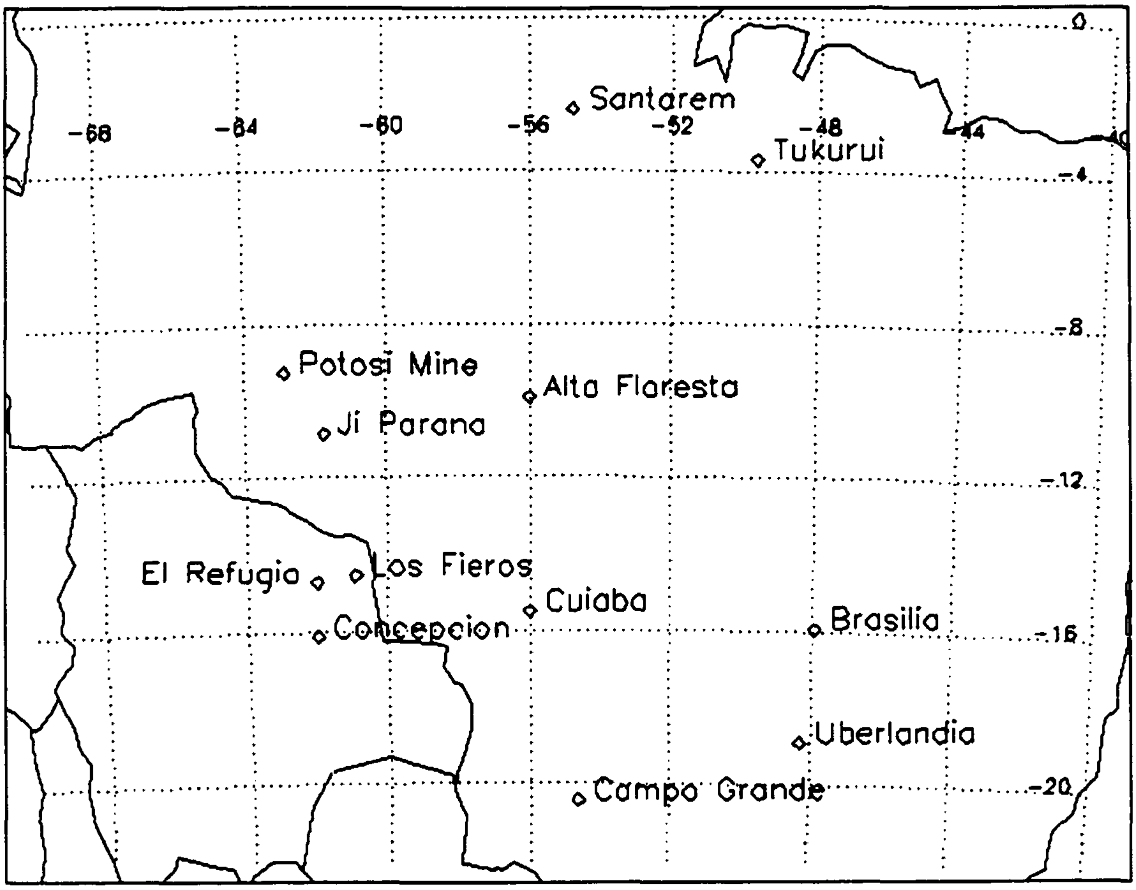

Figure 9.1 – Distribution of the AERONET sites in South America during the SCAR-B experiment in 1995 (except for Los Fieros and Concepcion, which operated in 1998).

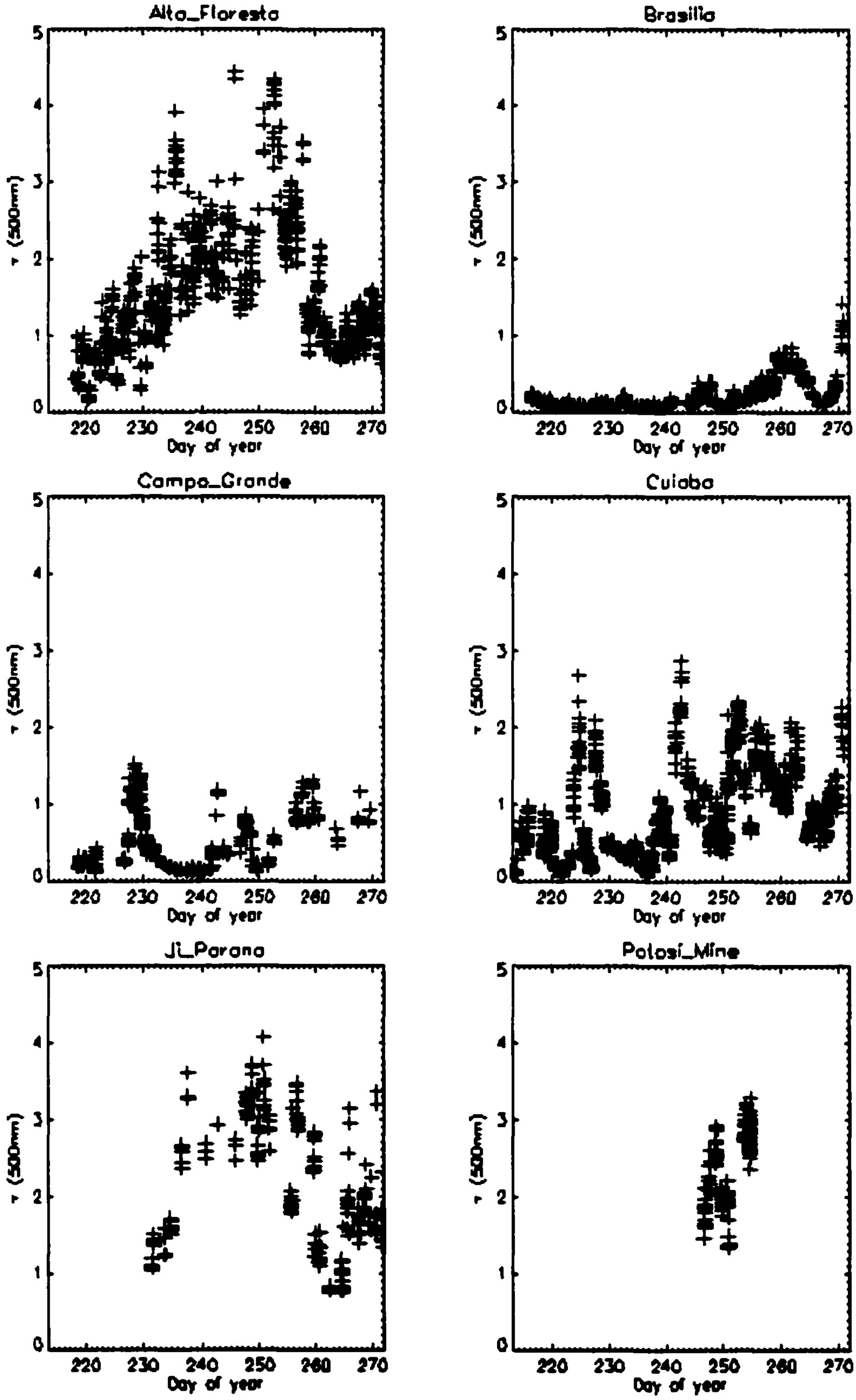

Figure 9.2 – Aerosol optical depth time series at the six AERONET validation sites.

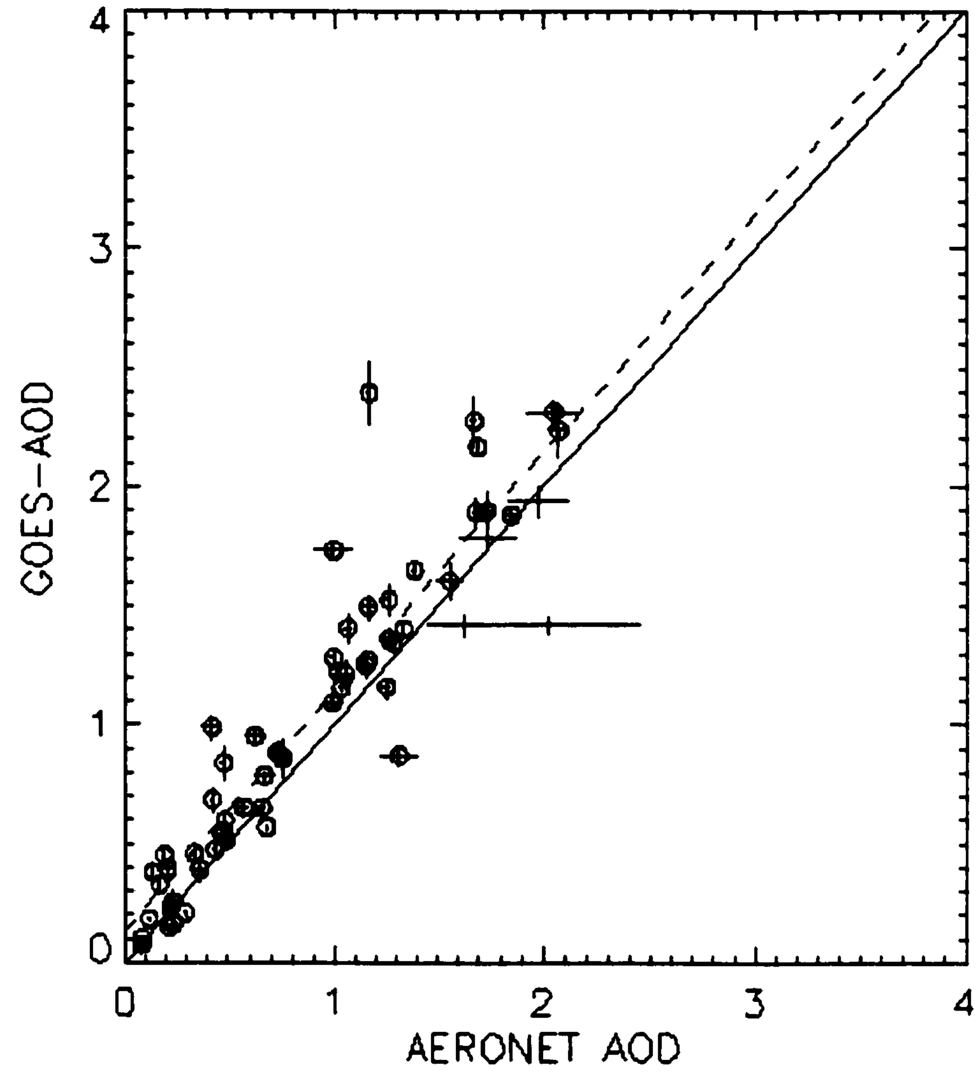

Figure 9.3 – GOES-AOD vs. AERONET AOD at Cuiaba. Solid line is the one-to-one line and the dashed line is the linear regression with the equation: $\tau_G = 1.00\tau_A + 0.13$.

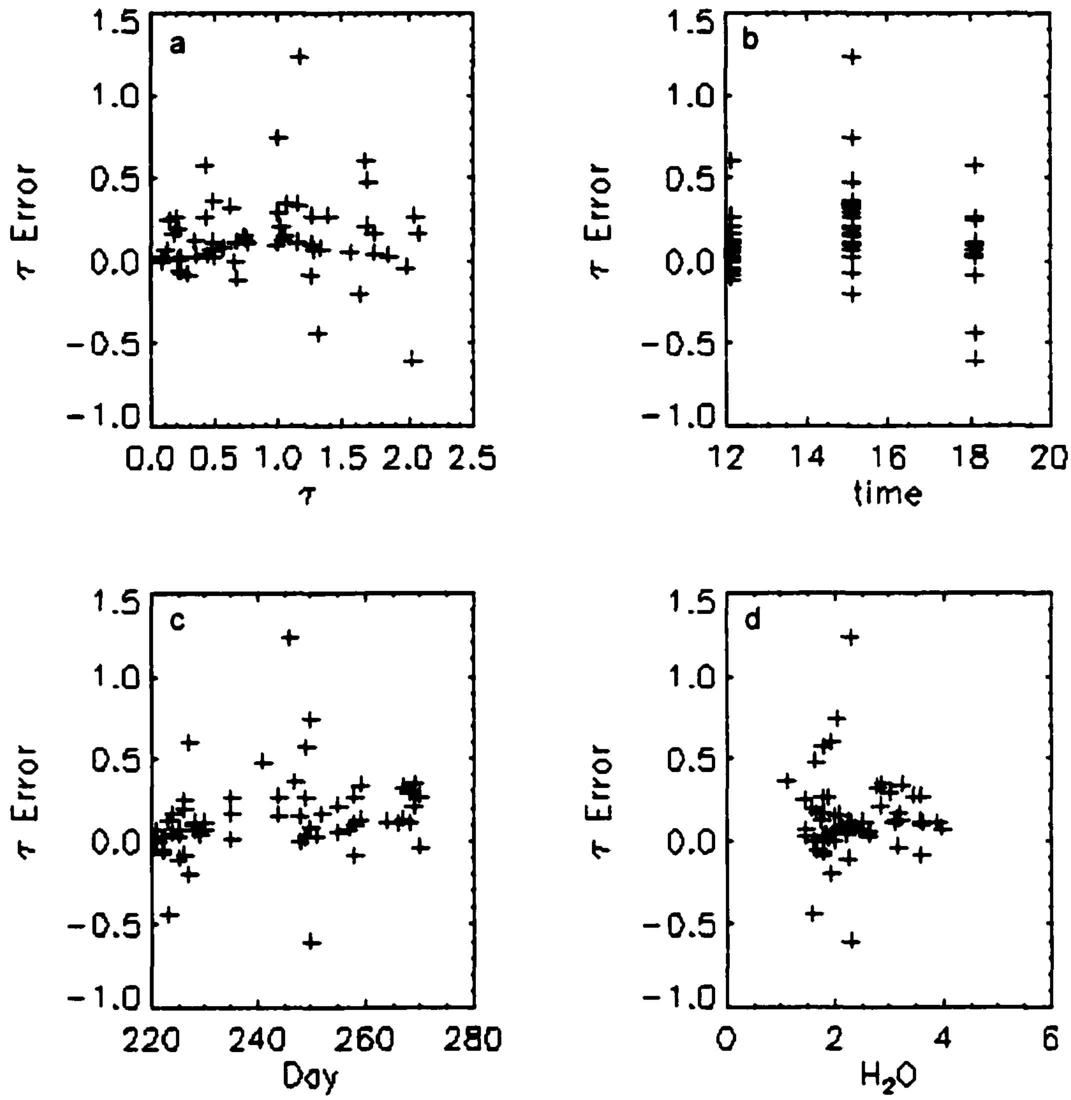

Figure 9.4 – τ_r at Cuiaba vs. various parameters: a) τ, b) time of day, c) day of year, and d) H_2O column water vapor.

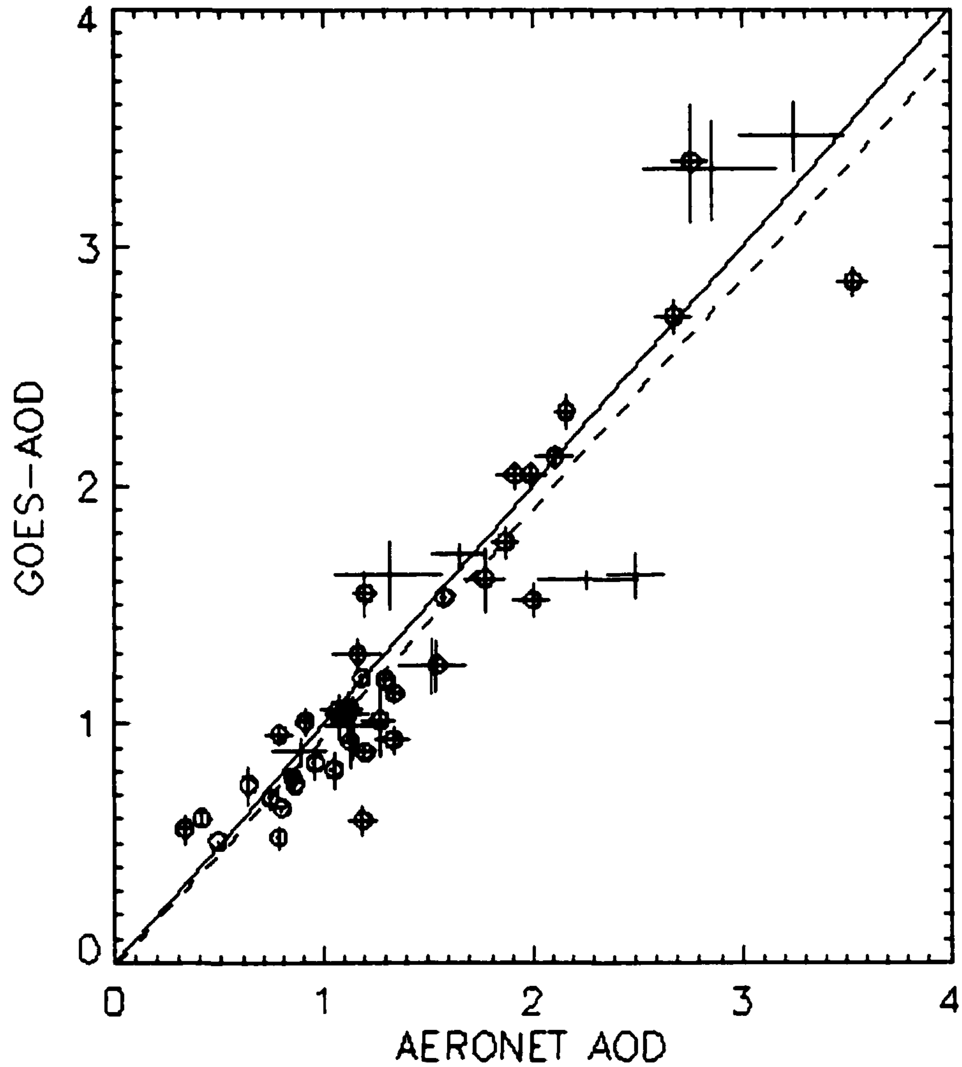

Figure 9.5 – Same as figure 9.3 except at Alta Floresta. The linear regression equation is $\tau_G = 0.96\tau_A - 0.02$.

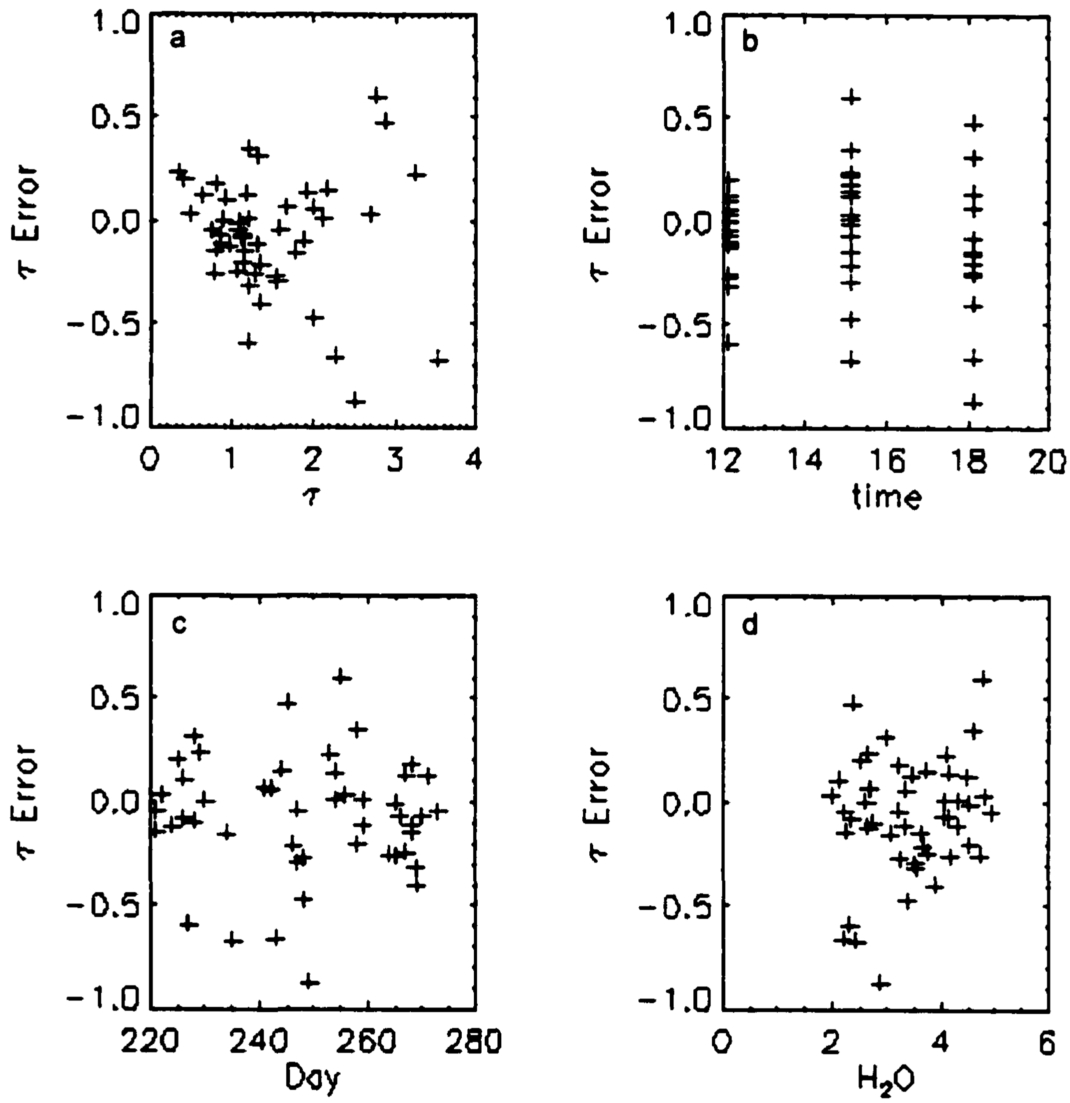

Figure 9.6 – Same as figure 9.4 except at Alta Floresta.

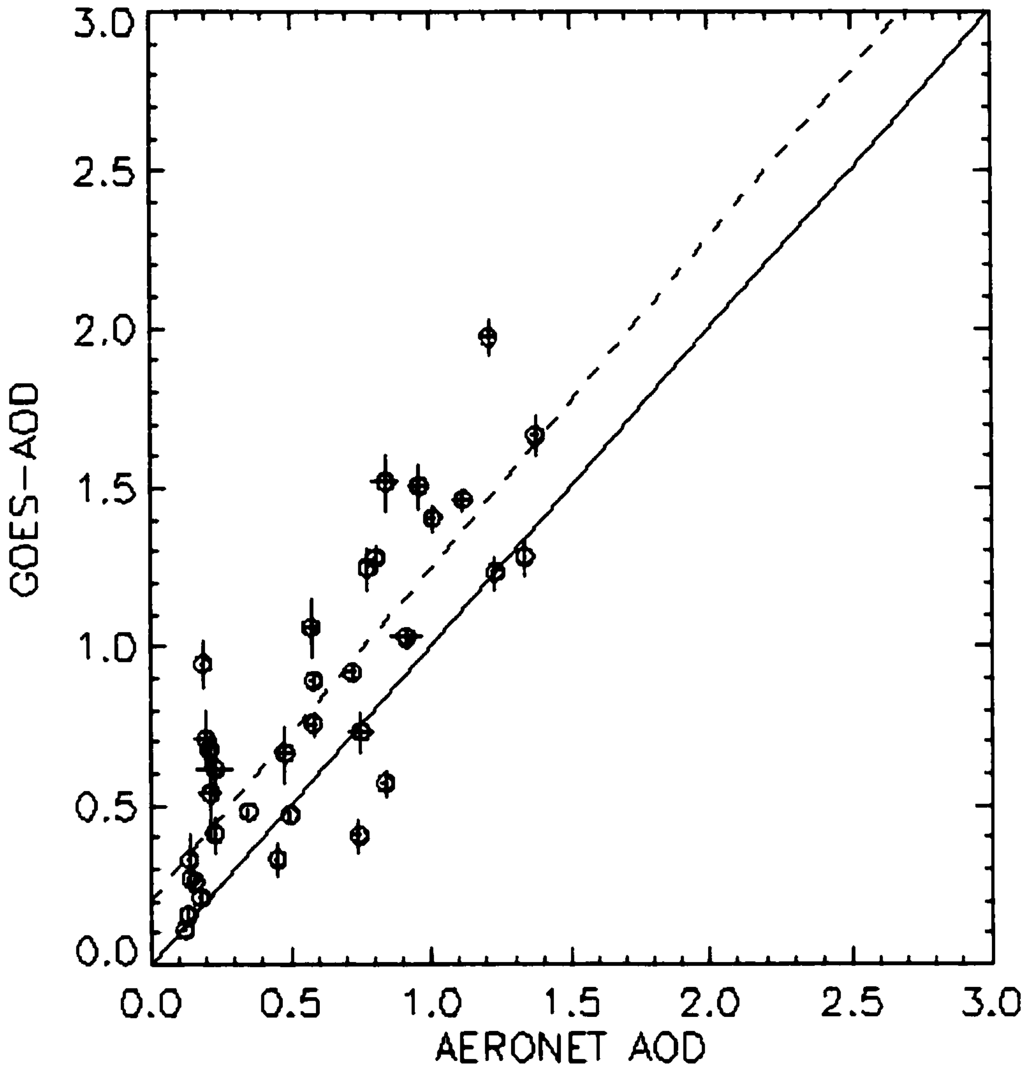

Figure 9.7 –Same as figure 9.3 except at Campo Grande. The linear regression equation is $\tau_G = 1.04\tau_A + 0.20$.

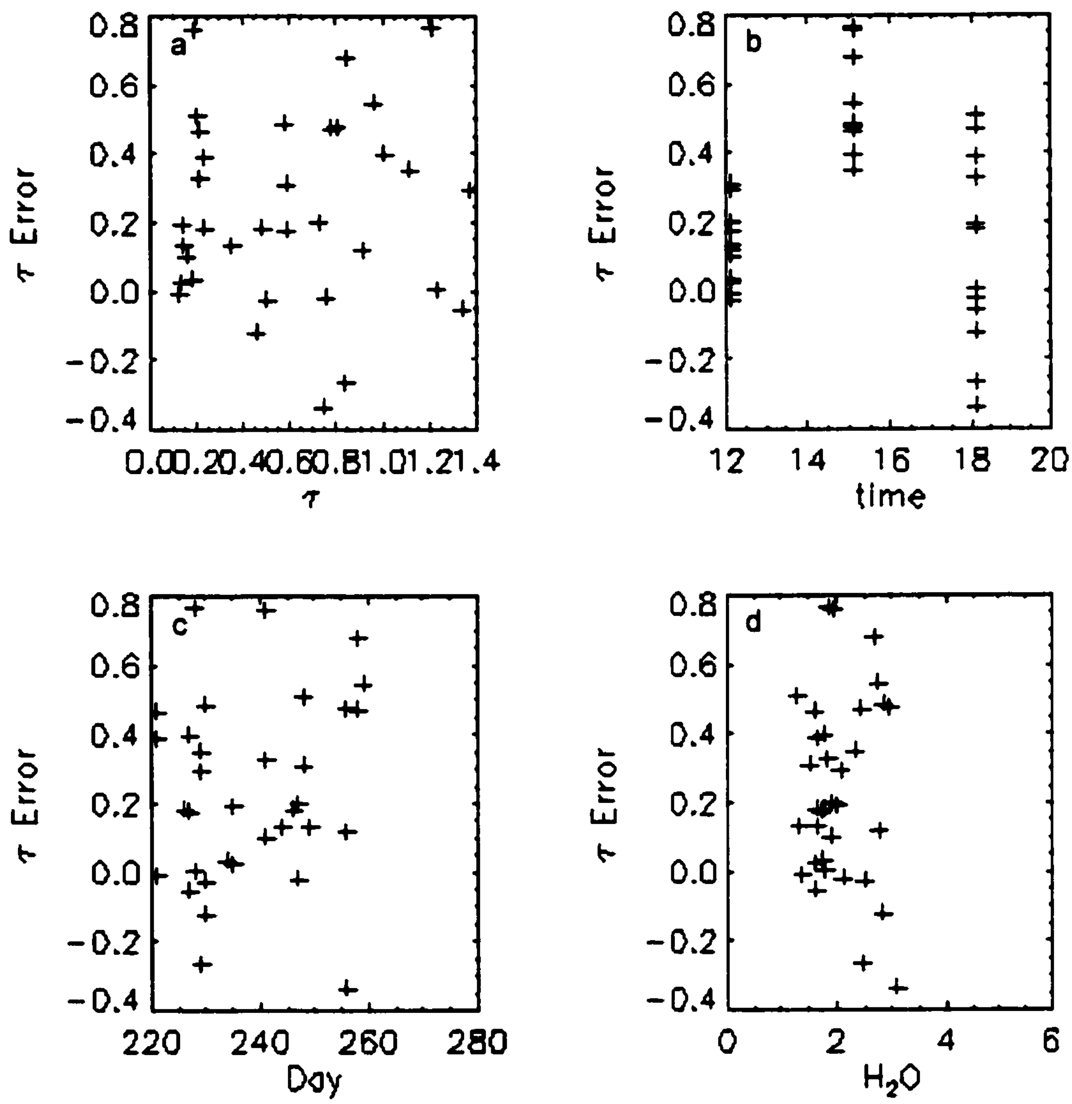

Figure 9.8 – Same as figure 9.4 except at Campo Grande.

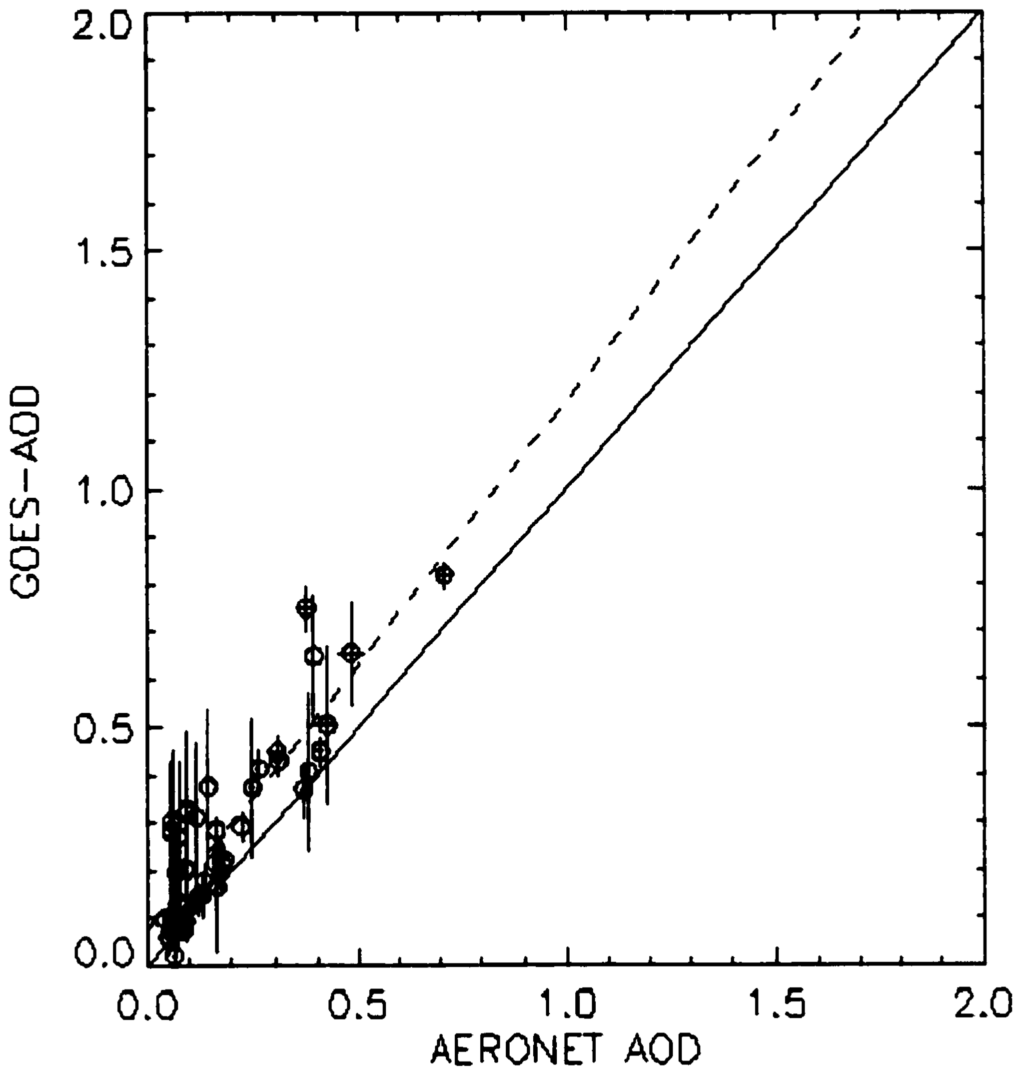

Figure 9.9 – Same as figure 9.3 except at Brasilia. The linear regression equation is $\tau_G = 1.11\tau_A + 0.08$.

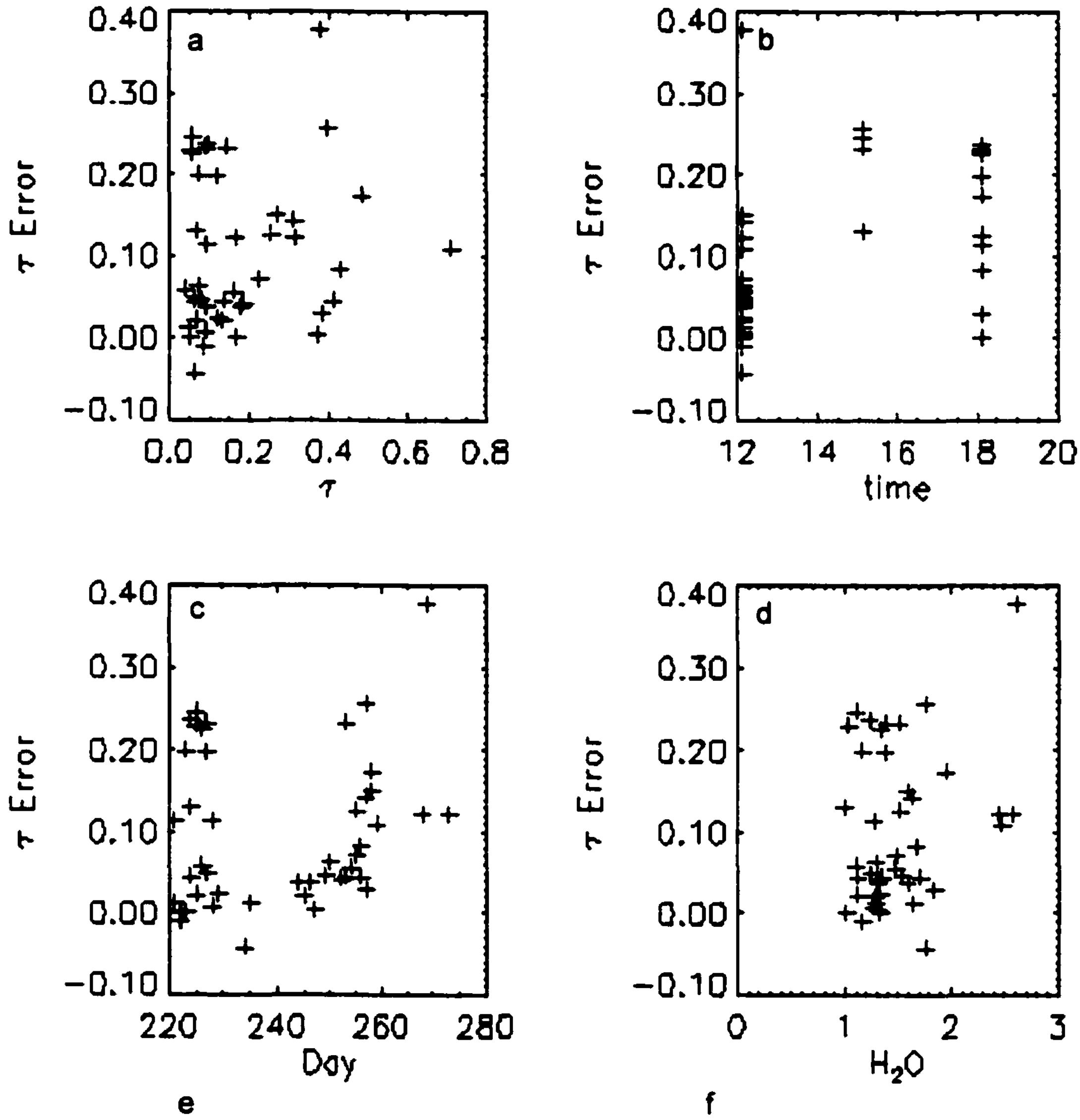

Figure 9.10 – Same as figure 9.4 except at Brasilia.

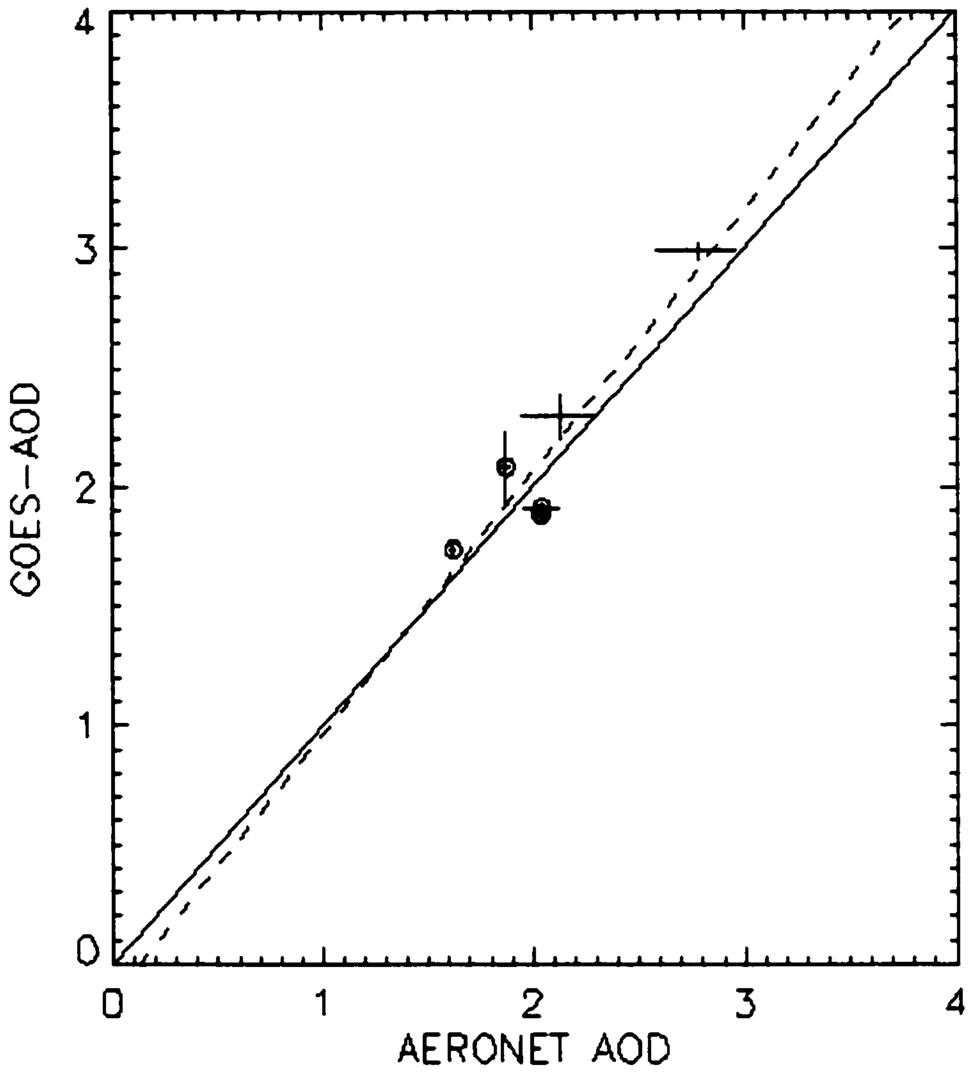

Figure 9.11 – Same as figure 9.3 except at Potosi Mine. The linear regression equation is $\tau_G = 1.10\tau_A - 0.13$.

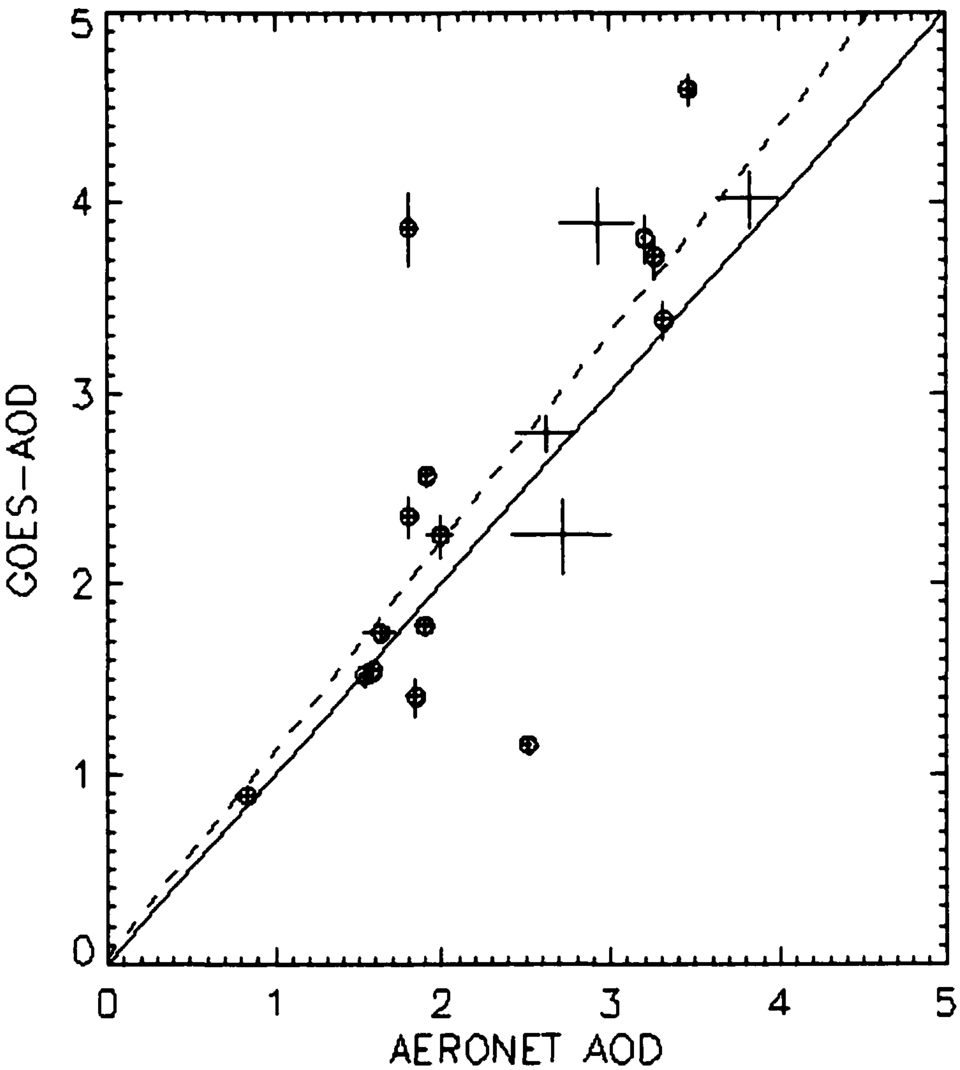

Figure 9.12 – Same as figure 9.3 except at Ji Parana. The linear regression equation is τ_G = 1.10 + 0.04.

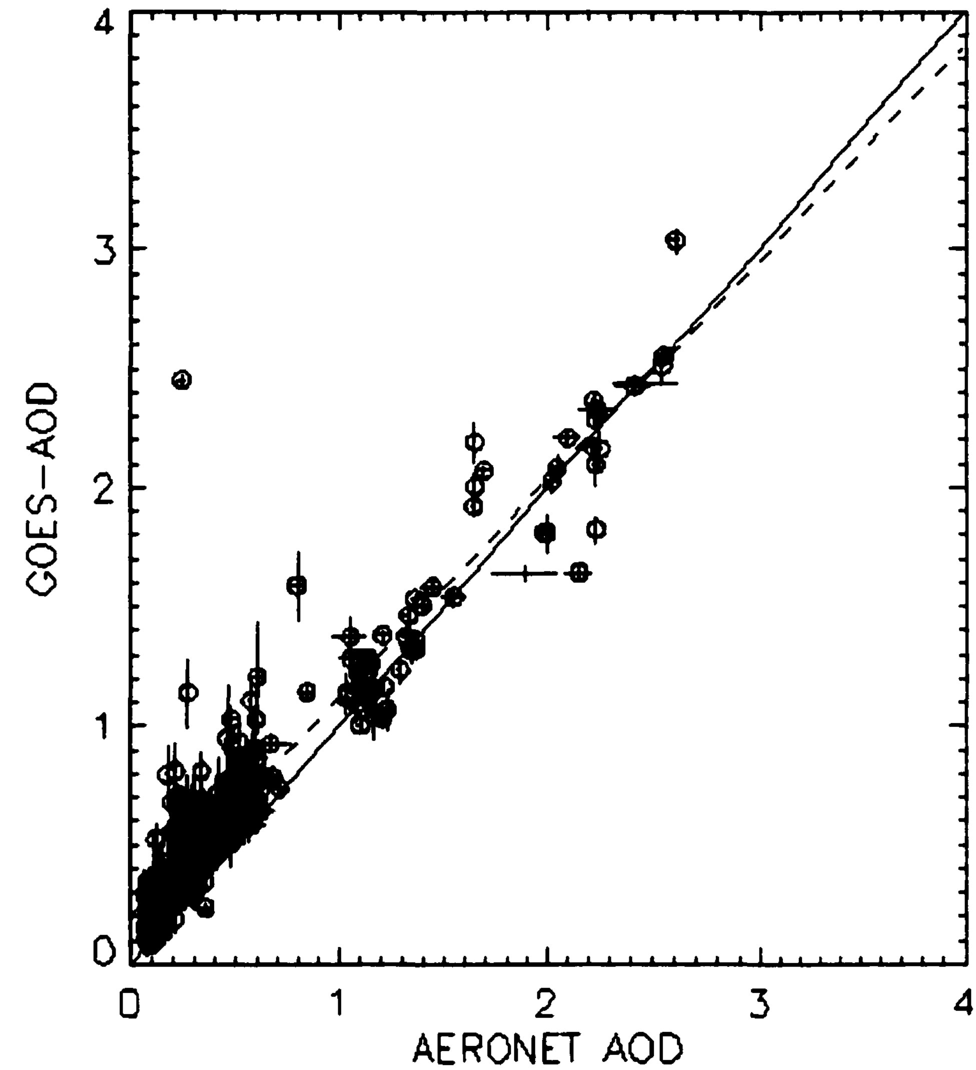

Figure 9.13 – Same as figure 9.3 except at Concepcion. The linear regression equation is τ_G = 0.92τ_A +0.2.

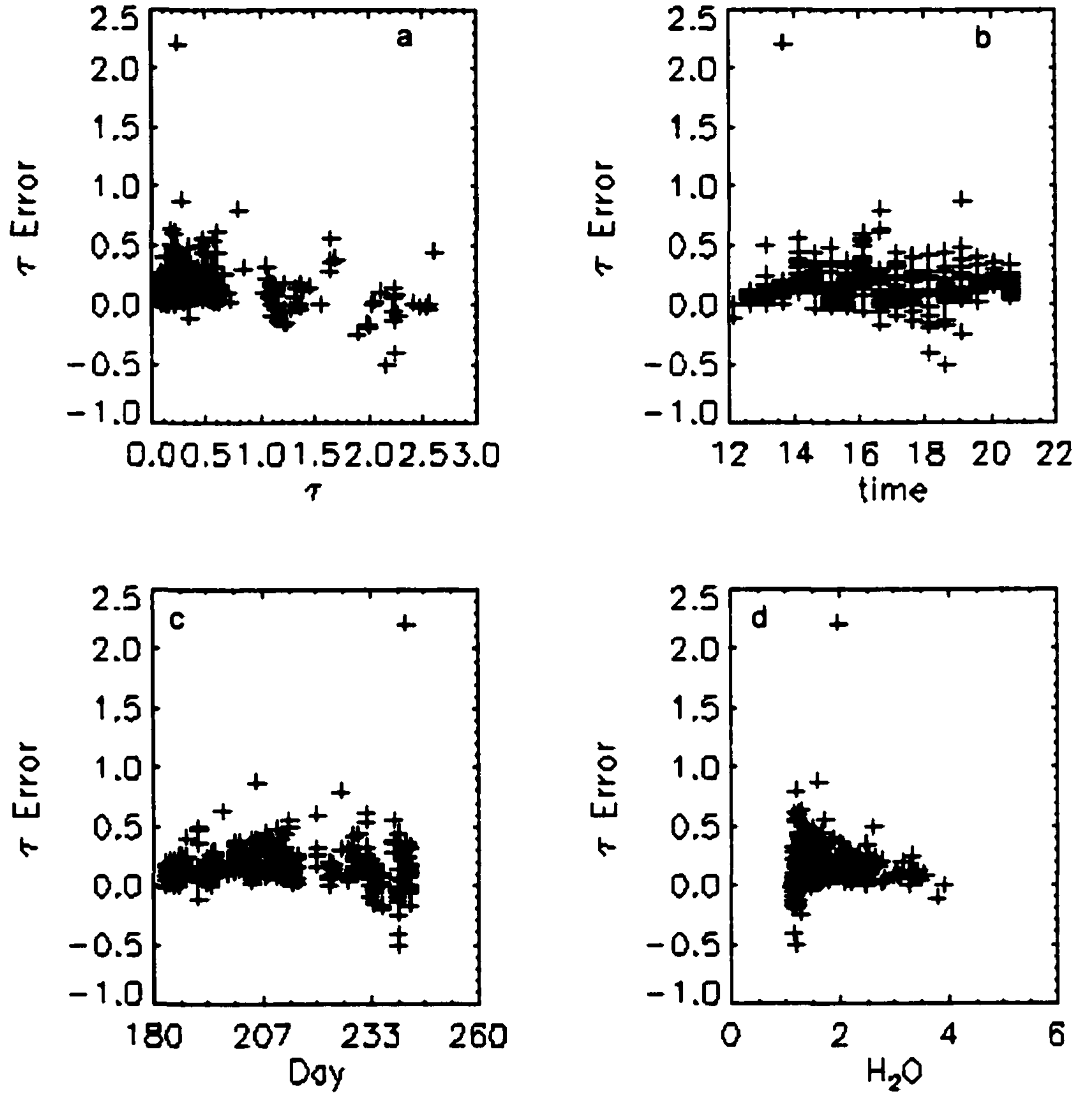

Figure 9.14 – Same as figure 9.4 except at Concepcion.

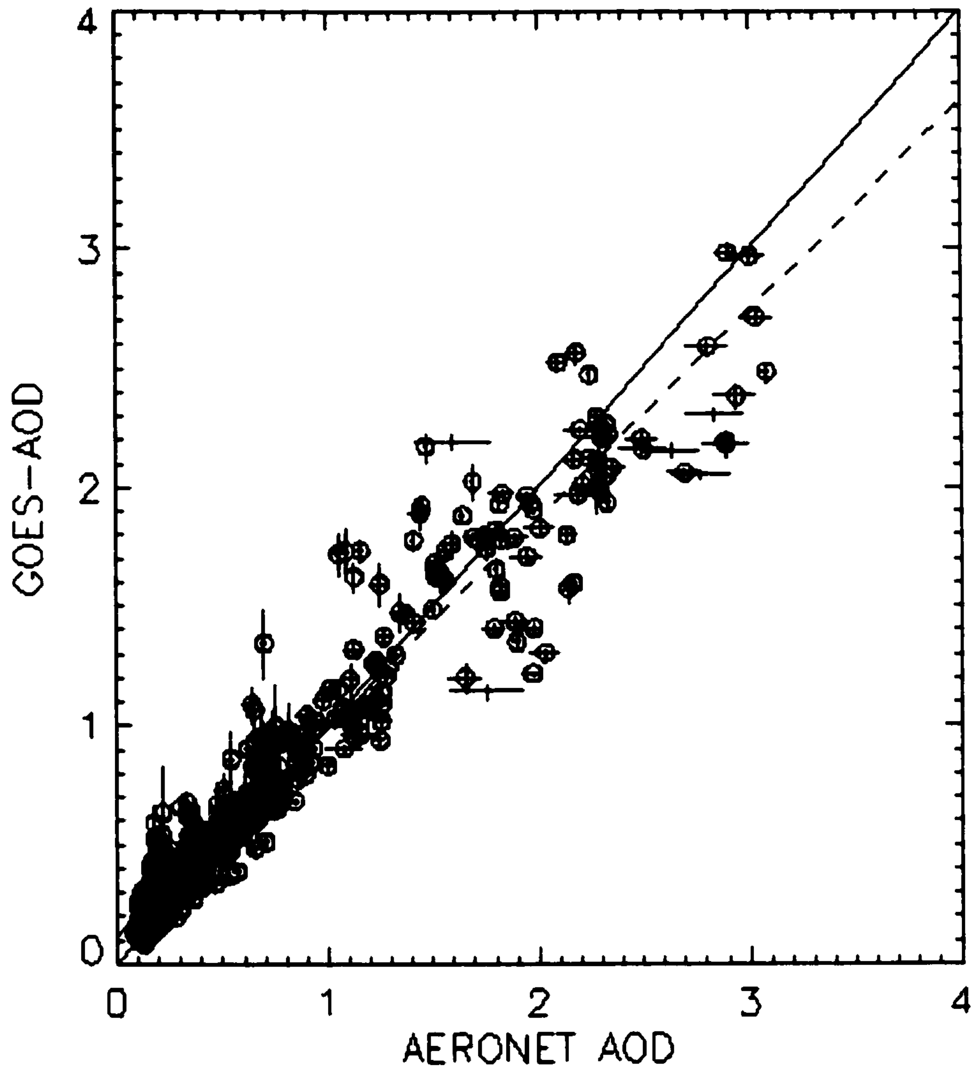

Figure 9.15 – Same as figure 9.3 except at Los Fieros. The linear regression equation is $\tau_G = 0.88\tau_A + 0.11$.

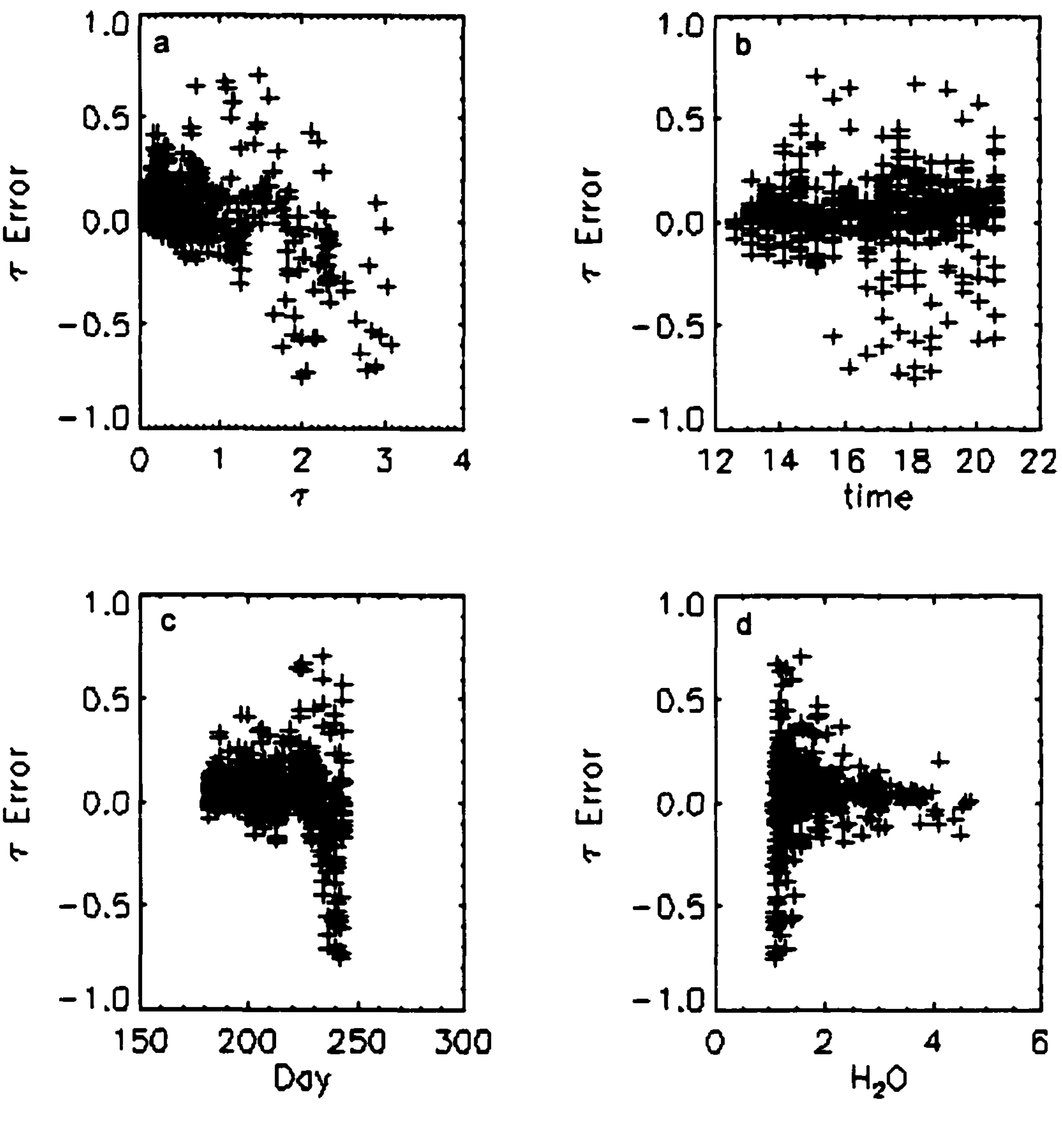

Figure 9.16 – Same as figure 9.4 except at Los Fieros site.

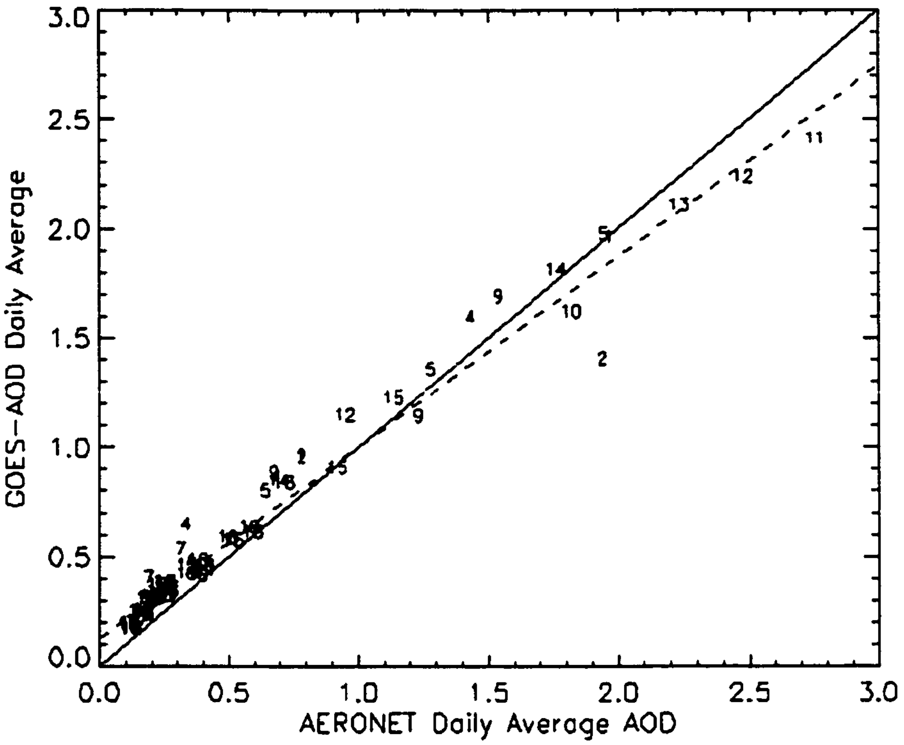

Figure 9.17 – Comparison of the Los Fieros daily-average GOES-AOD to the daily-average AERONET AOD at 500 nm for days when there were 4 or more GOES observations. The numbers represent the number of GOES observations that day. The solid line is the 1-1 line. The dashed line is the LR with the equation: $\tau_G = 0.87\tau_A + 0.13$.

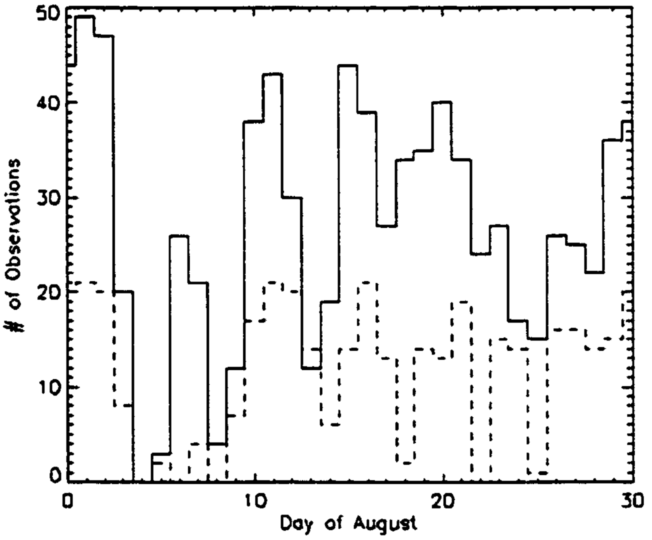

Figure 9.18 – The number of atmosphere observations for each day of August 1998 made by the AERONET photometer (solid) and GOES-8 (dashed).

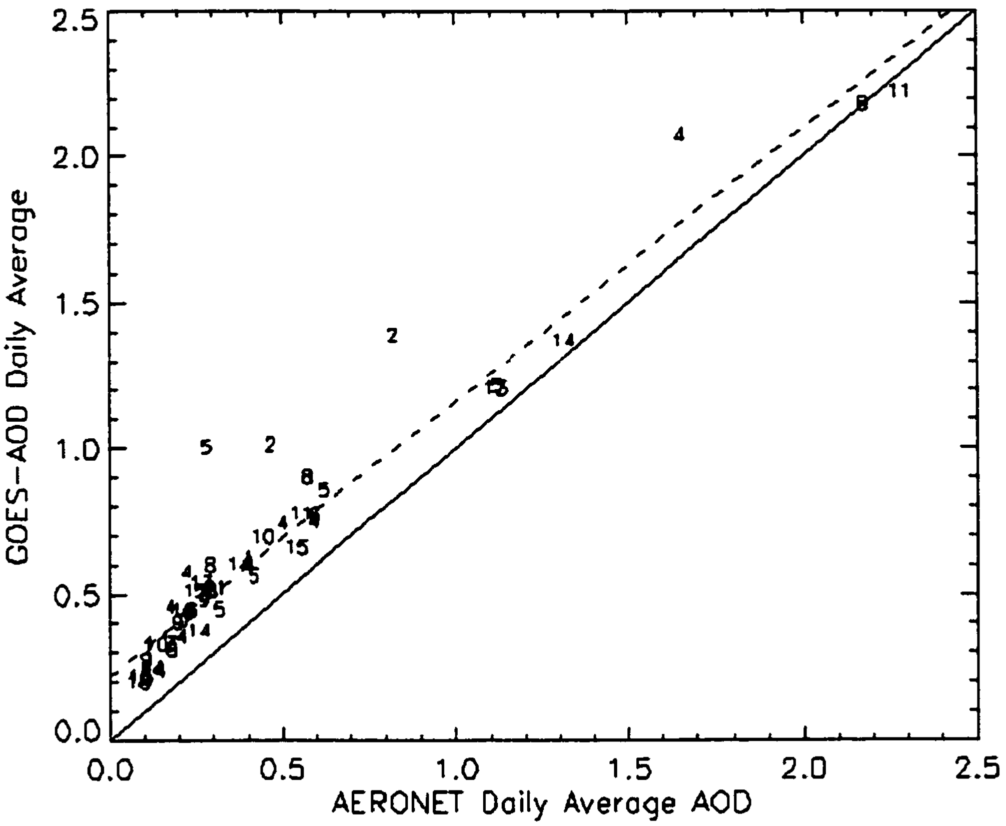

Figure 9.19 – Same as figure 9.17 except for AERONET is the Concepcion site. The LR is $\tau_G = 0.94\tau_A - 0.22$.

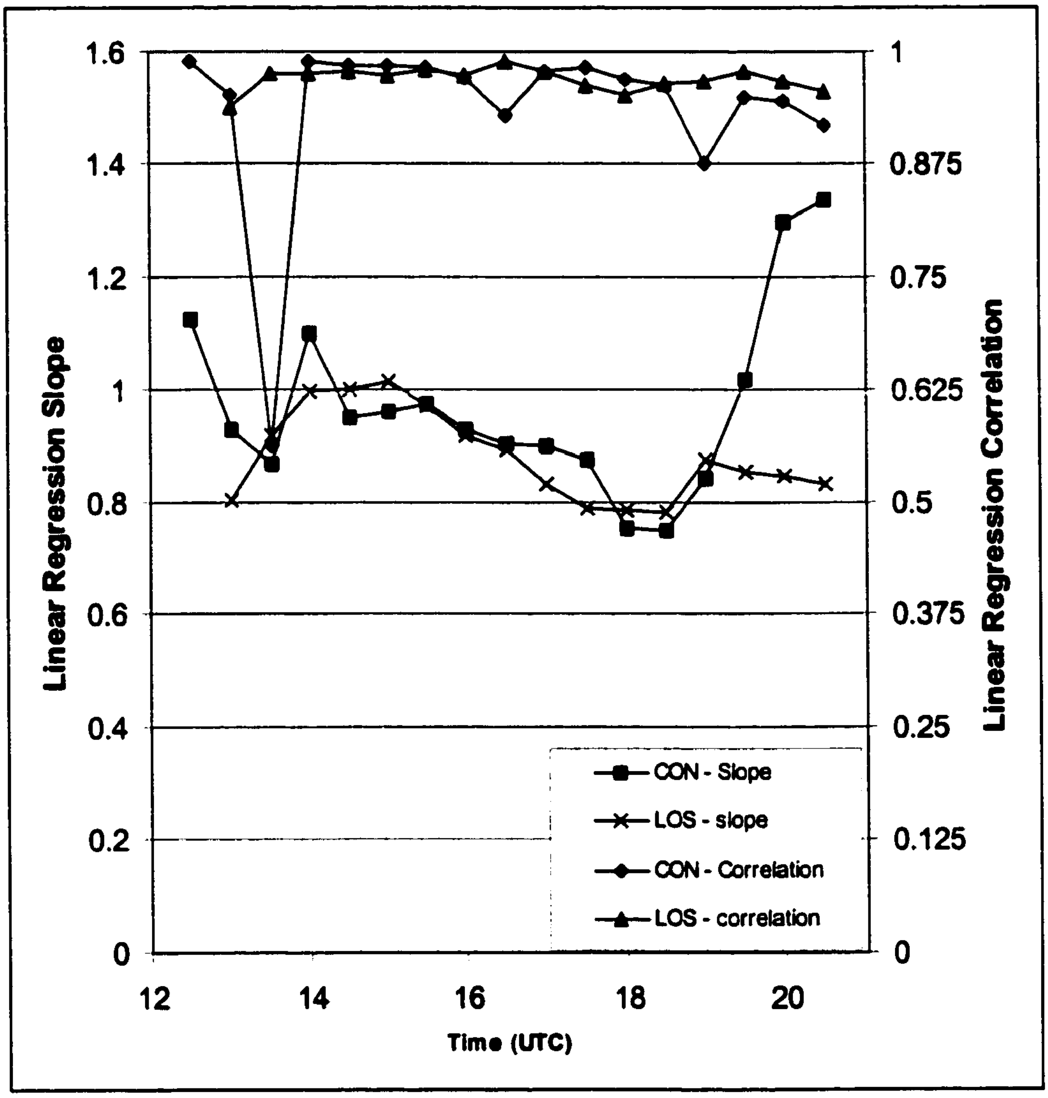

Figure 9.20 – Correlation and linear regression slope as a function of time for the 1998 comparisons: Concepcion and Los Fieros.

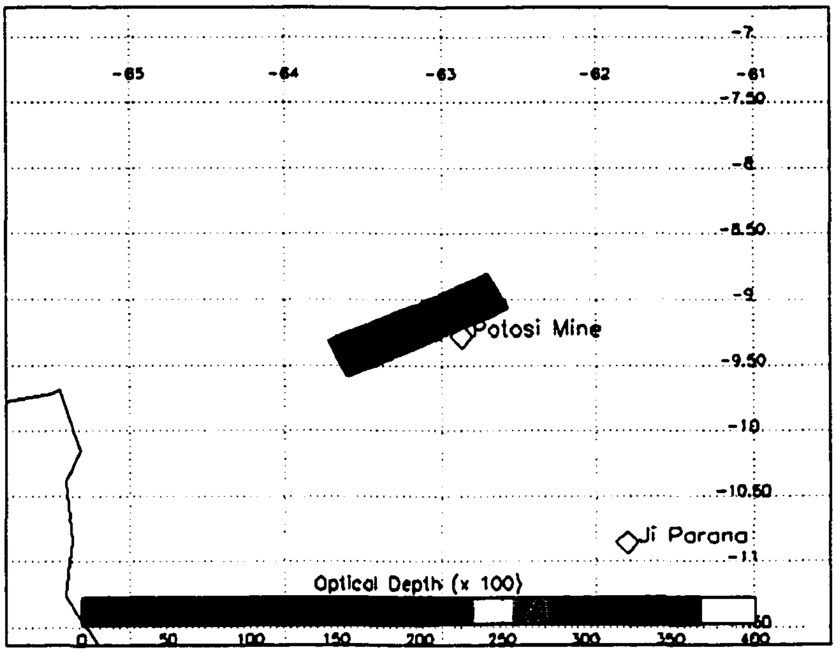

Figure 9.21 – MODIS-Land AOD from MAS flight # 12 on 4 September 1995.

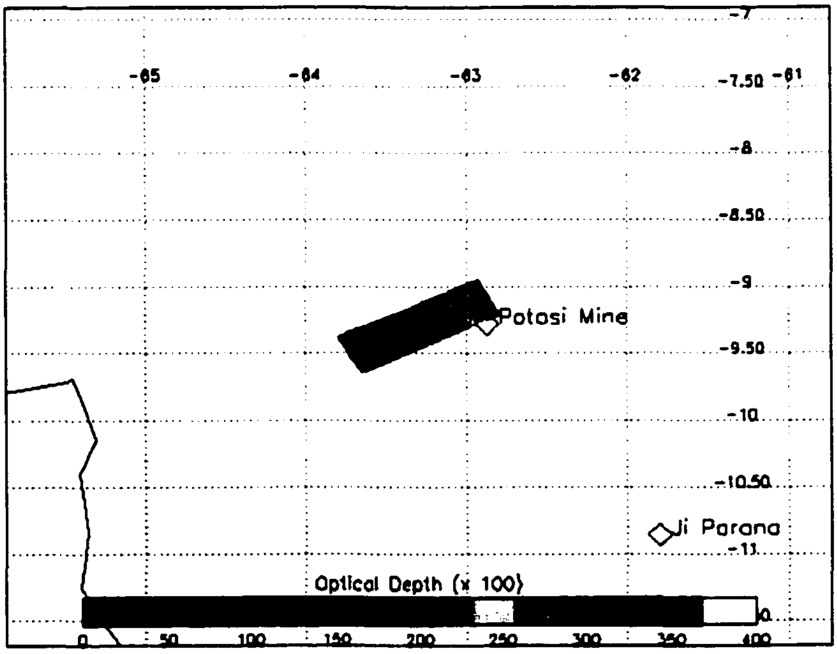

Figure 9.22 – MODIS-Land AOD from MAS flight # 13 on 4 September 1995.

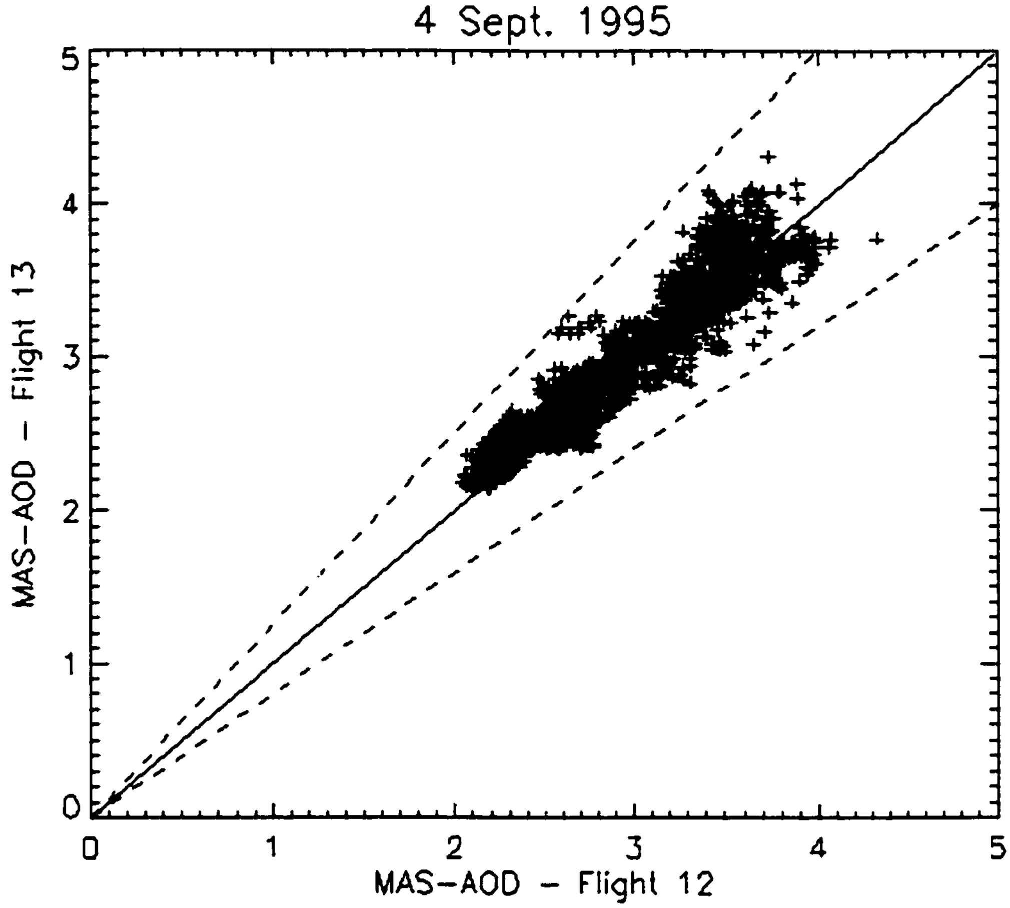

Figure 9.23 – Comparison of AOD retrieved from flight legs where MAS retraced its path over a smoke plume (difference in time during the two legs is no greater than 27 minutes). The dashed lines represent ±25%.

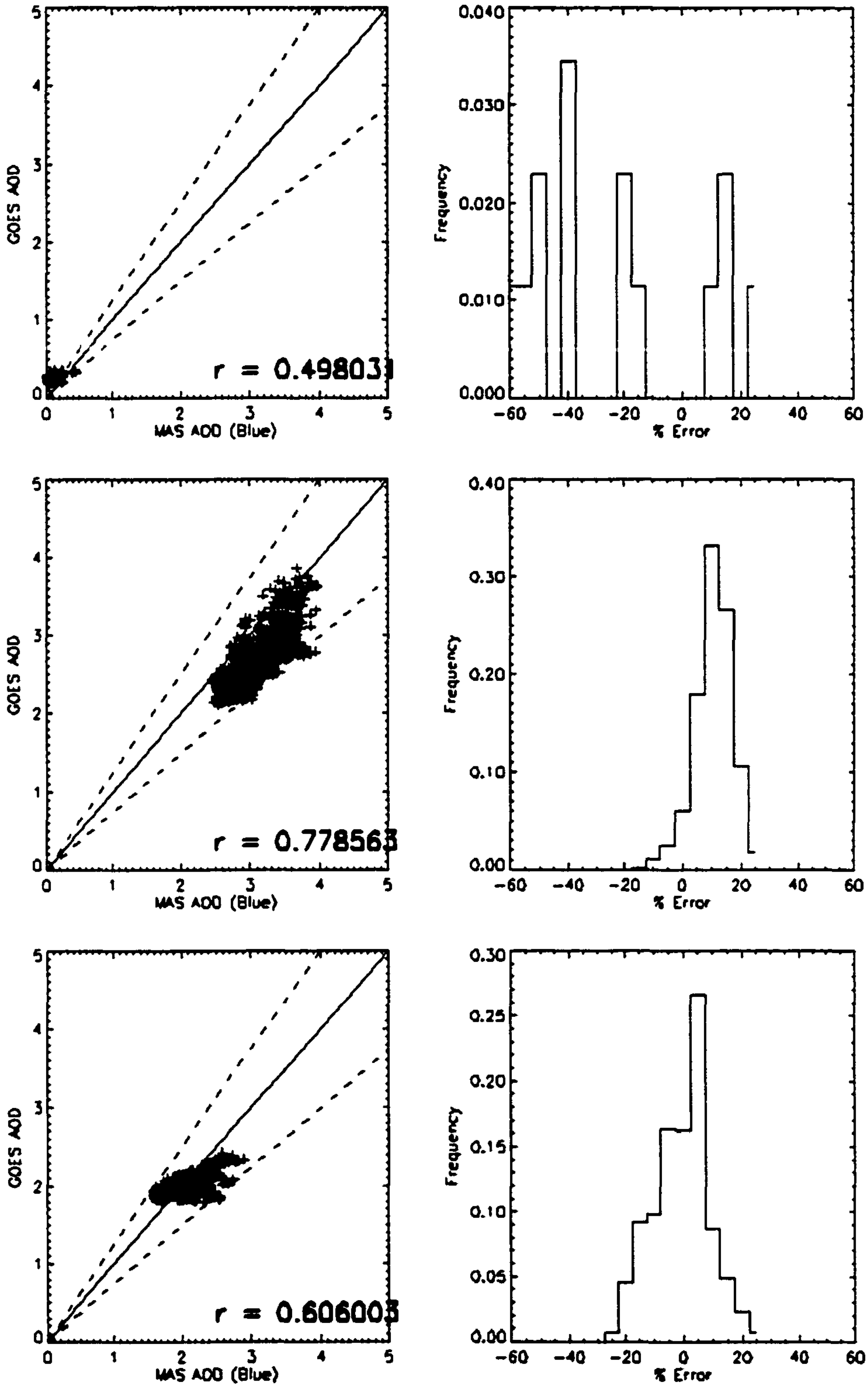

Figure 9.24 – Comparison of GOES-AOD and MAS-AOD with the PDF for comparisons 1-3. The solid line is the one-to-one line and the dashed lines are the ±25% lines.

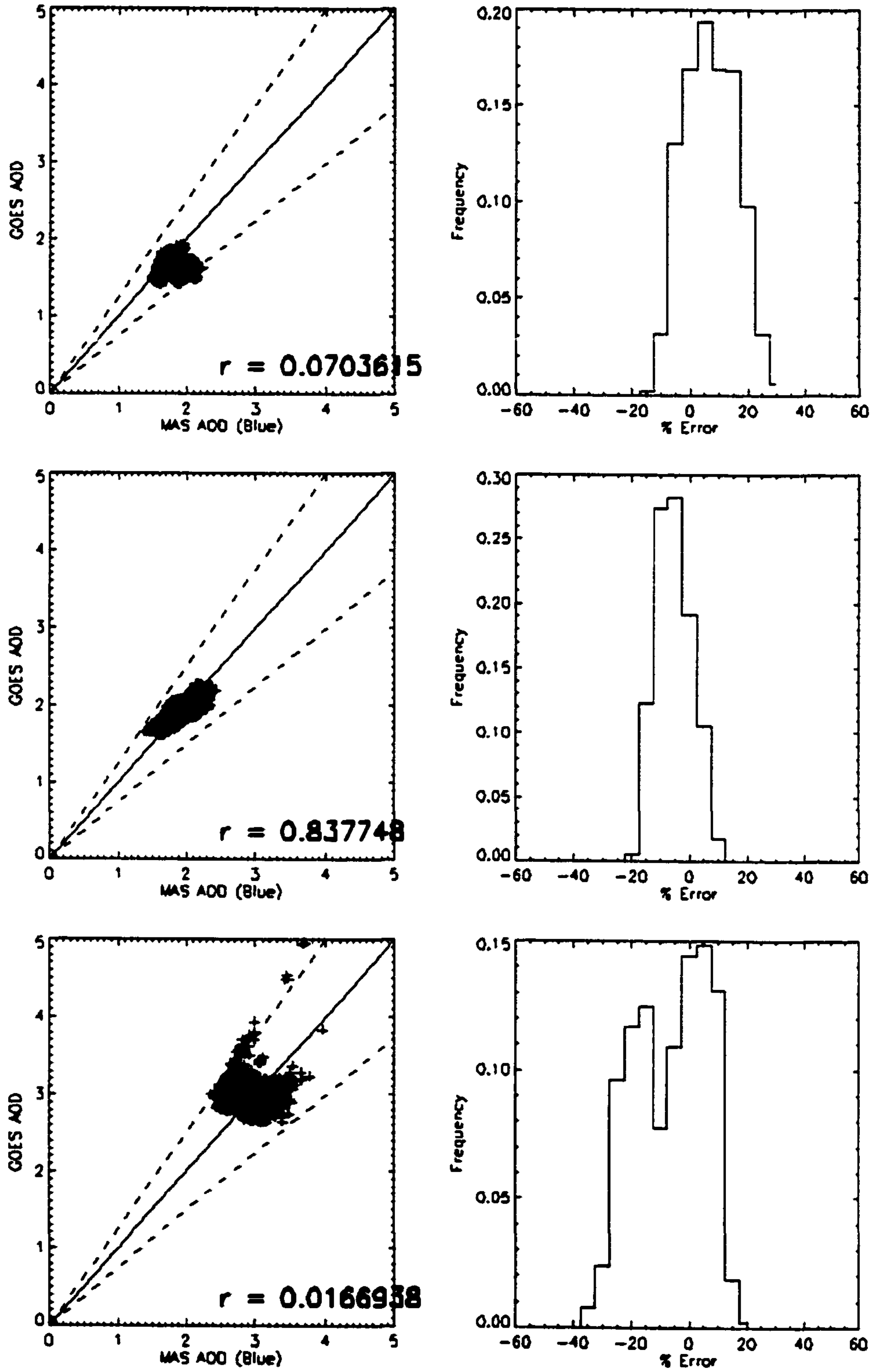

Figure 9.25 – Same as figure 9.24 except for comparisons 4-6.

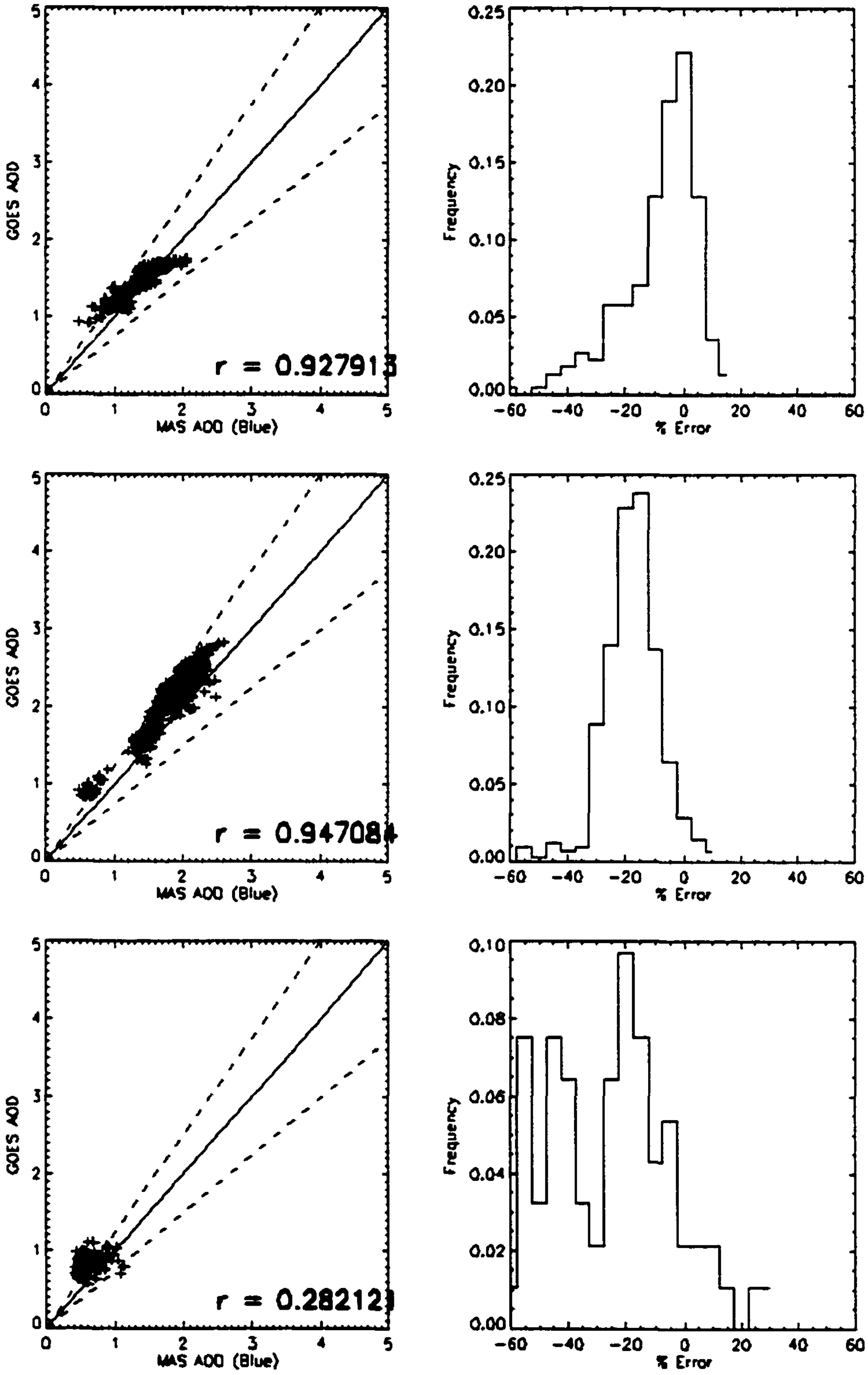

Figure 9.26 – Same as figure 9.24 except for comparisons 7-9.

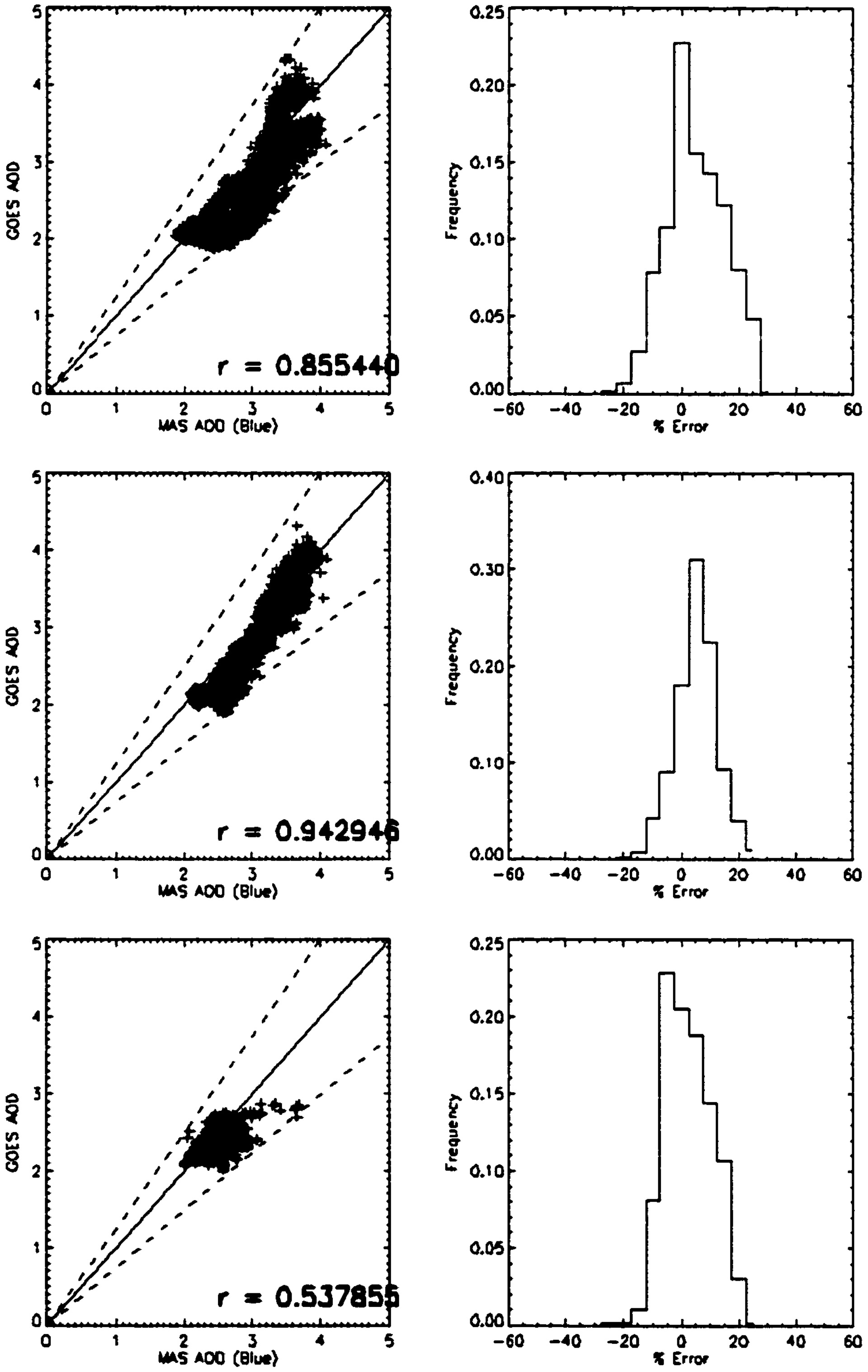

Figure 9.27 – Same as figure 9.24 except for comparison 10-12.

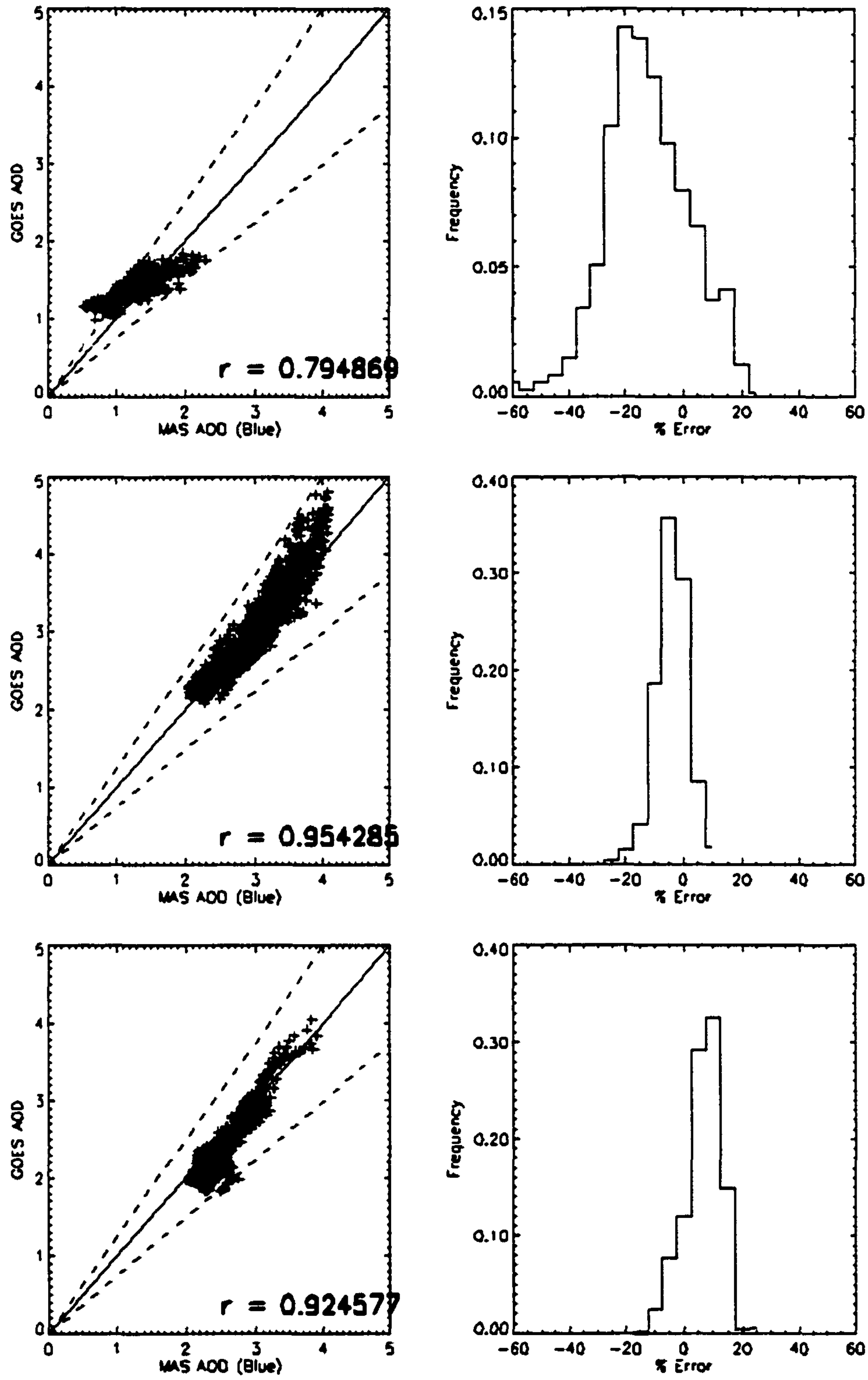

Figure 9.28 – Same as figure 9.24 except for comparison 13-15.

10. GOES-AOD and Aerosol Direct Radiative Forcing

The aerosol direct radiative effect is the increase of solar radiation scattered away from the Earth by atmospheric aerosols. Essentially, it is an increase in the local albedo of the atmosphere and reduces the available shortwave radiation at the ground. For instance, observations made in Africa show that on days with visibilities less than 10 km (and thus an atmosphere with a high aerosol optical depth), the daily maximum temperature was less on than days with less aerosol (e.g., Legrand et al., 1988).

This increase in the reflected radiance to space can be measured by satellite sensor. However, the spectrally wide response of ERBE, CERES and other broadband sensors allows the estimation of broadband fluxes, while other sensors (e.g. AVHRR) have spectrally narrow responses. These instruments measure the radiant energy emitted (in the longwave) or reflected (in the shortwave) to space. These radiance measurements are converted to irradiance estimates via angular dependence models (ADMs). ADMs have been developed for many atmospheric states (clear ocean, clear land, partly cloudy ocean, overcast, etc.) from ERBE observations. The ADMs developed during ERBE were also used in the processing of the CERES data to produce the ERBE-like dataset, used herein. Further data processing will make use of the scene identification of the co-located VIRS data.

Since the irradiance increase is directly related to the aerosol optical depth, it would seem that the shortwave aerosol radiative forcing (SWARF) could be inferred from the GOES-AOD estimates. This chapter describes the attempt to correlate GOES-AOD with shortwave (SW) fluxes estimated from CERES. The CERES instrument and dataset is described in the following section, followed by the result of the comparisons.

The CERES data for longwave and shortwave fluxes are compared to the GOES-AOD to find possible correlations.

10.1 CERES Data

The Clouds and the Earth's Radiant Energy System (CERES) instrument was launched on the Tropical Rainfall Measuring Mission (TRMM) satellite in 1997. The instrument design and intent are fully described by Wielicki et al. (1996) and are summarized here. The instrument is designed after the ERBE scanner and its primary goal is to quantify the radiant energy leaving the Earth-atmosphere system. Radiances are measured for three spectral intervals: the "atmospheric window": 8-12 um, the shortwave: 0.2-5μm and the total radiance 0.2-100μm. The longwave radiance is calculated as the difference between the total and shortwave radiances. These radiances are converted to fluxes through angular-dependence models (ADMs). ADMs were developed for ERBE for a number of types of scenes. The initial data release for CERES is an "ERBE-like" product, which is used here for comparison to GOES-AOD.

An example of the scene identification (ID) is shown for 1 August 1998 over South America in Figure 10.1; the highly inclined orbit of the TRMM satellite is also evident. The CERES image covers a time span from 12:00 to 21:00 UTC. Scene ID numbers 0 through 4 are clear sky, 5 through 7 are partly cloudy, 8 through 10 are mostly cloudy and 11 is overcast. The GOES image at 17:45 UTC is also shown in figure 10.2. In general, the cloudy areas in the GOES-8 image compare well with the areas identified as partly cloudy or overcast by the CERES-algorithm.

As an aside, an area of deforestation can be seen in the GOES-8 image (circled in gray). The bright area north of the Bolivian border, with distinct lines showing burn areas extending into the forest, is also detectable in the CERES data. Figures 10.3 and 10.4 show the shortwave and longwave fluxes (respectively) calculated from the "ERBE-like" algorithm. (Note: The color scale has been reversed for the IR image so warmer colors represent less emitted radiation and vice-versa) The deforested area reflects more radiation in the shortwave image and is emitting more IR radiation in the longwave image. While this does not constitute any portion of the SWARF, it does show that biomass burning can affect the climate through land cover change in addition to the increase of atmospheric aerosols. These land cover changes affect the distribution of radiation, in this case turning a dark, cool forest to a warm, bright area.

10.2 Radiative Forcing from GOES AOD

Biomass burning in central South America primarily occurs during the dry season between July and October. The CERES satellite collected data from January 1997 through August 1998. The instrument was shutdown on 1 September 1998, in preparation for comparisons with instruments aboard the recently-launched Terra satellite. Thus, August 1998 provides the best measurements of biomass burning and the best chance for comparison with the GOES-AOD algorithm.

Four sectors were processed using the GOES-AOD algorithm. Sector 1 is over the Los Fieros and Concepcion validation sites. Sector 2 is located over the Alta Floresta site from the SCAR-B experiment. Sector 3 was chosen to the east of sector 2. Sector 4 has the same central location as sector 3, but twice the area coverage – each pixel represents a 2x2km area. Sectors 1,2 and 4 are used for comparison to the CERES data.

The CERES footprint is approximately 20×20km^2, thus requiring significant averaging of the GOES-AOD pixels which can include many clouds. Cloud detection for this comparison was estimated by calculating an optical depth signal-to-noise (SNR_τ) ratio over the 20×20km^2 domain of the GOES-AOD by:

$$SNR_\tau = \frac{\bar{\tau}}{\sigma_\tau} \qquad ()$$

where $\bar{\tau}$ is the spatial average of optical depth and σ_τ is the standard deviation over the averaging domain. σ_τ and $\bar{\tau}$ for 20×20km^2 areas on day 215 at 16:45 UTC are compared in figure 10.5 (along with similar calculations from the GOES-8 Imager counts, DN). The images resemble the arches described by Stephens (1994), which are used to delineate clouds over the ocean. The points of the arch represent a homogenous surface: aerosols at low $\bar{\tau}$ and cloud for large $\bar{\tau}$. The arch itself represents the transition from clear skies to partly cloudy (large σ_τ and increasing $\bar{\tau}$) to overcast skies (low σ_τ and large $\bar{\tau}$). The points of the arch for the DN are broader due to the surface effects, which are removed in the GOES-AOD retrieval algorithm. The problem of cloud filtering is in drawing the delineation between cloudy and aerosol in this seemingly continuous set of data. It is hypothesized that clouds decrease the SNR_τ value by increasing the σ_τ, thus only the largest SNR_τ values are compared to the CERES data. Further, $\bar{\tau}$ > 4. are excluded from comparison, as AERONET measurements rarely were larger than 3 during the month. So $\bar{\tau}$ values with large SNR which are less than 4 and obtained within ±30 minutes of the CERES fly-by are compared to CERES calculated shortwave and longwave flux.

Tables 10.1, 10.2, and 10.3 show comparisons of GOES-AOD to CERES data for sectors 1, 2, and 4 (respectively). Days with less than 50 total comparison points are excluded. The number of comparisons can be quite large, and is largest for sector 4 due to its larger size. The τ_{min} and τ_{max} values represent the minimum and maximum τ values in each comparison; the amount of aerosol signal can be estimated from these values. That is, there are areas where the signal is low where τ_{min} is close to the assumed τ_b assumed in the GOES-AOD. Possible clouds are present in cases where τ_{max} approaches 5.

Figures 10.6 through 10.8 show scatter plots for a portion of these comparisons. Figure 10.6 shows comparisons having strong correlations with the SW fluxes and no correlation with LW fluxes. The aerosol direct effect is the increase in reflected SW radiation to space, with little affect on the LW radiation. However, other cases are apparent in the data. For instance, some days have no correlation with SW or LW fluxes (e.g., Figure 10.7). Also, Figure 10.8 shows examples where there is a strong correlation with the SW radiation and a strong anti-correlation with LW radiation. This effect was proposed by Christopher et al. (submitted to *J. Geophys. Res.*) as a bias in the CERES data in using a clear-sky derived ADM modeling smoke fluxes. However in these comparisons, anti-correlation is the exception rather than the norm.

Correlation, herein, is defined by explaining 40% or more of the variance. The GOES-AOD is correlated to SW flux in 16 of 51 comparisons. These comparisons are too numerous to show, so only three days with correlation are shown (one for each site) in figure 10.6. Conversely, GOES-AOD is correlated to LW flux in only 2 of 51 comparisons (figure 10.8). One of the days has a significantly low number of points (figure 10.8a). The second day (figure 10.8b), however, has a high correlation. It is likely that on this day, sufficient sub-pixel clouds are affecting the SW reflectance as well as the LW emitted radiation.

Lack of correlation between the SW flux and the GOES-AOD is likely due to: 1) Co-location of the GOES-8 and CERES data is uncertain, significantly affecting areas of large spatial variations, or 2) Large variations in surface reflectance would cause different intercepts (SW flux where GOES-AOD is zero), which would also decrease correlation.

The correlation of SW flux with τ_r increases as the number of points in the comparison increases (figure 10.9). The general maximum correlations are around 0.8, but as the number increases, the frequency of poorly correlated values decreases. The slope also tends toward a value between 10 and 40 as the number of correlation points increase. The slope of 153 (sector 1 comparison 3), is due to a small range in τ_r, which had little aerosol signal.

10.3 Conclusions

The GOES-AOD retrieval seem to be positively correlated with SW fluxes, as estimated from the CERES instruments, This preliminary comparison, however, seems to be affected by cloud contamination and co-location errors. Nonetheless, the aerosol direct effect is evident.

Table 10.1 – Comparison of GOES-AOD with CERES data for Sector 1 (15 comparisons).

			SW		LW			
Day	Time (UTC)	n	r	slope	r	slope	τ_{min}	τ_{max}
1	17.75	3998	0.12	6.21	-0.17	-3.24	0.01	5.00
2	16.25	3266	0.46	153.02	0.16	11.97	0.07	0.73
3	16.75	4118	0.11	4.33	-0.10	-0.99	0.09	4.98
4	15.75	963	0.21	5.03	-0.22	-1.80	0.36	4.98
8	14.25	1658	-0.26	-3.87	-0.02	-0.08	0.13	4.99
10	13.25	1285	0.14	3.11	-0.29	-1.63	0.08	4.98
11	12.25	3202	0.77	40.41	0.43	10.09	0.08	1.49
12	12.25	3644	0.58	46.53	0.03	0.49	0.11	1.62
13	11.25	358	0.49	3.85	-0.11	-0.35	0.74	5.00
24	20.75	4405	0.35	20.18	-0.51	-17.32	0.50	2.62
25	19.25	792	0.04	0.51	0.16	1.46	1.28	4.99
27	18.75	1644	0.06	3.05	0.24	5.48	1.15	2.87
28	19.25	1836	0.62	38.15	-0.23	-7.40	0.46	2.75
29	17.75	5812	0.73	25.62	0.30	2.61	0.24	4.47
30	18.25	2042	0.68	72.83	-0.36	-13.02	0.18	2.01

Table 10.2 – Comparison of GOES-AOD with CERES data for Sector 2 (15 comparisons).

			SW		LW			
Day	Time (UTC)	n	r	slope	r	slope	τ_{min}	τ_{max}
1	17.75	786	0.20	2.56	-0.20	-1.39	0.08	4.77
2	16.25	269	0.59	45.82	0.05	0.60	0.08	1.83
3	16.75	219	0.31	4.66	0.02	0.09	0.09	4.77
4	15.25	415	0.83	58.79	-0.02	-0.25	0.10	1.83
6	14.75	718	0.77	46.56	0.25	5.27	0.23	1.28
8	13.75	2062	0.53	20.86	-0.51	-16.67	0.08	0.86
10	13.25	1490	0.79	39.70	0.15	2.40	0.08	1.24
11	11.75	190	0.53	9.60	0.14	0.59	0.08	3.48
12	12.25	692	0.14	8.26	-0.09	-1.22	0.22	1.40
13	11.25	680	0.44	14.61	0.25	4.87	0.10	1.04
24	18.75	92	0.09	2.02	0.28	1.81	0.24	4.69
25	19.25	305	0.77	8.90	-0.32	-2.15	1.40	5.00
27	18.25	100	0.59	18.83	-0.36	-4.68	1.47	2.69
28	17.25	1739	0.48	7.77	-0.11	-0.72	1.08	4.63
30	16.25	1758	0.77	14.73	-0.47	-5.55	0.60	4.99

Table 10.3 – Comparison of GOES-AOD with CERES data for Sector 4 (21 comparisons).

			SW		LW			
Day	Time (UTC)	n	r	slope	r	slope	τ_{min}	τ_{max}
1	17.75	3096	0.39	10.38	0.00	0.02	0.08	4.94
2	18.25	491	0.50	7.21	-0.37	-3.22	0.08	4.29
3	16.75	1721	0.63	13.04	-0.16	-0.72	0.12	5.00
4	15.75	475	0.56	9.11	-0.02	-0.08	0.19	4.99
6	14.75	1191	0.56	41.95	0.59	18.34	0.09	0.57
7	15.25	97	-0.50	-4.17	-0.73	-2.34	0.09	3.51
8	14.25	2050	0.36	10.18	-0.22	-3.50	0.10	2.24
10	13.25	3203	0.76	33.10	-0.19	-3.45	0.08	1.33
11	13.75	1396	0.73	90.48	-0.06	-1.64	0.08	0.89
12	12.25	5904	0.54	23.22	-0.19	-1.80	0.09	2.44
13	11.25	698	0.04	1.08	-0.18	-1.68	0.26	1.93
14	11.75	638	0.26	6.79	0.27	3.75	0.26	3.72
21	20.75	878	0.07	2.09	-0.33	-2.39	0.24	4.77
23	20.75	1931	0.44	14.00	0.42	7.84	0.08	4.44
24	19.25	66	-0.16	-3.22	-0.12	-0.94	0.21	4.88
25	19.25	2278	0.76	13.74	0.48	3.98	0.10	4.99
26	17.75	171	0.60	23.12	0.32	3.23	0.79	3.80
27	18.75	1082	0.87	21.19	-0.71	-5.89	0.46	4.22
28	17.25	1869	0.65	15.71	0.19	1.50	0.08	4.22
29	17.75	3026	0.68	25.42	-0.01	-0.06	0.67	4.75
30	16.75	4158	0.66	12.52	-0.33	-2.75	0.57	4.99

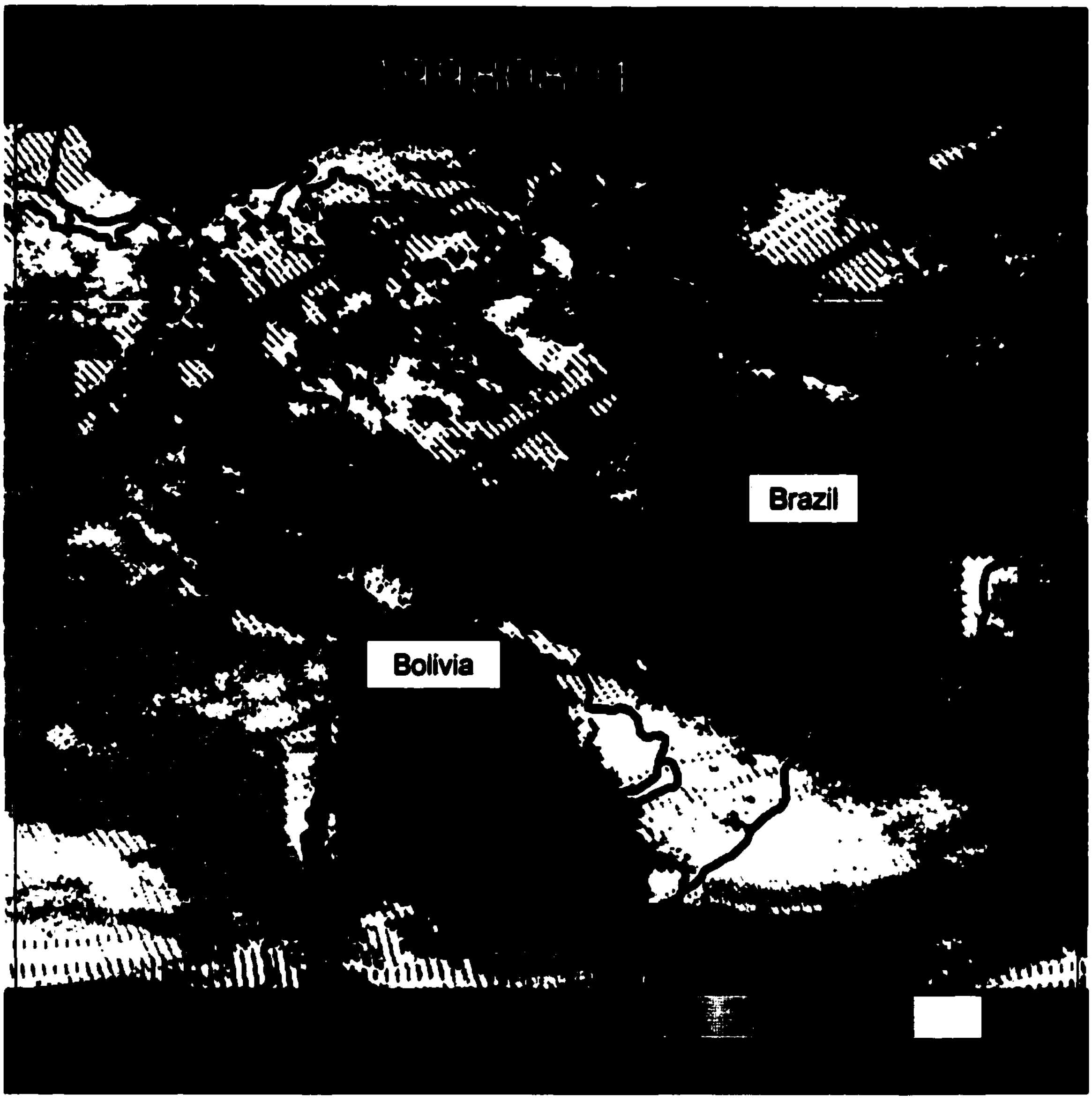

Figure 10.1 – Scene identification from TRMM/CERES for 1 August 1998 over South America. The CERES scans span the time range from 9:45 UTC (in the lower right corner) to 20:45 UTC (upper left corner). The orbit going through Bolivia is near 17:45 UTC.

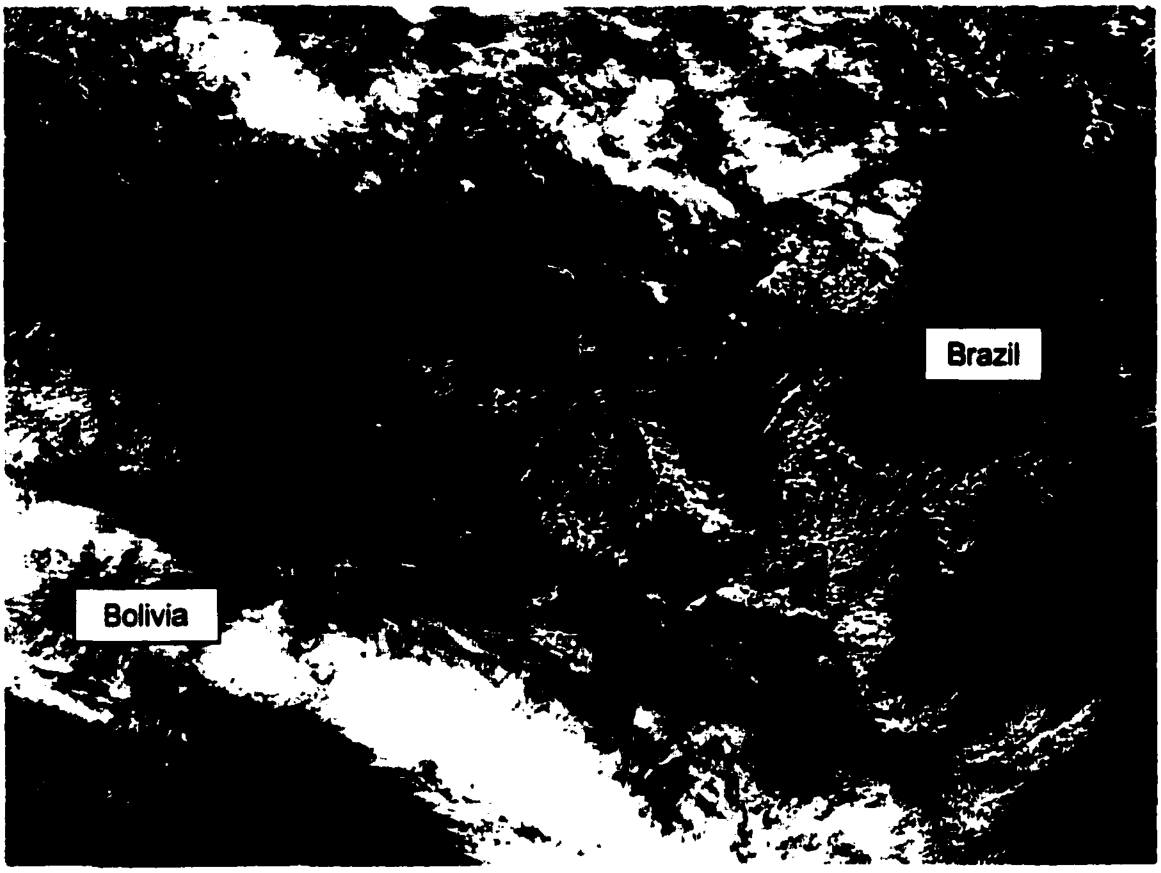

Figure 10.2 –GOES-8 visible image from 1 August 1998 at 17:45 UTC. Note area of forest clearing circled in gray (note: the image is displayed histogram equalized to enhance the surface features).

Figure 10.3 – "ERBE-like" Shortwave flux (W/m^2) calculated by CERES for 1 August 1998 (same data as the image in figure 10.1).

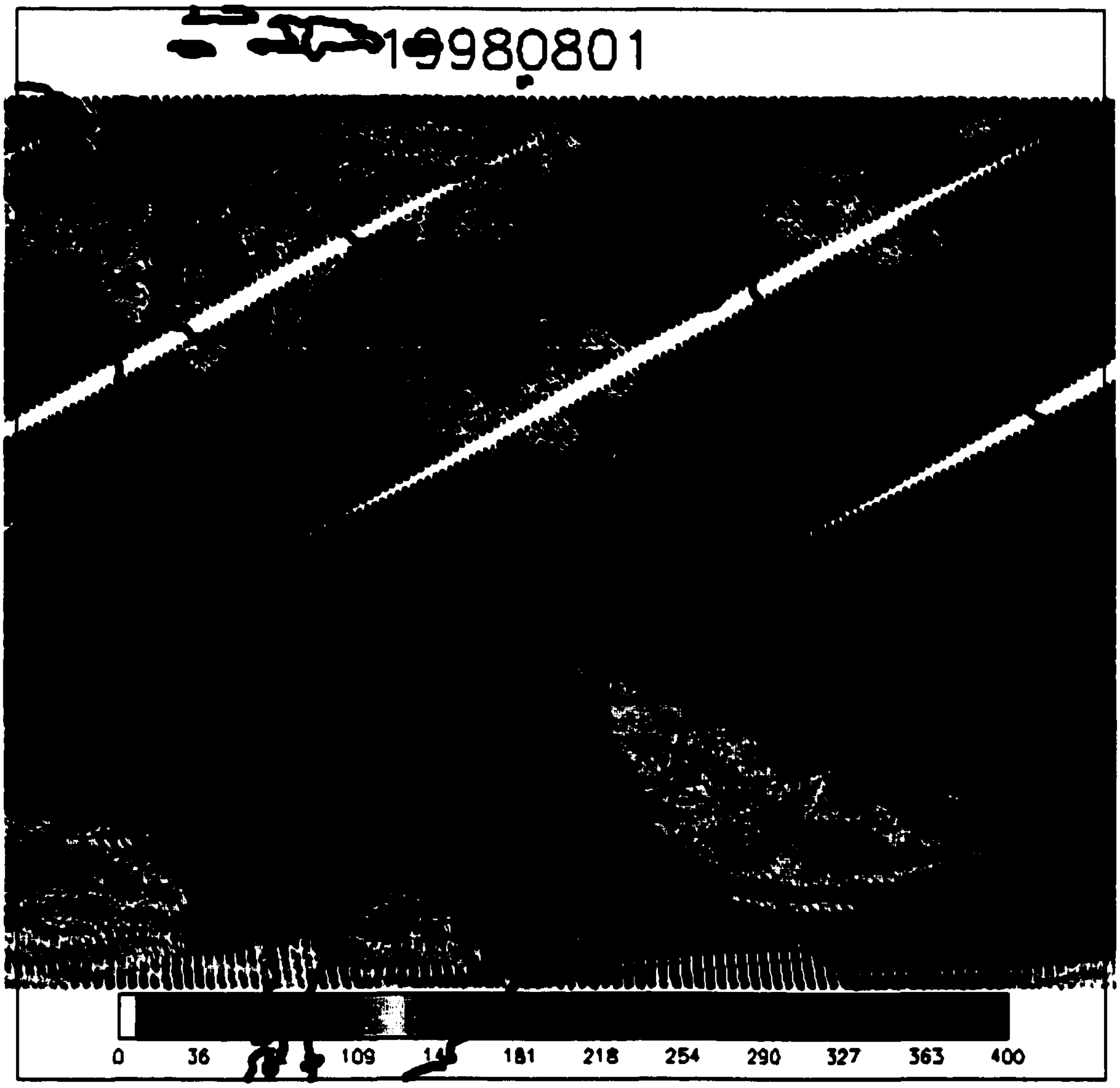

Figure 10.4 – "ERBE-like" Longwave flux (W/m^2) calculated by CERES for 1 August 1998 (same day as figure 10.1). Note: color table has been reversed for better comparison to figure 10.3.

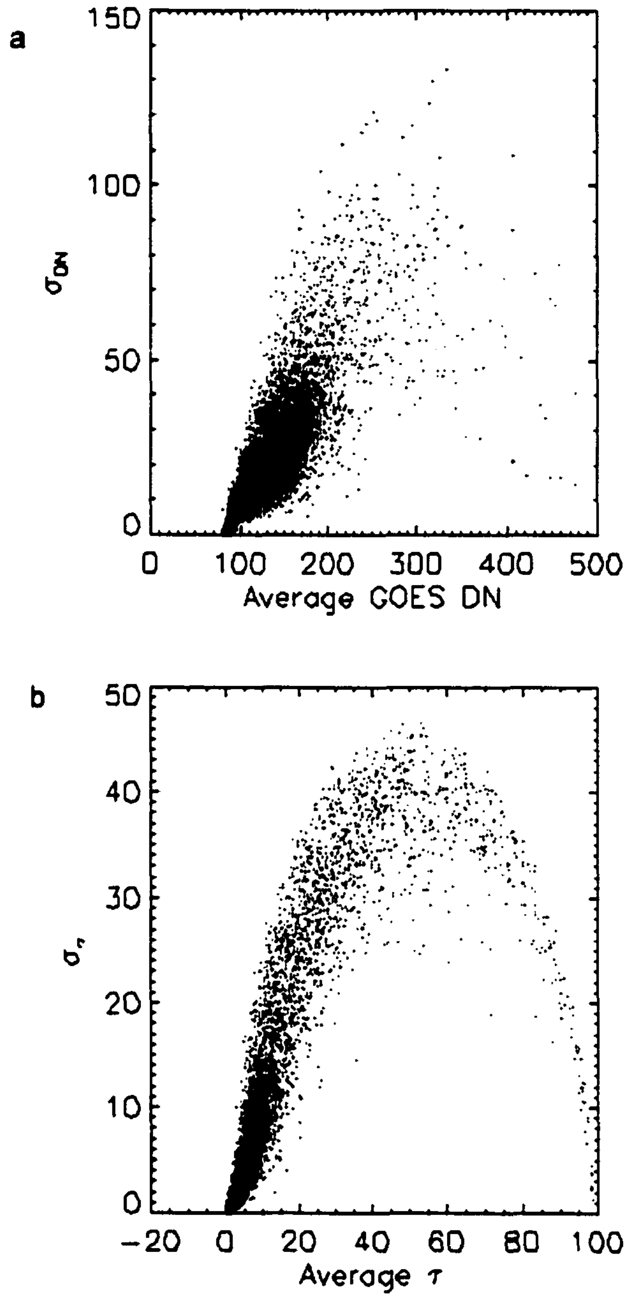

Figure 10.5 – Standard deviation of GOES-8 visible DN vs. average DN for a 20×20km^2 area for 16:45 UTC, 3 August 1998, b) same as a except using the GOES-AOD τ_r values.

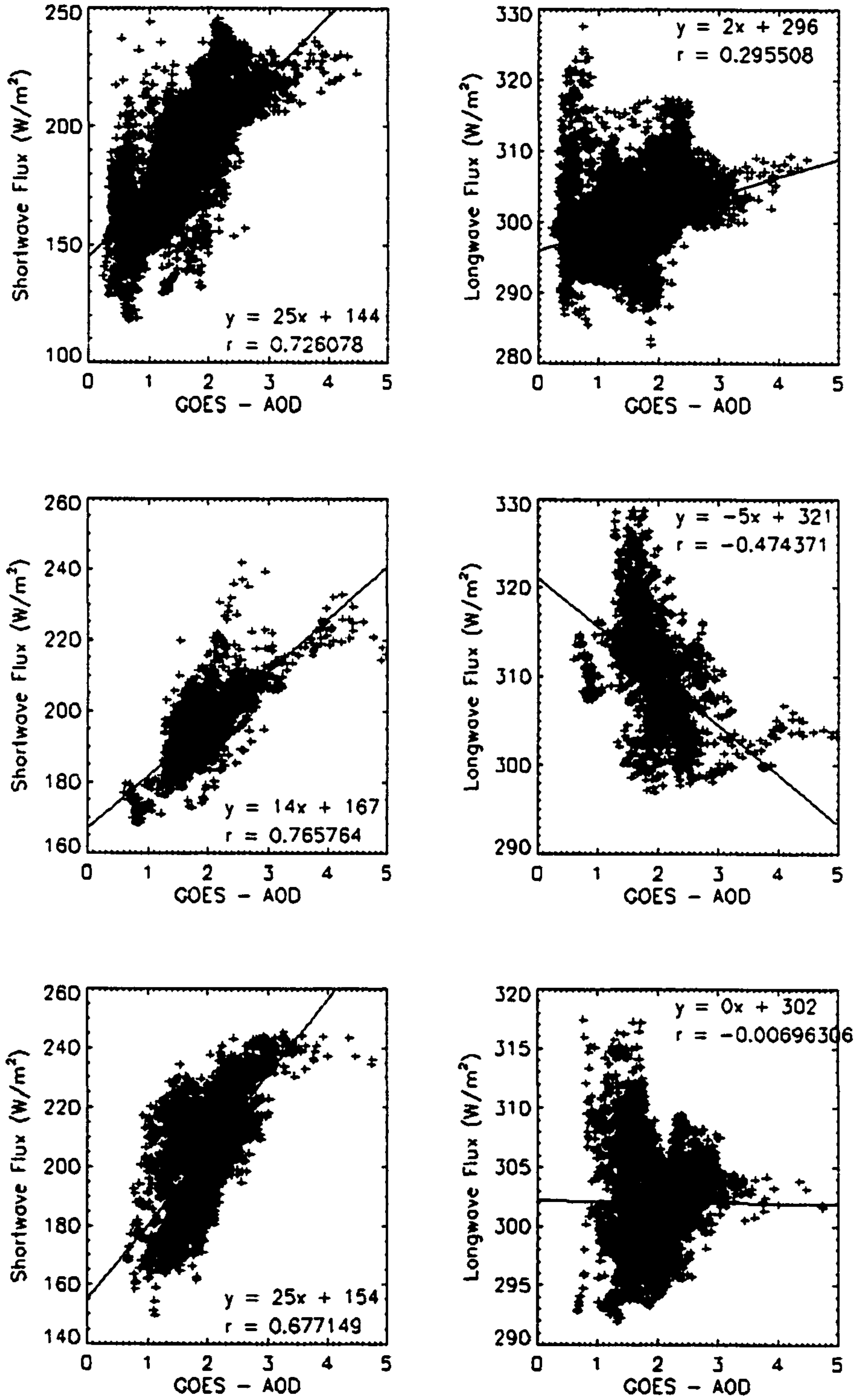

Figure 10.6 – Three CERES comparisons with good correlation to τ_r a) sector 1 – 29 August, b) sector 2 –30 August, c) sector 4 – 29 August

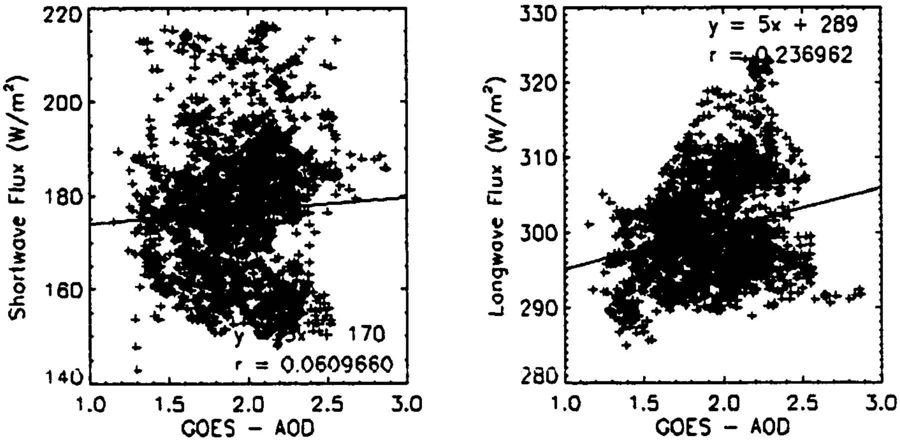

Figure 10.7 – CERES vs. τ_r comparisons for sector 1, 27 August with poor correlation.

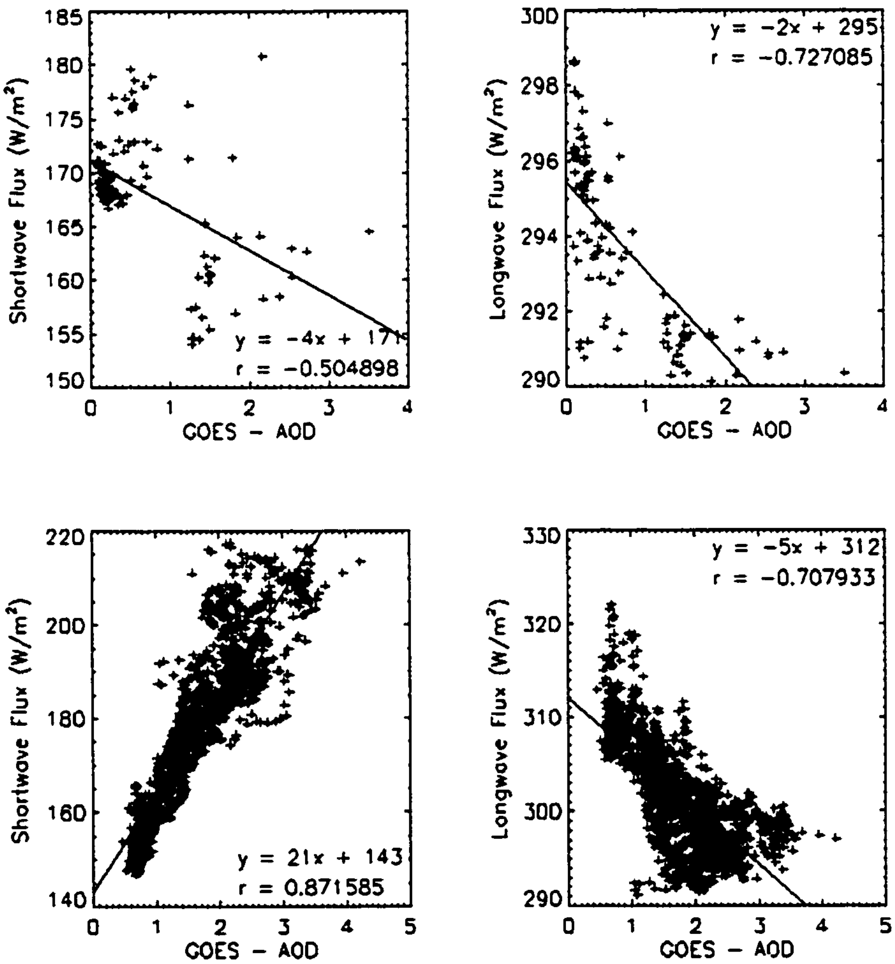

Figure 10.8 – CERES vs. τ_r comparisons for the two locations with significant correlation to LW fluxes (both from sector 4): a) 7 August, b) 27 August.

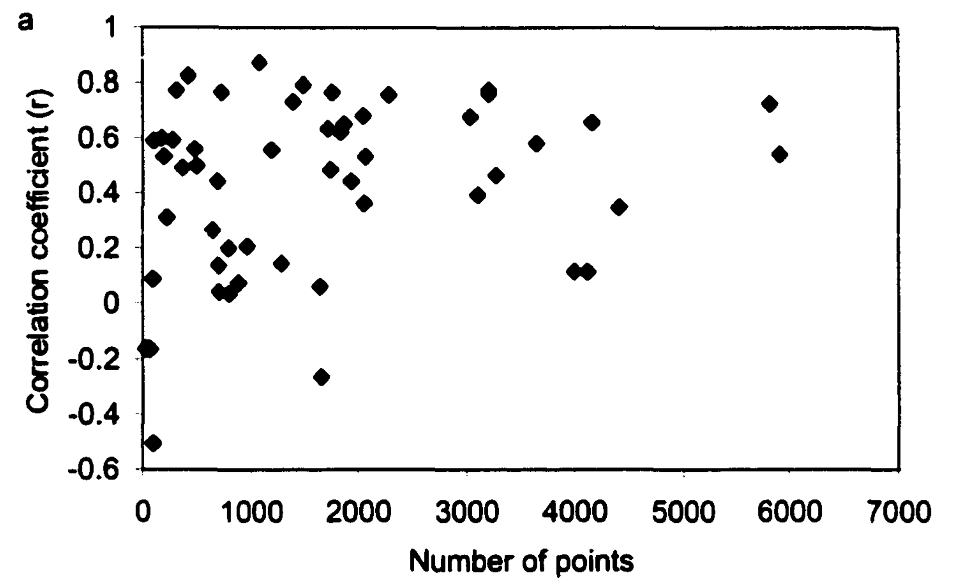

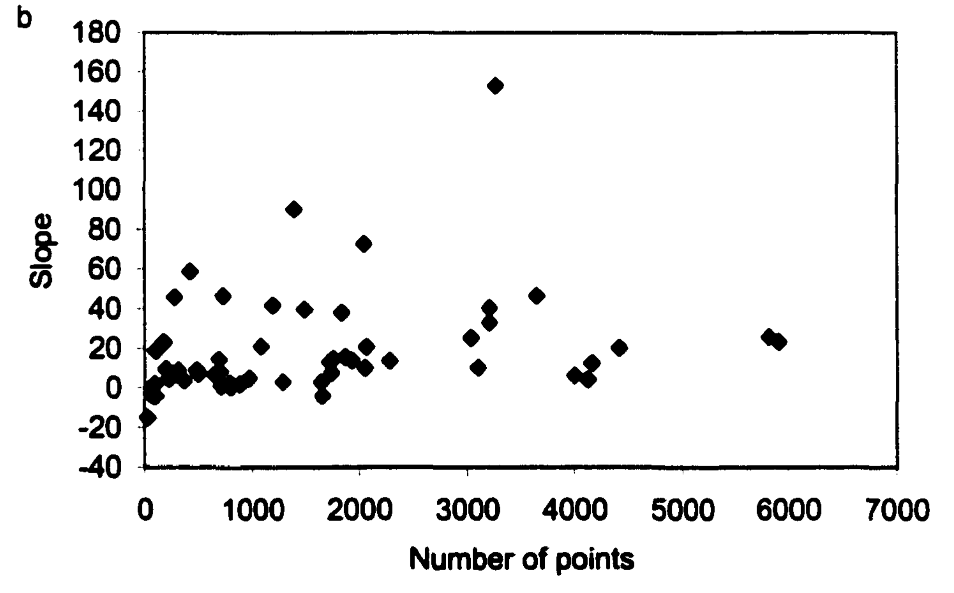

Figure 10.9 – a) The correlation coefficient of SW flux vs. τ_r as a function of number of points in the comparison. b) The slope of the SW flux vs. τ_r relationship.

11. GOES-AOD and Biomass Burning Emissions

Biomass burning in the tropics can severely affect the chemical and radiative properties of the tropical atmosphere. The extent to which this occurs is still under investigation by many scientists. An example of these studies is the collaborative effort of SCAR-B, in which the chemical, microphysical and radiative properties of aerosols emitted from biomass burning in Brazil were investigated. Aerosol mass emission can be used to estimate the transport of biomass burning smoke palls in Brazil (Trosnikov and Nobre, 1997).

The mass of the aerosol plumes can be estimated from the GOES-AOD retrievals using the mass extinction efficiency, which in turn is used here to estimate the emission rates of fires. One method uses one GOES-AOD retrieval and estimates of the atmospheric winds. A second method uses two successive images (30 minutes apart) to estimate the change in mass of the smoke plume. This second method requires a temporal resolution better than that available from polar orbiting sensors, thus it is unique to the GOES-AOD. The estimated emission rates from the two methods are then compared to each other for consistency.

11.1 Single Image Method

The estimation of aerosol mass emissions from a single image requires: an optical depth retrieval, wind speed and direction estimates at the image time, and a mass extinction efficiency parameter for the observed aerosol. The following is a derivation of the emission rate.

Figure 11.1 shows a conceptual smoke plume being transported away from a single fire at some speed U. The mass of the plume, m, inside the bounding box is then a function of the emission rate, e, and the transport time, dt, from the fire to the downwind boundary of the box. This is expressed by:

$$m = e \cdot dt \tag{11.1}$$

The mass of the smoke plume can also be estimated from satellite data. The mass extinction efficiency, α_m, relates the extinction of an aerosol to the mass of the aerosol. Thus the mass of the aerosol in the bounding box is simply:

$$M = \sum \frac{\tau}{\alpha_m} \tag{11.2}$$

However, not all aerosol in the image will be due to the fire; some aerosol are transported into the box, thus, the actual mass emitted from the fire is approximately:

$$m_i = \sum \frac{(\tau - \tau_{nf})}{\alpha_m} \tag{11.3}$$

where τ_{nf} is the "non-fire" aerosol optical depth transported into the box. τ_{nf} is estimated by calculating the average τ along the upwind portion of the box. Last, the transport rate is approximated by the wind speed (U) and the distance (D_i) is from the lead edge of the plume to the downwind edge of the box. Thus, the transport time is calculated:

$$dt = \frac{D_i}{U} \tag{11.4}$$

Therefore, the mass emission rate can be estimated from a single image (e_{si}) by retrieving τ, defining the bounding box, estimating the wind speed and manipulating Equations 11.1, 11.3 and 11.4 for:

$$e_{si} = \frac{U\sum\frac{(\tau-\tau_b)}{\alpha_m}}{D_i} \tag{11.5}$$

This method assumes:

1. The GOES-AOD is accurate.
2. The non-fire aerosol optical depth is spatially homogeneous (thus the subtraction in equation 11.3 is valid).
3. The mass extinction efficiency is constant over the smoke plume.
4. The flux of mass across the cross wind boundaries is negligible.
5. The wind speed used represents the average transport of the smoke plume.
6. Only one fire is present in the bounding box (secondary fires are difficult to detect visually, but could be accounted for)

A fire is denoted in figure 11.2 by a circle which is analyzed to determine e_{si}. It is also circled in the GOES-AOD image in figure 11.3. The bounding box is visually selected and shown in figure 11.4. The smoke plume is assumed to denote the wind direction. The average τ along the upwind boundary of the box is 1.6. Figure 11.4b shows the denoted smoke plume. τ_b is subtracted from this in figure 11.4c where the optical depths are smaller and the plume is easier to detect. The mass extinction efficiency is specified as α_m = 2.73 (Trosnikiv and Nobre, 1997), then the mass is calculated using equation 10.5, $m_i = 1.15 \times 10^8$g. The wind is estimated as 8 m s^{-1} at 850mb from ECMWF reanalysis data. The distance from the fire to the downwind boundary of the box is 22 km. Thus with a transport time of 41 minutes, the emission of this fire at 17:45 UTC is approximately 47 kg s^{-1}.

The uncertainty of the emission rate, e_{si}, is dependent upon the uncertainty of the individual parameters of equation 11.5. First let $f = \tau - \tau_b$, then:

$$\sigma_f = \sqrt{\sigma_\tau^2 + \sigma_\tau^2} = \sqrt{2}\sigma_\tau$$

The uncertainty in the emission rate estimate is:

$$\frac{\sigma_{si}}{e_{si}} = \sqrt{\left(\frac{\sigma_U}{U}\right)^2 + \left(\frac{\sqrt{2}\sigma_\tau}{\tau}\right)^2 + \left(\frac{\sigma_\alpha}{\alpha}\right)^2 + \left(\frac{\sigma_D}{D}\right)^2} \quad (11.6)$$

Where σ_U, σ_τ, σ_α, and σ_D represent the standard deviation of the uncertainty with respect to the aerosol transport speed (u), τ, mass extinction efficiency (α) and distance (D), respectively. The relative uncertainty in the wind speed estimates can be due to model uncertainty as well as the level of aerosol transport. Thus, $\sigma_U/U \sim 0.5$ (or 50%). The optical depth, as shown from validation with surface measurements is between 20 and 30%. The mass extinction can vary with the evolution of the smoke plume – from a young plume to an aged plume – thus the uncertainty is also nearly 50%. Also, the distance estimate is dependent upon the location of the fire center. This is likely estimated within 5 km; transport distances of 50 km result in a 10% uncertainty. Thus, the overall uncertainty in the single image method, σ_{si}, is 80%. This uncertainty can be decreased by analyzing temporal changes in the aerosol field.

11.2 Multi-Image Method

The estimation of aerosol mass emissions from satellite imagery can also be performed using temporal changes in plumes. This assumes that a change in a smoke plume from one image to another image at Δt minutes later is primarily due to the emission of aerosols into the atmosphere by the source. In this method, a box is defined on two successive images. The mass of aerosol in each box is calculated using Equation 10.3. Then, the temporal emission rate, e_{ml}, is calculated:

$$e_{ml} = \frac{m_{t+\Delta t} - m_t}{\Delta t}, \tag{11.7}$$

where m_t is evaluated using Equation 11.5. This method is not available for the 1995 retrievals, because Δt = 3 hours. However, imagery during 1998 is available at 30-minute intervals, and should provide insight into aerosol mass emissions.

This method assumes:

1. The GOES-AOD is accurate between image times,
2. The background aerosol optical depth is spatially homogeneous (thus the subtraction in equation 10.3 is valid).
3. The mass extinction efficiency is constant over the smoke plume.
4. The flux of mass across the cross wind and downwind boundaries is zero.
5. The only source of aerosols is the fire and no significant sinks are present in the time between images.

An example of this method is demonstrated in figure 11.5. The smoke plume is notably smaller (at 15:45 and 16:15 UTC) then at 17:45 UTC. The bounding box is defined in both images where the smoke plume is fully encompassed by the box. This is important, because in this temporal method, no significant aerosol mass is assumed to be transported through the downwind edge of the box. Using equation 11.3, the mass of the plume is noted to grow from 1.35×10^8g to 1.98×10^8g. The aerosol mass emission is then estimated at 17.5 kg s^{-1}. This fire is further investigated at other times and the two results are compared below.

This method is valuable because it makes use of the high temporal resolution of geostationary imagery. While the single-image method could also be used by a polar-orbiting sensor, this method cannot.

It is clear from equation 11.7 that the temporal emission rate estimate is dependent upon fewer parameters than e_{si}. The uncertainty, σ_{mi}, is calculated as:

$$\sigma_{mi} = \sqrt{\left(\frac{2\sigma_{\tau}}{\tau}\right)^2 + \left(\frac{\sigma_{\alpha}}{\alpha}\right)^2} \tag{11.8}$$

The uncertainties used in the σ_{si} estimate result in an uncertainty of σ_{mi}/e_{mi} = 67%, somewhat lower than the σ_{si}/e_{si} estimate. However, this result is likely more accurate because two estimates of τ are differenced, which removes a bias. However, no measurements of aerosol mass emission rates of fires were reported during the SCAR-B experiment. However, emission rate estimates can be compared to: 1) the emission rate used in the smoke plume modeling study by Trosnikov and Nobre (1998) and 2) ABBA estimates of fire data.

11.3 Results

11.3.1 General Results

The fire in figure 11.3 is further analyzed using both emission rate estimates. The time series of the fire emission rate shown in figure 11.7. A similar trend is noted, where the emission rate peaks between 17 and 19 UTC. However, it is evident that e_{mi} is subject to uncertainties that can cause negative emissions.

Analysis of GOES-AOD imagery shows that in estimating e_{mi}, the single fire assumption is violated. The method assumes that the change in mass is solely due to the fire. Figure 11.6 demonstrates how defining the smoke plume can be ambiguous after significant transport and with other smoke plumes in the area. Figure 11.6 shows the smoke plume at different times. Other plumes seem to be appearing in the primary smoke plume. This is further shown in the overall plume mass plotted as a function of time in figure 11.8. It can be seen that the plume size was changed after 18:15 UTC, causing the mass to decrease and the emission rates to be negative. However, until 18:15 UTC, the plume is seen to steadily increase.

Two other fires were investigated showing a large range in emission rates. A fire on 31 August 1998 showed large values of e_{si} with smaller values of e_{mi} (figure 11.9). Emission rate values were in a similar range to the fire shown in figure 11.7. However, a fire on 21 August 1998 showed a large plume generated and transported more than 100 kilometers down wind within 3 hours. In this case, e_{mi} went from near zero to 600 kg/s (figure 11.10). The e_{si} method was much lower, likely because the transport speed was underestimated. While small changes in fire emission rates are less than the large uncertainties, these estimates of emission rates show the possibility of distinguishing between smoldering and faster burning fires.

11.3.2 Comparison with ABBA

The emission rates were also calculated for fires during the SCAR-B experiment in 1995. In 1995, the ABBA algorithm was used to detect fires using GOES-8 3.9 μm imagery. The ABBA algorithm estimates fire temperature and fire area for each fire pixel a fire is detected. The emission rates, e_{si}, are combined with the ABBA fire area to determine a emission rate per area of fire (kg s^{-1} m^{-2}). The temporal method was not used because Δt = 3 hours was deemed too long for the assumptions to be valid. The area-weighted emission rate is compared to fire temperature for fires in the Alta Floresta area (figure 11.11a) and Ji Parana (figure 11.11b). Emission rates tend to increase with fire temperature.

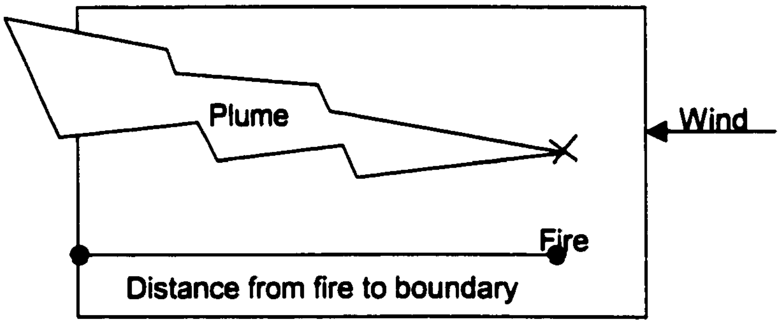

Figure 11.1 – Conceptual diagram of deriving fire mass emissions from a single GOES-AOD retrieval.

Figure 11.2 – GOES-8 visible image on 31 August 1998 over Central Brazil showing biomass burning fires (circled).

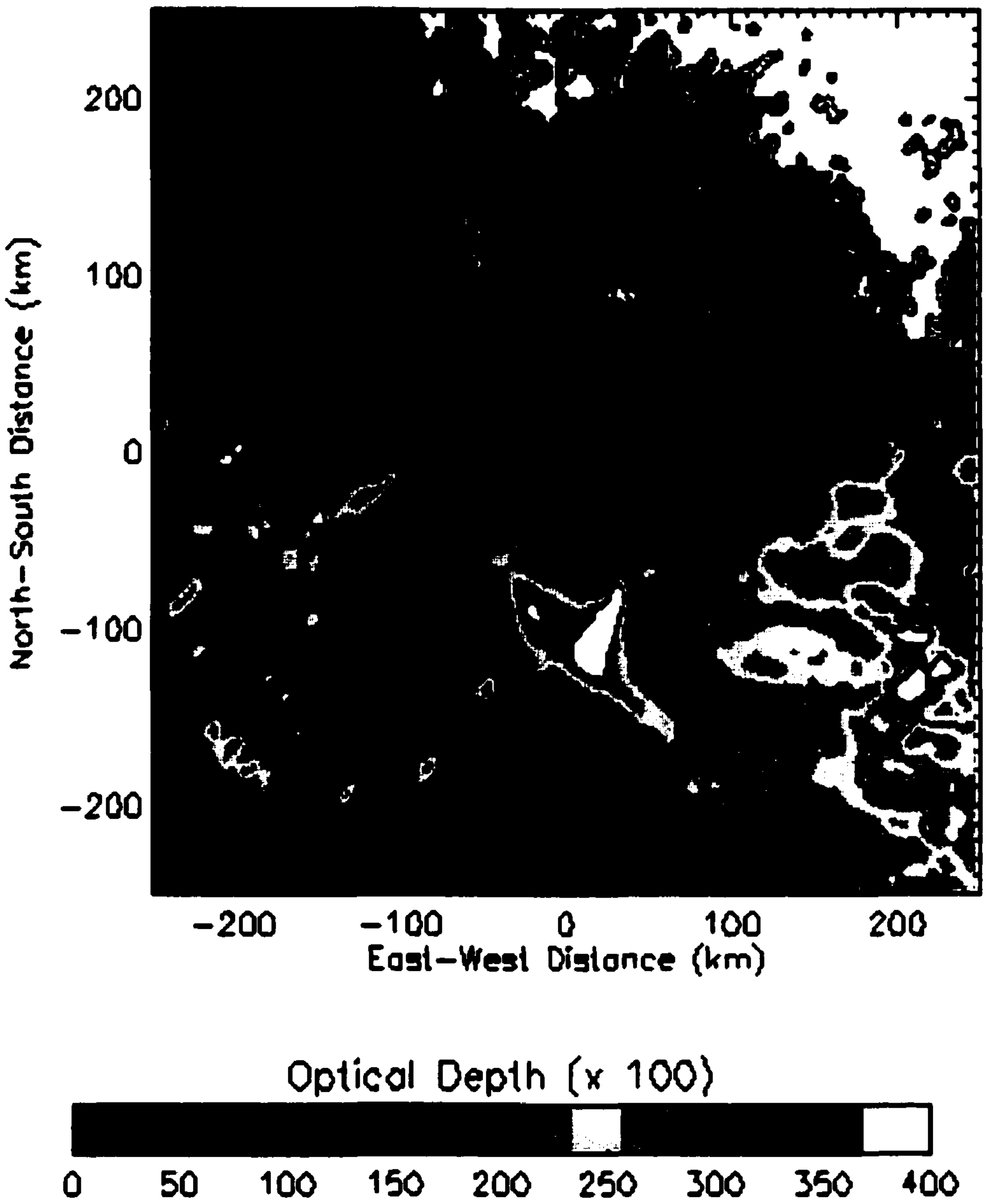

Figure 11.3 – GOES-AOD retrieval for the image in figure 11.2. Fire circled in figure 11.2 is also circled here.

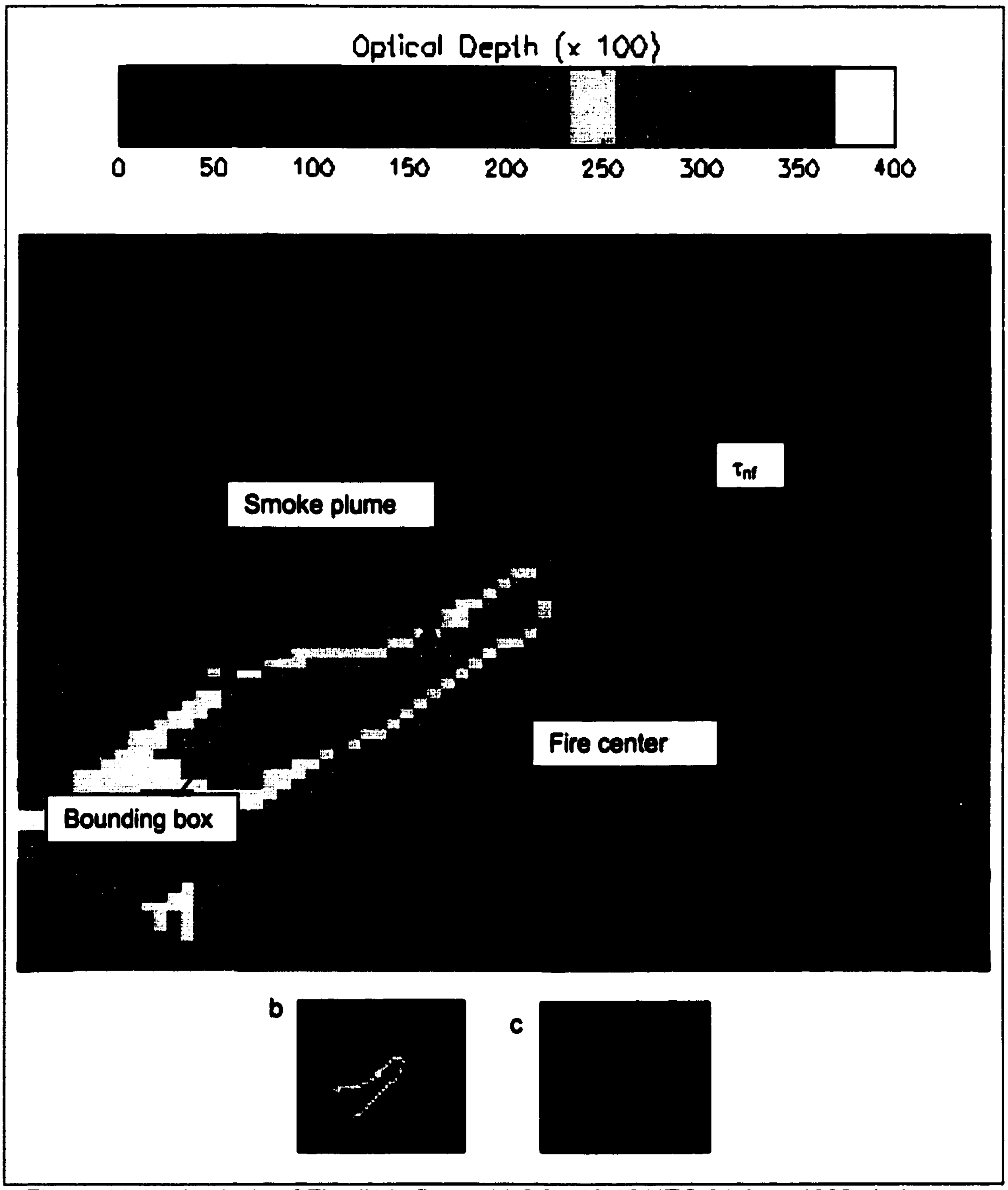

Figure 11.4 – Analysis of Fire #1 in figure 11.2 for 16:45 UTC 31 Aug. 1998 a) close up view of fire pixels, b) same as part a, but smaller, c) same as part b minus τ_{nf}.

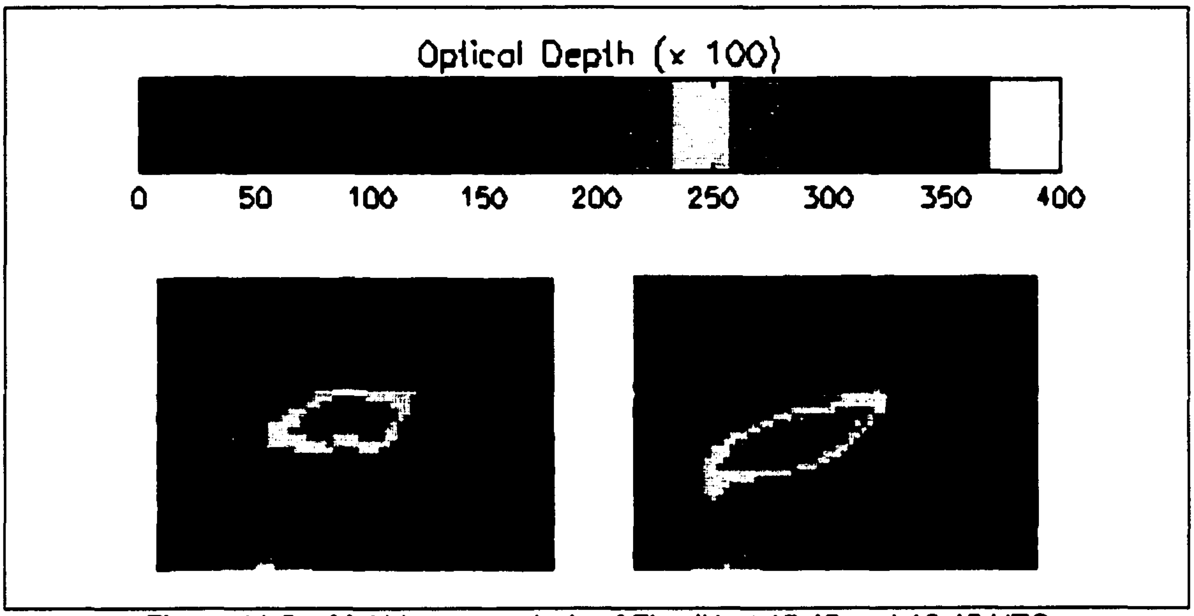

Figure 11.5 – Multi-image analysis of Fire #1 at 15:45 and 16:45 UTC

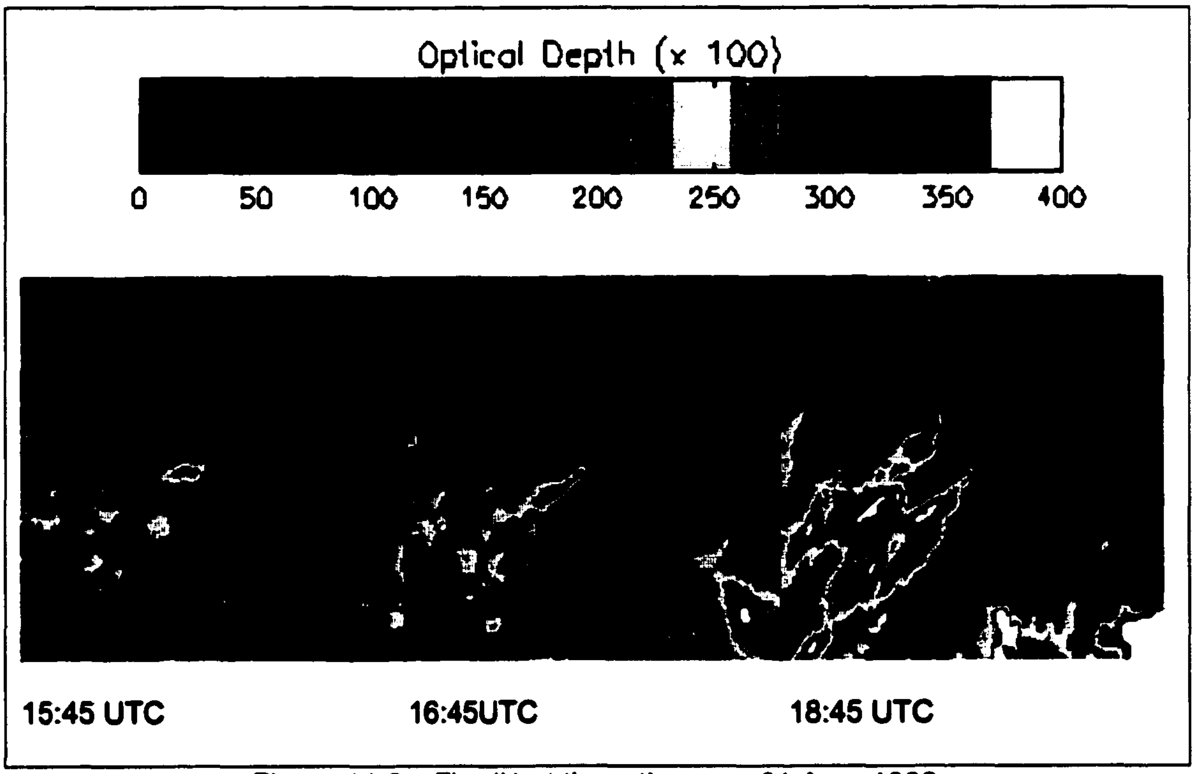

Figure 11.6 – Fire #1 at three times on 31 Aug. 1998.

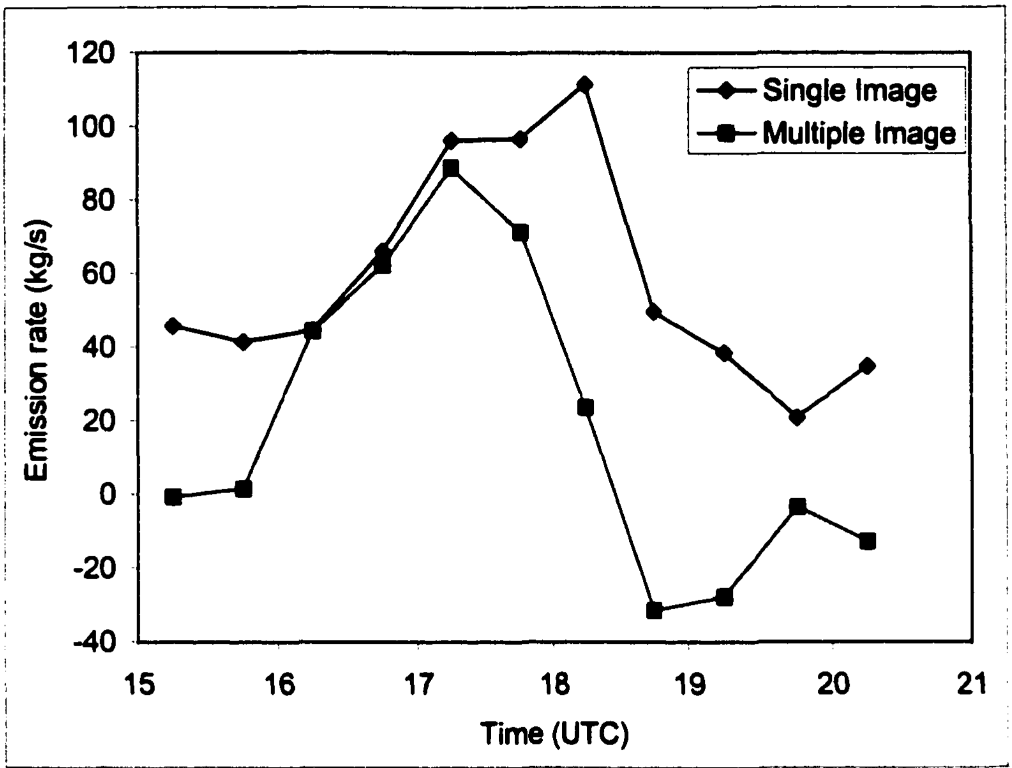

Figure 11.7 – Comparison of the two emission rate estimates.

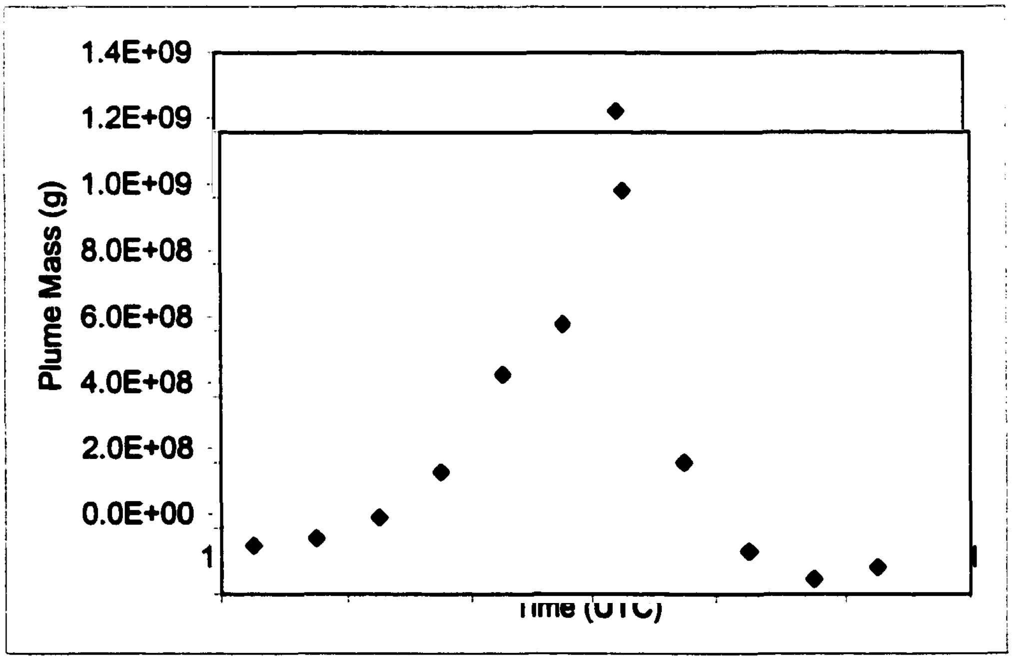

Figure 11.8 – Plume mass as a function of time

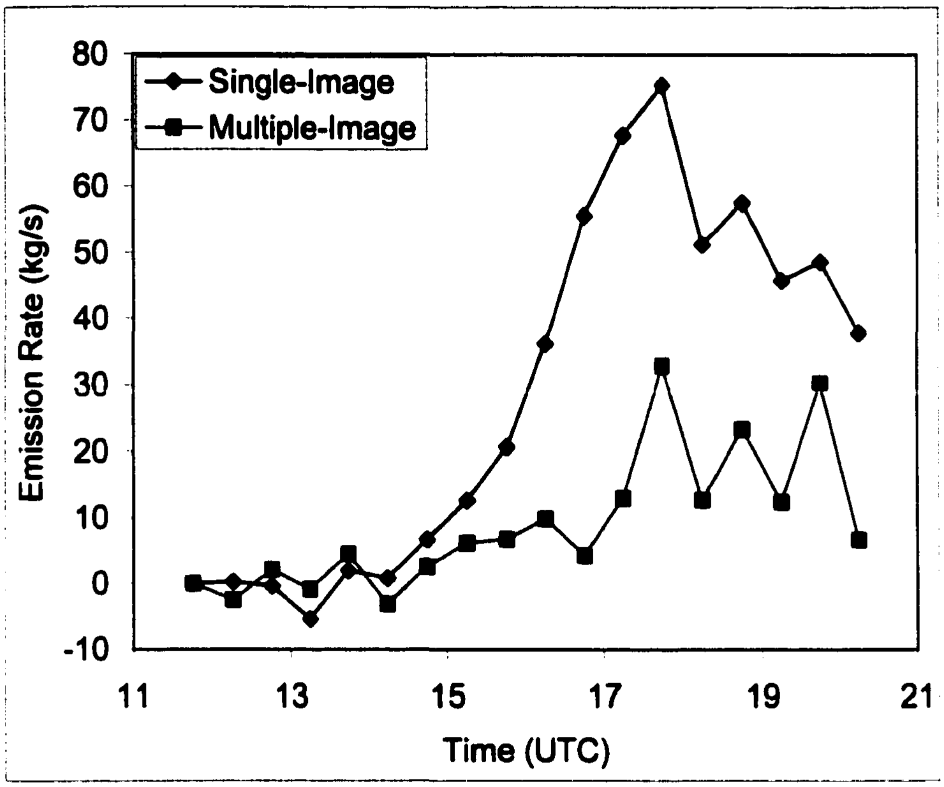

Figure 11.9 – Comparison of emission rate estimates for fire on 31 August 1998.

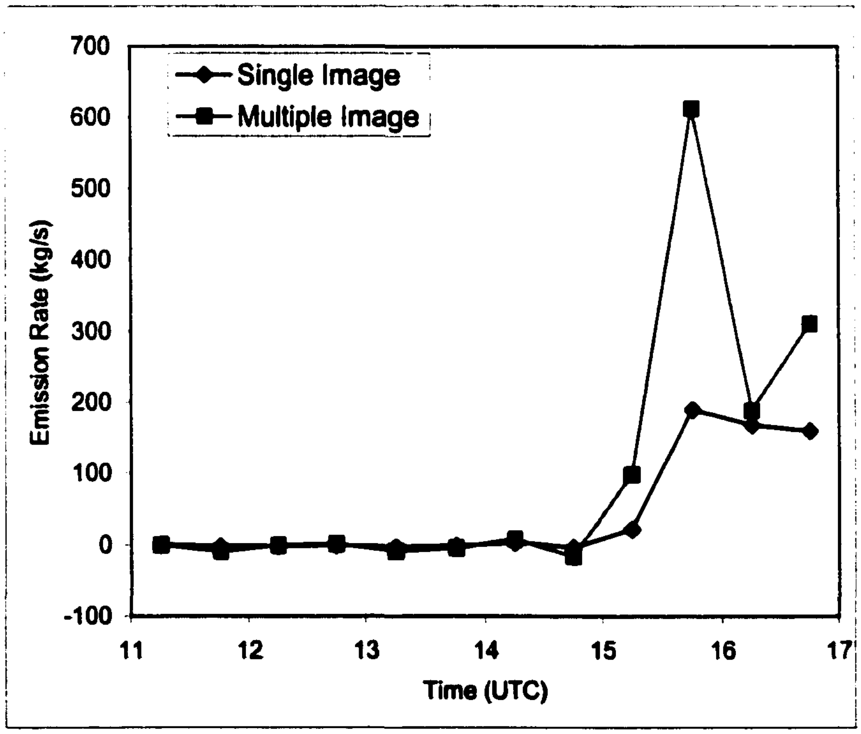

Figure 11.10 – Comparison of emission rate estimates for fire on 21 August 1998.

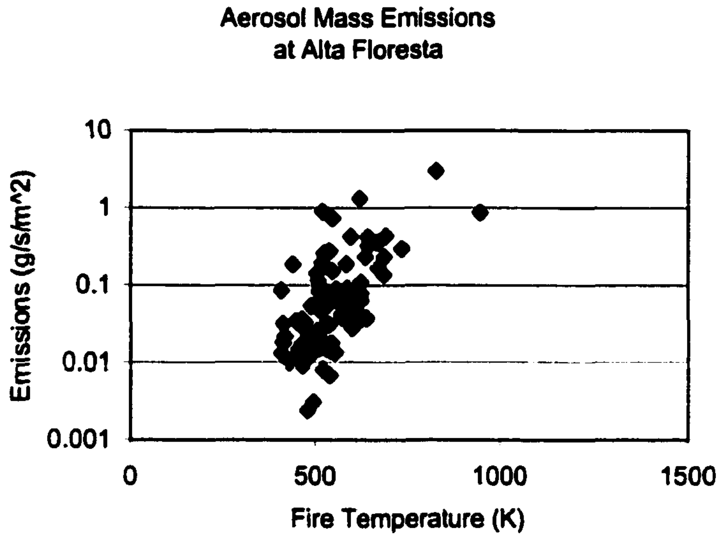

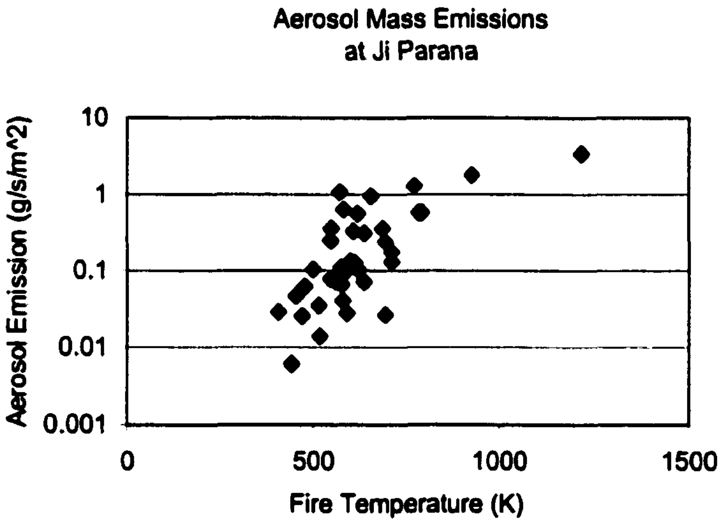

Figure 11.11 – Emission rates for areas near Alta Floresta and Ji Parana for 1995 normalized by the fire area compared to the fire temperature (both quantities derived from ABBA estimates).

12. Conclusions

The following summarizes the conclusions of the previous chapters. For further results, or explanations, refer to the chapter from which the results were discussed.

12.1 Discussion

A precursor to developing and testing the GOES-AOD algorithm was the calibration of the GOES-8 sensor. The sensor was calibrated to within ±5% using the ocean surface in a relatively aerosol-free area of the world. The calibration compared well with previous reports of calibration adjustments. It also provided a time series of the calibration degradation showing that the response is continuing to decline. These results have proven useful to the research community, having been accepted for publication in the *Journal of Atmospheric and Oceanic Technology* as well as being referenced by Christopher (1999) and making the retrievals in this work possible.

The aerosol retrieval algorithm used the DISORT model to solve the radiative transfer equation. The model calculated aerosol scattering for eight wavelength bands at which the GOES-8 visible imager is sensitive. The gaseous absorption is estimated from a tropical atmosphere and the vertical distribution of aerosols is assumed to have a maximum at the surface.

Retrievals are made utilizing a three step process on a pixel-by-pixel basis. The first step is the creation of a mosaic where, for each observation time, the darkest pixel is chosen to represent "background" (or clear-sky) conditions. Then atmospheric correction is performed to transform the "background" radiance to a surface reflectance value. Lastly, satellite detected radiances from other days are transformed into aerosol optical depth using the surface reflectance obtained at that pixel. These processes are discussed in detail below.

The backbone of this approach is the creation of a background image from a time-series of satellite images. An image is created for each satellite observation time; in the case of SCAR-B, these occur at 11:45, 14:45 and 17:45 UTC. For each time period, the images are co-located to minimize minute variations in the satellite orbit. While choosing the darkest pixel removes any cloud contamination, cloud masking is required to remove cloud shadows that occur at large solar zenith angles which can contaminate a background image.

The second step removes atmospheric effects on the satellite-detected radiance using the radiative transfer approached described above. Atmospheric effects, including gaseous absorption, molecular scattering and aerosol extinction, are removed via inversion of the satellite detected radiance for a surface reflectance estimate (ρ_s). Normal variations in the atmospheric state which cause subtle changes in gaseous absorption and molecular scattering generally are generally undetectable by the GOES-8 imagery. Thus the primary uncertainty in this step results from the assumption of the background AOD.

The third step compares imagery from other days of the month to the surface reflectance from step 2. The change in radiance is assumed to be due to biomass burning aerosol, and is retrieved as such using the radiative transfer method described above. The retrieved AOD (GOES-AOD) is valid at 0.50 μm.

The following conclusions are grouped by the chapter in which they were described:

Conclusions of the sensitivity study include:

- Overall uncertainty is $\Delta\tau = \pm 0.34\tau$ (34%) for an aerosol with unknown characteristics or if the aerosol model is completely unknown.
- Uncertainty decreases to $\Delta\tau = \pm 0.18\tau$ (18%) when the aerosol characteristics are relatively well-known
- The retrieval uncertainty also increases as ρ_s increases.
- Retrieval uncertainty varies with aerosol type and is largest for the mineral dust aerosol model.
- If the aerosol model is completely unknown, it is best to guess the industrial aerosol, which results in an overall uncertainty of approximately ±0.21 and relatively no bias (for random aerosol distributions).
- A bias is likely to occur if the aerosol model is incorrectly estimated. Again, bias errors are largest when incorrectly assuming a dust aerosol.
- Retrievals are most sensitive to the assumed single scatter albedo and refractive index and less to the calibration
- Conversely, the retrieved ρ_s is more sensitive to calibration than to aerosol optical properties.
- Independently estimating the sensitivity of the retrieval to each parameter, then combining these sensitivities using the sum of the squares overestimates the retrieval uncertainty
- Uncertainty increases with scattering angle.
- Error in the height of the aerosol layer causes an AOD retrieval error less than 0.06.
- Nonspherical particles can cause a negative bias in the GOES-AOD algorithm.

- NO_2 absorption causes negligible error in the GOES-AOD retrieval of biomass burning areas, yet becomes important in heavily polluted urban environments.
- The 6S simulation suggests the Lambertian surface reflectance assumption error can be large, especially for brighter cerrado regions.
- The temporal changes in surface reflectance during a two month composite should be small, but could still affect the retrieval accuracy.
- Conclusions of the validation against ground truth (AERONET) include:
- Comparisons to eight AERONET sites show high correlation. Correlations ranged from 0.78 to 0.97. These high correlations occurred for both the 1995 SCAR-B comparisons as well as the two observation sites in 1998.
- Relative errors were less than 38% with the exception of Brasilia and Campo Grande. The larger Brasilia error was due to low optical depths and an aerosol not well represented by biomass burning. The Campo Grande site provided larger error because the albedo in the region was higher and the region was cerrado. As shown in chapter 8, the uncertainty of assuming a Lambertian surface in the cerrado regions is larger.
- Relative uncertainties were generally within those estimated from the sensitivity study presented in chapter 8.
- Comparisons were biased; seven of eight sites showed a positive bias. This bias could result from an incorrect aerosol model, particularly the single scatter albedo. The bias was weakest at Alta Floresta, a site located close to the burning regions. Sites further away would encounter aged smoke, which would have a larger single scatter albedo, thus biasing the measurements high.
- Diagnostic analysis of the retrieval error provided insight to the cause of some discrepancies. The error at Los Fieros and Concepcion showed correlation

between the error and optical depth, suggesting a different aerosol model would be more accurate or possibly a calibration error. A significant trend in the error at Campo Grande as a function of time of day suggests either an incorrect aerosol phase function, or significant BRDF contamination.

- Daily averaging of comparisons significantly decreases the retrieval noise. Hundreds of comparisons were averaged for 46 and 55 daily comparisons at Concepcion and Los Fieros, respectively. In both cases, the standard deviation and relative error decreased. Also, the correlation increased for daily averaging.
- Comparisons grouped by time of day showed significant trends. While the correlations were high, the slope of the comparisons ranged from 0.8 to 1.4. This suggests either an error in the aerosol size distribution (causing the phase function to be incorrect) or contamination from the BRDF of the forest.
- The GOES imager provides numerous images of a smoke plume per day. The number of observations ranged from a minimum of at least four to as many as 20 (with half hour temporal resolution).
- The GOES-AOD performed retrievals with a much lower "loss rate" than a polar orbiter. The GOES-AOD missed 14% of the days on which an AERONET observation was made. This is a large increase from the 60-70% loss rate possible from a polar orbiting instrument. The loss of the 14% is due to either 1) days where data was not archived or 2) days where fewer images were available.
- Conclusions of the comparison to MAS-AOD include:
- The GOES-AOD retrieval showed comparable ability to the "state-of-the-art" retrieval performed using the MODIS Airborne Simulator. Comparisons between

GOES-AOD and MAS-AOD showed large correlations and low standard errors. Nine of fifteen comparisons had correlations larger than 0.71.

Conclusions of the comparison of GOES-AOD retrievals to CERES flux measurements include:

- GOES-AOD is correlated to CERES SW flux in 16 of 51 comparisons during August 1998.
- Poor correlation is likely due to: insufficient number of comparison points, surface reflectance variations, cloud contamination and co-location errors between GOES and CERES data.
- Poor correlations are also present where the range in τ_r is small.
- Only 2 comparisons had significant correlation between GOES-AOD and CERES LW flux, which is expected, since aerosols have a small effect on longwave radiation.
- The slopes for the CERES SW flux vs. GOES-AOD ranged from 5 to 45 W/m^2 for comparisons with a sufficiently large number of points and range in τ_r which is in the range described by Li et al (1999, manuscript submitted to *J. Appl. Met.*) and Christopher et al. (1999, manuscript submitted to *Geophys. Res. Letters*)

Conclusions of the estimation of aerosol mass emission rates from biomass burning fires include:

- Two methods were derived for the estimation of the aerosol mass emission rates from fires: a single image method and a temporal method.
- Comparison of the methods showed agreement when the smoke plume was easily detectable from other smoke plumes.
- The methods showed large differences when the smoke plume is small and when the plume overlaps with nearby fire plumes.

- The temporal estimation method is susceptible to negative emission rates.

12.2 Future Work

Future Work resulting from this research could include:

- Expand the GOES-AOD to areas over the continental U.S. where the aerosol optical properties are different and the optical depths are lower.
- Investigate this method with the Meteosat Second Generation satellite, which will have an AVHRR-like channel selection in the visible region.
- Incorporate a better understanding of aerosol transport in the emission rate estimates.
- Automate the emission rate estimates and use GOES-AOD to estimate the total aerosol mass emissions during daylight observations of GOES-8 to monitor biomass burning.

13. References

Abdou, W. A., J. V. Martonchik, R. A. Kahn, R. A. West, and D. J. Diner, A modified linear mixing method for calculating atmospheric path radiances of aerosol mixtures, *J. Geophys. Res.*, **102**, 16883-16888, 1997.

Ackerman, S. A., Remote sensing aerosols using satellite infrared observations, *J. Geophys. Res.*, **102**, 17069-17080, 1997.

Bohren, C. F. and D. R. Huffman, *Absorption and Scattering of Light by Small Particles*, John Wiley & Sons, pp. 530, 1983.

Bremer, J. C., J. G. Baucom, H. Vu, M. P. Weinreb and N. Pinkine, Estimation of long-term throughput degradation of GOES-8 and –9 visible channels by statistical analysis of star measurements. *Conference on Earth Observing Systems III, 20 July 1998*, W. L. Barnes, Ed., 1998.

Bréon, F. M., D. Tanré, P. Lecomte and M. Herman, Polarized reflectance of bare soils and vegetation: Measurements and models, *IEEE Trans. Geosci. Remote Sens.*, **33**, 487-499, 1995.

Carlson, T. N. and J. M. Prospero, The large-scale movement of Saharan air outbreaks over the Northern Equatorial Atlantic, J. Appl. Met., 11, 283-297, 1972.

Carlson, T. N. and P. Wendling, Reflected radiance by NOAA 3 VHRR as a function of optical depth for Saharan dust, *J. Appl. Met.*, **16**, 1368-1371, 1977.

Carlson, T. N., Atmospheric turbidity in Saharan dust outbreaks as determined by analyses of satellite brightness data, *Mon. Wea. Rev.*, **107**, 322-335, 1979.

Christopher, S. A., Satellite remote sensing of aerosol optical properties over biomass burning regions, proceedings of *AGU 1999 Fall Meeting*, F205, 1999.

Chu, D. A., Y. J. Kaufman, L. A. Remer, and B. N. Holben, Remote sensing of smoke from MODIS airborne simulator during the SCAR-B experiment, , *J. Geophys. Res.,* **103**, 31979-31988, 1998.

Csiszar, I. and G. Gutman, Mapping global land surface albedo from NOAA AVHRR, *J. Geophys. Res.*, **104**, 6215-6228, 1999.

Dave, J. V., Effect of aerosols on the estimation of total ozone in an atmospheric column from the measurement of its ultraviolet radiation, *J. Atmos. Sci.*, **35**, 899-911, 1978.

Diner, D. J., W. A. Abdou, T. P. Ackerman, K. Crean, H. R. Gordon, R. A. Kahn, J. V. Martonchik, S. R. Paradise, B. Pinty, M. M. Versteraete, M. Wang, and R. A. West, Multi-angle Imaging Spectro-Radiometer: Level 2 Aerosol retrieval algorithm, *EOS ATBD-JPL D-11400, Rev. B*, 81 pp., 1996

Durkee, P. A., The relationship between marine aerosol particles and satellite-detected radiance, *Ph. D. Dissertation at Colorado State University*, Atmospheric Science Paper #380, 124 pp., 1984.

Durkee, P. A., D. R. Jensen, E. E. Hindman, and T. H. Vonder Haar, The relationship between marine aerosol particles and satellite-detected radiance, *J. Geophys. Res.*, **91**, 4063-4072, 1986.

Durkee, P. A., F. Pfeil, E. Frost and R. Shema, Global analysis of aerosol particle characteristics, *Atm. Environ.*, **25A**, 2457-2471, 1991.

Ellrod, G. P., R. V. Achutuni, J. M. Daniels, E. M. Prins, and J. P. Nelson III, An assessment of GOES-8 Imager Data Quality. *Bull. Amer. Meteor. Soc.*, **79**, 2509-2526, 1998.

Fraser, R. S., Satellite measurement of mass of Saharan dust in the atmosphere, *Appl. Optics*, **15**, 2471-2479, 1976.

Fraser, R. S., Y. J. Kaufman, and R. L. Mahoney, Satellite measurements of aerosol mass and transport, Atm. Env., 18, 2577-2584, 1984.

Fraser, R. S., and Y. J. Kaufman, Calibration of satellite sensors after launch. *Appl. Opt.*, **25**, 1177-1185, 1986.

Greenwald, T. J. and G. L. Stephens, *Application of a Adding-Doubling Model to Visibility Problems*, C.S.U. Atm. Sci. Paper, 89 pp, 1988.

Greenwald, T. J., S. A. Christopher, and J. Chou, Cloud liquid water path comparisons from passive microwave and solar reflectance satellite measurements: Assessment of sub-field-of-view cloud effects in microwave retrievals, *J. Geophys. Res.*, **102**, 19585-19596, 1997.

Griggs, M, Measurement of atmospheric aerosol optical thickness over water using ERTS-1 data, J. Air Poll. Control. Assoc., 25, 622-626, 1975.

Haywood, J.M., V. Ramaswamy and B. J. Soden, Tropospheric aerosol climate forcing in clear-sky satellite observations over the oceans, *Science*, **283**, 1299-1303, 1999.

Herman, J. R., P. K. Bhartia, O. Torres, C. Hsu, C. Seftor, and E. Celarier, Global distributions of UV-absorbing aerosols from Nimbus-7/TOMS data, *J. Geophys. Res.*, **102**, 16911-16922, 1997.

Herman, M., J. L. Deuzé, C. Devaux, P. Goloub, F. M. Bréon, and D. A. Tanré, Remote sensing of aerosols over land surfaces induing polarization measurements and application to POLDER measurements, *J. Geophys. Res.*, **102**, 17039-17050, 1997.

Hess, M., P. Koepke, and I. Schult, Optical properties of aerosols and clouds: The software package OPAC, *Bull. Amer. Met. Soc.*, **79**, 831-844, 1998.

Hindman, E. E., P. A. Durkee, P. C. Sinclair, and T. H. Vonder Haar, Detection of marine aerosol particles in coastal zones using satellite imagery, *Int. J. Remote Sensing*, **5**, 577-586, 1984.

Holben, B. N., T. F. Eck, I. Slutsker, D. Tanré, J. P. Buis, A. Setzer, E. Vrmote, J. A. Reagan, Y. J. Kaufman, T. Nakajima, F. Lavenu, I. Jankowiak, and A. Smirnov, AERONET -- A federated instrument network and data archive for aerosol characteristics, *Remote Sens. Environ.*, 66, 1-16, 1998.

Houghton, H. G., *Physical Meteorology*, MIT Press, Cambridge, MA, 442 pp., 1985.

Husar, R. B., J. M. Prospero, and L. L. Stowe, Characterization of tropospheric aerosols over the oceans with the NOAA advanced very high resolution radiometer optical thickness product, *J. Geophys. Res.*, **102**, 16889-16909, 1997.

Jankowiak, I and D. Tanré, Satellite climatology of Saharan dust outbreaks: method and preliminary results, *J. of Climate*, **5**, 646-656, 1992.

Kaufman, Y. J., Satellite sensing of aerosol absorption, *J. Geophys. Res.*, **92**, 4307-4317, 1987.

Kaufman, Y. J., R. S. Fraser, and R. A. Ferrare, Satellite measurement of large-scale air pollution: methods, *J. Geophys. Res.*, **95**, 9895-9909, 1990.

Kaufman, Y. J., and J. H. Jospeph, Determination of surface albedos and aerosol extinction characteristics from satellite imagery, *J. Geophys. Res.*, **87**, 1287-1299, 1982.

Kaufman, Y, J, and C. Sendra, Algorithm for automatic atmospheric correction to visible and near-IR satellite imagery, *Int. J. Remote Sens.*, **8**, 1357-1381, 1988.

Kaufman, Y. J. and L. A. Remer, Detection of forests using mid-IR reflectance: An application for aerosol studies, *IEEE Trand. Geosci. Remote Sens.*, **32**, 672-683, 1994.

Kaufman, Y. J., D. Tanré, L. A. Remer, E. F. Vermote, A. Chu and B. N. Holben, Operational remote sensing of tropospheric aerosol over land from EOS moderate resolution imaging spectro-radiometer, *J. Geophys. Res.*, **102**, 17051-17068, 1997.

Kaufman, Y. J., P. V. Hobbs, V. W. J. H. Kirchhoff, P. Artaxo, L. A. Remer, B. N. Holber, M. D. King, D. E. Ward, E. M. Prins, K. M. Longo, L. F. Mattos, C. A. Nobre, J. D. Spinhirne, Q, Ji, A. M. Thompson, J. F. Gleason, S. A. Christopher, and S.-C. Tsay, Smoke, Clouds, and Radiation-Brazil (SCAR-B) experiment, *J. Geophys. Res.,* **103**, 31783-31805, 1998.

Kaufman, Y. J., Tanré, D., Karnieli, A., and Remer, L. A., Re-evaluation of dust absorption and radiative forcing of climate using satellite and ground based remote sensing. submitted to *Science*, 1999.

Kidder, S. Q. and T. H. Vonder Haar, *Satellite Meteorology: An introduction,* Academic Press, Inc., pp. 466, 1995.

King, M. D., Y. J. Kaufman, D. Tanré, and T. Nakajima, Remote sensing of tropospheric aerosol from space: Past, present and future, *Bull. Amer. Met. Soc.*, **80**, 2229-2259, 1999.

Legrand, M., J. J. Bertrand, M. Desbois, L. Menenger, and Y. Fouquart, The potential of infrared satellite data for retrieval of Saharan-Dust optical depth over Africa, *J. Climate*, **28**, 309-318, 1989.

Legrand, M., M. Debois, and K. Vovoir, Satellite detection of Saharan dust: Optimized imaging during nighttime, *J. Clim.,* **1**, 256-265, 1988.

Lenoble, J. and C. Brogniez, A comparative review of radiation aerosol models, *Beitr. Phys. Atmosph.*, **57**, 1-20, 1984.

Leroy, M., J. L. Deuzé, F. M. Bréon, O. Hautecoeur, M. Herman, J. C. Buriez, D. Tanré, S. Bouffiès, P. Chazette, and J. L. Roujean, Retrieval of atmospheric properties and surface bi-directional reflectances from POLDER/ADEOS, *J. Geophys. Res.*, **102**, 17023-17038, 1997.

Liu, C. H., A. J. Chen and G. R. Liu, An image-based retrieval algorithm of aerosol characteristics and surface reflectance for satellite images, *Int. J. Remote Sens.*, **17**, 3477-3500, 1996.

Lyons, W. A., J. C. Dooley, Jr. and K. T. Whitby, Satellite detection of long-range pollution transport and sulfate aerosol hazes, *Atm. Env.*, **12**, 621-631, 1978.

Lushine, J. B., A dust layer in the Eastern Caribbean, Mon. Wea. Rev., 103, 454-455, 1975.

McClatchey, R. A., R. W. Fenn, J. E. A. Selby, F. E. Volz, and J. S. Garing, Optical properties of the atmosphere, AFCRL-TR-71-0279, Enviro. Res. Papers, No. 354, L. G. Hanscom Field, Bedford, MA, 1971.

McLellan, A., Satellite remote sensing of large scale local atmospheric pollution, In *Proc. Int. Clean Air Congr.*, Pittsburgh, PA, Air Pollution Control Assoc., 1380-1388, 1971.

Martonchik, J. V., Determination of aerosol optical depth and land surface bi-directional reflectance using multiangle imagery, *J. Geophys. Res.*, **102**, 17015-17022, 1997.

Mayfield, B. M., Sahara dust over the Atlantic, Mar. Wea. Log, 19, 346-347, 1975.

Mekler, Y. and Y. J. Kaufman, The effect of Earth's atmosphere on contrast reduction for a nonuniform surface albedo and the 'two-halves' field, *J. Geophys. Res.*, **85**, 4067-4083, 1980.

Menzel, W. P. and J. F. W. Purdom, Introducing GOES-I: The first of a new generation of Geostationary Operational Environmental Satellites. *Bull. Amer. Meteor. Soc.*, **75**, 757-781, 1994.

Minnis, P and W. L. Smith Jr., Cloud and radiative fields derived from GOES-8 during SUCCESS and the ARM-UAV spring 1996 flight series. *Geophys. Res. Lett.*, **25**, 1113-1116, 1998.

Mishchenko, M. I., A. A. Lacis, B. E. Carlson, and L. D. Travis, Nonsphericity of dust-like tropospheric aerosols: implications for aerosol remote sensing and climate modeling, *Geophys. Res. Letters*, **22**, 1077-1080, 1995.

Mishchenko, M. I., L. D. Travis, and D. W. Mackowski, T-matrix computations of light scattering by nonspherical particles: a review, *J. Quant. Spectrosc. Radiat. Transfer*, **55**, 535-575, 1996.

Nakajima, T. and A. Higurashi, AVHRR remote sensing of aerosol optical properties in the Persian Gulf region, summer 1991, *J. Geophys. Res.*, **102**, 16935-16946, 1997.

Norton, C. C., F. R. Mosher, B. Hunton, D. W. Martin, D. Santek, and W. Kuhlow, A model for calculating desert aerosol turbidity over the oceans from geostationary satellite data, *J. Appl. Met.*, **19**, 633-644, 1980.

Prins, E. M., J. M. Fetz, W. P. Menzel, and D. E. Ward, An overview of GOES-8 diurnal fire and smoke results for SCAR-B and 1995 fire season in South America, *J. Geophys. Res.*, **103**, 31821-31835, 1998.

Prospero, J. M., D. Westphal, and R. Poirot, The great northeastern United Stated haze event of 16-17 July 1999: A comparison of chemical transport models and measurement, in *Proc.AGU 1999 Fall Mtg.*, San Francisco, CA, pg. 211, 1999.

Rahman, H., B. Pinty, and M. M. Verstraete, Coupled surface atmosphere reflectance (CSAR) model 2. Semiempirical surface model usable with NOAA advanced very high resolution radiometer data, *J. Geophys. Res.*, **98**, 20791-20801, 1993.`

Rondeaux, G. and M. Herman, Polarization of light reflected by crop canopies, *Remote Sens. Environ.*, **38**, 68-75, 1991.

Russell, P. B., P. V. Hobs and L. L. Stowe, Aerosol properties and radiative effects in the United States East Coast haze plume: An overview of the tropospheric aerosol radiative forcing observational experiment (TARFOX), *J. Geophys. Res.*, **104**, 2213-2222, 1999.

Sandmeier, S. and K. I. Itten, A physically-based model to correct atmospheric and illumination effects in optical satellite data of rugged terrain, *IEEE Trans. Geosci. Rem. Sens.*, **35**, 708-717, 1997.

Soufflet, V., D. Tanré, A. Royer, and N. T. O'Neill, Remote sensing of aerosols over Boreal forest and lake water from AVHRR data, *Remote Sens. Env.*, **60**, 22-34, 1997.

Stamnes, K. and R. Swanson, A new look at the discrete ordinate method for radiative transfer calculations in anisotropically scattering atmospheres, *J. Atmos. Sci.*, **38**, 387-399, 1981.

Stamnes, K., S. C. Tsay, W. Wiscombe and K. Jayaweera, Numerically Stable Algorithm for Discrete-Ordinate-Method Radiative Transfer in Multiple Scattering and Emitting Layered Media, *Appl. Opt.* **27**, 2502-2509, 1988.

Stephens, G. L., *Remote sensing of the lower atmosphere: An introduction*, Oxford University Press, New York, 523 pp., 1994.

Stroeve, J., A. Nolin, and K. Steffen, Comparison of AVHRR-derived and in situ surface albedo over the Greenland ice sheet, *Rem. Sens. Env.*, **62**, 262-272, 1997.

Stowe, L. L., A. M. Ignatov, and R. R. Singh, Development, validation and potential enhancements to the second-generation operational aerosol product at the national environmental satellite, data and information service of the national oceanic and atmospheric administration, *J. Geophys. Res.*, **102**, 16923-16934, 1997.

Tanré, D., P. Y. Deschamps, C. Devaux, and M. Herman, Estimation of Saharan aerosol optical thicknass from blurring effects in Thematic Mapper data, *J. Geophys. Res.*, **93**, 15955-15964, 1988.

Tanré, D. and M. Legrand, On the satellite retrieval of Saharan dust optical thickness over land: Two different approaches, *J. Geophys. Res.*, **96**, 5221-5227, 1991.

Tanré, D. , Y. J. Kaufman, M. Herman, and S. Mattoo, Remote sensing of aerosol optical properties over oceans using MODIS/EOS spectral radiances, *J. Geophys. Res.*, **102**, 16971-16988, 1997.

Trosnikov, I. V. and C. A. Nobre, Estimation of aerosol transport from biomass burning areas during the SCAR-B experiment, *J. Geophys. Res.*, **103**, 32129-32137, 1998.

Tsay, S.-C., M. D. King, G. T. Arnold, and J. Y. Li, Airborne spectral measurements of surface anisotropy during SCAR-B, *J. Geophys. Res.*, **102** 31943-31953, 1997.

Tsonis, A. A., and W. R. Leaitch, Minimum detectable pollution levels from satellite imagery, *Geophys. Res. Letters*, **13**, 56-59, 1986.

Twomey, S., *Introduction to the mathematics of inversion in remote sensing and indirect measurements*, Dover Publications, Inc., New York, 243 pp., 1977.

Veefkind, J. P., G. de Leeuw, and P. A. Durkee, Retrieval of aerosol optical depth over land using two-angle satellite radiometry during TARFOX, *Geophys. Res. Letters*, **25**, 3135-3138, 1998.

Vermote, E. F., D. Tanré, J. L. Deuzé, M. Herman, and J.-J. Morcrette, Second simulation of the satellite signal in the solar spectrum, 6S: An overview. *IEEE Trans. Geosci. Remote Sens.*, **35**, 675-686, 1997.

Wallace, J. M. and P. V. Hobbs, *Atmospheric Science: An introductory survey,* Academic Press, Inc., pp. 467, 1977.

Wentz F. J., A well-calibrated ocean algorithm for SSM/I, *J. Geophys. Res.*, **102**, 8703-8718, 1997.

Wielicki, B. A., B. R. Barkstrom, E. F. Harrison, R. B. Lee, III, G. L. Smith, and J. E. Cooper, Clouds and the Earth's Radiant Energy System (CERES): An Earth Observing System Experiment, *Bull. Amer. Met. Soc.*, **77**, 853-868, 1996.

Williams, D. H. and J. L. Cogan, Estimation of visibility from satellite imagery, *Appl. Optics*, **30**, 414-419, 1991.

World Meteorological Organization (CAS)/Radiation Commission of IAMAP Meeting of experts on aerosol and their climatic effects, WCP 55, Williamsburg, Virginia, USA, 28-30, March 1983.